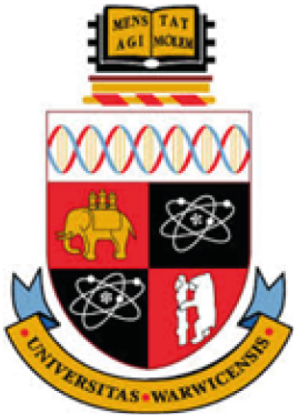

Electrochemistry and Applications of sp^2 Carbon Materials: From Graphite to Graphene

by

Guohui Zhang

Thesis

Submitted to the University of Warwick

for the Degree of

Doctor of Philosophy

Supervisor: Prof. Patrick R. Unwin

Department of Chemistry

September 2016

In memory of my beloved grandpa, Mr. Deshun Zhang (張德順), *without whom I would have never made it this far in my life. Miss you forever!*

Table of Contents

List of Figures

List of Tables

Acknowledgements

Over the period of my PhD study in the UK, I am so lucky to have a chance to know and work with many great people, who have kindly helped me in different aspects.

First and foremost, I would like to express my deep gratitude to my supervisor, Prof. Patrick Unwin, for his professional instructions, continuous support and encouragement throughout my PhD. His wide horizon of knowledge, and commitment and attitude in both research and life inspire me a lot.

I would also like to thank Prof. Julie Macpherson for general discussions and her willingness to help on many kinds of things.

I deeply appreciate the help of Dr. Paul Kirkman, Dr. Aleix Güell, Dr. Kim McKelvey, Dr. Yangrae Kim, Dr. Anatolii Cuharuc, Dr. Maxim Joseph, Dr. Robert Lazenby, Dr. Stanley Lai, Dr. Anisha Patel, Ashley Page, Minkyung Kang, Faduma Maddar, Dr. Barak Aaronson, Dr. Thomas Miller, Sze-yin Tan, Dr. Joshua Byers, Dr. Rehab Al Botros, Dr. Changhui Chen, Sharel Pei E., Danqing Liu, and Lingcong Meng on the projects carried out in different stages of my PhD. I owe a thank you to all the people in the Warwick Electrochemistry and Interfaces Group and I enjoy the years with you guys. I am proud to be one of the WEIGers!

I also want to thank my friends, Xiyan Tong, Liping Zhang, Dr. Liang Sun, Zhongnan Wang, Dr. Shuai Hou, Chongyu Zhu, Haojia Chen, Zhida Li, Siqing Liang and Dr. Juan Wei, for the hugs and laughs, and we have had a wonderful time together. ‘Shandong Guild Hall’ has been an important part in our oversea study.

A special thanks with love goes to Yimimi, who is always sweet and comforting, and brings me sunshine. I appreciate the enormous tolerance and care from her. She is the treasure of my life and it is great to have her by

my side. *Will you marry me and spend one lifetime with me?* I would also like to thank my family – especially my dad, Shizhong Zhang, my mom, Guichun Wang, and my sister, Wenyu Zhang, for their generous support and considerable understanding, making me get to the goals step by step. I love you!

Declaration

This thesis is submitted to the University of Warwick in support of my application for the degree of Doctor of Philosophy. It has been composed by myself and has not been submitted in any previous application for any degree. All work contained is entirely my own, except for the contributions specified below:

Chapter 1 As detailed below, part of the text was taken from the work I prepared for 2 review articles with Prof. Patrick. R. Unwin, Dr. Aleix G. Güell and Miss. Sze-yin Tan.

Chapter 2 Figures 2.2 and 2.4 were prepared by Dr. Paul M. Kirkman.

Chapter 3 Simulation was performed by Dr. Anatolii Cuharuc. Scanning tunnelling microscopy image was recorded by Dr. Aleix G. Güell.

Chapter 4 Simulation was performed by Miss. Sze-yin Tan and surface activity imaging measurement was done by Dr. Anisha N. Patel.

Chapter 5 Data analysis of fast scan cyclic voltammetry was done with help of Dr. Kim McKelvey and Dr. Paul M. Kirkman. Simulation was performed by Dr. Anatolii Cuharuc. Surface reactive patterning was done by Dr. Anisha N. Patel. Some figures were improved by Dr. Paul M. Kirkman.

Chapter 6 Conductive-atomic force microscopy and transmission electron microscopy imaging were done by Dr. Aleix G. Güell and Dr. Robert A. Lazenby, respectively. Some figures were improved by Dr. Aleix G. Güell.

Chapter 7 X-ray photoelectron spectroscopy characterisation was performed by Dr. Marc Walker from the Department of Physics at Warwick.

Parts of this thesis have been published, as detailed below:

Chapter 1

Patrick R. Unwin, Aleix G. Güell, and Guohui Zhang. Nanoscale Electrochemistry of sp^2 Carbon Materials: From Graphite and Graphene to Carbon Nanotubes. *Acc. Chem. R*es., **2016**, *49*, 2041–2048.

Aleix G. Güell, Sze-yin Tan, Patrick R. Unwin, and Guohui Zhang. Electrochemistry at Highly Oriented Pyrolytic Graphite (HOPG): Toward a New Perspective. *Electrochemistry of Carbon Electrodes*. Wiley-VCH Verlag GmbH & Co. KGaA, **2015**, ch. 2, 31–82.

Chapter 3

Guohui Zhang, Anatolii S. Cuharuc, Aleix G. Güell, and Patrick R. Unwin. Electrochemistry at Highly Oriented Pyrolytic Graphite (HOPG): Lower Limit for the Kinetics of Outer-sphere Redox Processes and General Implications for Electron Transfer Models. *Phys. Chem. Chem. Phys.*, **2015**, *17*, 11827-11838.

Chapter 4

Guohui Zhang, Sze-yin Tan, Anisha N. Patel, and Patrick R. Unwin. Electrochemistry of $Fe^{3+/2+}$ at Highly Oriented Pyrolytic Graphite (HOPG) Electrodes: Kinetics, Identification of Major Electroactive Sites and Time Effects on the Response. *Phys. Chem. Chem. Phys.*, **2016**, *18*, 32387-32395.

Chapter 5

Guohui Zhang, Paul M. Kirkman, Anisha N. Patel, Anatolii S. Cuharuc, Kim McKelvey, and Patrick R. Unwin. Molecular Functionalization of Graphite Surfaces: Basal Plane versus Step Edge Electrochemical Activity. *J. Am. Chem. Soc.* **2014**, *136*, 11444-11451.

Chapter 6

Guohui Zhang,† Aleix G. Güell,† Paul M. Kirkman, Robert A. Lazenby, Thomas S. Miller, and Patrick R. Unwin. Versatile Polymer-Free Graphene

Transfer Method and Applications. *ACS Appl. Mater. Interfaces*, **2016**, *8*, 8008–8016. († equal contribution)

Chapter 7

Guohui Zhang, Marc Walker, and Patrick R. Unwin. Low-Voltage Voltammetric Electrowetting of Graphite Surfaces by Ion Intercalation/Deintercalation. *Langmuir*, **2016**, *32*, 7476–7484.

Work to which I have contributed, but is not featured in this thesis, is detailed below:

Guohui Zhang, Paul M. Kirkman, Aleix G. Güell, and Patrick R. Unwin. Tunable Electrochemical Patterning of the Electrical Properties of Graphene. (In preparation)

Anatolii S. Cuharuc,† Guohui Zhang,† and Patrick R. Unwin. Electrochemistry of Ferrocene Derivatives on Highly Oriented Pyrolytic Graphite (HOPG): Quantification and Impacts of Surface Adsorption. *Phys. Chem. Chem. Phys.*, **2016**,*18*, 4966-4977. († equal contribution)

Aleix G. Güell,† Anatolii S. Cuharuc,† Yang-Rae Kim,† Guohui Zhang, Sze-yin Tan, Neil Ebejer, and Patrick R. Unwin. Redox-Dependent Spatially Resolved Electrochemistry at Graphene and Graphite Step Edges. *ACS Nano*, **2015**, *9*, 3558–3571. († equal contribution)

Yang-Rae Kim, Stanley C. S. Lai, Kim McKelvey, Guohui Zhang, David Perry, Thomas S. Miller, and Patrick R. Unwin. Nucleation and Aggregative Growth of Palladium Nanoparticles on Carbon Electrodes: Experiment and Kinetic Model. *J. Phys. Chem. C*, **2015**, *119*, 17389–17397.

Abstract

This thesis can be divided into three themes: (i) the electrochemistry of sp^2 carbon materials, with a focus on graphite and graphene, where electron transfer (ET) kinetics and surface functionalisation were considered; (ii) methodology development for graphene transfer, to facilitate the fabrication of versatile tools for microscopy research and allow the properties of supported and suspended graphene to be readily assessed and compared; (iii) the electrowetting of graphite, providing a new mechanism for droplet actuation on a conducting surface with an applied electric field.

There is a large body of literature that the basal plane of highly oriented pyrolytic graphite (HOPG) is inert or has little electroactivity for outer-sphere redox couples and adsorbed species. Here, the model is revisited with the macroscopic ET kinetics studies of three classical (outer-sphere) redox couples on different grades of HOPG using a droplet-cell setup. It is shown that the ET kinetics for all of the redox species studied is fast on all grades of HOPG (comparable to metal electrodes), despite the low density of electronic states (DOS) on graphite. This is in line with the results where the 'special' redox couple, $Fe^{3+/2+}$, associated with a slow kinetics, is tested. Moreover, localised surface mapping measurements of HOPG using scanning electrochemical cell microscopy (SECCM), reveal a relatively uniform activity on basal plane and step edges of HOPG towards $Fe^{3+/2+}$, highlighting that the basal plane is electroactive and the major site for the ET kinetics of $Fe^{3+/2+}$.

The next goal is to elucidate whether adsorbed electroactive anthraquinone-2,6-disulfonate (AQDS) can be used as a marker of step edges, previously regarded as the main electroactive sites of graphite. Step edges are shown to have little effect on the extent of adsorbed electroactive AQDS in macroscopic studies. The amount of adsorbed electroactive AQDS and the ET kinetics are independent of the step edge coverage, as determined by fast scan cyclic voltammetry-SECCM. Further, SECCM reactive patterning

shows essentially uniform and high activity across the basal surface of HOPG, indicative of the dominance of basal plane in HOPG electroactivity.

Regarding the close relation between graphene and graphite, effort is put to introduce a polymer-free method for transferring chemical vapour deposition (CVD)-grown graphene, to arbitrary substrates, using an organic/aqueous biphasic configuration. Avoiding any polymeric contamination, graphene is coated on arbitrary substrates, such as atomic force microscopy (AFM) tips and transmission electron microscopy (TEM) grids, generating tools for conductive AFM and high resolution TEM imaging. Furthermore, electrochemical and wetting measurements at either a freestanding graphene film or a copper-supported graphene area, are readily made and compared.

As an example of the myriad potential applications of graphite, electrowetting is demonstrated at HOPG, using cyclic voltammetry, with significant changes in contact angle and relative contact diameter seen. These are comparable to the widely studied electrowetting-on-dielectric (EWOD) system, but over a much lower voltage range. Electrowetting is found to be due to the intercalation/de-intercalation of anions between the graphene layers of graphite, driven by the applied potential, providing a new mechanism for electrowetting and diversifying the means by which electrowetting can be controlled and applied.

Abbreviations

AC Alternating current

AFM Atomic force microscopy

AHDS Anthrahydroquinone-2,6-disulfonate

AQDS Anthraquinone-2,6-disulfonate

BPPG Basal plane pyrolytic graphite

CA Contact angle

CE Counter electrode

CNT Carbon nanotube

CV Cyclic voltammetry

CVD Chemical vapour deposition

DC Direct current

DOS Density of electronic states

DP Dirac point

ECP Electrochemical pretreatment

EPPG Edge plane pyrolytic graphite

ET Electron transfer

EWOD Electrowetting-on-dielectric

FEM Finite element method

FSCV Fast scan cyclic voltammetry

FWHM Full width at half-maximum

GC Glassy carbon

HOPG Highly oriented pyrolytic graphite

LDOS Local density of electronic states

MWNT Multi-walled carbon nanotube

PDMS Polydimethylsiloxane

PMMA Polymethylmethacrylate

QRCE Quasi-reference counter electrode

RCD Relative contact diameter

RE Reference electrode

SCCM Standard cubic centimetres per minute

SECCM Scanning electrochemical cell microscopy

SECM Scanning electrochemical microscopy

SECM-AFM Combined scanning electrochemical microscopy-atomic force microscopy

SEM Scanning electron microscopy

SLG Single-layer graphene

SMCM Scanning micropipette contact method

STM Scanning tunneling microscopy

STS Scanning tunneling spectroscopy

SWNT Single-walled carbon nanotube

TEM Transmission electron microscopy

TM-AFM Tapping mode-AFM

WE Working electrode

XPS X-ray photoelectron spectroscopy

Glossary of Symbols

A Area

C_d Double layer capacitance

C^0 Differential capacitance

C_O Concentration of species O

C_O^* Bulk concentration of species O

C_R Concentration of species R

C_R^* Bulk concentration of species R

D Diffusion coefficient

D_O Diffusion coefficient of species O

D_R Diffusion coefficient of species R

D_{Redox} DOS of the redox species O and R

d Contact diameter

E Potential

E^0 Standard redox potential

$E^{0\prime}$ Formal electrode potential

E_{eq} Equilibrium potential

E_{surf} Surface potential in SECCM

ΔE_p Peak-to-peak separation

E_1 Starting potential in CV

E_2 Reversal potential in CV

$E_{1/2}$ Half-wave potential in voltammetry

$E_{1/4}$ Potential value at i/i_p =1/4

$E_{3/4}$ Potential value at i/i_p =3/4

F Faraday's constant

$f = F/RT$

f_a Active site fractional surface coverage

g Gravitational acceleration (9.8 m s^{-2})

h Height of droplet

I Electron tunnelling current

I_D D band intensity of Raman spectrum

I_{2D} 2D band intensity of Raman spectrum

I_G G band intensity of Raman spectrum

i Electrochemical current

i_{AC} AC component of SECCM barrel current

i_a Anodic current

i_{act} Surface current in SECCM

i_c Cathodic current

i_{DC} DC component of SECCM barrel current

i_{Ini} The i_{DC} value of meniscus before contact

i_{nf} Nonfaradaic current

i_p Peak current in voltammetry

k Boltzmann constant

k_0 Standard heterogeneous electron transfer rate constant

k_b Backward reaction rate constant

k_{exc} Exchange rate constant

k_f Forward reaction rate constant

k_s Standard ET rate constant at the defect

k_t Mass transport rate constant

$\boldsymbol{n}$ The unit vector normal to a surface

n Electrons transferred; number of measurements

O Oxidised form of the redox species

Q Charge

R Molar gas constant; Reduced form of the redox species

R_u Uncompensated resistance

r Radius of droplet

r_s Surface roughness

T Temperature

V Voltage in STS

V_1 Bias between QRCEs

V_2 Applied potential in SECCM

V_{sol} Potential difference applied between the WE and CE

V_u Ohmic loss of potential

v Scan rate

W_O Probability density function for species O

W_R Probability density function for species R

α Charge transfer coefficient

Γ_{ads} Surface coverage of absorbed electroactive material

Γ_O^* Maximum surface coverage of species O

γ_{LV} Liquid-vapour surface tension

Δ The Laplace operator in cylindrical coordinates

ε_F^0 Standard Fermi level of redox species

ε_O The most probable energy level of the solution states for species O

ε_R The most probable energy level of the solution states for species R

η Overpotential

Θ_{ads} Fractional surface coverage of absorbed electroactive material

θ CA of a droplet

θ_0 CA of a droplet on a flat surface

θ_r CA of a droplet on a rough surface

λ Reorganisation for electron transfer

λ_i Inner component of the reorganisation energy

λ_s Outer component of the reorganisation energy

λ_O The reorganisation energy for species O

λ_R The reorganisation energy for species R

ρ Solution density

σ Solution conductivity

Φ The least squares correlation

φ Electric potential in FEM simulations

ψ Dimensionless kinetic parameter

Chapter 1 Introduction

This chapter presents an overview of carbon materials and, in particular, the structure and electronic properties of highly oriented pyrolytic graphite (HOPG). It further introduces some fundamental electrochemistry theories that will be considered in this thesis. Previous electrochemistry studies of HOPG are summarised and new insights from recent correlative-electrochemical microscopy measurements are provided. Graphene production and transfer methods are generally discussed and electrowetting is briefly elucidated. These topics are developed in subsequent chapters.

1.1 Carbon Materials

1.1.1 Allotropes of Carbon

Carbon is an important element with widespread abundance in nature. When a group of carbon atoms are bonded together, a variety of allotropes of carbon materials are formed, such as diamond, graphite, graphene, (single-walled and multi-walled) carbon nanotube (SWNT/MWNT), fullerene, amorphous carbon and glassy carbon (GC) (Figure 1.1). Due to excellent electric, electrochemical and mechanical properties, carbon materials - prepared in different ways - are widely used in fundamental studies and myriad applications.

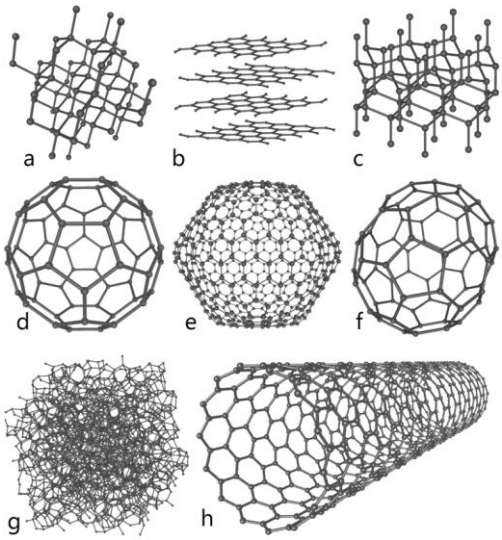

Figure 1.1 Representative allotropes of carbon materials: (a) diamond, (b) graphite, (c) lonsdaleite, (d-f) fullerences, (g) amorphous carbon and (h) carbon nanotube. Courtesy of Michael Ströck.

Carbon materials can be classified into different categories, according to the hybridisation of carbon atoms, which describes the mixing of original atomic orbitals into hybrid orbitals for connection with other atoms. There are three kinds of hybridisation concerning carbon atoms, *i.e.* sp, sp^2 and sp^3, corresponding to a carbon atom that can be bonded to two, three and four other atoms, respectively (Figure 1.2). Among the allotropes of carbon, diamond comprises of pure sp^3 hybridised carbon atoms, whereas other carbon materials (*e.g.* graphite, graphene and carbon nanotubes) are

composed of sp^2 hybridised atoms and regarded as the research focus of this thesis.

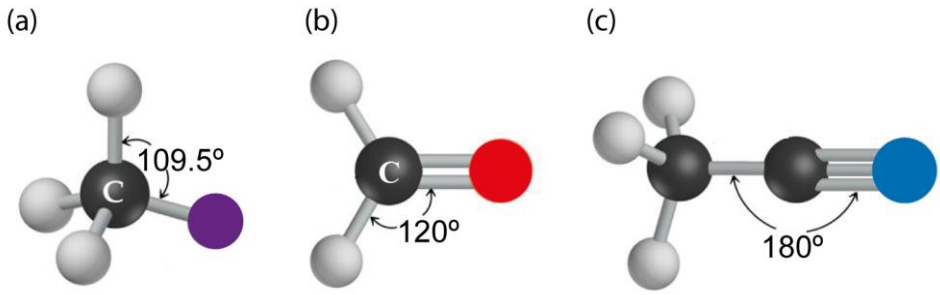

Figure 1.2 Three types of hybridisation for carbon atoms: (a) sp^3, (b) sp^2 and (c) sp.

In reviewing the sp^2 carbon materials, graphene, a one-atom thick planar sheet of carbon atoms that are arranged in a two-dimensional (2D) honeycomb crystal lattice, is considered as the basic element of some other sp^2 carbon structures.[1,2] As shown in Figure 1.3, the 2D graphene layer can be partially wrapped up into 0D buckyballs, rolled into 1D nanotubes (buckytubes), or wholly stacked into 3D graphite. As a result, different surface structure motifs are generated, sphere for buckyballs, sidewalls and open ends for carbon nanotubes, and basal plane and step edges for graphite/graphene, as well as point defects (most are vacancies) on the surfaces in some cases due to the practical sample preparation processes. These materials are closely related and the roles played by the structural features for applications have been extensively characterised by many techniques.

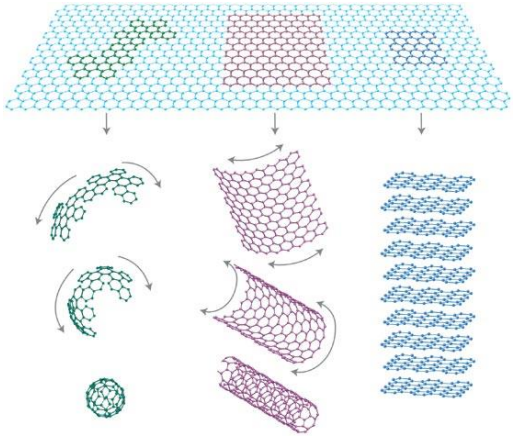

Figure 1.3 Schematic illustration of graphene as a building material for other carbon allotropes of different dimensionalities, from which 0D buckyballs, 1D carbon nanotubes and 3D graphite can be formed. Adapted from Ref. [1].

1.1.2 Highly Oriented Pyrolytic Graphite

1.1.2.1 Structure

Highly oriented pyrolytic graphite (HOPG), consisting of stacked graphene layers (Figure 1.4), with the inter-plane spacing or stacking distance between the layers of 0.3354 nm,[3] has been studied intermittently for several decades, and is usually adopted as a model material and as a comparison to other types of carbon materials, due to the well-defined structures (basal plane and step edges) and ease with which the surface can be prepared (by Scotch tape and mechanical cleavage).[4]

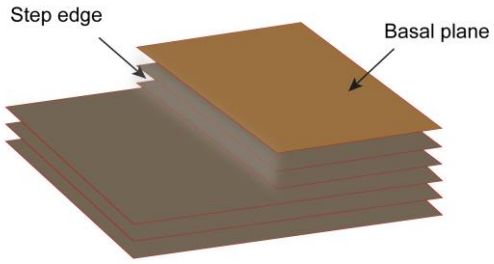

Figure 1.4 Structural illustration of HOPG.

In each graphene sheet of HOPG, there are two crystallographically equivalent atoms in the unit cell, designated A and B (Figure 1.5a). Each carbon atom in graphene is bonded to each of its three nearest neighbours

by a strong planar σ-bond. At equilibrium, the C-C σ-bonds are 0.142 nm long and are at an angle of 120˚ to each other.[3] These bonds are responsible for the planar structure of graphene and for its exceptional mechanical[5] and thermal properties.[6] The fourth valence electron of carbon, in the half-filled $2p_z$ orbital, orthogonal to the graphene plane, forms a weak π-bond by overlap with other $2p_z$ orbitals.[7] Thus, there is a significant difference in strength between planes (easy exfoliable[7]), and within the plane (Young's modulus of 1 TPa[5,8]).

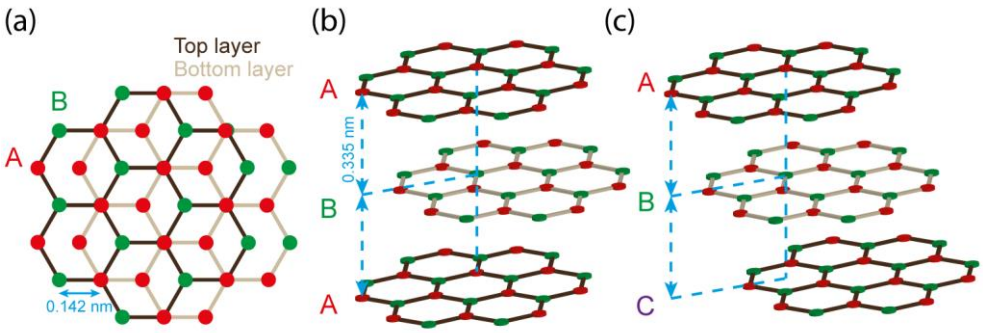

Figure 1.5 (a) Schematics of the graphite crystal structure of AB stacked graphite. Side views for (b) Bernal (ABA) stacking and (C) rhombohedral (ABC) stacking.

The graphene sheets in HOPG can adopt two possible arrangements or stacking order: hexagonal and rhombohedral,[9] with the type of stacking having important implications for the electronic structure.[10,11] Hexagonal or Bernal stacking is the most stable arrangement and the one most observed in HOPG.[3] In the simple case of a graphene bilayer, the A atom of one hexagonal layer is situated directly above the B atom of the other, and is known as AB stacking. When a third layer is introduced so that it mirrors the first layer, the resulting arrangement is Bernal, or ABA, stacking (Figure 1.5b). Rhombohedral, or ABC, stacking involves displacing the third graphene layer with respect to the second layer with the same vector as the second layer with respect to the first, such that the A atom in the third layer is directly above the B atom in the second layer (Figure 1.5c). Rhombohedral or ABC stacking is less stable and is found in HOPG or natural crystal graphite in a proportion less than 10 %.[12]

It is common to provide the mosaic spread as a parameter to quantify the degree of perfection of HOPG; the lower the angle, the higher the quality of HOPG. HOPG quality is categorised with a grade terminology which depends on the suppliers, with the main ones being GE Advanced Ceramics (GEAC) and SPI Supplies. The highest quality is termed ZYA (GEAC) or SPI-1 with mosaic spread of 0.4 ± 0.1˚. HOPG grades of lower quality are: ZYB or SPI-2 (mosaic spread 0.8 ± 0.2˚); ZYD (1.2 ± 0.2˚); and ZYH or SPI-3 grades (3.5 ± 1.5˚). An exceptional high-quality but ungraded HOPG sample, originating from Dr. A. Moore, Union Carbide (now GE Advanced Ceramics), termed AM grade[4,13] in this thesis, exhibits a low density of step edges and large basal plane areas, and has been used extensively in some studies (*vide infra*).

HOPG is particularly suitable for providing considerable large areas of pristine, clean atomically flat surfaces by simple exfoliation. The use of Scotch tape to peel off the top layers of HOPG and reveal a fresh surface is the most common procedure,[14] but alternative mechanical cleavage procedures are also available.[15] Due to this simplicity in sample preparation, HOPG surfaces have been widely characterised at the atomic level with scanning probe techniques such as scanning tunnelling microscopy (STM) [14,16] and atomic force microscopy (AFM).[17]

Atomic resolution images of the graphite basal plane highlight particular technique-dependent features that provide considerable information on the local structure. For STM imaging, for example, basal plane surfaces exhibit a triangular lattice instead of the honeycomb structure expected for the hexagonal crystal lattice of graphite (Figure 1.6). This is because STM creates images of the local density of electronic states (LDOS) at the Fermi level[18] rather than of the atomic arrangement, thereby revealing the non-equivalence of the carbon atoms on the surface as shown in Figure 1.6, as a consequence of the influence of the underlying layer of graphite structure. This behaviour is also observed in graphene flakes with two or more atomic-thick layers.[19] In the absence of this interlayer coupling (or for monolayer

graphene), all surface carbon atoms are identical and a symmetrical honeycomb structure is seen in the STM image.

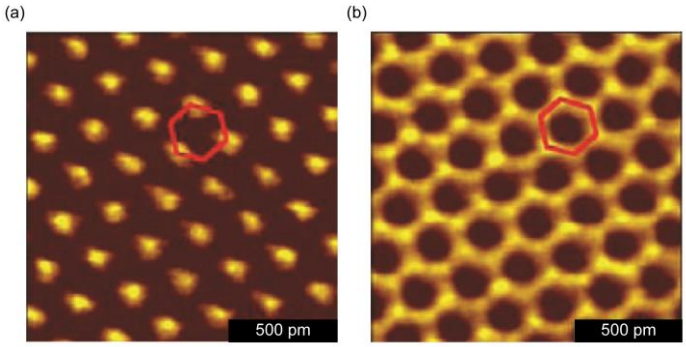

Figure 1.6 Atomic resolution STM images of the surface of (a) graphite and (b) graphene. While the graphite surface shows a triangular structure, the graphene surface exhibits a honeycomb structure with all six atoms visible. Adapted from Ref. [19].

When an HOPG surface is examined with AFM on a larger scale, one can discern step edges ranging from single atomic steps (with a height of 0.335 nm) to several atomic layers.[4] Depending on the HOPG sample quality, *i.e.* the mosaic spread angle and crystallite size, step edge density (the number of step edges per unit area) varies significantly, and this is an important factor of which to take account when considering electrochemistry at HOPG, as is discussed further below. Evidently, surface structure in general, and step edge density in particular, have been considered to play a key role in HOPG electroactivity, even for simple outer-sphere processes.[20-22] Thus, a deep and precise characterisation of the surface structure and properties is essential to establish unequivocal structure-function correlations.

In Figure 1.7, typical tapping mode-AFM (TM-AFM) images of the surface topography of 6 different grades of HOPG are presented,[4,13] namely AM, ZYA, ZYH, SPI-1, SPI-2 and SPI-3, mechanically cleaved for AM grade and Scotch tape cleaved for the rest. These images clearly show that on HOPG surfaces both basal and edge plane sites can be found, with a very wide range of step edge densities evident across these different samples. Mechanically cleaved AM HOPG provides by far the most superior surface in terms of low step density, a surface quality that is also obtained when Scotch

tape cleavage is employed.[4,23] The other grades of HOPG show increasing step densities in the order ZYA, ZYH, SPI-1, SPI-2 and SPI-3. This variety of surface has enabled any significance of step edges on the HOPG electrode response to be explored and identified as discussed herein. Interestingly, SPI-1 grade, shows a much higher step density than ZYA grade, highlighting the need for AFM topographic analysis, rather than relying only on the values of mosaic spread (*vide supra*).

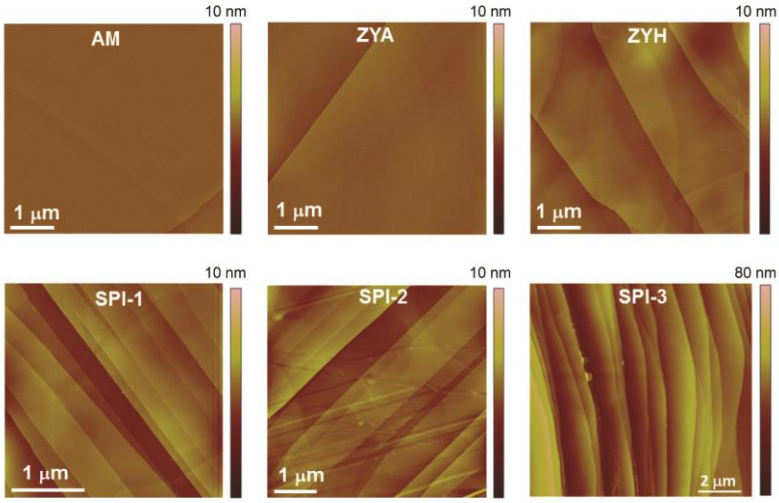

Figure 1.7 AFM images of freshly cleaved HOPG surfaces of different grades. Note the differences in scale bars (lateral and height). Adapted from Refs. [4,13].

A quantitative analysis of step edge coverage[4,13] on these different HOPG grades is summarised in Table 1.1. Step edge character is defined in two ways: (i) as the step edge length (μm) in unit area of the surface (μm^2), not taking account of the step height (monolayer, bilayer, etc.) and (ii) as the total step edge area per unit geometric area of the surface, which takes account of different step edge heights. The results highlight the fact that the average step edge coverage varies significantly across the different grades by >2 orders of magnitude, and also that within a grade the range can vary by about an order of magnitude from one area to another. It is also shown that most of the HOPG grades exhibit predominantly monolayer and bilayer steps, with multilayer steps found extensively on the cleaved surface of SPI-3 grade HOPG.[4,13]

Table 1.1 Summary of some key properties of different grades of HOPG. Data from Refs. [4,13].

	AM	ZYA	ZYH	SPI-1	SPI-2	SPI-3	BPPG
Step density range (μm μm^{-2}) from AFM	0.003-0.12	0.1-0.7	0.5-2.3	0.3-3.6	1-3.5	2.5-21.9	-
Mean step-edge density (μm μm^{-2}) from AFM	0.02±0.02	0.5±0.1	1.2±0.6	1.5±0.2	2.1±0.9	8±5.8	-
Average step-edge coverage on basal plane (%)	0.09±0.09	0.3±0.25	0.8±0.4	1.7±1.6	2.2	30±24	110±5
Step-edge coverage range (%)	0.006-0.48	0.03-1	0.2-2.1	0.5-3.4	0.6-6.7	10.1-78	105-120
Capacitance (μF cm^{-2})	2.4±1.5	2.0±0.3	-	2.9±1.2	-	-	-

It is also useful to comment on *basal plane pyrolytic graphite* (BPPG), which is sometimes considered as an equivalent substrate to HOPG since the basal graphite plane is exposed.[20,24-30] Although the BPPG surface shows oval basal domains up to 20 nm in height, the sides of these features consist of an abundance of step edges. Interestingly, while *edge plane pyrolytic graphite* (EPPG) has substantial edge character, a considerable proportion of basal plane is exposed as well. Thus, there is little difference in the quantity of edge plane defects between BPPG and EPPG, as judged by Raman spectroscopy.[31]

1.1.2.2 Electronic Properties

In simple models of electronic structure to determine the physical properties of graphite, it is often sufficient to consider uniquely the hexagonal planes of carbon atoms with a weak interaction between the layers. This is reflected in the band structure models for graphite, first developed by Wallace,[32] and subsequently modified by Sloczenwski, Weiss and McClure.[33,34] The SWMcC model considers graphite as stacked graphene layers, linked by weak forces.[35,36]

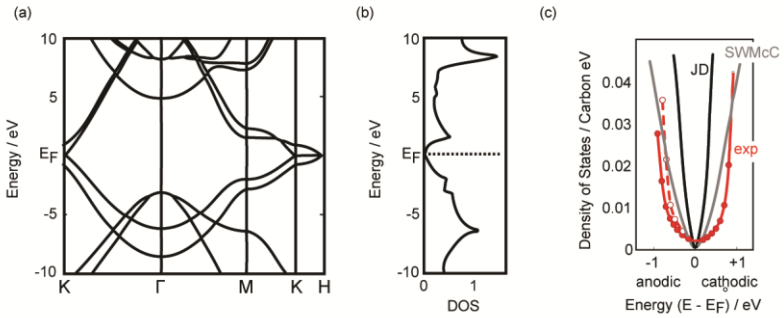

Figure 1.8 (a) Graphite electronic band structure along high-symmetry lines in the Brillouin zone. (b) Electronic DOS of graphite. (c) Curves representing the DOS for pyrolytic graphite determined by Gerischer using capacitance measurements, compared with the curves obtained by the SWMcC and JD models for energy bands near the HK axis. Adapted from Refs. [37] and [38].

The model for graphite band structure was developed, and complemented, by Johnson and Dresselhaus (JD)[39] and unified by Tatar and Rabii.[40] With new terms introduced, a better description of the interaction between layers is provided (Figure 1.8). In the case of single-layer graphene (SLG), the valence and conduction bands just touch at the *K* point of the Brillouin zone, leading to a zero gap. In contrast, for bilayer graphene, the interaction between the B carbon atoms of next nearest neighbour planes[34,41] yields an overlap of about 0.16 meV between the bands. With an increasing number of graphene layers, the overlap at the *K* point reaches about 41 meV for graphite,[41] conferring the semimetallic behaviour that has been observed experimentally.[41,42]

A particular feature of the band structure of HOPG is that at the intrinsic Fermi level the density of electronic states (DOS) is low (Figure 1.8),[41] *ca.* 0.0022 states atom^{-1} eV^{-1}.[37,43] This contrasts with metals such as Au, for which the DOS is around 0.28 states atom^{-1} eV^{-1} and more or less constant for a wide range of energies.[44] The DOS at graphitic materials can be modified by disorder in the crystal structure, by the presence of step edges,[45] local defects,[46,47] dangling bonds[48] or rotation/detachment of the graphene planes.[49,50] These surface modifications result in defect states with energies between the conduction and valence bands, modifying the DOS near the Fermi level. However, most of these modifications (step edges and local

defects) are very much localised and are only detectable with high resolution techniques, such as STM/scanning tunnelling spectroscopy (STS). For these defects to have an effect on the overall DOS of macroscopic HOPG samples, they must be found in relatively large quantity (surface density). However, this is not usually the case, as the point defect density for cleaved HOPG is estimated to be in the range 0.1 – 10 μm^{-2}.[51-56]

As mentioned above, STM produces images that are influenced by the electronic states of the surface being studied. Most significantly, STS[57] can be used to obtain a spectrum of the DOS as a function of the electron energy by measuring the electron tunnelling current (*I*) while the voltage (*V*) between an STM tip and HOPG sample is swept. The slope of the resulting *I*-*V* curve (d*I*/d*V*) at a particular potential is proportional to the LDOS.[57]

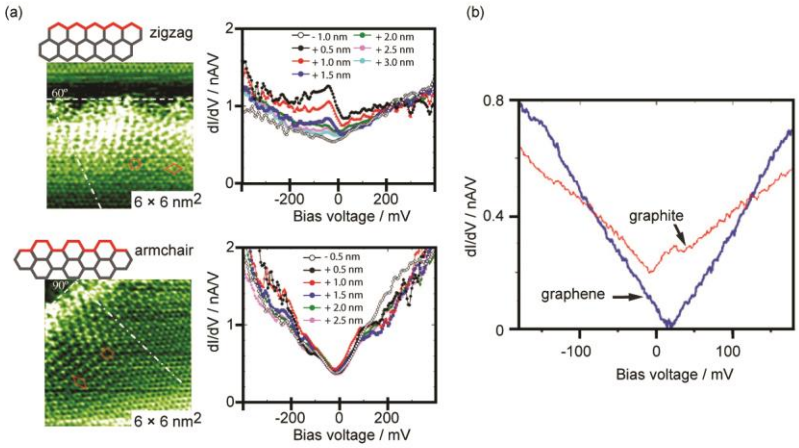

Figure 1.9 (a) STM images and STS spectra near monoatomic steps of an HOPG sample with zigzag edge (top) and armchair edge (bottom). The colour key on the spectra assigns the lateral distance of the tip from the step edge. (b) STS spectra of graphene and graphite, showing a finite differential conductance at the neutrality point for graphite, consistent with the finite DOS. Adapted with from Refs. [45,58].

The bias dependence of the tunnelling conductance, d*I*/d*V*, shows a clear enhancement in the LDOS at the intrinsic Fermi level at zigzag edges, compared to the basal surface, but not at the armchair edges (Figure 1.9a). For this step edge enhancement to noticeably affect the overall DOS of

HOPG (by 20 %), the step spacing of zigzag edges needs to be less than 4 nm.[45] Thus, one would not expect significant differences in the overall DOS of different HOPGs, since such a high step density is not found on any grade of HOPG, except perhaps for SPI-3 grade, and even here the armchair edge most likely dominates.

HOPG can also exhibit macroscopic defects. As a layered material, there is the possibility of a decoupling of the graphene layers, which affects the electronic structure, in general, but especially at the Fermi level, leading to a decrease of DOS at the Fermi level. This is exemplified in Figure 1.9b, where STS spectra for graphite and single layer graphene (graphite sample with the top layer decoupled) are shown.[19,58] For graphene, the DOS has a V-shape and vanishes at the Dirac Point (DP), while for two or more graphene layers the coupling produces additional states at the DP leading to a finite DOS.[59]

1.2 Fundamental Electrochemistry

1.2.1 Interfacial Electrochemical Reactions

For a reaction occurring at the solution-electrode interface, $\mathrm{O} + ne^- \rightleftharpoons \mathrm{R}$, there are several steps involved, *i.e.* mass transport, chemical reactions before or after the electron transfer (ET), other surface-bound reactions (such as adsorption and desorption), and electron transfer at the surface of electrode (Figure 1.10).[60] The slowest step can be a limiting factor for the overall electrochemical processes.

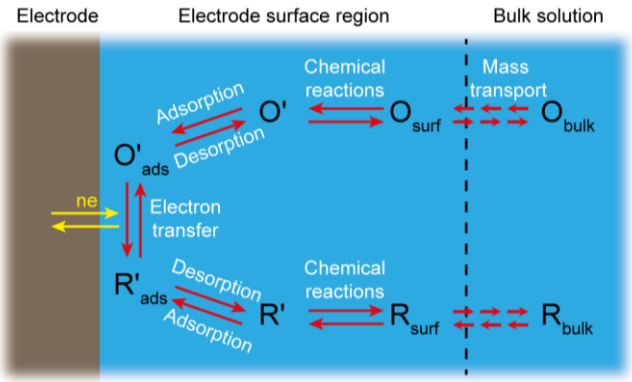

Figure 1.10 Schematic for the steps of an electrochemical reaction.

There are three types of mass transport in electrochemical systems, *i.e.* migration, diffusion and convection. Migration occurs when charged species move under the influence of an electric field; diffusion accounts for movement of species driven by a gradient of chemical potential (*e.g.* concentration gradient); convection movement of species is triggered by mechanical stirring or density gradients. Diffusion is the most commonly seen mass transfer mode and the diffusion profiles are different on electrodes of different dimensions. As shown in Figure 1.11, planar diffusion is observed for macroscale electrodes and spherical diffusion is found for micro/nanoscale electrodes under steady-state conditions.[61]

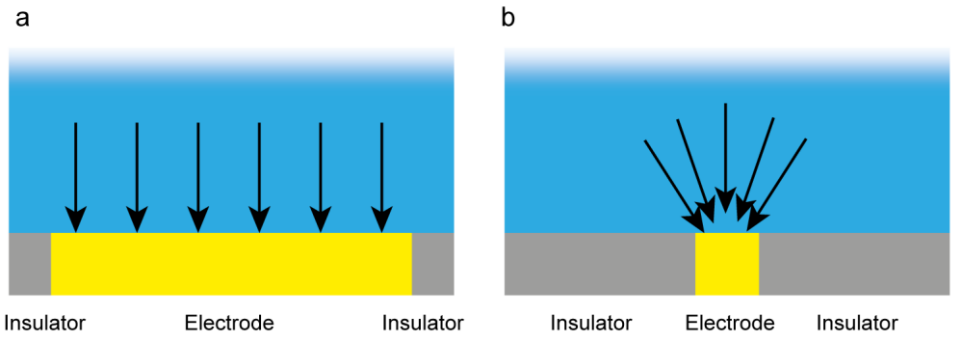

Figure 1.11 Profiles for (a) planar diffusion and (b) spherical diffusion at the electrode-solution interface, subject to the size of electrode area.

1.2.2 Electron Transfer Kinetics

1.2.2.1 Overpotential

An overpotential, η, is often needed to drive electrochemical reactions, where ET occurs. The driving force is defined as the difference of the applied potential (E) and the equilibrium potential (E_{eq}):

$$\eta = E - E_{eq} \qquad \text{(eq. 1.1)}$$

For a system (one–electron reaction) in a state of equilibrium, it is governed by the Nernst equation and E_{eq} can be derived from eq.1.2

$$E = E^{0\prime} + \frac{RT}{F} \ln \frac{C_O^*}{C_R^*} \qquad \text{(eq.1.2)}$$

where $E^{0\prime}$ is the formal potential, R is the gas constant, T is temperature, F is Faraday's constant, C_O^* and C_R^* are the bulk concentrations of the oxidised and reduced species, respectively.

1.2.2.2 Butler–Volmer Equation

The current as a result of applied overpotential in an electrochemical system can be predicted using Butler-Volmer equation.[60] For a simple one-electron reaction process,

$$\mathrm{O} + e^- \underset{k_b}{\overset{k_f}{\rightleftharpoons}} \mathrm{R} \qquad \text{(eq. 1.3)}$$

where k_f and k_b are the heterogeneous rate constants for the forward (reduction) and backward (oxidation) reactions, respectively. The overall current, i, is the difference of cathodic current (i_c) and anodic current (i_a), expressed as

$$i = i_c - i_a \qquad \text{(eq. 1.4)}$$

While the current for either direction is dependent on the corresponding heterogeneous rate constant (k_b or k_f),

$$i_c = FAk_fC_O \qquad \text{(eq. 1.5)}$$

$$i_a = FAk_bC_R \qquad \text{(eq. 1.6)}$$

where A is area, C_i is the concentration of species i of the redox couple (O or R). Then the net current is

$$i = FA(k_fC_o - k_bC_R) \qquad \text{(eq. 1.7)}$$

While k_f and k_b can be deduced as a function of standard heterogeneous rate constant (k_0) following the Arrhenius equation:

$$k_f = k_0 e^{-\alpha f(E-E^{0\prime})} \qquad \text{(eq. 1.8)}$$

$$k_b = k_0 e^{(1-\alpha)f(E-E^{0\prime})} \qquad \text{(eq. 1.9)}$$

where the coefficient $f = F/RT$ and the transfer coefficient, α is a dimensionless parameter (often assumed as 0.5).

So, the reaction current can be obtained as

$$i = FAk_0[C_O e^{-\alpha f\left(E-E^{0\prime}\right)} - C_R e^{(1-\alpha)f\left(E-E^{0\prime}\right)}] \qquad \text{(eq. 1.10)}$$

1.2.3 Redox Couples

Redox couples can be classified into outer-sphere and inner-sphere groups. Outer-sphere redox species do not interact strongly with the electrode surfaces (during electron transfer) and are normally separated from the electrodes by a distance of at least a solvent layer. In contrast, the inner-sphere species interact with the electrode surface strongly, where specific adsorption processes are often involved. Thus, the redox reactions of outer-sphere species are less dependent on the electrode materials compared with inner-sphere species.[60]

1.2.4 Energy View from Marcus Microscopic Model

When a heterogeneous outer-sphere reduction process at an electrode, involving one-electron transfer (see eq.1.3), or a homogeneous electron transfer process (in which O is reduced to R by another reactant in solution), is considered, there are two fundamental aspects[60]: (i) since electron transfer process is radiationless, the electron must move from an initial state to a receiving state of the same energy, known as isoenergetic electron transfer; (ii) the reactants and products do not change their configurations during the transfer, based on the Franck-Condon principle, *i.e.* O and R share the same nuclear configuration at the moment of transfer.

As a potential is applied on the electrode, standard free energy of activation is changed to overcome the barrier for oxidation or reduction, but electron transfer would only occur at the transition state, where O and R have the same configuration. Here, the reorganization energy λ, which defines the

energy required to transform the nuclear configurations in the reactant and the solvent to those of the product state, plays an important role.

$$\lambda = \lambda_i + \lambda_s \qquad \text{(eq. 1.11)}$$

where λ_i represents the inner component from (bond) reorganization of species O, and λ_s the outer component from reorganization of the solvent.

1.2.5 Cyclic Voltammetry

Cyclic voltammetry (CV) is the most used potential-sweeping technique in the field of electrochemistry.[61] The potential of the electrode is changed linearly with time between two chosen values, E_1 and E_2, while the electrochemical current is recorded as a function of applied potential, generating a cyclic voltammogram (Figure 1.12).

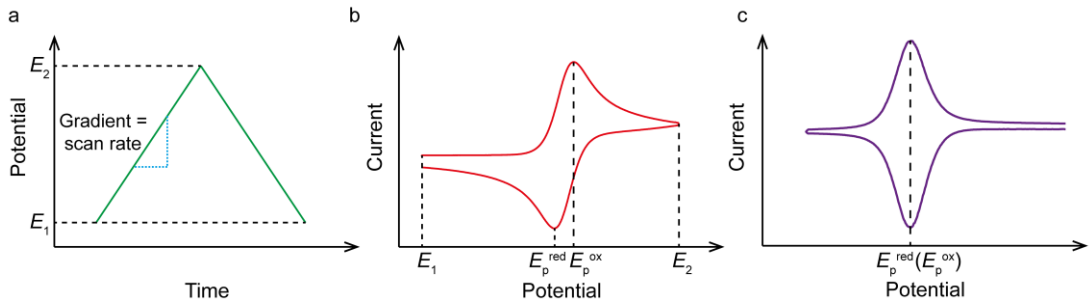

Figure 1.12 (a) Profile of potential applied with time in cyclic voltammetry. A typical waveform of current response for (b) diffusion- and (c) adsorption-controlled processes as a function of potential. E_1 and E_2 are the starting and reversal potentials, respectively.

The observed current is due to both faradaic and nonfaradaic processes. Nonfaradaic current (i_{nf}) derives from double layer charging of the electrode, affected by scan rate (v) and double layer capacitance (C_d).

$$i_{nf} = vC_d \qquad \text{(eq. 1.12)}$$

The faradaic current needs to be considered in two cases. For a planar diffusion-controlled (reversible) reaction (Figure 1.12b), the peak current is

governed by Randles–Sevcik equation, which indicates that the peak current (i_p) is proportional to the square root of the scan rate.

$$i_p = 0.4463 \frac{n^{3/2} F^{3/2}}{R^{1/2} T^{1/2}} A D_O^{1/2} C_O^* v^{1/2} \qquad \text{(eq. 1.13)}$$

where n is the electrons transferred, D_O is the diffusion coefficient of the oxidised species.

For a reaction involving adsorbed species (Figure 1.12c), the peak current increase linearly with scan rate.

$$i_p = \frac{n^2 F^2}{4RT} v A \Gamma_O^* \qquad \text{(eq. 1.14)}$$

where Γ_O^* is the maximum surface coverage of species O. For an ideal adsorption peak, the full width at half-maximum (FWHM) should be 90.6/n mV.[60]

It should be noted that the peak-to-peak separation ΔE_p obtained from CV can be an indication of reaction reversibility and a measure of electron transfer kinetics.[60,62] For a reversible process (with high k_0), the redox species can be rapidly adjusted to those required by the Nernst equation and an electrochemical equilibrium is maintained at electrode surface, resulting in a small ΔE_p (59/n mV for a diffusion process; 0 for an adsorption process). However, for quasi-reversible and irreversible processes associated with sluggish kinetics (low k_0), Nernstian concentrations cannot be achieved and a significant activation overpotential (driving force) is need to motivate electron transfer, leading to shifts of peak potentials and an increase in ΔE_p.

1.3 Electrochemistry of HOPG

1.3.1 Formative Studies of HOPG Electrochemistry

The aim of this part is to give an overview of the field, with a particular focus on recent work that allows key models of HOPG electrochemistry to be assessed. These studies are developed significantly herein.

A major outcome of early studies was that the basal surface of HOPG was characterised by extremely slow kinetics compared to step edges, so that step edges were responsible for most, if not all, of the activity.[20] This view has become ingrained in the electrochemistry community, in text books[63] and key reviews.[20,21]

With the advent of new sp^2 carbon materials, namely carbon nanotubes,[64,65] and then graphene,[66-68] HOPG re-emerged as an important reference material for electrochemical studies, where a popular view was established that the basal plane of sp^2 carbon was inert for ET, even for classical outer-sphere redox couples.[29,69] This view of an inert basal surface for outer-sphere ET was extended to SWNTs for which open oxygenated ends were considered to be the active site for electrochemistry.[70-72] In contrast, other studies showed that the sidewall of SWNTs was highly active for electrochemistry.[73-75] This difference in the apparent behaviour of MWNTs and SWNTs, in different experimental formats, naturally raised questions as to the true behaviour of HOPG, not least because macroscopic measurements may have significant limitations for providing definitive (unambiguous) models for microscopic spatially heterogeneous reactivity, as we show herein.

The emergence of graphene as an electrode material made studies of HOPG even more significant, not least because some initial reports on graphene[76-78] found that graphene displayed higher ET kinetics for various outer-sphere redox couples than in earlier work on HOPG.[79-82] Yet, graphene has a lower DOS than graphite.[19] Within a framework of non-adiabatic ET one might thus expect graphene to have slower ET kinetics than graphite[83] (and the same kinetics for adiabatic ET).[84-86] On the other hand, substrate effects (*e.g.* doping, and changes in morphology such as wrinkles and ripples, etc.[86-88]) may be important in graphene studies, as well as the source of the graphene (*e.g.* synthesis by CVD vs. exfoliated). Other factors, such as time from exfoliation/synthesis, surface contamination,[4,89] etc., also require consideration. These issues make a clear understanding of the

electrochemical properties of graphite, and particularly the basal plane of HOPG, imperative.

Recent developments in scanning probe microscopy have provided new opportunities to determine the electrical and electrochemical characteristics of graphite (and other sp^2 carbon materials) with unprecedented detail and spatial resolution. In this light, we assess early electrochemical measurements at HOPG, which tended to rely on macroscopic measurements and correlations between different macroscopic quantities. Since many of these measurements have been reviewed extensively,[20,21] most of this chapter discusses more recent electrochemical studies which are able to target particular features of graphite surfaces at high spatial resolution (especially the basal surface in isolation from step edges) and probe the associated electrochemistry. This enables microscopic models to be tested rigorously and predictions to be made about the behaviour of macroscopic electrodes. These studies highlight new features in the behaviour of freshly cleaved HOPG, and also time-dependent (and electrochemical flux) effects that complicate the electrochemical response and analysis of HOPG, with implications for related materials such as graphene. These recent studies provide new opportunities for understanding fundamental electrochemical processes at graphite, and for the design of optimal graphite-based electrodes, particularly for sensing and energy-related applications. More generally, the new understanding of HOPG electrodes has implications for wider electrochemistry.

1.3.1.1 Early Macroscopic Voltammetric Measurements and Correlations

Some of the earliest electrochemical studies of redox reactions at graphite found that the apparent standard rate constant, k_0, for several redox processes, especially the ferri/ferrocyanide redox couple, $Fe(CN)_6^{4-/3-}$ in aqueous solution, were extremely variable (by many orders of magnitude) even on the same grade of HOPG.[90] It was therefore postulated that the reactions could be driven by surface defects[20,21] and so surface modification procedures were introduced, sometimes accompanied by Raman spectroscopy, to determine the relationship between carbon microstructure

and heterogeneous ET.[90-92] Increased edge plane density (as revealed by Raman spectroscopy (D band)) appeared to correlate with increased ET rate, from which it was concluded that the basal surface of HOPG was essentially inactive or of very low activity, with edge plane defects providing essentially all of the activity. Indeed it was proposed that $Fe(CN)_6^{4-/3-}$ could be used to probe the step edge density of graphite surfaces and this has become a popular method[20-22,29,69,93,94] to assess the quality of HOPG (*vide infra*) between different experiments. However, it is important to comment on the usefulness of Raman analysis for HOPG samples, as Raman spectra can only highlight relatively highly defective samples. Many different grades of HOPG yield the same defect-free spectra.[13]

The early apparent correlation between step edge density and k_0 for the $Fe(CN)_6^{4-/3-}$ redox couple led to the use of this couple as an electrochemical 'validation' standard to identify low surface defect density HOPG electrode surfaces.[95] Thus, before many electrochemical measurements on HOPG, voltammetry of $Fe(CN)_6^{4-/3-}$ for this couple was first run with the inverted droplet cell, before any subsequent measurements.[95-97] ΔE_p > 700 mV at 0.2 V s^{-1} was regarded as mandatory to 'validate' an HOPG surface as being low in defects. Surfaces that resulted in ΔE_p < 700 mV were discarded and considered to be highly defective.[98]

CVs of 1 mM $K_4Fe(CN)_6$ in 1 M KCl resulted in a mean peak-to-peak separation, ΔE_p of 459 ± 331 mV and a range of 58–1200 mV, even on the same grade of HOPG.[95-97] Yet, this corresponds to the standard rate constant (for the entire surface) changing by at least 6 orders of magnitude.[95-97] This immediately raises questions as to the validity of this couple as a measure of step density because the step edge density within a particular grade of HOPG only varies by one order of magnitude at most. Although it was concluded that the different ΔE_p reflected the amount of surface (edge) defects present, with large ΔE_p corresponding to low defect density, it is important to note that $Fe(CN)_6^{4-/3-}$ is notorious for various surface interactions and non-ideality,[21,99,100] notably degradation with time and

exposure to light. It is by no means a 'simple' or well-behaved redox mediator.[21,101]

Comparisons were often made between electrochemical activities of the highest quality (low step edge density) AM grade HOPG and laser-activated GC.[102,103] For eight quasi-reversible one electron redox systems, the GC rates were 1–5 orders of magnitude higher than those measured for $Fe(CN)_6^{4-/3-}$ 'validated' AM grade HOPG samples and this effect was attributed to the high density of edge sites on GC and the low DOS of HOPG.[95] From Marcus theory, the simplest form of the relationship between log k_0 and log k_{exc} (k_{exc} is the exchange rate constant), predicts a linear relationship with a slope of 0.5.[95] However, most of the GC values are diffusion-limited (reversible) and therefore this correlation could not be observed. In contrast, consistently lower values were observed for HOPG, but the correlation of k_0 with the square root of homogeneous rate constant was weak, with a slope of 0.29 rather than 0.5.

The impact of laser ablation of HOPG on the resulting capacitance, C^0, and k_0 for $Fe(CN)_6^{4-/3-}$ was investigated.[104,105] Over a power density range of 0 to 130 MW cm^{-2}, k_0 increased by more than 5 orders of magnitude while C^0 increased by a factor of 8.[62,104,106] It was concluded that the apparent correlation of k_0 and C^0, by inference, indicated a correlation of k_0 and step edge density. However, capacitance values >3 µF cm^{-2} have been considered to indicate rather defected surfaces.[20,21,106] Moreover, the ablation treatment, while creating defects, could easily clean the surface or remove poorly attached (resistive) flakes on the HOPG surface. Recent studies on the double layer capacitance of graphite suggest that capacitance is a weak indicator of surface quality.[107,108]

Other macroscopic correlations have been proposed between the surface coverage, Γ_{ads}, of electroactive adsorbates with k_0 for $Fe(CN)_6^{4-/3-}$, C^0, and, by inference, the step edge density. However, the only attempt to correlate step edge density measured directly and Γ_{ads} of electroactive adsorbed anthraquinone-2,6-disulfonate (AQDS), focused on a very narrow range of step densities on cleaved HOPG samples (from 0.7 to 1.6 %) and there was

a relatively high uncertainty in the absolute step edge density such that the errors associated covered the entire range studied.[52] Moreover, it is important to point out that the apparent correlation between the measured step edge coverage and the AQDS adsorption required 30 times the step edge area than could be accounted for by the steps alone, and it was proposed that there was a pronounced electronic disturbance extending 5 nm from the step edges, where electrochemistry could occur, with no electrochemistry on the basal surface.[22] To support this, a constant height STM image was reported that showed higher current at the edge over such a distance. However, this measurement is ambiguous because the higher current could come from an edge that was slightly detached from the surface. Moreover, this result is not in accord with what is now known about the LDOS at HOPG step edges, where only zigzag edges have a higher LDOS, and only over a distance *ca.* 1 nm, with little change in the LDOS at armchair edges.

It was later shown by AFM imaging,[98,109] that the adsorption of AQDS showed full coverage across the entire HOPG surface but this did not correlate with the surface coverage calculated from voltammograms that measured the amount of adsorbed AQDS. It was therefore suggested that AQDS adsorption occurred indiscriminately on basal and step edges, but only adsorbate present at step edges was electrochemically active.[98,109]

1.3.1.2 Macroscopic Voltammetry and Modelling

It was proposed that HOPG is an electrochemically inert material [29]. The CV response was analysed numerically with linear diffusion simulations (Digisim©), along with finite difference simulations on a heterogeneous HOPG electrode with some spatial zones (edges) being more active than others (basal surface), resulting in an 'array of microelectrodes',[29,69,110] with the basal to edge plane ratio depending on HOPG quality. This 'partially blocked' electrode model was used to analyse the CV response, as a means of deducing the fractional coverage of step edges on HOPG electrode surfaces.[29]

A CV for the oxidation of $Fe(CN)_6^{4-}$ recorded on EPPG and another at a cleaved surface of HOPG[29] is shown in Figure 1.13a. The best result of fitting the experimental HOPG voltammogram to the simulation (Digisim©) is shown in Figure 1.13b.

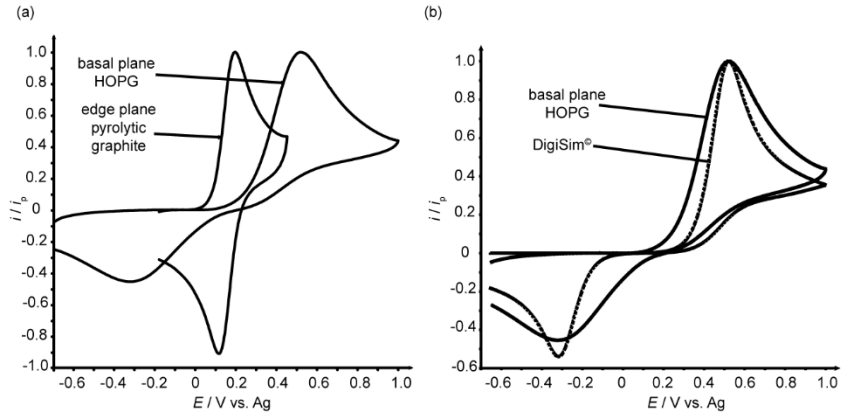

Figure 1.13 (a) CVs recorded at EPPG and basal plane HOPG. (b) Comparison of the basal plane HOPG voltammograms with the best fit to linear diffusion CV simulations for the oxidation of 1 mM $Fe(CN)_6^{4-}$ (1 M KCl) at 1 V s^{-1}. Adapted from Ref. [29].

Both the experimental forward and back peaks are wider than predicted theoretically and the experimental back peak is significantly smaller than predicted. It was attributed to the structural heterogeneity of HOPG,[26,29,69] from which it was concluded that the oxidation of $Fe(CN)_6^{4-}$ only occurs at HOPG step edges, with the k_0 for the basal plane $<10^{-9}$ cm s^{-1}, at least 10^7 times lower than at edge planes, such that the basal plane had essentially no influence on voltammetry. However, this model could not be used quantitatively to determine the edge plane coverage of cleaved HOPG surfaces because in order to model the data, the edge plane coverage applied theoretically had to be 100 times smaller than the actual step edge coverage value (from AFM). It is important to point out that these conclusions, while widely adopted, seem to have been reached using just one voltammogram.[26,29,69]

1.3.1.3 Alternating Current (AC) Voltammetric Methods

Great irreversibility was found when the $Fe(CN)_6^{4-/3-}$ couple was studied at ZYH grade HOPG electrodes, with extreme $\Delta E_p > 1$ V in CV measurements. When the surface was maltreated by hand polishing or by cleaving with a glass pipette tip to introduce defect sites onto the HOPG surface, a 'mini cyclic voltammogram' appeared in the voltammogram and this was attributed to fast $Fe(CN)_6^{4-/3-}$ electrochemistry at the edge plane defects in this region.[94]

It was proposed that the percentage of edge plane defect coverage could be estimated based on k_0 for $Fe(CN)_6^{4-/3-}$, C^0 and AC harmonic peak current data obtained on ZYH grade HOPG after both hand polishing and electrochemical pretreatment (ECP) methods.[111,112] However, intrinsic ZYH grade HOPG is characterised by quite high defect (step edge) density itself, and based on the capacitance measured (3.4 to 76.5 μF cm^{-2})[93] one would have expected a close to reversible process for all the surfaces within the defect model of McCreery.[21]

1.3.1.4 Critical Comparison of Macroscopic Data

It is interesting to compare the CV data outlined above, leading to similar conclusions that the electroactivity of HOPG is dominated by step edges. Typical CVs were reported by different groups working on different grades of HOPG. A typical CV for $Fe(CN)_6^{4-/3-}$ on AM grade HOPG gives a ΔE_p ~700 mV, SPI-1 and ZYH grade HOPG, which have 10–100 times higher density of steps, give a slower response (larger ΔE_p). Given the discrepancies in the literature, it is evident that further scrutiny of the HOPG ET model is required, particularly at the microscopic level, as considered in the next section.

1.3.2 New Views of Electrochemistry at HOPG

Given the heterogeneity in structure and electronic properties, reliable models for the electrochemistry of sp^2 carbon materials can only be obtained through studies that either access particular features (*e.g.* graphene/graphite basal plane, step edges, and defects), or through larger scale measurements

where the type and quantity of these structural motifs are thoroughly characterised and systematically varied. In this section, recent experimental approaches are highlighted to test the models derived from earlier measurements, producing results that lead to major new insights on HOPG electrochemistry for a range of reactions. Furthermore, these studies are essential in providing a baseline understanding for other forms of sp^2 carbon.

1.3.2.1 Outer-Sphere Redox Processes

The most important question concerning HOPG electrochemistry in recent years has been: does the basal surface, free from the influence of step edges, have any (significant) activity or does electrochemistry only occur at step edges? There had been widely differing views, even for outer-sphere redox processes,[4,22,26] where the redox couple does not interact strongly with the electrode surface, but recent high resolution imaging data provide irrefutable evidence for the high activity of the basal surface.

The scanning micropipette contact method (SMCM) was introduced as the first means of probing the electroactivity of tiny regions of an HOPG surface, defined by meniscus contact with an electrolyte solution in a micropipette or nanopipette, containing a quasi-reference counter electrode (QRCE).[113] For these studies, the pipette size (*ca.* 580 nm) was smaller than the inter-step spacing on the basal surface (*ca.* 2 μm). In the case of the one-electron oxidation of (ferrocenylmethyl)trimethylammonium ($FcTMA^+$), experimental data revealed Nernstian (reversible) ET. A similar, fast ET response was found for $Fe(CN)_6^{4-/3-}$, but measurements had to be made rapidly following HOPG cleavage, to avoid a deterioration of the response.[113]

Although SMCM can now be used with pipettes as small as 100 nm diameter,[114] scanning electrochemical cell microscopy (SECCM)[115,116] is a much more powerful method for visualizing electroactivity, because it tracks both surface activity and topography. In the case of HOPG, the response informs on the location of the measurement, *i.e.* the basal surface alone, or intersected by step edge(s).[117] The probe is a dual-barrel (theta) nanopipette filled with electrolyte solution that produces a meniscus across the two

barrels at the sharp end. This acts as an electrochemical cell upon coming into contact with the substrate of interest. A vertical sinusoidal oscillation is usually imposed on the tip position to create an alternating current component of the ion conductance current, due to a bias between QRCEs in each barrel, at the oscillation frequency that serves as a feedback parameter to maintain a stable tip-substrate separation while the meniscus is in contact with the surface.[115] The resolution of SECCM approximates to the tip size, which can be as small as 90 nm.[118]

With precise position control of the probe and sample, high-resolution electrochemical imaging (current, with the working electrode potential controlled by two voltages) on a variety of substrates is possible.[4,73,75,80,115,117-119] SECCM imaging was carried out[117] on freshly cleaved HOPG with two redox couples, $Ru(NH_3)_6^{3+/2+}$ and $Fe(CN)_6^{4-/3-}$. High and uniform surface electroactivity was observed across the basal surface (indistinguishable from reversible ET). Lower limits for the standard ET rate constants, $k_0 > 0.5$ cm s^{-1} and > 1 cm s^{-1} were estimated for $Ru(NH_3)_6^{3+/2+}$ and $Fe(CN)_6^{4-/3-}$, respectively,[117] many orders of magnitude higher than previous macroscopic CV measurements (by more than 9 orders of magnitude in the case of $Fe(CN)_6^{4-/3-}$).[26,120] For aged HOPG samples exposed to air, both the surface conductivity and the electrochemical response deteriorated, attributed to airborne contamination (mainly hydrocarbon[89]) of the surface and/or delamination of the top layer(s) from the main body of the HOPG.[4,118] These issues need to be considered carefully for the characterisation of the intrinsic electrochemical properties of HOPG and exfoliated graphene surfaces.[118,121,122]

Combined scanning electrochemical microscopy-AFM (SECM-AFM),[123,124] likewise enables electroactivity to be directly and simultaneously related to substrate topography, with high spatial resolution.[125,126] It was found[125] that the basal surface of freshly cleaved HOPG was ‘as active as template-stripped gold’ for $Ru(NH_3)_6^{3+/2+}$ with $k_0 > 9.4$ cm s^{-1}, but that over time (up to several hours) k_0 diminished to 1.9×10^{-2} cm s^{-1}. SECM-AFM measurements on HOPG using a metal-AFM tip functionalised with a tagged ferrocene-

based redox mediator,[127] clearly showed that the basal surface of HOPG displayed high electrochemical activity, although some – but not all – step edges had slightly enhanced currents.[127] In a further study,[128] fully-reversible ET was observed at basal plane HOPG.

High electroactivity of HOPG has also been seen in several SECM studies: (i) high resolution imaging studies of the basal surface using the one-electron oxidation of FcMeOH;[129] (ii) in fixed spot measurements with $Fe(CN)_6^{4-/3-}$;[130] and (iii) in nanogaps, for $FcTMA^{+/2+}$,[131] without taking into account the adsorption of $FcTMA^{+}$ on HOPG[132] and $FcTMA^{2+}$ on glass.[133]

1.3.2.2 Complex Multi-Step Reactions: Neurotransmitter Oxidation

Studies of the electrochemical oxidation of catecholamines on HOPG have demonstrated that the process is neither slow nor solely catalysed by graphite step edges,[13,130,134,135] as had previously been proposed.[21] Rather, the electro-oxidation of catecholamines on the basal surface of HOPG is facile. SECCM 'reactive patterning' studies translated the SECCM meniscus across an HOPG surface at a sufficient rate to deduce the response of the fresh surface, but leaving behind polymeric products that acted as a surface marker.[134,135] This allowed the electrochemical activity to be related directly to the local surface character at the nanoscale by the subsequent use of complementary microscopy in the same area.[135]

Nanoscale measurements predicted that macroscopic CV measurements of catecholamine electro-oxidation would be dominated by the basal surface, which was confirmed in studies of dopamine and epinephrine electro-oxidation.[13,134,135] An independent SECM study on the redox behaviour of dopamine/dopaminequinone on HOPG, also found fast ET characteristics.[130] These studies are important for the design of optimal carbon electrodes for sensing. The low interfacial capacitance of graphite basal electrode surfaces, and the fact that the oxidation reaction occurs easily, lead to far superior concentration detection limits, compared to other carbon electrode materials.[13]

1.3.2.3 Surface Functionalisation

The grafting of diazonium radicals on carbon electrodes is a popular method for surface modification and there has been debate as to whether it proceeds more readily (and exclusively) at defect sites (step edges and defects),[98,136] and whether it involves covalent modification at all.[56] The reduction of carboxybenzenediazonium was studied and found that the electrochemistry and modification were independent of step edge density.[137] Moreover, SECCM was able to confine the electrochemical modification to isolate the contribution of the basal plane alone, showing unambiguously that step edges were not required for modification. Furthermore, confined electrochemical measurements (1 µm diameter meniscus) allowed to rule out the need for defect sites, given the low density of point defects on HOPG (between 0.1 and 10 μm^{-2}).[51,52] Covalent modification was proved with micro-Raman spectroscopy[137] and this type of modification has also been demonstrated to proceed readily at defect-free sites at graphene and graphite by STM.[138,139]

1.4 Electrochemistry of Graphene

Although there is a vast literature on 'graphene' electrochemistry, the materials are of variable quality, making fundamental studies difficult.[140] Exfoliated graphene is found to have high quality and so better for fundamental studies. The electrochemistry of two outer-sphere redox couples, $Ru(NH_3)_6^{3+/2+}$ and $FcTMA^{+/2+}$ was studied at exfoliated graphene (Figure 1.14), using SECCM, which allowed the independent interrogation of different graphene flakes and step edges within the same sample.[118] The ET with $FcTMA^{+/2+}$ was found to be fast and reversible on SLG and multilayer graphene. The results with $Ru(NH_3)_6^{3+/2+}$ were more interesting, because the standard potential is close to the intrinsic Fermi level of graphene/graphite,[95] where the DOS is low, and for graphene is theoretically zero. For this redox couple, there was a strong dependence of the ET kinetics on the number of graphene layers, with SLG having the lowest rate. There was enhanced activity at some, but not all, step edges, possibly subject to the arrangement

of steps (Figure 1.14c, d). The effect was subtle and complementary studies of HOPG showed that this electroactivity contrast developed with exposure time of sample.[118] Spontaneous delamination[4,118] was proposed to occur with time, leading to a surface made of electronically decoupled regions that are SLG, few-layer and multilayer graphene on top of otherwise intact HOPG, associated with different profiles of DOS (especially at the intrinsic Fermi level). As a consequence, it becomes understandable why, for $Ru(NH_3)_6^{3+/2+}$ in particular, SECCM images feature enhanced currents at exposed step edges (Figure 1.14d, e), where the apparent rate constant scales with overall step height (Figure 1.14e, f).

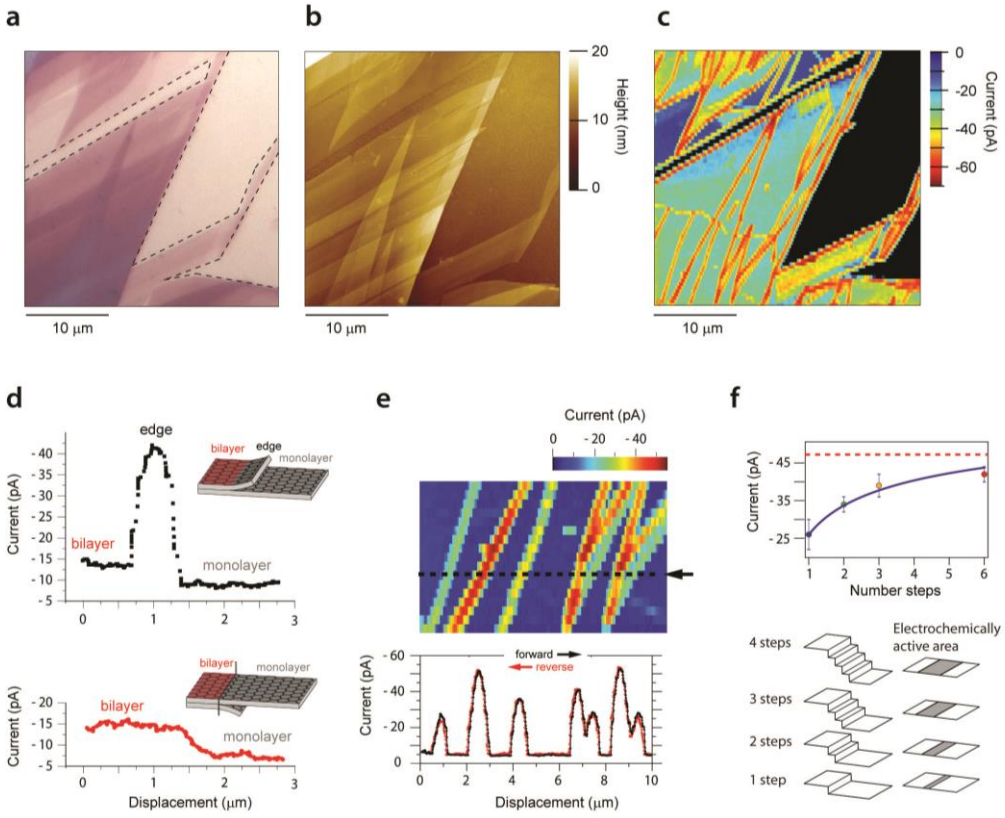

Figure 1.14 (a) Optical microscopy image, (b) AFM image and (c) SECCM electroactivity map of the reduction of $Ru(NH_3)_6^{3+}$ for the same area of an exfoliated graphene sample on a silicon/silicon oxide substrate. (d) SECCM current scan profiles of two characteristics over step edges: electrochemically active (top) and non-active (bottom) depending on the step edge being exposed or buried. (e) SECCM electroactivity map of step edges of different overall height (from AFM, not shown) and thus different electrochemically active areas (f). Adapted from Ref. [118].

To elucidate the behaviour at edges, voltammetric-SECCM[118] was developed where a local CV was recorded at each pixel in an electrochemical image of an aged HOPG sample. These measurements established that the voltammetric response at the basal surface and edges were closely similar in shape, but with a small additional overpotential for the basal surface. Therefore, with $Ru(NH_3)_6^{3+/2+}$, whose standard potential is close to the intrinsic Fermi level of graphene and graphite, the local electronic structure of graphene becomes a limiting factor in the overall ET rate, leading to a dependency of the observed kinetics on the number of (graphene) layers and step edges.

1.5 Graphene Production and Transfer

Many methods have been developed to obtain graphene layer(s), in which mechanical exfoliation and chemical vapour deposition (CVD) are commonly used (Figure 1.15). In the former method, graphite is mechanically exfoliated with Scotch tape to generate graphene layers on the tape. This method is easy to perform, accessible to high quality (low defect) graphene, however, it is irreproducible regarding the size and layer number of graphene obtained.

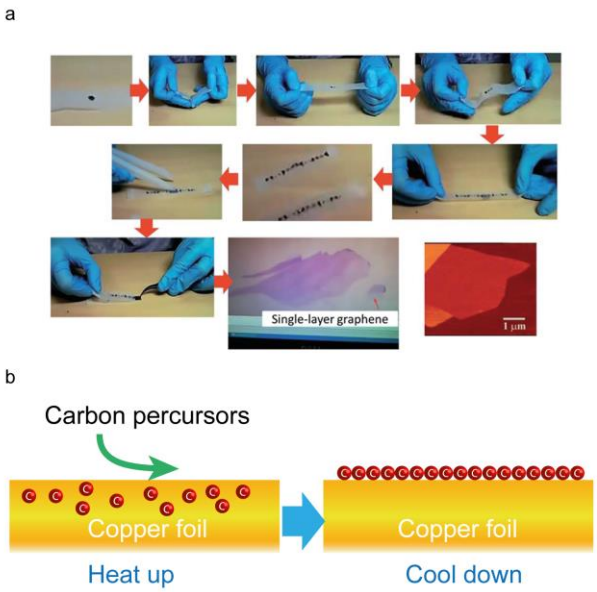

Figure 1.15 Graphene generation by (a) mechanical exfoliation of graphite and (b) chemical vapour deposition. Figure 1.15a adapted from Ref. [141].

Alternatively, chemical vapour deposition approach is suitable for yielding large area, reasonably high quality graphene of controlled layer number [142,143]. Under a high temperature atmosphere (~1000 °C), percursor gases will be decomposed, leading to dissolution of carbon atoms in catalytic metal substrates for growth. A thin layer of graphene will be formed on the surface of substrates after being cooled down.

For the graphene obtained by CVD growth, methods have been sought to transfer graphene from catalytic substrates to those of interest. They include the polymer-supported processes, using polymethylmethacrylate (PMMA),[144,145] and polydimethylsiloxane (PDMS)[76,146] and polymer-free method.[147] The graphene transfer with PMMA is shown in Figure 1.16.

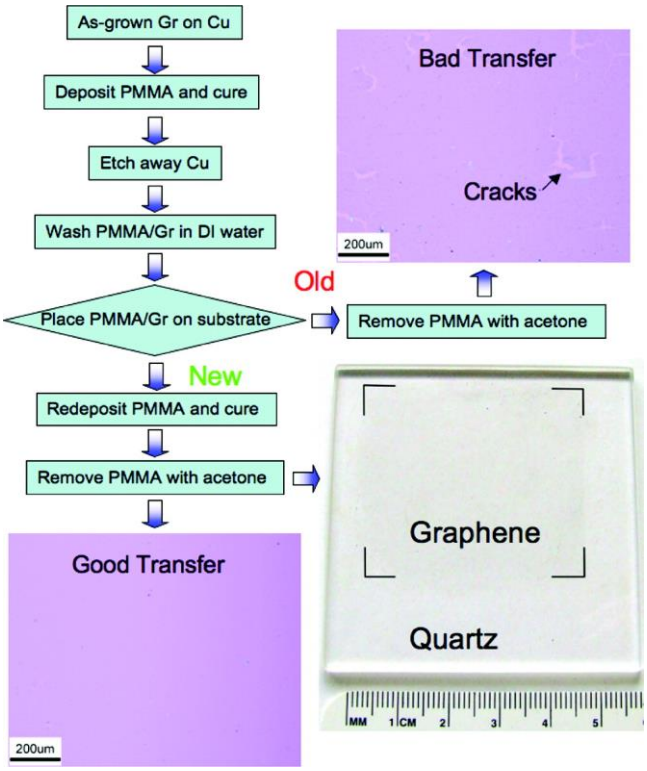

Figure 1.16 PMMA-assisted transfer of graphene films. The top-right and bottom-left insets are the optical images of graphene transferred on Si/SiO_2 wafers with “bad” and “good” transfer, respectively. Adapted from Ref. [144].

1.6 Electrowetting

Electrowetting concerns the wetting of droplets on substrate surfaces induced by application of an electric field.[148] The electrowetting-on-dielectric (EWOD) setup is best known (Figure 1.17).

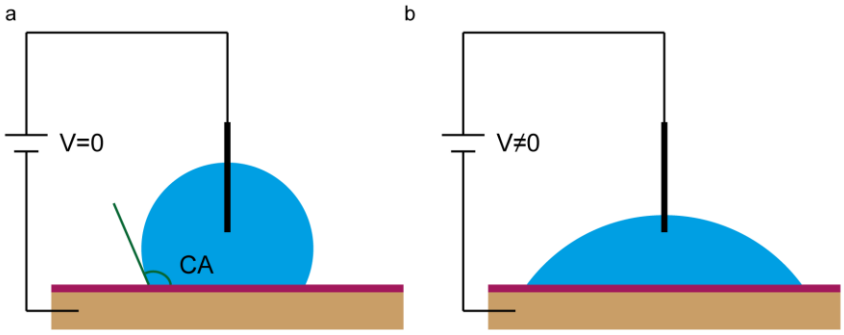

Figure 1.17 Illustration for the EWOD setup (a) before and (b) after the application of a voltage.

A thin dielectric layer is coated onto a substrate (electrode) to avoid electrochemical reactions at the electrode. A droplet is then put atop the modified surface, followed by the assembly of a counter electrode into it. When a bias potential is applied between two electrodes, changes in contact angles will be introduced, due to the electrostatic forces as a result of non-uniform charge distribution.[149]

1.7 Aim of this Thesis

The main aim of this thesis is to revisit the literature model that basal plane of HOPG is largely or entirely inert by testing the electrochemistry of HOPG with a range of redox species, including classical outer-sphere species and adsorbed materials, on different grades (step edge coverage) of HOPG. Electrochemical measurements from macroscale to nanoscale are carried out in combination of complementary techniques for surface characterisation to elucidate the structure-activity effects, if any. In addition, application-oriented studies of graphitic carbon materials are done, in forms of developing new methodology for graphene transfer and actuating droplets on HOPG by electrowetting.

In Chapter 3, the electrochemistry of three classical outer-sphere redox couples is studied on HOPG samples with step edge density differing by >2 orders or magnitude, using a droplet cell setup, and lower limits for fast ET kinetics can be deduced. A comparison of the results on HOPG to those on metal electrodes is made, to explore whether electronic properties can possibly influence the ET kinetics of the reactions studied herein.

In Chapter 4, the electrochemistry of $Fe^{3+/2+}$, known to have slow ET kinetics is studied on two significantly different grades of HOPG, as done in Chapter 3, enabling the kinetic values of $Fe^{3+/2+}$ on HOPG to be readily obtained (based on the simulation results to the macroscopic experimental data). SECCM reactive imaging is carried out on HOPG to reveal nanoscale views of surface electroactivity. Again, the results can be compared with those reported for metals, to further review the possible influence of electronic properties on ET kinetics. The possible time effect after surface cleavage on wetting and electrochemistry of $Fe^{3+/2+}$ on HOPG is also investigated to assess the role of surface history in the study herein, often associated with the use of carbon materials.

In Chapter 5, a powerful technique, fast scan cyclic voltammetry-SECCM (FSCV-SECCM), is introduced to track adsorbed electroactive AQDS on localised areas of HOPG, which can be extensively characterised by complementary techniques (*e.g.* AFM and SEM) to reveal corresponding structural information. SECCM reactive patterning enables surface electroactivity to be monitored when a pipette is scanned from basal plane of HOPG, across step edge and then back to basal plane, and the same spots can be revisited by AFM to generate topographical details. The correlative-electrochemical microscopy approach provides further insights about the electroactivity of local structures of HOPG beyond macroscopic measurements.

In Chapter 6, a new polymer-free method is developed for graphene transfer, taking advantage of a liquid-liquid (organic-aqueous) interface, at which graphene can be transferred after removal of metals, to avoid the issues associated with polymer-supported processes. Transfer of graphene on three

dimensional substrates, such as AFM tips and transmission electron microscopy (TEM) grids is sought to fabricate tools for microscopy imaging and provide platforms where the properties of supported graphene and suspended graphene can be readily studied and compared.

In Chapter 7, electrowetting of aqueous droplets on HOPG surfaces is measured in a configuration where electrochemistry (CV) and optical images for the wetting droplets can be recorded simultaneously. By correlating the geometry changes of droplet with applied potential, a new mechanism of ion intercalation/de-intercalation can be proposed, different from those for the EWOD setup, opening up new avenues to understand electrowetting phenomenon and seek the potentials for applications.

1.8 References

(1) Geim, A. K.; Novoselov, K. S. *Nat. Mater.* **2007**, *6*, 183.

(2) Novoselov, K. S.; Geim, A. K.; Morozov, S. V.; Jiang, D.; Zhang, Y.; Dubonos, S. V.; Grigorieva, I. V.; Firsov, A. A. *Science* **2004**, *306*, 666.

(3) Bernal, J. D. *Proc. R. Soc. Lond. A* **1924**, *106*, 749.

(4) Patel, A. N.; Collignon, M. G.; O'Connell, M. A.; Hung, W. O.; McKelvey, K.; Macpherson, J. V.; Unwin, P. R. *J. Am. Chem. Soc.* **2012**, *134*, 20117.

(5) Lee, C.; Wei, X.; Kysar, J. W.; Hone, J. *Science* **2008**, *321*, 385.

(6) Balandin, A. A.; Ghosh, S.; Bao, W.; Calizo, I.; Teweldebrhan, D.; Miao, F.; Lau, C. N. *Nano Lett.* **2008**, *8*, 902.

(7) Spanu, L.; Sorella, S.; Galli, G. *Phys. Rev. Lett.* **2009**, *103*, 196401.

(8) Blakslee, O. L.; Proctor, D. G.; Seldin, E. J.; Spence, G. B.; Weng, T. *J. Appl. Phys.* **1970**, *41*, 3373.

(9) Pauling, L. *Proc. Natl. Acad. Sci. U. S. A.* **1966**, *56*, 1646.

(10) Aoki, M.; Amawashi, H. *Solid State Commun.* **2007**, *142*, 123.

(11) Mak, K. F.; Shan, J.; Heinz, T. F. *Phys. Rev. Lett.* **2010**, *104*, 176404.

(12) Lipson, H.; Stokes, A. R. *Proc. R. Soc. Lond. A* **1942**, *181*, 101.

(13) Patel, A. N.; Tan, S. Y.; Miller, T. S.; Macpherson, J. V.; Unwin, P. R. *Anal. Chem.* **2013**, *85*, 11755.

(14) Tománek, D.; Louie, S. G. *Phys. Rev. B* **1988**, *37*, 8327.

(15) Chang, H.; Bard, A. J. *Langmuir* **1991**, *7*, 1143.

(16) Binnig, G.; Rohrer, H.; Gerber, C.; Weibel, E. *Appl. Phys. Lett.* **1982**, *40*, 178.

(17) Binnig, G.; Quate, C. F.; Gerber, C. *Phys. Rev. Lett.* **1986**, *56*, 930.

(18) Tersoff, J.; Hamann, D. R. *Phys. Rev. Lett.* **1983**, *50*, 1998.

(19) Li, G.; Luican, A.; Andrei, E. Y. *Phys. Rev. Lett.* **2009**, *102*, 176804.

(20) McCreery, R. L. In *Electroanal. Chem.*; Bard, A. J., Ed.; Marcel Dekker: New York, 1991; Vol. v17, p 221.

(21) McCreery, R. L. *Chem. Rev.* **2008**, *108*, 2646.

(22) McCreery, R. L.; McDermott, M. T. *Anal. Chem.* **2012**, *84*, 2602.

(23) Zhang, G.; Kirkman, P. M.; Patel, A. N.; Cuharuc, A. S.; McKelvey, K.; Unwin, P. R. *J. Am. Chem. Soc.* **2014**, *136*, 11444.

(24) Banks, C. E.; Compton, R. G. *Analyst* **2005**, *130*, 1232.

(25) Banks, C. E.; Crossley, A.; Salter, C.; Wilkins, S. J.; Compton, R. G. *Angew. Chem., Int. Ed.* **2006**, *45*, 2533.

(26) Banks, C. E.; Davies, T. J.; Wildgoose, G. G.; Compton, R. G. *Chem. Commun.* **2005**, 829.

(27) Banks, C. E.; Moore, R. R.; Davies, T. J.; Compton, R. G. *Chem. Commun.* **2004**, 1804.

(28) Ji, X.; Banks, C. E.; Crossley, A.; Compton, R. G. *ChemPhysChem* **2006**, *7*, 1337.

(29) Davies, T. J.; Moore, R. R.; Banks, C. E.; Compton, R. G. *J. Electroanal. Chem.* **2004**, *574*, 123.

(30) Pumera, M. *Electrochem. Commun.* **2013**, *36*, 14.

(31) Reich, S.; Thomsen, C. *Phil. Trans. R. Soc. A* **2004**, *362*, 2271.

(32) Wallace, P. R. *Phys. Rev* **1947**, *71*, 622.

(33) McClure, J. W. *Phys. Rev* **1957**, *108*, 612.

(34) Slonczewski, J. C.; Weiss, P. R. *Phys. Rev* **1958**, *109*, 272.

(35) Dresselhaus, M. S.; Dresselhaus, G.; Fischer, J. E. *Phys. Rev. B* **1977**, *15*, 3180.

(36) Chung, D. D. L. *J. Mater. Sci.* **2002**, *37*, 1475.

(37) Gerischer, H.; McIntyre, R.; Scherson, D.; Storck, W. *J. Phys. Chem.* **1987**, *91*, 1930.

(38) Trickey, S. B.; Müller-Plathe, F.; Diercksen, G. H. F.; Boettger, J. C. *Phys. Rev. B* **1992**, *45*, 4460.

(39) Johnson, L. G.; Dresselhaus, G. *Phys. Rev. B* **1973**, *7*, 2275.

(40) Tatar, R. C.; Rabii, S. *Phys. Rev. B* **1982**, *25*, 4126.

(41) Partoens, B.; Peeters, F. M. *Phys. Rev. B* **2006**, *74*, 075404.

(42) Brandt, N. B.; Chudinov, S. M.; Ponomarev, Y. G. *Semimetals: 1. Graphite and its Compounds*; Elsevier, 2012.

(43) Gerischer, H. *J. Phys. Chem.* **1985**, *89*, 4249.

(44) Kokko, K.; Ojala, E.; Mansikka, K. *Phys. Status Solidi B* **1989**, *153*, 235.

(45) Niimi, Y.; Matsui, T.; Kambara, H.; Tagami, K.; Tsukada, M.; Fukuyama, H. *Phys. Rev. B* **2006**, *73*, 085421.

(46) Ruffieux, P.; Melle-Franco, M.; Gröning, O.; Bielmann, M.; Zerbetto, F.; Gröning, P. *Phys. Rev. B* **2005**, *71*, 153403.

(47) Ugeda, M. M.; Brihuega, I.; Guinea, F.; Gómez-Rodríguez, J. M. *Phys. Rev. Lett.* **2010**, *104*, 096804.

(48) Kobayashi, K. *Phys. Rev. B* **1993**, *48*, 1757.

(49) Lopes dos Santos, J. M. B.; Peres, N. M. R.; Castro Neto, A. H. *Phys. Rev. Lett.* **2007**, *99*, 256802.

(50) Li, G.; Luican, A.; Lopes dos Santos, J. M. B.; Castro Neto, A. H.; Reina, A.; Kong, J.; Andrei, E. Y. *Nat. Phys.* **2010**, *6*, 109.

(51) Chang, H.; Bard, A. J. *J. Am. Chem. Soc.* **1991**, *113*, 5588.

(52) McDermott, M. T.; McCreery, R. L. *Langmuir* **1994**, *10*, 4307.

(53) Stevens, F.; Kolodny, L. A.; Beebe, T. P. *J. Phys. Chem. B* **1998**, *102*, 10799.

(54) Chang, H.; Bard, A. J. *J. Am. Chem. Soc.* **1990**, *112*, 4598.

(55) Zoval, J. V.; Stiger, R. M.; Biernacki, P. R.; Penner, R. M. *J. Phys. Chem.* **1996**, *100*, 837.

(56) Ma, H.; Lee, L.; Brooksby, P. A.; Brown, S. A.; Fraser, S. J.; Gordon, K. C.; Leroux, Y. R.; Hapiot, P.; Downard, A. J. *J. Phys. Chem. C* **2014**, *118*, 5820.

(57) Tersoff, J.; Hamann, D. R. *Phys. Rev. B* **1985**, *31*, 805.

(58) Luican, A.; Li, G.; Andrei, E. Y. *Solid State Commun.* **2009**, *149*, 1151.

(59) Castro Neto, A. H.; Guinea, F.; Peres, N. M. R.; Novoselov, K. S.; Geim, A. K. *Rev. Mod. Phys.* **2009**, *81*, 109.

(60) A. J. Bard; Faulkner, L. R. *Electrochemical Methods: Fundamentals and Applications*; 2nd ed.; John Wiley& Sons, Inc.: New York, 2001.

(61) Cynthia, G. Z. *Handbook of Electrochemistry*; Elsevier: Amsterdam, The Netherlands, 2007.

(62) Nicholson, R. S. *Anal. Chem.* **1965**, *37*, 1351.

(63) Swain, G. M. In *Handbook of Electrochemistry*; Zoski, C. G., Ed.; Elsevier: Amsterdam, 2007, p 111.

(64) Wang, J. *Electroanalysis* **2005**, *17*, 7.

(65) Dumitrescu, I.; Unwin, P. R.; Macpherson, J. V. *Chem. Commun.* **2009**, 6886.

(66) Shao, Y.; Wang, J.; Wu, H.; Liu, J.; Aksay, I. A.; Lin, Y. *Electroanalysis* **2010**, *22*, 1027.

(67) Chen, D.; Tang, L.; Li, J. *Chem. Soc. Rev.* **2010**, *39*, 3157.

(68) Ambrosi, A.; Chua, C. K.; Bonanni, A.; Pumera, M. *Chem. Rev.* **2014**, *114*, 7150.

(69) Davies, T. J.; Banks, C. E.; Compton, R. G. *J. Solid State Electrochem.* **2005**, *9*, 797.

(70) Chou, A.; Bocking, T.; Singh, N. K.; Gooding, J. J. *Chem. Commun.* **2005**, 842.

(71) Gooding, J. J. *Electrochim. Acta* **2005**, *50*, 3049.

(72) Holloway, A.; Wildgoose, G.; Compton, R.; Shao, L.; Green, M. H. *J. Solid State Electrochem.* **2008**, *12*, 1337.

(73) Güell, A. G.; Meadows, K. E.; Dudin, P. V.; Ebejer, N.; Macpherson, J. V.; Unwin, P. R. *Nano Lett.* **2014**, *14*, 220.

(74) Kim, J.; Xiong, H.; Hofmann, M.; Kong, J.; Amemiya, S. *Anal. Chem.* **2010**, *82*, 1605.

(75) Güell, A. G.; Ebejer, N.; Snowden, M. E.; McKelvey, K.; Macpherson, J. V.; Unwin, P. R. *Proc. Natl. Acad. Sci. U. S. A.* **2012**, *109*, 11487.

(76) Kim, K. S.; Zhao, Y.; Jang, H.; Lee, S. Y.; Kim, J. M.; Kim, K. S.; Ahn, J.-H.; Kim, P.; Choi, J.-Y.; Hong, B. H. *Nature* **2009**, *457*, 706.

(77) Reina, A.; Jia, X.; Ho, J.; Nezich, D.; Son, H.; Bulovic, V.; Dresselhaus, M. S.; Kong, J. *Nano Lett.* **2008**, *9*, 30.

(78) Novoselov, K. S.; Jiang, D.; Schedin, F.; Booth, T. J.; Khotkevich, V. V.; Morozov, S. V.; Geim, A. K. *Proc. Natl. Acad. Sci. U. S. A.* **2005**, *102*, 10451.

(79) Valota, A. T.; Kinloch, I. A.; Novoselov, K. S.; Casiraghi, C.; Eckmann, A.; Hill, E. W.; Dryfe, R. A. W. *ACS Nano* **2011**, *5*, 8809.

(80) Güell, A. G.; Ebejer, N.; Snowden, M. E.; Macpherson, J. V.; Unwin, P. R. *J. Am. Chem. Soc.* **2012**, *134*, 7258.

(81) Li, W.; Tan, C.; Lowe, M. A.; Abruña, H. D.; Ralph, D. C. *ACS Nano* **2011**, *5*, 2264.

(82) Ritzert, N. L.; Rodríguez-López, J.; Tan, C.; Abruña, H. D. *Langmuir* **2013**, *29*, 1683.

(83) Ignaczak, A.; Schmickler, W. *J. Electroanal. Chem.* **2003**, *554–555*, 201.

(84) Schmickler, W. *J. Electroanal. Chem.* **1986**, *204*, 31.

(85) Luque, N. B.; Schmickler, W. *Electrochim. Acta* **2013**, *88*, 892.

(86) Zhu, W.; Low, T.; Perebeinos, V.; Bol, A. A.; Zhu, Y.; Yan, H.; Tersoff, J.; Avouris, P. *Nano Lett.* **2012**, *12*, 3431.

(87) Martin, J.; Akerman, N.; Ulbricht, G.; Lohmann, T.; Smet, J. H.; von Klitzing, K.; Yacoby, A. *Nat. Phys.* **2008**, *4*, 144.

(88) Xu, K.; Cao, P.; Heath, J. R. *Nano Lett.* **2009**, *9*, 4446.

(89) Li, Z.; Wang, Y.; Kozbial, A.; Shenoy, G.; Zhou, F.; McGinley, R.; Ireland, P.; Morganstein, B.; Kunkel, A.; Surwade, S. P.; Li, L.; Liu, H. *Nat. Mater.* **2013**, *12*, 925.

(90) Bowling, R. J.; Packard, R. T.; McCreery, R. L. *J. Am. Chem. Soc.* **1989**, *111*, 1217.

(91) Bowling, R.; Packard, R. T.; McCreery, R. L. *Langmuir* **1989**, *5*, 683.

(92) Bowling, R.; Packard, R. T.; McCreey, R. L. *J. Electrochem. Soc.* **1988**, *135*, 1605.

(93) Lee, C.-Y.; Bond, A. M. *Anal. Chem.* **2008**, *81*, 584.

(94) Lee, C.-Y.; Guo, S.-X.; Bond, A. M.; Oldham, K. B. *J. Electroanal. Chem.* **2008**, *615*, 1.

(95) Kneten, K. R.; McCreery, R. L. *Anal. Chem.* **1992**, *64*, 2518.

(96) McDermott, M. T.; Kneten, K.; McCreery, R. L. *J. Phys. Chem.* **1992**, *96*, 3124.

(97) Cline, K. K.; McDermott, M. T.; McCreery, R. L. *J. Phys. Chem.* **1994**, *98*, 5314.

(98) Kariuki, J. K.; McDermott, M. T. *Langmuir* **1999**, *15*, 6534.

(99) Chen, P.; Fryling, M. A.; McCreery, R. L. *Anal. Chem.* **1995**, *67*, 3115.

(100) Huang, W.; McCreery, R. L. *J. Electroanal. Chem.* **1992**, *326*, 1.

(101) Pharr, C. M.; Griffiths, P. R. *Anal. Chem.* **1997**, *69*, 4673.

(102) Poon, M.; McCreery, R. L. *Anal. Chem.* **1986**, *58*, 2745.

(103) Poon, M.; McCreery, R. L.; Engstrom, R. *Anal. Chem.* **1988**, *60*, 1725.

(104) Rice, R. J.; McCreery, R. L. *Anal. Chem.* **1989**, *61*, 1637.

(105) Rice, R. J.; Pontikos, N. M.; McCreery, R. L. *J. Am. Chem. Soc.* **1990**, *112*, 4617.

(106) Bowling, R.; McCreery, R. L. *Anal. Chem.* **1988**, *60*, 605.

(107) Luque, N. B.; Schmickler, W. *Electrochim. Acta* **2012**, *71*, 82.

(108) Zhou, Y.; Holme, T.; Berry, J.; Ohno, T. R.; Ginley, D.; O'Hayre, R. *J. Phys. Chem. C.* **2009**, *114*, 506.

(109) Ta, T. C.; Kanda, V.; McDermott, M. T. *J. Phys. Chem. B.* **1999**, *103*, 1295.

(110) Davies, T. J.; Hyde, M. E.; Compton, R. G. *Angew. Chem., Int. Ed.* **2005**, *44*, 5121.

(111) Bond, A. M.; Duffy, N. W.; Guo, S.-X.; Zhang, J.; Elton, D. *Anal. Chem.* **2005**, *77*, 186A.

(112) Zhang, J.; Guo, S.-X.; Bond, A. M.; Marken, F. *Anal. Chem.* **2004**, *76*, 3619.

(113) Williams, C. G.; Edwards, M. A.; Colley, A. L.; Macpherson, J. V.; Unwin, P. R. *Anal. Chem.* **2009**, *81*, 2486.

(114) Takahashi, Y.; Kumatani, A.; Munakata, H.; Inomata, H.; Ito, K.; Ino, K.; Shiku, H.; Unwin, P. R.; Korchev, Y. E.; Kanamura, K.; Matsue, T. *Nat, Commun.* **2014**, *5*, 5450.

(115) Ebejer, N.; Schnippering, M.; Colburn, A. W.; Edwards, M. A.; Unwin, P. R. *Anal. Chem.* **2010**, *82*, 9141.

(116) Ebejer, N.; Guell, A. G.; Lai, S. C.; McKelvey, K.; Snowden, M. E.; Unwin, P. R. *Annu. Rev. Anal. Chem.* **2013**, *6*, 329.

(117) Lai, S. C. S.; Patel, A. N.; McKelvey, K.; Unwin, P. R. *Angew. Chem. Int. Ed.* **2012**, *51*, 5405.

(118) Güell, A. G.; Cuharuc, A. S.; Kim, Y. R.; Zhang, G.; Tan, S. Y.; Ebejer, N.; Unwin, P. R. *ACS Nano* **2015**, *9*, 3558.

(119) Byers, J. C.; Güell, A. G.; Unwin, P. R. *J. Am. Chem. Soc.* **2014**, *136*, 11252.

(120) McDermott, M. T.; Kneten, K.; McCreery, R. L. *J. Phys. Chem.* **1992**, *96*, 3124.

(121) Zhang, G.; Cuharuc, A. S.; Güell, A. G.; Unwin, P. R. *Phys. Chem. Chem. Phys.* **2015**, *17*, 11827.

(122) Li, Z.; Kozbial, A.; Nioradze, N.; Parobek, D.; Shenoy, G. J.; Salim, M.; Amemiya, S.; Li, L.; Liu, H. *ACS Nano* **2016**, *10*, 349.

(123) Macpherson, J. V.; Unwin, P. R. *Anal. Chem.* **2000**, *72*, 276.

(124) Kranz, C.; Friedbacher, G.; Mizaikoff, B.; Lugstein, A.; Smoliner, J.; Bertagnolli, E. *Anal. Chem.* **2001**, *73*, 2491.

(125) Frederix, P. L.; Bosshart, P. D.; Akiyama, T.; Chami, M.; Gullo, M. R.; Blackstock, J. J.; Dooleweerdt, K.; de Rooij, N. F.; Staufer, U.; Engel, A. *Nanotechnology* **2008**, *19*, 384004.

(126) Wain, A. J.; Pollard, A. J.; Richter, C. *Anal. Chem.* **2014**, *86*, 5143.

(127) Anne, A.; Cambril, E.; Chovin, A.; Demaille, C.; Goyer, C. *ACS Nano* **2009**, *3*, 2927.

(128) Anne, A.; Bahri, M. A.; Chovin, A.; Demaille, C.; Taofifenua, C. *Phys. Chem. Chem. Phys.* **2014**, *16*, 4642.

(129) Sun, T.; Yu, Y.; Zacher, B. J.; Mirkin, M. V. *Angew. Chem. Int. Ed.* **2014**, *53*, 14120.

(130) Lhenry, S.; Leroux, Y. R.; Hapiot, P. *Anal. Chem.* **2012**, *84*, 7518.

(131) Nioradze, N.; Chen, R.; Kurapati, N.; Khvataeva-Domanov, A.; Mabic, S.; Amemiya, S. *Anal. Chem.* **2015**, *87*, 4836.

(132) Cuharuc, A. S.; Zhang, G.; Unwin, P. R. *Phys. Chem. Chem. Phys.* **2016**, *18*, 4966.

(133) Tan, S.-y.; Zhang, J.; Bond, A. M.; Macpherson, J. V.; Unwin, P. R. *Anal. Chem.* **2016**, *88*, 3272.

(134) Patel, A. N.; Tan, S. Y.; Unwin, P. R. *Chem. Commun.* **2013**, *49*, 8776.

(135) Patel, A. N.; McKelvey, K.; Unwin, P. R. *J. Am. Chem. Soc.* **2012**, *134*, 20246.

(136) Allongue, P.; Delamar, M.; Desbat, B.; Fagebaume, O.; Hitmi, R.; Pinson, J.; Savéant, J.-M. *J. Am. Chem. Soc.* **1997**, *119*, 201.

(137) Kirkman, P. M.; Güell, A. G.; Cuharuc, A. S.; Unwin, P. R. *J. Am. Chem. Soc.* **2014**, *136*, 36.

(138) Greenwood, J.; Phan, T. H.; Fujita, Y.; Li, Z.; Ivasenko, O.; Vanderlinden, W.; Van Gorp, H.; Frederickx, W.; Lu, G.; Tahara, K.; Tobe, Y.; Uji-i, H.; Mertens, S. F. L.; De Feyter, S. *ACS Nano* **2015**, *9*, 5520.

(139) Stevenson, K. J.; Veneman, P. A.; Gearba, R. I.; Mueller, K. M.; Holliday, B. J.; Ohta, T.; Chan, C. K. *Faraday Discuss.* **2014**, *172*, 273.

(140) Patten, H. V.; Velický, M.; Dryfe, R. A. W. In *Electrochemistry of Carbon Electrodes*; Wiley-VCH Verlag GmbH & Co. KGaA: 2015, p 121.

(141) Yi, M.; Shen, Z. *J. Mater. Chem. A* **2015**, *3*, 11700.

(142) Zhang, Y.; Zhang, L.; Zhou, C. *Acc. Chem. Res.* **2013**, *46*, 2329.

(143) Yan, K.; Fu, L.; Peng, H.; Liu, Z. *Acc. Chem. Res.* **2013**, *46*, 2263.

(144) Li, X.; Zhu, Y.; Cai, W.; Borysiak, M.; Han, B.; Chen, D.; Piner, R. D.; Colombo, L.; Ruoff, R. S. *Nano Lett.* **2009**, *9*, 4359.

(145) Reina, A.; Son, H.; Jiao, L.; Fan, B.; Dresselhaus, M. S.; Liu, Z.; Kong, J. *J. Phys. Chem. C* **2008**, *112*, 17741.

(146) Liu, W.; Jackson, B. L.; Zhu, J.; Miao, C.-Q.; Chung, C.-H.; Park, Y. J.; Sun, K.; Woo, J.; Xie, Y.-H. *ACS Nano* **2010**, *4*, 3927.

(147) Lin, W.-H.; Chen, T.-H.; Chang, J.-K.; Taur, J.-I.; Lo, Y.-Y.; Lee, W.-L.; Chang, C.-S.; Su, W.-B.; Wu, C.-I. *ACS Nano* **2014**, *8*, 1784.

(148) Klarman, D.; Andelman, D.; Urbakh, M. *Langmuir* **2011**, *27*, 6031.

(149) Gupta, R.; Olivier, G. K.; Frechette, J. *Langmuir* **2010**, *26*, 11946.

Chapter 2 Experimental Methods

This chapter lists the chemicals and materials, experimental methodologies, sample characterisation approaches and data analysis methods used for the studies in this thesis.

2.1 Chemicals and Materials

All the solutions were freshly prepared using water purified with a Millipore Milli-Q system (resistivity 18.2 MΩ cm at 25 °C). All the chemicals were used as received unless otherwise stated. Details of the chemicals and materials adopted herein are listed in Table 2.1.

Table 2.1 Chemicals and materials used for the studies

Chemical	Supplier
Hexaammineruthenium (III) chloride ($Ru(NH_3)_6Cl_3$, 99.00%)	Strem Chemicals
Potassium hexachloroiridate (IV) (K_2IrCl_6, 99.99%)	Aldrich
Potassium hexacyanoferrate (II) trihydrate ($K_4Fe(CN)_6 \cdot 3H_2O$, 99.99%)	Sigma-Aldrich.
Potassium chloride (KCl, 99%)	Sigma-Aldrich.
Iron (III) perchlorate hydrate ($Fe(ClO_4)_3 \cdot xH_2O$, 98%)	Sigma-Aldrich
Iron (II) perchlorate hydrate ($Fe(ClO_4)_2 \cdot xH_2O$, 98%)	Sigma-Aldrich
Ammonium persulfate ($(NH_4)_2S_2O_8$, ≥98 %)	Sigma-Aldrich
(ferrocenylmethyl)trimethylammonium hexafluorophosphate ($FcTMAPF_6$)	Prepared through in-house metathesis
Perchloric acid ($HClO_4$, 70 %)	Acros Organics
Sodium perchlorate ($NaClO_4$, ≥98%)	Sigma-Aldrich
Sodium phosphate tribasic dodecahydrate (Na_3PO_4•12 H_2O, ≥98%)	Sigma-Aldrich
Sodium sulphate (Na_2SO_4, ≥99%)	Sigma-Aldrich
Fluorescein sodium salt ($C_{20}H_{10}O_5Na_2$)	Sigma-Aldrich
Phosphoric acid (H_3PO_4, ≥85%)	Sigma-Aldrich
Disodium anthraquinone-2,6-disulfonate (AQDS)	Acros Organics

Dichlorodimethylsilane ($Si(CH_3)_2Cl_2$, >99 %)	Acros Organics
Acetone	VWR Chemicals
Propan-2-ol	Fisher
n-Hexane (99 %)	VWR Chemicals
Gold nanoparticles (10nm diameter, stabilised suspension in citrate buffer)	Sigma-Aldrich
Material	**Supplier**
AM grade HOPG	Courtesy of Prof. Richard L. McCreery (University of Alberta, Canada), originating from Dr. Arthur Moore, Union Carbide (now GE Advanced Ceramics)
ZYA grade HOPG	SPI Supplies (West Chester, PA).
ZYB grade HOPG	NT-MDT (Moscow, Russia).
SPI-1 grade HOPG	SPI Supplies (West Chester, PA).
SPI-3 grade HOPG	SPI Supplies (West Chester, PA).
Dual-channel borosilicate pipette (O.D. 1.5 mm, I.D. 1.2 mm, TGC150-10)	Harvard Apparatus
AFM tips (RFESP and SNL-10)	Bruker
Copper (Cu) TEM grids (3 mm, 1500 meshes)	SPI Supplies
Acheson Electrodag (1415M)	Agar Scientific
Copper (Cu) foil (#13382, 25 µm, 99.8%)	Alfa Aesar
Silicon/silicon oxide (Si/SiO_2) wafer (4-inch diameter, 525 µm thick, 1-10 Ω cm resistivity, n-type, single side polished, 300 nm thermal oxide layer)	IDB Technologies Ltd.

Silver wire (0.25 mm diameter, 99.9 %)	MaTecK GmbH
Insulated silver (Ag) wire (0.25 mm diameter with a 24 µm thick PTFE cladding)	Goodfellow, UK
Palladium (Pd) wire (0.25 mm diameter, >99.95 %)	MaTecK GmbH
Sandpaper (P 4000)	Buehler

2.2 Sample Preparation

2.2.1 Cleavage of HOPG

All HOPG samples were carefully mounted on a gold coated (100 nm) silicon wafer with Acheson Electrodag, and an electrical connection was established by attaching a metal wire to the gold surface. Prior to each experiment, the HOPG sample used was cleaved with Scotch tape, by peeling back the top layers to reveal a clean, fresh surface, with the cleaving direction maintained to avoid deformation, until the tape was totally covered with HOPG, as used routinely.[1-13] It has been shown elsewhere that AM HOPG is characterised by a particularly low step edge density (high quality).[2] Fresh surfaces of this material were also revealed by mechanically cleaving with a clean razor blade, inserted perpendicular to the basal plane with a gentle rocking motion until a small piece delaminated spontaneously, as adopted elsewhere.[8,14,15] It is worth to point out that for AM grade HOPG there is little difference between the apparent quality of HOPG surfaces cleaved mechanically and using Scotch tape, as judged by AFM and capacitance measurements.[1,2] For FSCV-SECCM measurements, both procedures were used for preparation of AM grade HOPG, with samples respectively labelled as AM_S (via Scotch tape cleavage) and AM_M (via mechanical cleavage).

2.2.2 CVD Growth and Transfer of Graphene

2.2.2.1 CVD Growth of Graphene

Monolayer graphene was synthesized in a commercial low-pressure CVD system (NanoCVD 8G, Moorefield Associates, UK) (Figre 2.1a). Copper foil was cut into ~1 cm × 1 cm square substrates and subsequently cleaned with

acetone, propan-2-ol and water before being put into the CVD growth chamber. A purge regime was performed, pumping the system to vacuum and back filling with Ar, five times. Subsequently, the sample was heated to 900 °C as quickly as possible, under a flow of 190 standard cubic centimeters per minute (sccm) Ar and 10 sccm H_2, before maintaining 900 °C for 2 minutes (Figure 2.1b). The temperature was then quickly increased to 1000 °C under the same gas flow conditions. The pressure regime of the system was also changed, and set to maintain a chamber pressure of 10 Torr. The system was left to stabilize for 15 min to anneal the copper foils, before 17 % (of total gas flow) CH_4 was introduced for 10 min, promoting graphene growth. Post-growth, the CH_4 flow was halted, while a flow of 120 sccm Ar and 10 sccm H_2 was still maintained, allowing the system to cool down to 100 °C, at which point the system was vented and the sample was taken into air to cool down to room temperature (Figure 2.1c).

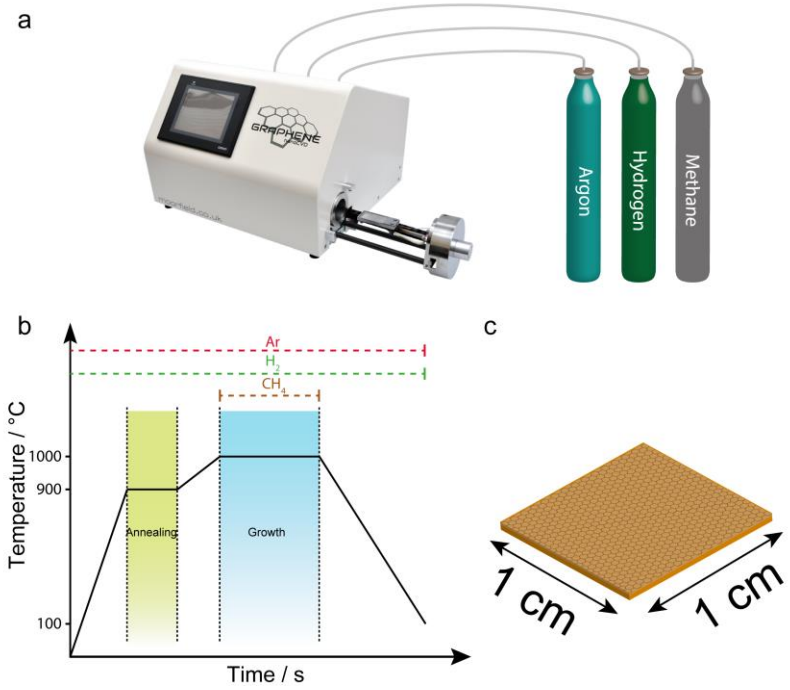

Figure 2.1 (a) CVD system for graphene growth, with conditions shown in (b). (c) Schematic of graphene coated copper sample after CVD growth.

2.2.2.2 Polymer-free Graphene Transfer

The polymer-free biphasic transfer method developed and discussed in Chapter 6 is illustrated schematically in Figure 2.2. Monolayer graphene was

grown on polycrystalline Cu foils in a low-pressure commercial CVD system, using methane as the carbon source. After polishing the back of the Cu foil with sandpaper (to remove the graphene grown on the backside and facilitate the subsequent etching), the sample was initially floated (graphene side up) atop a 0.1 M ammonium persulfate ($(NH_4)_2S_2O_8$) etching solution, which has been shown to minimise residues compared to the other commonly used $FeCl_3$ and $Fe(NO_3)_3$ solutions.[16,17] At this point, a non-polar hexane layer was gently added dropwise to the surface of the etchant solution with a syringe, so that the graphene/Cu sample was trapped at the resulting organic/aqueous biphasic interface, with the exposed face of the hydrophobic graphene in contact only with the hexane, and the Cu foil exposed to the etchant solution. After sufficient etching time (~12 h), only the synthesised graphene sheet remained trapped at the interface. Note that the surface tension for the hexane/water interface is *ca.* 45 mN m^{-1}, [18,19] lower than that of the air/water interface, which prevents the water layer pulling the sheet apart, as would be the case if the non-polar layer were not present.[18] The 'soft support' from the hexane layer also protects the graphene sheet by minimising physical drift at the interface.

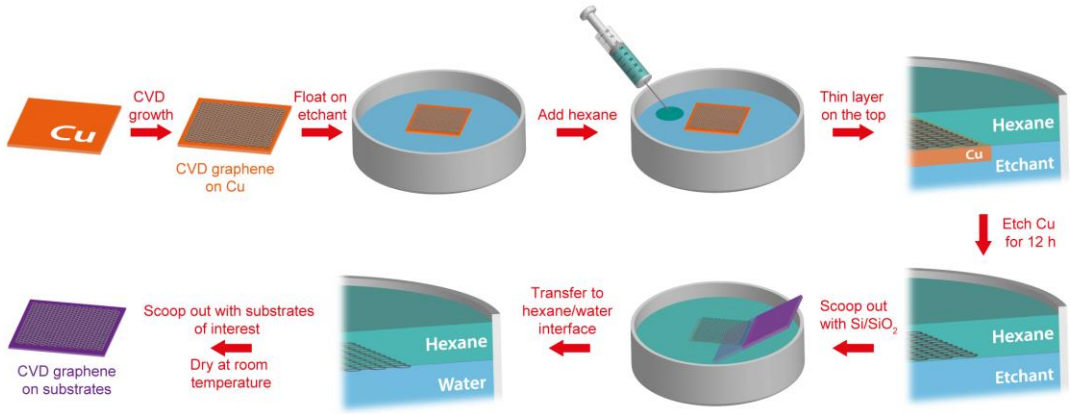

Figure 2.2 Schematic of the polymer-free biphasic method for CVD graphene transfer.

To further minimise any possible contamination from etchant salts produced, the monolayer graphene sheet was scooped out with a clean Si/SiO_2 substrate, completing the first transfer step and transferred to a new hexane/pure water interface with the aid of an Si/SiO_2 wafer. The graphene

sheet was kept there for 5 h. After this cleaning step, the freestanding graphene sheet was scooped out from the interface using an arbitrary substrate of interest (*e.g.* Si/SiO_2 wafers, AFM tips and TEM grids for the studies herein) in a single swift motion, before being left to dry at room temperature. For the coating of AFM tips and copper TEM grids, these substrates were temporarily glued onto a small piece of Si/SiO_2 as a support to facilitate manipulation with tweezers and scoop out the graphene sheet.

2.2.2.3 PDMS-assisted Graphene Transfer

The PDMS-assisted transfer method has been reported to be a most developed methodology in the literature,[20,21] and is widely adopted in the graphene community. It was important to demonstrate that the polymer-free biphasic transfer method did not produce more mechanically-introduced defects in the graphene, as compared to this polymer-support route. Thus, comparative experiments using a traditional PDMS-supported transfer process were carried out. Graphene samples were synthesised under the same CVD chamber conditions as used for biphasic transfer studies, to ensure the starting material was of the same quality. The as-grown graphene/Cu samples were polished on the back, as described in section 2.2.2.2, and then coated with a PDMS layer. For the preparation of PDMS films, the pre-polymer and curing agent (Sylgard 184 elastomer), with a ratio of 10:1 (w/w), were fully mixed in a petri dish and then degassed in a desiccator for 30 min. A tiny amount of the mixture was poured slowly onto the front side of the sample, developing a thin layer on top of the graphene, and the sample was then kept at 70 °C in an oven for one hour. After cooling down, the PDMS-coated sample was gently laid on the surface of 0.1 M $(NH_4)_2S_2O_8$ aqueous solution, with the polymer side facing up, and wet etched for the same period of time (~12 h) as our biphasic method. The sample was subsequently transferred to pure water with the aid of an Si/SiO_2 wafer, to remove possible salt contaminants. After an appropriate time (~5 h), the sample was scooped out using an Si/SiO_2 wafer and left in air to dry.

2.3 Electrochemistry

2.3.1 Macroscopic Studies

2.3.1.1 Macroscopic Electrochemistry of Classical Redox Couples

For studies of $IrCl_6^{2-/3-}$, $Ru(NH_3)_6^{3+/2+}$ and $Fe(CN)_6^{4-/3-}$ electrochemistry in Chapter 3, cyclic voltammetry was carried out in a three-electrode configuration using a 760C potentiostat (CH Instruments, Inc.), with the HOPG sample serving as the working electrode (WE), a platinum wire or gauze as the counter electrode (CE) and a silver chloride (AgCl)-coated silver (Ag) wire as the reference electrode (RE), respectively (Figure 2.3). Two types of reference electrodes were used, one was bare Ag wire (0.25 mm diameter) coated with AgCl, and one an insulated Ag wire with the exposed end coated with AgCl. Each acted as an Ag/AgCl electrode (potential defined by the KCl concentration in the solution used). A droplet with a volume of 20 µL was placed on the HOPG surface within 3 s of cleavage, with the counter and reference electrodes then placed into the droplet as quickly as possible, minimising possible surface history effect (*e.g.* airborne hydrocarbon contamination[22]). The area of HOPG surface covered by the droplet varied very slightly from experiment to experiment but was typically 0.21 cm^2. CV measurements started <1 min from cleavage of the sample, usually at scan rates between 1 V s^{-1} and 10 V s^{-1}.

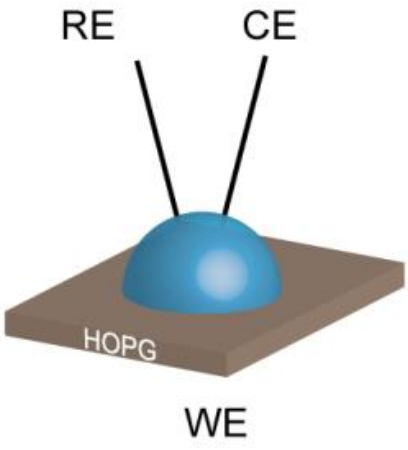

Figure 2.3 Droplet-cell configuration of a three-electrode system.

2.3.1.2 Macroscopic Electrochemistry of $Fe^{3+/2+}$

For the macroscopic measurements of $Fe^{3+/2+}$ in Chapter 4, a three-electrode setup with a droplet-cell configuration was used (Figure 2.3), in which the HOPG sample was employed as the WE, and a platinum wire and a palladium wire (saturated with H_2 at -3 V for 30 min in 0.1 M $HClO_4$ solution), served as the CE and RE, respectively. After cleavage of the HOPG samples, a 20 µL droplet of the solution of interest was gently placed on top of the surface in a quick motion (<3 s), followed by the assembly of the CE and RE into the droplet cell, as was adopted previously.[23,24] CV measurements were then immediately carried out using a 760C potentiostat (CH Instruments, Inc.), at a range of scan rates of 0.1, 0.5, 1, 2, 3, 4, 5, 6, 7, 8, 9 and 10 V s^{-1}(randomly chosen). For comparison, CVs were also measured using an O-ring (radius 3.1 mm, see section 2.3.1.3) to confine the contact area of droplet (with a volume of 50 µL) on the WE. Finally, for time effect studies, HOPG was freshly cleaved with Scotch tape and then left exposed in air for different times, *i.e.* 10 min, 20 min, 30min, 1 h, 2h, 4h, and 12 h, before a droplet was deposited on the surface for CV measurements.

2.3.1.3 Macroscopic Electrochemistry of AQDS

CV measurements in Chapter 5 were carried out with a computer-controlled potentiostat (CH Instruments Model 750A, Austin, Texas) utilising a standard three-electrode configuration, where the contacted HOPG sample served as the working electrode, and an Ag/AgCl electrode and a platinum gauze electrode acted as the reference and counter electrodes respectively. An O-ring gently placed on the freshly cleaved HOPG surface with minimal applied force, was utilized in order to obtain a well-defined working electrode area (a disc-shaped area with the diameter of 6.2 mm; Figure 2.4). Using this arrangement, the electrode contact area was defined as a ~30 mm^2 disc. The solution (10 µM AQDS in 0.1 M $HClO_4$) with a volume of *ca.* 70 µL was introduced to the surface within a minute of sample cleaving. The reference and counter electrodes were placed into the solution immediately after. The validity of this arrangement was confirmed by also making measurements with a simple droplet cell, as reported previously.[2] Broadly similar data were

obtained, but the O-ring cell allowed more precise determination of the electrode area. All CVs were recorded between 0.1 and -0.5 V vs Ag/AgCl at a scan rate of 0.1 V s^{-1}, after 10 s of solution contact time with the surface, unless otherwise stated.

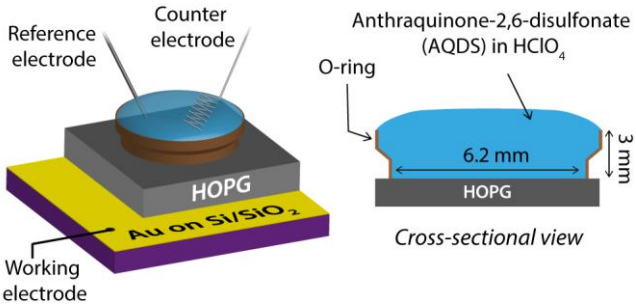

Figure 2.4 Schematic of the O-ring cell used to hold solution on HOPG with a defined contact area.

2.3.2 FSCV-SECCM

FSCV-SECCM measurements in Chapter 5 were carried out using a dual-channel borosilicate pipette pulled to a sharp taper using a CO_2-laser puller (P-2000, Sutter Instruments), to create an opening of *ca.* 1 μm diameter, which was subsequently polished to an opening of *ca.* 18 μm diameter on a polishing wheel. The pipette was silanised using dichlorodimethylsilane to ensure a hydrophobic outer wall, before filling with a solution of 1 μM AQDS in 0.05 M $HClO_4$ and inserting an AgCl coated Ag wire into each channel to serve as QRCEs. The order of magnitude lower concentration of AQDS, compared to the macroscopic measurements, ensured that the evolution of AQDS adsorption at the microscale could be followed in real time.

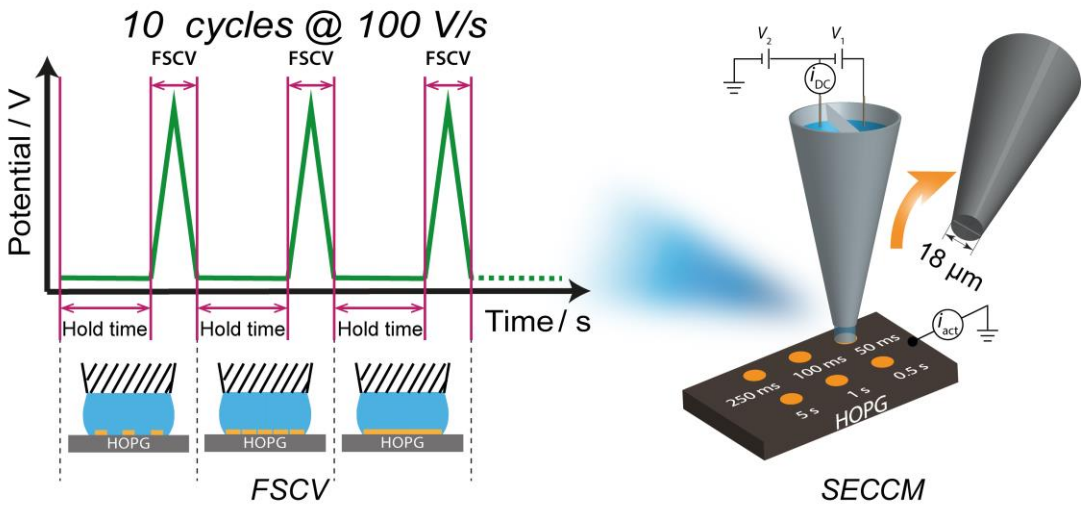

Figure 2.5 Schematic for FSCV-SECCM configuration.

The pipette was mounted on a high-dynamic *z*-piezoelectric positioner (P-753.3CD LISA, Physik Instrumente), and positioned just above freshly cleaved AM grade HOPG, which was mounted on an *xy*-piezoelectric stage (P-622.2CL PIHera, Physik Instrumente). A moat of saturated aqueous KCl solution around the substrate was employed to provide a humid atmosphere, preventing evaporation of water from the tip opening. A schematic showing the FSCV-SECCM setup is given in Figure 2.5. A potential bias (V_1) of 0.05 V was applied between the QRCEs, which gave rise to a conductance current (i_{DC}) across the meniscus at the end of the pipette (typically *ca.* 0.1 nA). The pipette was approached to the HOPG surface (at a rate of 0.1 µm s^{-1}) using the *z*-piezoelectric positioner, whilst floating at a potential (V_2) of -0.1 V with respect to ground, so that the substrate experienced a potential of -(V_2 + ½V_1), *i.e.* 0.075 V vs Ag/AgCl QRCE, where there was negligible reduction of AQDS (see Chapter 5).

Note that in contrast to SECCM imaging[5,25-28] with much smaller tips, there was no modulation of the pipette position in these FSCV studies. The DC conductance current, i_{DC}, was adopted as the feedback signal during approach. The approach was immediately halted upon meniscus contact, where an electrochemical cell was formed between the tip and the substrate, as determined by a sudden, dramatic increase in the conductance current (typically by *ca.* 4 nA). The substrate potential was then maintained (at 0.075

V vs Ag/AgCl) for a pre-determined *hold time*, during which AQDS adsorption occurred, before a CV was performed at 100 V s^{-1}, over a substrate potential range of 0.075 to -0.825 V vs Ag/AgCl QRCE. After completion of the first CV, nine subsequent CVs were performed, with the same *hold time* employed between each of them. This procedure was performed for a wide range of *hold times*, specifically 50 ms, 100 ms, 250 ms, 0.5 s, 1 s and 5 s, each at a fresh area of HOPG, requiring the tip to be retracted, moved, and re-approached multiple times, but taking < ~30 min in total for all the measurements. High-speed data acquisition at 29412 points per second (each point the average of 16 equally spaced readings) was achieved using an FPGA card (PCIe-7852R) with a LabVIEW 2013 interface, providing a measured data point roughly every 34 µs.

2.3.3 SECCM Reactive Patterning and Imaging

For SECCM reactive patterning of AQDS on HOPG in Chapter 5 (Figure 2.6), a dual-channel borosilicate pipette (1.5 mm o.d., 1.2 mm i.d., TGC150-10, Harvard Apparatus) was pulled to a sharp taper (as in the FSCV measurements, but without further polishing), creating two identical pipettes: one was used for SECCM and the second imaged with FE-SEM to accurately measure the opening dimensions. The pipette employed was *ca.* 350 nm in diameter, and was again silanised to ensure a hydrophobic outer wall, before being filled with 100 µM AQDS (in 0.1 M $HClO_4$). The AQDS concentration was an order of magnitude higher for the macroscopic measurements, such that the diffusional electrochemical flux at the surface was measured, to complement the FSCV studies which measured adsorbed material. Ag/AgCl wires served as QRCEs, and the pipette and AM HOPG sample were mounted as outlined for FSCV measurements. In this case, V_1 = 0.3 V and V_2 = 0.25 V with respect to ground, and hence the substrate experienced a potential of -0.4 V vs Ag/AgCl, where diffusion-limited AQDS reduction occurred (see Chapter 5).[29] The pipette was approached to the HOPG surface, whilst being oscillated normal to the surface in a sinusoidal fashion (20 nm peak-to-peak amplitude at 233.3 Hz herein) through the *z*-piezoelectric positioner using a lock-in amplifier (SR830, Stanford Research

Instruments). Upon meniscus contact, this oscillation produced an alternating current (i_{AC}) component of the conductance current due to the periodic deformation of the liquid meniscus.[29,30] The AC magnitude was picked out by the lock-in amplifier, and used to halt the approach and as a set point to maintain a constant tip-to-substrate separation during imaging and patterning, ensuring that the pipette itself never physically touched the sample. During SECCM experiments the topography, surface electroactivity and conductivity of the solution between the barrels of the probe were recorded simultaneously.[29] For the studies herein, a spiral line-pattern covering a length of 560 μm over the HOPG surface at a scan speed of 1 μm s^{-1} was created. The data acquisition rate was 78 points per second (each point the average of 512 readings), corresponding to a pixel size in the scan direction of *ca.* 13 nm, and resulting in >40,000 individual current measurements.

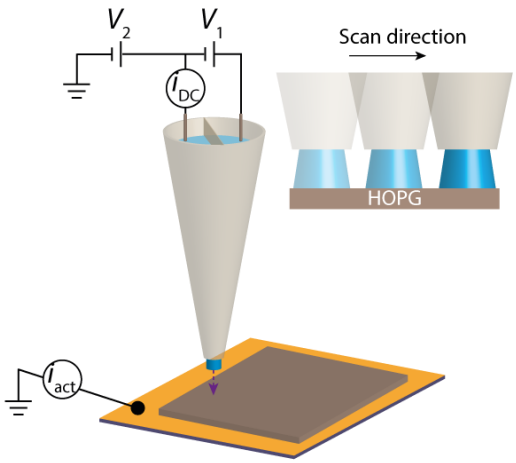

Figure 2.6 Schematic demonstration of SECCM configuration for surface reactive patterning and imaging.

SECCM surface electroactivity mapping of AM HOPG was carried out using the same setup shown in Figure 2.6.[25,31] A dual-barrel borosilicate theta capillary was pulled with a CO_2 laser puller, to produce a tapered dual-channel pipette with a total opening of *ca.* 350 nm across. The pipette was silanised with dimethyldichlorosilane to ensure a hydrophobic outer wall, and then filled with a 2 mM $Fe(ClO_4)_2$ solution, with 0.1 M $HClO_4$ supporting electrolyte. A palladium wire, saturated with H_2 in 0.1 M $HClO_4$ (at -3 V for 30 min) was then inserted into each barrel, to act as a QRCE. The pipette was

mounted on a *z*-piezoelectric positioner and a potential bias (V_1) of 0.2 V was applied between two QRCEs, generating an ion conductance current in the meniscus across the two barrels at the end of the pipette. An oscillation (~40 nm peak-to-peak amplitude at 266.6 Hz herein) normal to the surface in a sinusoidal fashion using a lock-in amplifier was applied to the pipette while approaching the surface of AM grade HOPG. Upon meniscus contact between the pipette and HOPG substrate, this oscillation introduced a noticeable i_{AC} component of the conductance current due to the periodic deformation of the liquid meniscus. The AC magnitude value was used as a set point to halt the approach of the pipette and as a feedback set point to maintain a constant tip-to-substrate distance during imaging, ensuring that the pipette itself by no means touched the sample physically, but the features on the surface could be readily resolved. During SECCM scans over an area of 10 µm × 10 µm (32 forward and retrace lines, at 0.3 µm s^{-1}, ~30 min scan time), surface topography, electroactivity and conductivity of the solution between the barrels of the probe were recorded simultaneously, leading to maps of various quantities in the probed area. Imaging typically commenced within 15 min of sample cleavage. The data acquisition rate was 389 points per second (each point the average of 256 readings), corresponding to *ca.*12967 data points per line, and providing >400000 individual current measurements in the map.

2.3.4 SECCM Landing Measurements on Graphene TEM Grids

The experimental setup used for some of the studies in Chapter 6 is illustrated in Figure 2.7. A double barrel capillary was pulled to a ~400 nm tapered end, using a CO_2-laser puller. The pipette was filled with a solution containing the redox species of interest; either 1 mM $FcTMA^+$ or 1 mM $Ru(NH_3)_6^{3+}$, in 25 mM KCl. A bias, V_1 = 0.2 V, is applied between the QRCEs (an Ag/AgCl wire inserted into each barrel), to produce an ion conductance/migration current i_{DC} in the meniscus formed across the two barrels at the end of the pipette. When the meniscus comes into contact with the surface of a substrate (working electrode), its potential is controlled by tuning V_2. This platform confines the electrochemical cell to sub-micron

(nanoscale) dimensions, and allows either the Cu-supported graphene or suspended graphene on the TEM grid to be assessed individually by careful positioning of the SECCM probe in different places of sample. The setup was mounted on an inverted microscope, to facilitate the precise navigation and landing of the meniscus onto the graphene film. The pipette was firstly approached near to the graphene sheet, without establishing meniscus contact, by means of a micropositioner. The diffraction of light due to the presence of the pipette was clearly seen through the inverted microscope and used to locate the position of the pipette with respect to the TEM grid (on the suspended graphene or on the supported graphene). From this point, further finer pipette approach was achieved with high control of the *z*-piezo of the SECCM setup. The ion conductance current or i_{DC} can be indicative of the size of the meniscus between pipette and substrate,[5,29,31,32] and was used here to diagnose landing of the meniscus on the surface and control of the pipette (as described previously[1]). A data acquisition rate of 390 points per second (each point the average of 256 readings) was achieved using an FPGA card (PCIe-7852R) with a LabVIEW 2013 interface.

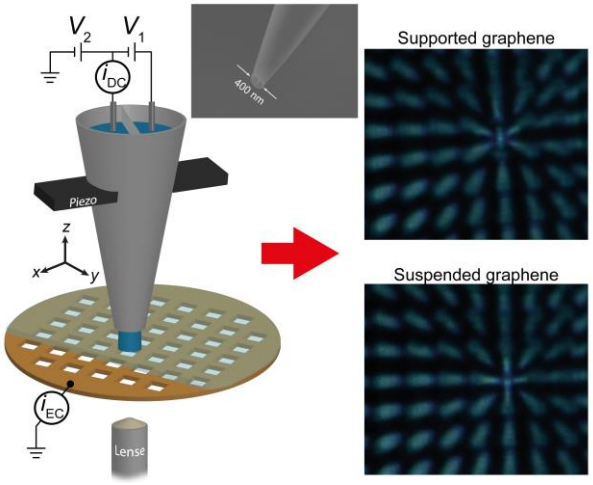

Figure 2.7 Schematic for SECCM pipette landing on a graphene-coated TEM grid, with the diffraction of pipette end shown while over supported graphene and suspended graphene. The inset shows the pipette dimension used.

2.3.5 Electrowetting Measurements

For the studies of electrowetting on HOPG (Chapter 7), a two-electrode configuration was used, in which the HOPG sample was employed as the WE, and an AgCl-coated Ag wire served as a combined CE/RE. The experimental setup is illustrated in Figure 2.8. Before each measurement, HOPG samples were cleaved with Scotch tape, to generate a fresh surface. The two grades of HOPG used show significantly different step edge coverage, as reported previously.[1-4,23] After cleavage of the HOPG samples, a 5 µL droplet of the solution of interest was gently placed atop the surface in a quick motion, followed by the assembly of the Ag/AgCl wire into the droplet, as described elsewhere.[23,24] CV was then immediately carried out with a custom-made potentiostat, with the potential window and scan rate controlled by the LabVIEW interface of an FPGA card (National Instruments). The data acquisition rate was typically 389 data points per second, each point being the average of 256 samples. This produced a potential resolution of 2.6 mV per data point for the scan rate of 1 V s^{-1} and finer potential resolution at slower scan rates.

Optical images of droplet electrowetting on the HOPG surface during CV scans were recorded simultaneously by using a camera (PixeLINK PL-B782U, equipped with a 2× magnification lens) with 1920×1080 pixels, at a frame rate of 12.5 fps, being controlled by the LabVIEW program so that images could be correlated precisely with CV data. All experiments were performed at room temperature (20 °C).

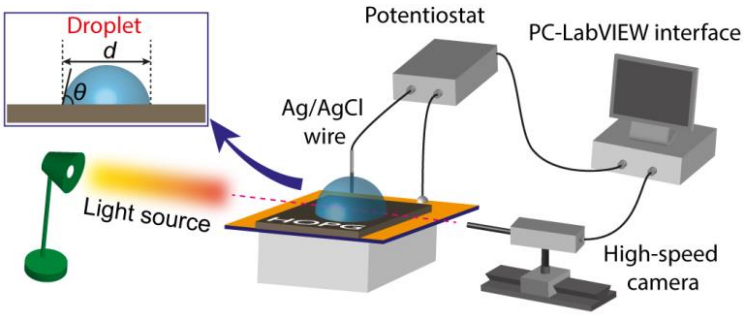

Figure 2.8 Schematic illustration of the experimental setup of droplet electrowetting measurements on HOPG (not to scale), with the contact angle (θ) and contact diameter (d) shown in the upper left inset.

2.4 Macroscopic Time-dependent Wetting of HOPG

Macroscopic measurements of contact angle (CA) were performed on HOPG using 5 µL droplets of pure water or a 5 mM $Fe(ClO_4)_3$ in 0.1 M $HClO_4$ aqueous solution on HOPG, as done in electrowetting work, but for the studies herein the substrate was unbiased. Measurements were made (solution added to the surface) after different times following HOPG cleavage with the contact angle used as a proxy for surface cleanliness and contamination.[22] Images were taken by a camera (PixeLINK PL-B782U, equipped with a 2× magnification lens) with 1920 ×1080 pixels, and analysed with SPIP (Scanning Probe Image Processor) software package.

2.5 Sample Characterisation

2.5.1 Atomic Force Microscopy (AFM)

Ex-situ AFM: AFM topography images of cleaved HOPG substrates and modified surfaces were recorded in air, using a Veeco Enviroscope AFM (Veeco, USA) with a Nanoscope IV controller, operated in tapping mode with silicon nitride tips. Conductive-AFM imaging of HOPG was carried out with a home-modified Innova AFM (Bruker).

2.5.2 Field-emission Scanning Electron Microscopy (FE-SEM)

FE-SEM images of SECCM pipettes, graphite, conductive graphene AFM tips and graphene TEM grids were obtained using a Zeiss SUPRA 55 VP, equipped with in-lens and secondary electron emission detectors.

2.5.3 Transmission Electron Microscopy (TEM)

For TEM imaging, a JEOL JEM-2000FX TEM was used to image the graphene-coated AFM probes. High-resolution TEM images of gold nanoparticles (10 nm diameter, in citrate buffer) on graphene-coated TEM grids were taken using a JEOL JEM-2100 LaB_6 TEM. Both microscopes were operated at 200 kV accelerating voltage.

2.5.4 Scanning Tunnelling Microscopy (STM)

STM measurements were carried out in air using a Veeco STM (Nanoscope E controller). In order to minimise tip-sample interactions, STM scanning parameters were set to 0.5 nA for the tunneling current and 500 mV for the tunneling bias. All STM images were obtained using mechanically cut Pt-Ir tips.

2.5.5 Raman Spectroscopy

Raman spectra and map were acquired using a Renishaw inVia micro-Raman microscope fitted with a CCD detector and a 633 nm Ar^+ laser. A laser power of ~6 mW was employed through a 50× magnification lens, resulting in a laser spot size on the graphene surface of ~1 μm in diameter.

2.5.6 X-ray Photoelectron Spectroscopy (XPS)

XPS data were collected using an Omicron Multiprobe at the University of Warwick Photoemission Facility. Two samples were prepared with a droplet of 1mM $NaClO_4$. One was an electrochemically-treated sample that was subjected to 30 repetitive CVs from 0 V to +2 V at a scan rate of 1 V s^{-1}, before being held at +1.5 V (on the reverse scan) for 30 s. With the substrate

held at this potential, the electrical contact was then disconnected and the droplet was removed with a short blast from an argon gas gun. The second sample was a control, where there was no electrochemistry, but the droplet was on the AM HOPG surface for the same time as the one subjected to electrochemistry, before removing the droplet in the same fashion. The HOPG samples were mounted on Omicron sample plates using electrically-conductive carbon tape and immediately loaded into the fast-entry chamber. Once a pressure of less than 1 × 10^{-7} mbar had been achieved, the samples were transferred to a 12-stage storage carousel, located between the preparation and main analysis chambers, for storage at a pressure of less than 2 × 10^{-10} mbar. XPS measurements were conducted in the main analysis chamber (base pressure 2 × 10^{-11} mbar), with the sample being illuminated using an XM1000 monchromatic Al kα x-ray source (Omicron Nanotechnology). The measurements were conducted at room temperature and at a take-off angle of 90° with respect to the sample surface. The photoelectrons were detected using a Sphera electron analyser (Omicron Nanotechnology), with the core level spectra recorded using a pass energy of 20 eV (resolution approx. 0.63 eV). The data were analysed using the CasaXPS package, using Shirley backgrounds, mixed Gaussian-Lorentzian (Voigt) lineshapes and asymmetry parameters, where appropriate. All binding energies were calibrated using the Fermi edge of a polycrystalline Ag sample, measured immediately prior to commencing the measurements. Compositional accuracy was ensured by calibrating the transmission function of the spectrometer using a variety of clean metal foils.

2.6 Data Analysis

2.6.1 ET Kinetics Analysis

Kinetics was deduced from macroscopic CVs using Nicholson's method.[33,34]

For a reduction process: O + ne^-→R, the following equation applies:

$$\psi = \left(\frac{D_O}{D_R}\right)^{\alpha/2} k_0 \Big/ \sqrt{\frac{\pi nF}{RT} \upsilon D_O} \qquad \text{(eq. 2.1)}$$

where ψ is a dimensionless kinetic parameter, determined by ΔE_p on Nicholson's working curve (data shown in Table 2.2). D_O and D_R are the diffusion coefficients for the oxidised and reduced forms of the redox species, respectively, v is the scan rate, α is the transfer coefficient and other parameters have their usual meanings.

Table 2.2 Dependence of ΔE_p on Ψ

ψ	ΔE_p / mV
20	61
7	63
6	64
5	65
4	66
3	68
2	72
1	84
0.75	92
0.50	105
0.35	121
0.25	141
0.10	212

2.6.2 Contact Angle Measurements

Images of droplet electrowetting under CV conditions and time-dependent measurements of contact angle (using pure water or a 5 mM $Fe(ClO_4)_3$ in 0.1 M $HClO_4$ aqueous solution) were analysed with the SPIP (Scanning Probe Image Processor) software package. The CA for the droplet at a particular potential was measured three times at the contact line and the average value was adopted. The relative contact diameter (RCD) of the droplet was defined as the ratio of contact diameter of droplet at a particular applied voltage to that of the pristine droplet (at 0 V bias).

2.7 References

(1) Zhang, G.; Kirkman, P. M.; Patel, A. N.; Cuharuc, A. S.; McKelvey, K.; Unwin, P. R. *J. Am. Chem. Soc.* **2014**, *136*, 11444.

(2) Patel, A. N.; Collignon, M. G.; O'Connell, M. A.; Hung, W. O.; McKelvey, K.; Macpherson, J. V.; Unwin, P. R. *J. Am. Chem. Soc.* **2012**, *134*, 20117.

(3) Patel, A. N.; Tan, S. Y.; Unwin, P. R. *Chem. Commun.* **2013**, *49*, 8776.

(4) Patel, A. N.; Tan, S. Y.; Miller, T. S.; Macpherson, J. V.; Unwin, P. R. *Anal. Chem.* **2013**, *85*, 11755.

(5) Lai, S. C. S.; Patel, A. N.; McKelvey, K.; Unwin, P. R. *Angew. Chem. Int. Ed.* **2012**, *51*, 5405.

(6) Edwards, M. A.; Bertoncello, P.; Unwin, P. R. *J. Phys. Chem. C* **2009**, *113*, 9218.

(7) Cline, K. K.; McDermott, M. T.; McCreery, R. L. *J. Phys. Chem.* **1994**, *98*, 5314.

(8) McDermott, M. T.; Kneten, K.; McCreery, R. L. *J. Phys. Chem.* **1992**, *96*, 3124.

(9) Kneten, K. R.; McCreery, R. L. *Anal. Chem.* **1992**, *64*, 2518.

(10) Rice, R. J.; McCreery, R. L. *Anal. Chem.* **1989**, *61*, 1637.

(11) Bowling, R. J.; Packard, R. T.; McCreery, R. L. *J. Am. Chem. Soc.* **1989**, *111*, 1217.

(12) Bowling, R. J.; Packard, R. T.; McCreery, R. L. *J. Am. Chem. Soc.* **1989**, *111*, 1217.

(13) Patel, A. N.; Tan, S. Y.; Unwin, P. R. *Chem. Commun.* **2013**, *49*, 8776.

(14) Chang, H.; Bard, A. J. *Langmuir* **1991**, *7*, 1143.

(15) Patel, A. N.; McKelvey, K.; Unwin, P. R. *J. Am. Chem. Soc.* **2012**, *134*, 20246.

(16) Suk, J. W.; Kitt, A.; Magnuson, C. W.; Hao, Y.; Ahmed, S.; An, J.; Swan, A. K.; Goldberg, B. B.; Ruoff, R. S. *ACS Nano* **2011**, *5*, 6916.

(17) Lupina, G.; Kitzmann, J.; Costina, I.; Lukosius, M.; Wenger, C.; Wolff, A.; Vaziri, S.; Ostling, M.; Pasternak, I.; Krajewska, A.; Strupinski, W.; Kataria, S.; Gahoi, A.; Lemme, M. C.; Ruhl, G.; Zoth, G.; Luxenhofer, O.; Mehr, W. *ACS Nano* **2015**.

(18) Lin, W.-H.; Chen, T.-H.; Chang, J.-K.; Taur, J.-I.; Lo, Y.-Y.; Lee, W.-L.; Chang, C.-S.; Su, W.-B.; Wu, C.-I. *ACS Nano* **2014**, *8*, 1784.

(19) Lange, N. A.; Forker, G. M. *Lange's Handbook of Chemistry*; 10th ed., 1967.

(20) Oznuluer, T.; Pince, E.; Polat, E. O.; Balci, O.; Salihoglu, O.; Kocabas, C. *Appl. Phys. Lett.* **2011**, *98*, 183101.

(21) Ching-Yuan, S.; Dongliang, F.; Ang-Yu, L.; Keng-Ku, L.; Yanping, X.; Zhen-Yu, J.; Lain-Jong, L. *Nanotechnology* **2011**, *22*, 185309.

(22) Li, Z.; Wang, Y.; Kozbial, A.; Shenoy, G.; Zhou, F.; McGinley, R.; Ireland, P.; Morganstein, B.; Kunkel, A.; Surwade, S. P.; Li, L.; Liu, H. *Nat. Mater.* **2013**, *12*, 925.

(23) Zhang, G.; Cuharuc, A. S.; Güell, A. G.; Unwin, P. R. *Phys. Chem. Chem. Phys.* **2015**, *17*, 11827.

(24) Cuharuc, A. S.; Zhang, G.; Unwin, P. R. *Phys. Chem. Chem. Phys.* **2016**, *18*, 4966.

(25) Ebejer, N.; Schnippering, M.; Colburn, A. W.; Edwards, M. A.; Unwin, P. R. *Anal. Chem.* **2010**, *82*, 9141.

(26) Lai, S. C. S.; Dudin, P. V.; Macpherson, J. V.; Unwin, P. R. *J. Am. Chem. Soc.* **2011**, *133*, 10744.

(27) Güell, A. G.; Ebejer, N.; Snowden, M. E.; Macpherson, J. V.; Unwin, P. R. *J. Am. Chem. Soc.* **2012**, *134*, 7258.

(28) Güell, A. G.; Ebejer, N.; Snowden, M. E.; McKelvey, K.; Macpherson, J. V.; Unwin, P. R. *Proc. Natl. Acad. Sci. U. S. A.* **2012**, *109*, 11487.

(29) Snowden, M. E.; Güell, A. G.; Lai, S. C.; McKelvey, K.; Ebejer, N.; O'Connell, M. A.; Colburn, A. W.; Unwin, P. R. *Anal. Chem.* **2012**, *84*, 2483.

(30) Rodolfa, K. T.; Bruckbauer, A.; Zhou, D.; Korchev, Y. E.; Klenerman, D. *Angew. Chem. Int. Ed.* **2005**, *44*, 6854.

(31) Ebejer, N.; Guell, A. G.; Lai, S. C.; McKelvey, K.; Snowden, M. E.; Unwin, P. R. *Annu. Rev. Anal. Chem.* **2013**, *6*, 329.

(32) Güell, A. G.; Cuharuc, A. S.; Kim, Y.-R.; Zhang, G.; Tan, S.-y.; Ebejer, N.; Unwin, P. R. *ACS Nano* **2015**, *9*, 3558.

(33) Nicholson, R. S. *Anal. Chem.* **1965**, *37*, 1351.

(34) Li, W.; Tan, C.; Lowe, M. A.; Abruña, H. D.; Ralph, D. C. *ACS Nano* **2011**, *5*, 2264.

Chapter 3 Electrochemistry at Highly Oriented Pyrolytic Graphite (HOPG): Lower Limit for the Kinetics of Outer-sphere Redox Processes and General Implications for Electron Transfer Models

In this chapter, the electrochemistry of classical outer-sphere redox couples is studied on different grades of HOPG (with step coverage varying by >2 orders of magnitude), by using CV in droplet-cell setup. Fast ET kinetics across all the grades of HOPG has been observed for the redox couples studied herein and lower limits for k_0 can be obtained to assess the electroactivity quantitively. It has been found that the ET kinetics for $IrCl_6^{2-/3-}$ and $Fe(CN)_6^{4-/3-}$ on HOPG is as least as fast as on Pt electrode and for $Ru(NH_3)_6^{3+/2+}$, it is comparable to Pt. In reviewing the fact that HOPG has much lower DOS (by 3 orders of magnitude than Au), the DOS does not play an important role in the ET kinetics of the redox couples used in this study, which show adiabatic behaviour. The basal plane of HOPG is revealed to be highly active by testing the partially active surface model that has been used hitherto.

3.1 Introduction

There is considerable interest in the electrochemical properties of HOPG, at least in part motivated by the close relation of graphite to carbon nanotubes (CNTs) and graphene.[1] Understanding similarities and differences in the electrochemical behaviour of graphite, on the one hand, and graphene and CNTs, on the other hand, has great potential to enrich our understanding of ET at sp^2 carbon materials. Moreover, because of the much lower, and strongly potential-dependent, DOS of sp^2 carbon materials compared to metals,[2-4] comparisons between ET kinetics at HOPG and metal electrodes are of significant value in understanding fundamental ET processes generally. Beyond intrinsic electrochemical measurements of HOPG, this material has found considerable application as a conductive support (electrode material) in studies of electrodeposition,[5-7] for the imaging of biomolecules,[8] including DNA,[9-12] for surface modification,[13-17] and for electrocatalysis.[18-20] Given these various applications, it is of paramount importance to have a true understanding of ET at HOPG.

A host of literature[2,21-30] in the past two decades resulted in a dominant opinion that step edges were responsible for all, or nearly all, of the observed electrochemical activity of HOPG electrodes. For example, studies of $Fe(CN)_6^{4-/3-}$ found standard rate constant, k_0, values at the basal plane ranging from nearly zero ($k_0 < 10^{-9}$ cm s^{-1})[31] to little activity ($k_0 < 10^{-6}$ cm s^{-1})[22,24]. The hugely enhanced activity at step edges, considered to have a standard rate constant up to 10^7 times higher than the basal surface, was ascribed to the higher LDOS at step edges[24,32] or to catalysis by specific functional groups[33,34] (even for outer-sphere redox couples). These ideas entered textbooks[35,36] and were extrapolated to explain the electrochemical activity of CNTs and graphene.[28,37,38] As part of some of these studies, deliberate damage of the HOPG surface with laser activation[22] or by mechanical means[29,30], was used to introduce defects into the graphite crystal structure, and was reported to result in marked improvement in the kinetics. Yet, it should also be pointed out that these protocols would also serve to clean the HOPG surface, were it contaminated, or to remove poorly

contacted graphite/graphene flakes that could be produced in the cleavage process.

In contrast to the above, recent research from our group[14,17,39-44] and other groups[8,45,46] for both HOPG and high quality (low defect concentration) SWNTs[47-51] has shown that the basal surface of sp^2 carbon materials can support fast ET, particularly for outer-sphere reactions. Notably, studies employing high resolution electrochemical imaging, such as SECCM,[52] a localised droplet-based technique, and combined SECM-AFM,[53] allowed the investigation of the electrochemical behaviour of basal plane HOPG *without any influence of step edges*.[8,14,39-41] The freshly cleaved basal plane was found to support fast ET kinetics (indistinguishable from diffusion-controlled), as exemplified by studies of $Fe(CN)_6^{4-/3-}$ [40,41] and $Ru(NH_3)_6^{3+/2+}$.[8,40,41] Subsequent macroscopic measurements of several electrochemical processes on HOPG samples of wide-ranging quality highlighted that ET for outer-sphere and electron-proton coupled reactions is fast at the basal surface.[17,39,40,42,43,54]

The goal of the present study is to attempt to obtain (lower limit) kinetic values for several key outer-sphere redox processes at HOPG, and to elucidate whether there is any influence of step edge density. We do this by studying three different grades of HOPG, which have a step edge density that varies by more than 2 orders of magnitude. We employ CV in a droplet-cell setup (see Chapter 2). This configuration is particularly suitable due to its simplicity and because minimal manipulation or handling of the sample of interest is required. It is thus suitable for the study of materials such as HOPG[2,22,55] and carbon nanotube networks.[56,57] This approach contrasts to some other studies, where the HOPG was clamped in a cell to define the area of working electrode,[31,58] which may impose mechanical strain on the rather fragile layered sample, causing damage and structural changes, while also possibly introducing impurities into the solution.

A significant feature of the droplet cell is that the droplet can be assembled on the working electrode within a short time (~3 s), after HOPG surface cleavage, followed by the rapid placement of counter and reference

electrodes into the droplet. This allows electrochemical measurements to be carried out on a very short time scale, minimising the time that elapses between cleavage and electrochemical measurement and reducing possible sources of contamination. We are particularly mindful of the fact that the fresh HOPG surface can be contaminated when exposed to the air (atmospheric contaminants),[40,59] although the effect (if any) and timescale of these on electrochemical processes is not known. The approach herein mitigates such problems in a straightforward and easy way. This is particularly advantageous for some couples, such as $Fe(CN)_6^{4-/3-}$, which may be complicated by side processes in certain situations and susceptible to changes in the HOPG surface after cleavage.[60] Although macroscopic CV measurements do not offer access to the highest electrode kinetics, the mass transport rates attainable (*vide infra*) are sufficient to draw meaningful conclusions on the lower limit for ET kinetics at HOPG and to allow comparison of data to that on other electrode materials.

It is also important to point out that the three-electrode droplet cell is rather different from more conventional electrochemical cells. One of the consequences of such an arrangement, as we show from the modelling developed in this work, is a greater possible effect of ohmic drop, which may have an important influence on the electrochemical response, especially if the concentration of supporting electrolyte is not sufficiently large compared to the concentration of the redox species. Modelling and test measurements allow us to identify conditions where ohmic effects can be minimised for subsequent kinetic analysis.

3.2 Theory and Simulations

Comprehensive analyses of uncompensated resistance and practical measures to reduce it in conventional electrochemical cells have been presented in literature.[61,62] However, to the best of our knowledge, a droplet-cell configuration has not yet been studied in this respect. In order to estimate the effect of ohmic drop in a droplet electrochemical cell (Figure 3.1), we modelled the distribution of the electric field by solving the Laplace

equation numerically for the electric potential $\boldsymbol{\varphi}$ (eq. 3.1), within the domain defined by the droplet size, with the boundary conditions defined by eq. 3.2-3.4:

$$\Delta\varphi = 0 \qquad \text{(eq. 3.1)}$$

$$\varphi = V_{sol}, on\ the\ anode \qquad \text{(eq. 3.2)}$$

$$\varphi = 0, on\ the\ cathode \qquad \text{(eq. 3.3)}$$

$$\boldsymbol{n}\ grad\ \varphi = 0, on\ the\ air/water\ interface \qquad \text{(eq. 3.4)}$$

where Δ is the Laplace operator in cylindrical coordinates, V_{sol} is the part of the overall potential difference applied between the CE and WE to carry the electrochemical current between the WE and CE, due to the WE reaction, and $\boldsymbol{n}$ is the unit vector normal to a surface (interface). The simulation was performed using the finite element method (FEM) modelling package Comsol Multiphysics 4.1 (Comsol AB, Sweden).

The sizes of the droplet and CE employed were measured under an optical microscope and these dimensions were used in the simulations, but the depths of immersion of the CE and RE in the droplet cell were more difficult to define and control precisely as they could vary in each experiment. To account for this, we considered several possible (relative) configurations of these electrodes that cover important experimental situations: the RE is far away from or close to the CE (Figure 3.1, positions 1, 2 and 3). Ohmic loss of potential, which we denote by V_u, will be a fraction of V_{sol} determined by the position of the RE with respect to WE.[61]

We idealise the situation by assuming that the RE is dimensionless and thus samples the potential from a point (in the cell), and so does not perturb the electric field of the cell. Placing the CE so that it coincides with the cylindrical axis of the WE/cell geometry (Figure 3.1), and rendering the RE dimensionless, significantly reduces computational effort by allowing the solution of the Laplace equation in cylindrical coordinates with axial

symmetry (2-D geometry) and adequately represents the experimental situation.

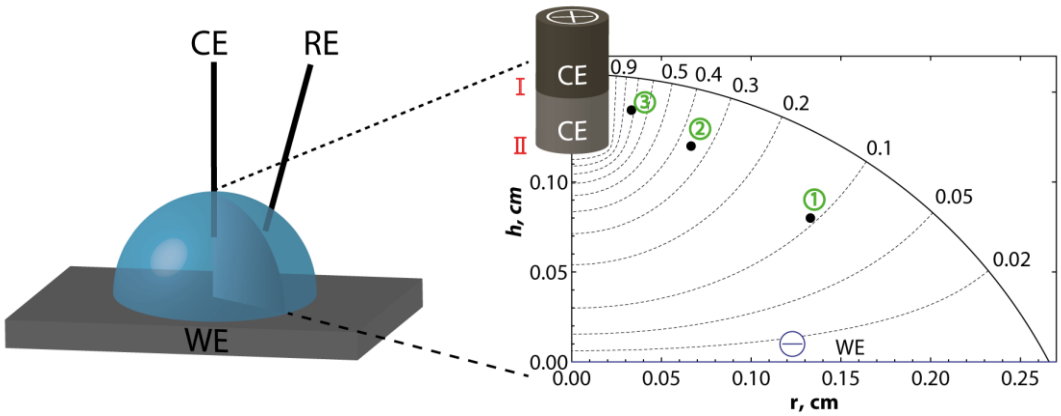

Figure 3.1 Simulation of the electric potential distribution inside the droplet cell (radius r = 0.26 cm and height h = 0.16 cm, volume = 20 µL). A point-size RE probe was placed at three different positions indicated with dots: $r/2$, $h/2$ (1); $r/4$, $3h/4$ (2); $r/8$, $7h/8$ (3), and the CE was immersed by $h/20$ (I) and $h/4$ (II). Distribution of equipotential surfaces is given for position II of the CE. Numbers around the domain indicate the fractions of V_{sol}.

As seen from Table 3.1, V_u can be significant and strongly depends on the relative position of the CE and RE in the cell. We considered two positions of the CE inside the droplet cell – 1/20 (position I) and 1/4 (position II) of the droplet height, measured from the top liquid/air boundary (Figure 3.1). Values for V_u along with the corresponding uncompensated resistance, R_u, were estimated on the basis that the peak current, i_p, on a CV recorded at 10 V s^{-1} amounts to *ca.* 120 µA for a redox mediator concentration of 0.25 mM (*vide infra*). It was determined from the simulation that the magnitude of V_{sol} required to pass this current through the droplet cell containing 0.1 M KCl (conductivity σ(25°C) = 0.013 S cm^{-1})[63] was 78 mV for the CE placed at position I and 43 mV for CE at position II. Then R_u is simply V_u/i_p.

In general, as the RE is moved from position 1 to 3 (move away from the WE towards the CE), the ohmic loss increases significantly, for both CE positions considered, as expected based on the field lines shown in Figure 3.1. Interestingly, as evident from Table 3.1, when the CE is held at position I (further from the WE), the total cell resistance increases dramatically and,

thus, a higher voltage between the CE and WE, V_{sol}, would be required to overcome it. However, V_u is smaller for all positions of the RE considered than for the CE at position II (closer to the WE). This is because the gradient of electric field is steepest close to the CE, and the CE-to-RE separation is always larger for CE position I than for CE position II. This overrides the effect of the increase in net cell resistance for CE position I.

Table 3.1 Ohmic loss of potential and respective uncompensated resistance at different positions of CE and RE, for a current of 120 μA passing through the cell geometry shown in Figure 3.1, with 0.1 M KCl.

RE position	CE position			
	I V_{sol} = 78 mV		II V_{sol} = 43 mV	
	V_u / mV	R_u / Ω	V_u / mV	R_u / Ω
1	3	22	5	38
2	9	73	15	125
3	20	167	31	258

Thus, the RE should be kept as far away as possible from the CE but close to the WE. This is in agreement with the conventional electrochemical cell arrangement, which ensures that RE intercepts with equipotential lines corresponding very closely to the potential difference that actually drives an electrochemical reaction.[61] In general, in contemporary studies in aqueous electrolyte solutions at typical cell current,[64] the electrochemical response is relatively immune to the RE placement. However, it is particularly important for the droplet-cell arrangement where ohmic effects are clearly magnified.

3.3 Results and Discussion

3.3.1 Assessment of Ohmic Loss of Potential

We first carried out some test measurements to optimise the cell configuration, so as to both highlight, and minimise, ohmic effects, in light of the simulation results presented above. In Figure 3.2, a set of CVs of the electrochemical reduction of 0.25 mM $Ru(NH_3)_6^{3+}$ in 0.1 M KCl is presented to expose the variability in the ΔE_p that may result between different cell setups, where the CE and RE were simply placed into the droplet cell. Although the general behaviour in the Figures 3.2a and 3.2b is similar, the peak-to-peak separation at 10 V s^{-1} differs quite significantly with values of 80 mV (Figure 3.2a) and 93 mV (Figure 3.2b), and both values are far from that for a reversible process (59 mV), which might have been expected in light of nanoscale measurements that report k_0 ~9 cm s^{-1} for this couple on freshly cleaved HOPG.[8] Similar variability was also found with $IrCl_6^{2-/3-}$ under the same concentration conditions (Figure 3.3). Furthermore, in studies of a range of concentrations of $Ru(NH_3)_6^{3+}$, *i.e.* 0.1, 0.25, 0.5, and 1 mM, in 0.1 M KCl, corresponding to a ratio between the concentration of supporting electrolyte and redox-active species of 1000, 400, 200 and 100, respectively, a significant increase in peak-to-peak separation with increase of redox-active mediator concentration was seen. Typical CVs are shown in Figure 3.4a, in which ΔE_p at 10 V s^{-1} increases from 64 mV to 170 mV as the concentration of mediator is increased from 0.1 mM to 1 mM. As with the data in Figure 3.2 and Figure 3.3, these would all, again, be regarded as reasonable concentrations of redox-active species and ratios of electrolyte to redox-active species concentration in conventional cells.[65] However, as with the data in Figure 3.1 and Table 3.1, these results highlight the need to use rather extreme electrolyte to redox-active species concentrations in droplet-cell kinetic measurements, and the importance of RE and CE placement.

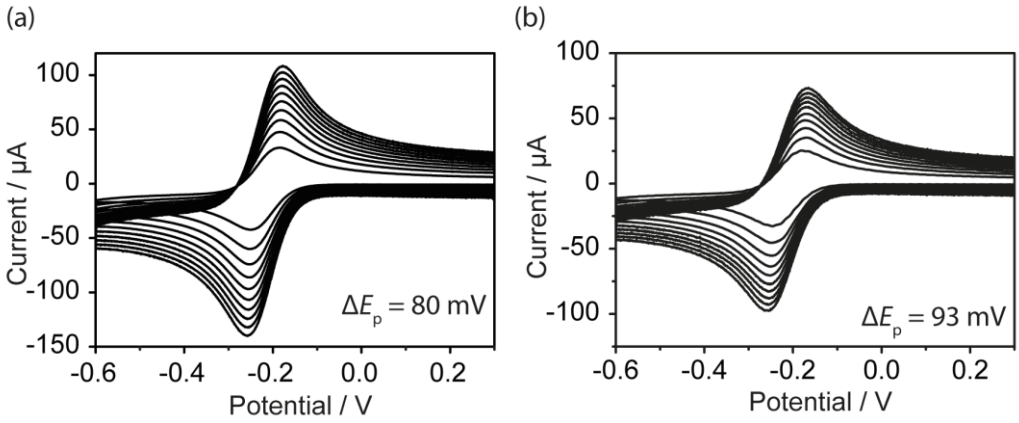

Figure 3.2 Cyclic voltammograms for the reduction of 0.25 mM $Ru(NH_3)_6^{3+}$ in 0.1 M KCl supporting electrolyte obtained on freshly cleaved AM grade HOPG in 2 different droplet cells. Scan rates: 1 (smallest current), 2, 3, 4, 5, 6, 7, 8, 9 and 10 (biggest current) V s^{-1}. The ΔE_p values indicated are the peak-to-peak separations at 10 V s^{-1}.

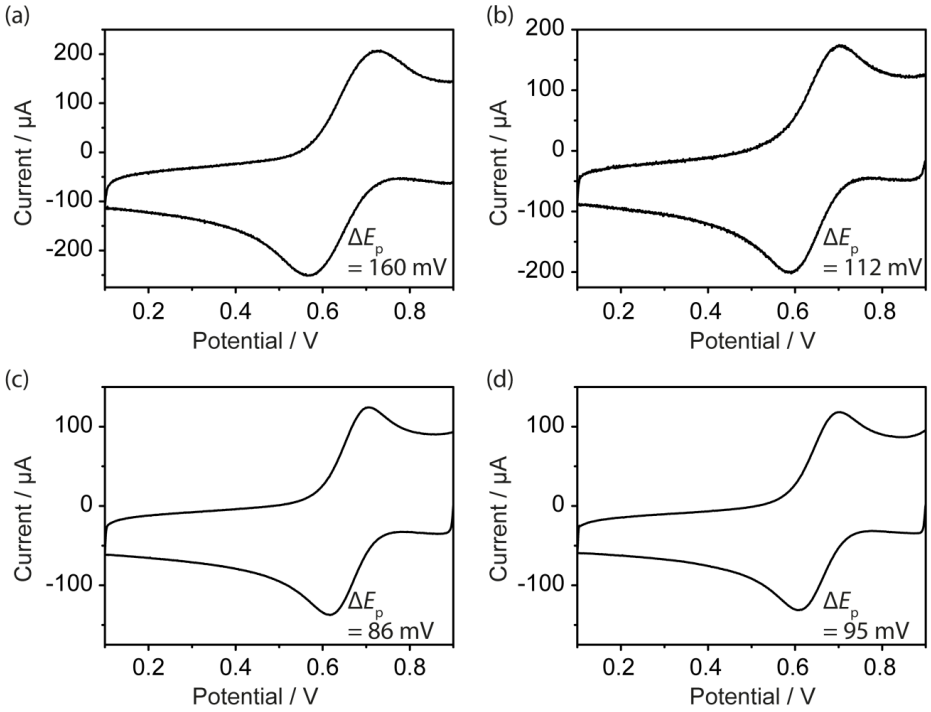

Figure 3.3 Cyclic voltammograms for the reduction of 0.25 mM $IrCl_6^{2-}$ in 0.1 M KCl on freshly cleaved (a)-(b) AM, and (c)-(d) SPI-3 HOPG, with a scan rate of 10 V s^{-1}, and each grade of HOPG studied in two different droplet cells. The numbers indicated are the peak-to-peak separations.

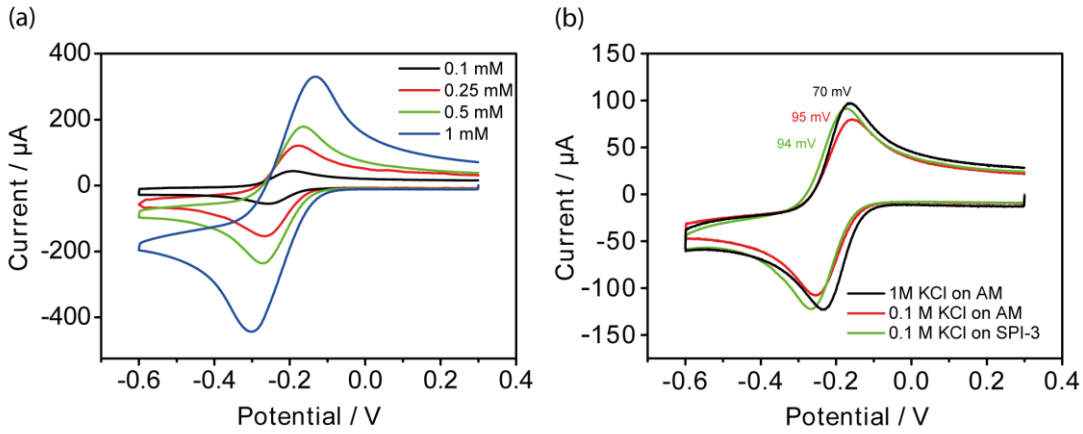

Figure 3.4 (a) Cyclic voltammograms for the reduction of different concentrations of $Ru(NH_3)_6^{3+}$ in a supporting electrolyte of 0.1 M KCl, on freshly cleaved AM grade HOPG, at 10 V s^{-1}; (b) Cyclic voltammograms of 0.25 mM $Ru(NH_3)_6^{3+}$ in supporting electrolyte of 1 M or 0.1 M KCl on AM or SPI-3 HOPG, recorded at a scan rate of 10 V s^{-1}, with ΔE_p indicated.

In order to diminish the dependence of the voltammetric response on the cell configuration, a larger concentration of supporting electrolyte, 1 M KCl (instead of 0.1 M), was used for the kinetic measurements herein, since this increases the conductivity of the solution by approx. 9 times (σ(25°C) = 0.11 S cm^{-1}).[63] As evidenced by Figure 3.4b, where 0.25 mM $Ru(NH_3)_6^{3+}$ is used, the ΔE_p, at a scan rate of 10 V s^{-1}, is significantly decreased by increasing the concentration of KCl from 0.1 M to 1 M, due to the reduced R_u in the solution. In addition, the use of an insulated Ag/AgCl RE minimised the exposition of bare wire, avoiding short-circuiting in the cell and corruption of the current lines.[62] In consideration of these issues, all the measurements from which we extracted k_0 values were done under 'optimised conditions': a solution of 0.25 mM redox species ensured the cell current would be relatively small but readily measurable, and an insulated Ag/AgCl wire RE (exposed only at the end) was put as close to the WE but as far away from the CE as possible, unless otherwise stated. Note that there was indistinguishable difference in the cyclic voltammograms when either platinum wire or gauze electrode was used, and thus a platinum wire was adopted as the CE throughout.

3.3.2 Kinetic Measurements

Three different redox couples, $Ru(NH_3)_6^{3+/2+}$, $IrCl_6^{2-/3-}$, and $Fe(CN)_6^{4-/3-}$, were employed together with high and low quality HOPG samples (AM, ZYB and SPI-3).

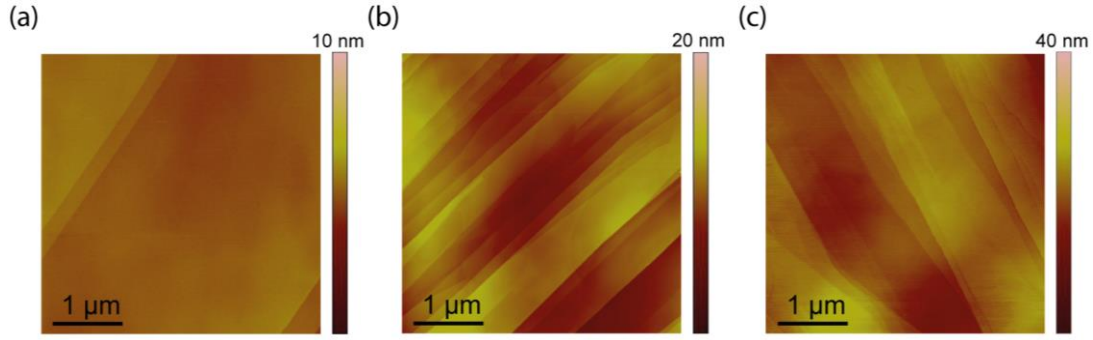

Figure 3.5 4 × 4 µm AFM images of (a) AM, (b) ZYB and (c) SPI-3 grade HOPG surfaces. Note the difference in height scales for (a), (b) and (c).

As evident from Figure 3.5, AM, ZYB, and SPI-3 grades of HOPG give surfaces with a wide range of distinct step edge density. AM HOPG is mainly covered by the basal plane surface with low step coverage (*ca.* 0.09 %),[40] ZYB has more step edges (0.3-0.8 %),[54] while SPI-3 HOPG is covered by the most step edges (*ca.* 30 %).[40,42,54]

Cyclic voltammetry was carried out at scan rates from 1 V s^{-1} to 10 V s^{-1}. Assuming D ~10^{-5} cm^2 s^{-1}, this corresponds to mass transport coefficients in the range of 0.0088–0.028 cm s^{-1} (based on the calculated current density from the Randles-Sevcik equation[66]). This is a reasonable range to at least make a comparison of the ET kinetics of HOPG to other materials, if the DOS of the electrode material were to be important.

Values of k_0 were estimated from Nicholson's method.[67,68] We first consider $IrCl_6^{2-/3-}$. We found ΔE_p of 56 ± 1 mV (n = 3) at all scan rates up to 10 V s^{-1} on both AM and SPI-3 HOPG, respectively (with two example CVs at 10 V s^{-1} shown in Figure 3.6). This indicates that the process is reversible even at this scan rate. Considering that for a reversible reaction we can assign a minimum ψ > 20 (ΔE_p < 61 mV), with $D \approx D_O \approx D_R = 7.5 \times 10^{-6}$ cm^2 s^{-1},[69] k_0 can be estimated to be >1.9 cm s^{-1}. This is at least as high as the k_0

measured for this mediator on Pt (1.9 cm s^{-1}) by a radial flow microring electrode.[69]

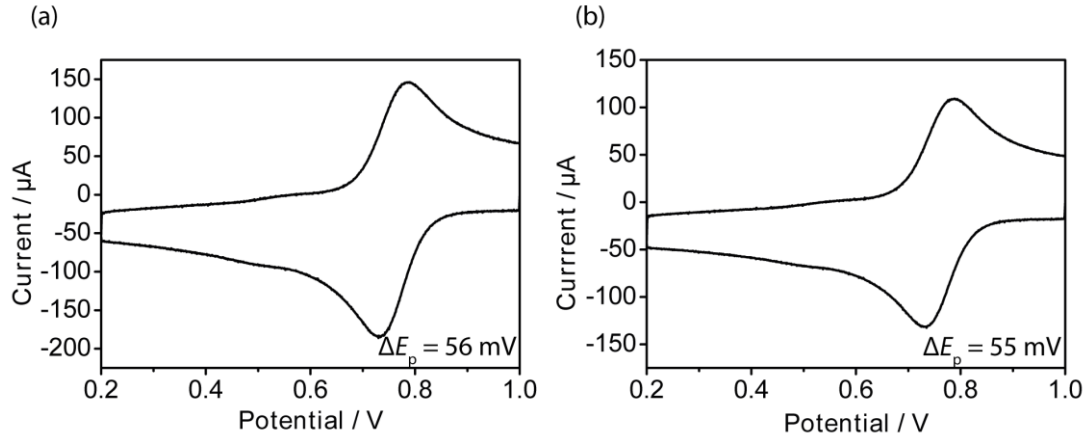

Figure 3.6 Cyclic voltammograms for the reduction of 0.25 mM $IrCl_6^{2-}$ on freshly cleaved (a) AM and (b) SPI-3 HOPG, respectively, with 1 M KCl as the supporting electrolyte, recorded at a scan rate of 10 V s^{-1}. The numbers indicated are the peak-to-peak separation values.

In the case of $Ru(NH_3)_6^{3+}$ reduction, ΔE_p changed from 61 ± 1 mV for v = 1 V s^{-1} to 70 ± 1 mV for v = 10 V s^{-1} on AM HOPG (Figure 3.7a), with 5 replicates (separate runs on freshly cleaved HOPG) carried out, while the voltammograms at the ZYB surface (Figure 3.7b) had ΔE_p of 68 ± 1 mV at 10 V s^{-1}, with good reproducibility across different HOPG samples (see Figures 3.8 and 3.9). The dimensionless parameter, ψ, determined from ΔE_p, shows a good linear trend with the reciprocal of the square root of the scan rate, $v^{-1/2}$, as expected Nicholson's equation and k_0, calculated from the slope of the line fitted to experimental data at AM HOPG (Figure 3.10) as an example, using D = 8 × 10^{-6} cm^2 s^{-1},[70] was 0.61 ± 0.02 cm s^{-1}. In consideration of our analysis of ohmic effects on the droplet cell, the small difference in the values of ΔE_p from the reversible limit, and other recent precautionary work on the danger of over-analysis of CV data close to this limit (leading to a high risk of recovering incorrect but physically meaningful values),[64] we consider this to be a lower limit for k_0 on HOPG.

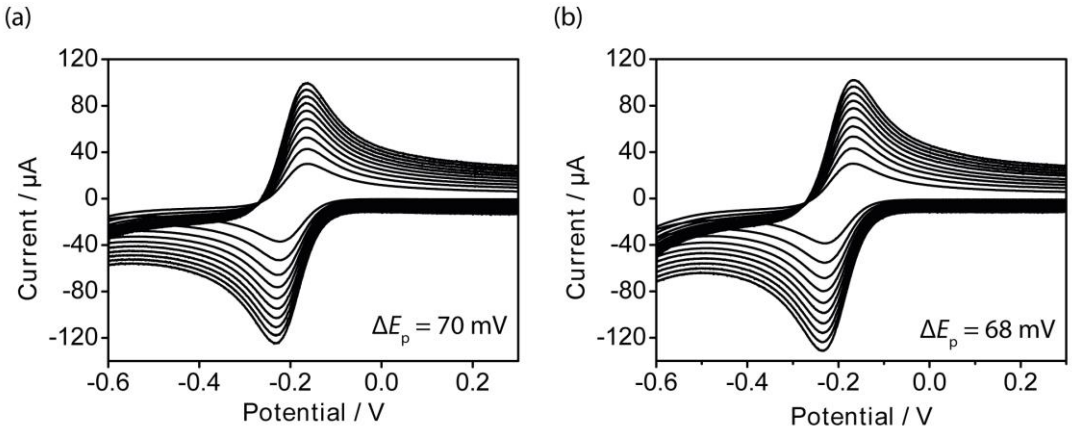

Figure 3.7 Cyclic voltammograms for the reduction of 0.25 mM $Ru(NH_3)_6^{3+}$ on freshly cleaved (a) AM and (b) ZYB HOPG, with 1 M KCl as the supporting electrolyte. Scan rates: 1 (smallest current), 2, 3, 4, 5, 6, 7, 8, 9 and 10 (biggest current) V s^{-1}. The ΔE_p values stated are the peak-to-peak separations at 10 V s^{-1}.

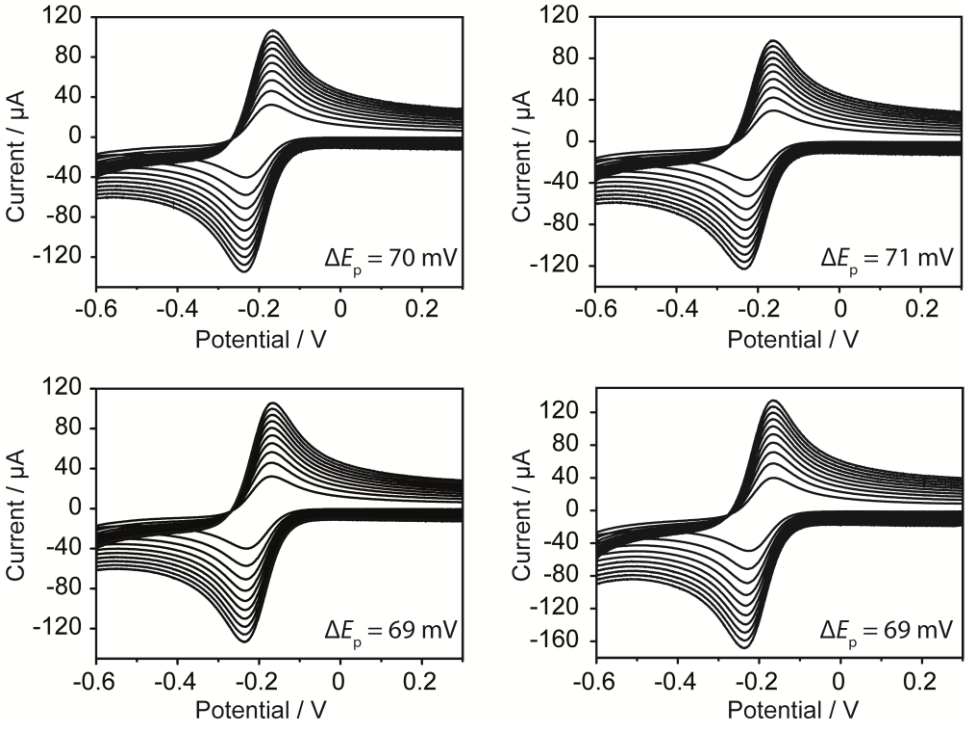

Figure 3.8 Cyclic voltammograms for the reduction of 0.25 mM $Ru(NH_3)_6^{3+}$ in 1 M KCl on AM grade HOPG in 4 different droplet cells (each a freshly cleaved piece of HOPG), recorded at a scan rate of 1 (smallest current), 2, 3, 4, 5, 6, 7, 8, 9 and 10 (biggest current) V s^{-1}, respectively. The numbers indicated are the peak-to-peak separations at 10 V s^{-1}.

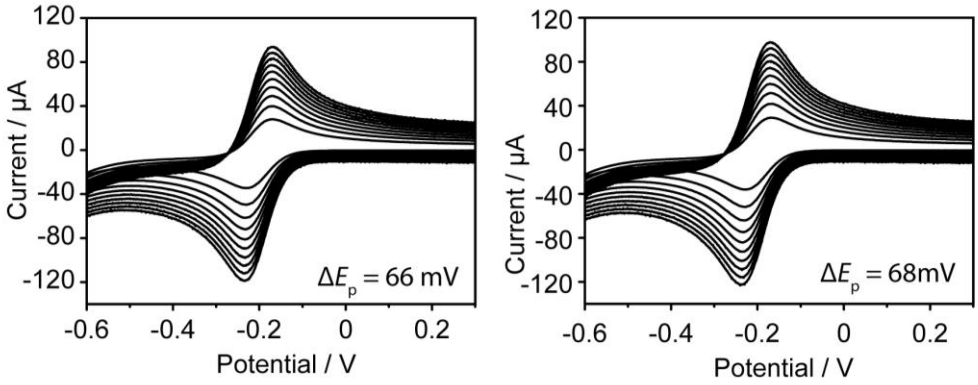

Figure 3.9 Cyclic voltammograms for the reduction of 0.25 mM $Ru(NH_3)_6^{3+}$ in 1 M KCl on SPI-3 grade HOPG in two different droplet cells (2 freshly cleaved pieces of HOPG), recorded at a scan rate of 1 (smallest current), 2, 3, 4, 5, 6, 7, 8, 9 and 10 (baggest current) V s^{-1}, respectively. The numbers indicated are the peak-to-peak separations at 10 V s^{-1}.

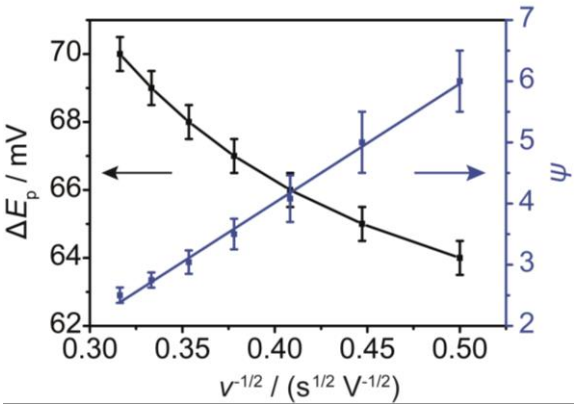

Figure 3.10 Plot of peak-to-peak separation, ΔE_p, and kinetic parameter ψ versus the reciprocal of the square root of the scan rate ($v^{-1/2}$) for a solution containing 0.25 mM $Ru(NH_3)_6^{3+}$, with a supporting electrolyte of 1 M KCl. The data shown here were obtained on freshly cleaved AM HOPG.

Voltammetry for the oxidation of $Fe(CN)_6^{4-}$, studied on AM and SPI-3 grade HOPG, was very similar to the two couples discussed above (Figure 3.11, Figures 3.12 and 3.13). The peak-to-peak separation at 10 V s^{-1} for $Fe(CN)_6^{4-}$ was 66 ± 2 mV (n = 6) on AM and 65 ± 3 mV (n = 6) on SPI-3, respectively. These values are very close to reversible, indicative of fast ET on both surfaces. The lower limit for k_0 for $Fe(CN)_6^{4-}$ oxidation obtained from the plot of Figure 3.14 is $k_0 > 0.46 \pm 0.03$ cm s^{-1}. This is very close to (and, if anything, higher than) the value for Pt electrodes.[69,71-74] It should be noted

that in this case, as a set of CVs were run within 3 min on a particular HOPG sample, no significant effect of surface history on the electrochemical behaviour was observed and reproducible CVs were recorded on all three grades of HOPG.

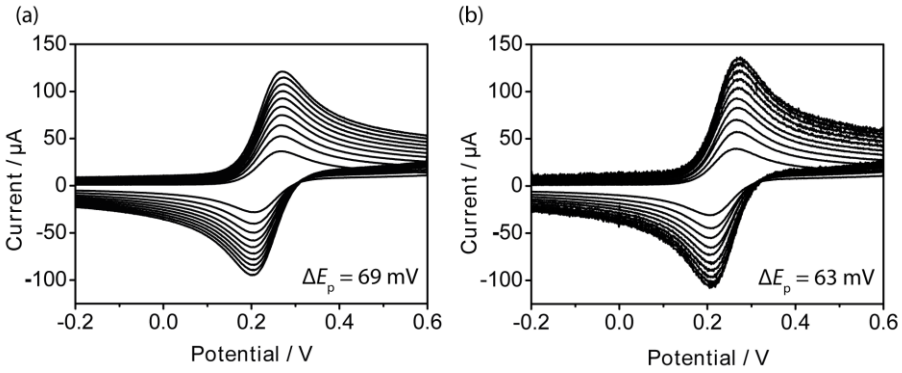

Figure 3.11 Typical cyclic voltammograms for the oxidation of 0.25 mM $Fe(CN)_6^{4-}$ in 1 M KCl on freshly cleaved (a) AM and (b) SPI-3 HOPG, respectively. Scan rates: 1 (smallest current), 2, 3, 4, 5, 6, 7, 8, 9 and 10 (biggest current) V s^{-1}. The numbers indicated are the peak-to-peak separations at 10 V s^{-1}.

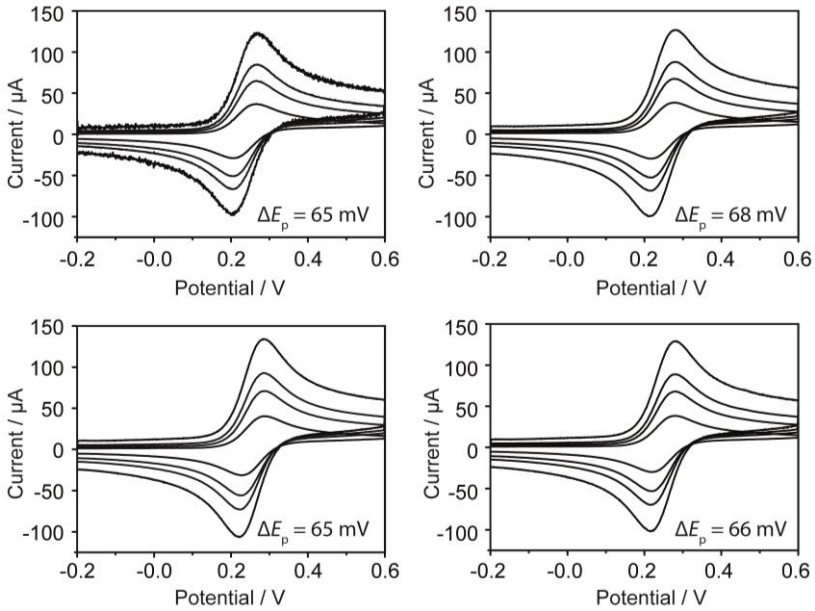

Figure 3.12 Cyclic voltammograms for the oxidation of 0.25 mM $Fe(CN)_6^{4-}$ in 1 M KCl on freshly cleaved AM grade HOPG in 4 different droplet cells (4 different pieces of HOPG), recorded at a scan rate of 1 (smallest current), 3, 5 and 10 (biggest current) V s^{-1}, respectively. The numbers indicated are the peak-to-peak separations at 10 V s^{-1}.

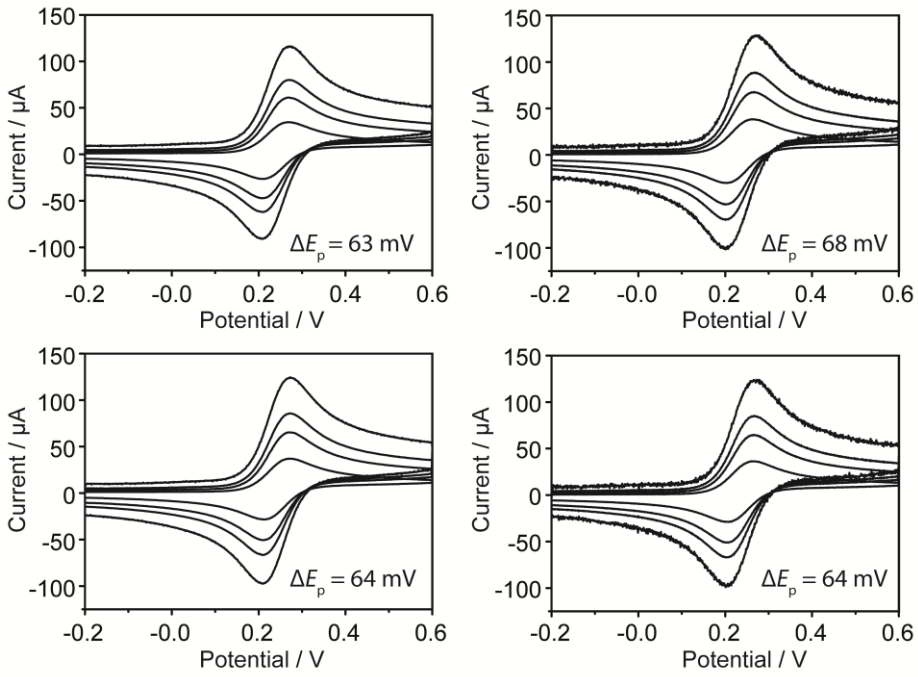

Figure 3.13 Cyclic voltammograms for the oxidation of 0.25 mM $Fe(CN)_6^{4-}$ in 1 M KCl on freshly cleaved SPI-3 grade HOPG in 4 different droplet cells (4 fresh samples), recorded at a scan rate of 1 (smallest current), 3, 5 and 10 (biggest current) V s^{-1}, respectively. The numbers indicated are the peak-to-peak separations at 10 V s^{-1}.

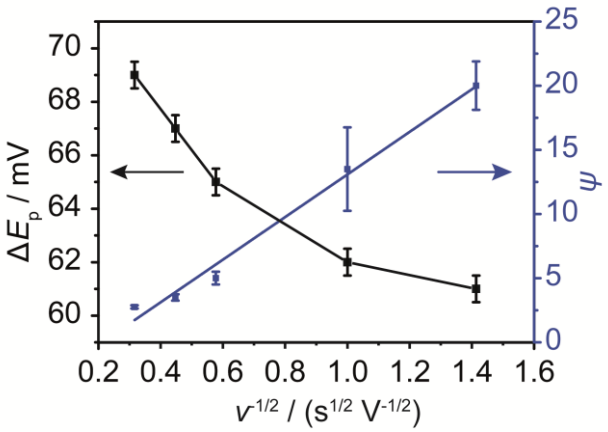

Figure 3.14 Plot of peak-to-peak separation, ΔE_p, and kinetic parameter ψ versus the reciprocal of the square root of the scan rate ($v^{-1/2}$) for a solution containing 0.25 mM $Fe(CN)_6^{4-}$, with a supporting electrolyte of 1 M KCl, respectively. The data shown here were obtained on freshly cleaved AM HOPG.

3.3.3 Test of Partially Active Surface Model and Comment on DOS

As highlighted at the start of this chapter, carbon materials are increasingly prominent as electrodes, in myriad applications, and a fundamental understanding of the origin of the ET activity is thus of great importance. Among carbon electrodes, the ultra-low activity of the basal surface of HOPG originated in arguments from McCreery's group[23,24] that were widely adopted and amplified by other groups.[2,75-77] One rationale for this view is that HOPG has a low DOS at the Fermi level, *ca.* 2.2×10^{-3} states $atom^{-1}$ eV^{-1},[3,4] which is about two orders of magnitude lower than those on metals (*e.g.* 0.28 states $atom^{-1}$ eV^{-1} for Au).[78] That the DOS could be important in outer-sphere ET processes at carbon electrodes relies on models mainly for semiconductors, for example, as developed by Gerischer[79] and Doganadze and Levich.[80] An important consideration is whether the DOS of an electrode is sufficiently low compared to the density of states of the solution species for the electrode kinetics for outer-sphere redox processes to depend on the electronic structure of the electrode.[66,81]

In this study, nearly identical electrochemical behaviour has been seen for all the redox couples, $IrCl_6^{2-/3-}$, $Ru(NH_3)_6^{3+/2+}$, and $Fe(CN)_6^{4-/3-}$, on different grades of HOPG, with step edge density spanning 2 orders of magnitude. We expect higher DOS for SPI-3 grade HOPG than AM grade, due to the enhanced DOS at zigzag edges,[82-84] and so these data tend to suggest that the electronic structure of the HOPG electrodes does not influence the ET kinetics. However, it is important to point out that all the reactions are close to the reversible limit, making an unequivocal assignment difficult.

The observation that the redox reactions considered are effectively diffusion-controlled fast ET processes on HOPG, as discussed herein (see Figure 3.15), is in line with microscopic and nanoscopic studies, which have shown that the basal surface has high electroactivity.[8,39-42,45,46] Even for the "problematic" couple,[60,85] $Fe(CN)_6^{4-/3-}$, a rapid ET reaction has been seen on all HOPG surfaces for the CV timescale investigated, including high quality (low step edge density) AM HOPG, and the lower limit of k_0 is $>10^5$ times higher than the upper limit reported earlier for the basal surface.[24] Indeed,

significantly, the lower limit for k_0 determined herein is of the same order as the value measured on Au and Pt (with no difference found between k_0 on the two metals).[1,69,86,87] This is further evidence that these reactions are not influenced by the electronic structure of the electrodes and that these outer-sphere processes are adiabatic on these different electrodes.

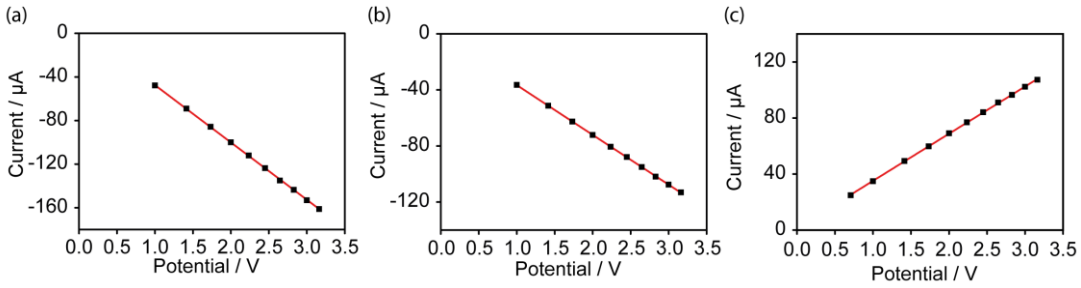

Figure 3.15 Plot of the reductive peak current for (a) $IrCl_6^{2-}$ and (b) $Ru(NH_3)_6^{3+}$, and (c) the oxidative peak current for $Fe(CN)_6^{4-}$ against the square root of the scan rate ($v^{1/2}$). Both experimental data (■) and a line of best fit (—) are shown.

Given the strong views in the literature that defects, originally focused on step edges,[21,22,24,25,27,28,88] but recently extended to point defects,[89] *are the only sites for ET on HOPG* even for outer-sphere processes, we can further analyse our data in terms of a partially active surface model for charge transfer (schematic Figure 3.16).[90] In line with this older work, we assume that the basal plane is inert, with two types of active site, *i.e.* strips (step edges) and point defects. Widths of 1 nm and 5 nm were considered for the active strips, with the lower value matching the region of enhanced DOS at zigzag step edge sites[82] and the upper value based on STM data from McCreery,[88] which is generous in light of STS data.[82] The strip site densities (1 µm/µm^2 or 2 µm/µm^2) are higher than found on typical AM HOPG,[40] to again exaggerate the influence of such features. The electronic disturbances associated with point defects are localised, even on graphite surfaces deliberately defected with hydrogen or argon plasmas.[91,92] It has been found that hydrogen-ion induced point defects give rise to an electronic disturbance over domains of 5 nm radius.[91] However, a diameter of ~3 Å was reported for argon-ion induced point defects.[92] In this study, we take the worst case (in terms of maximising the possible impact of such defects) and assign the

point defect to have a radius of 5 nm, while considering a point defect density of 0.1 or 10 μm^{-2} based on the lower and upper limits from STM measurements on cleaved HOPG.[93-95] It should be noted that such defects are rare and extremely difficult to find on cleaved HOPG surfaces, *e.g.* a recent STM study with more than 100 scans failed to find any point defects in the basal plane.[96] Likewise, for the study herein, we also carried out STM measurements on AM grade HOPG, with >100 images (each of 10 × 10 nm^2) obtained in randomly selected areas. We could not find a single defect in any of the images (*e.g.* Figure 3.17).

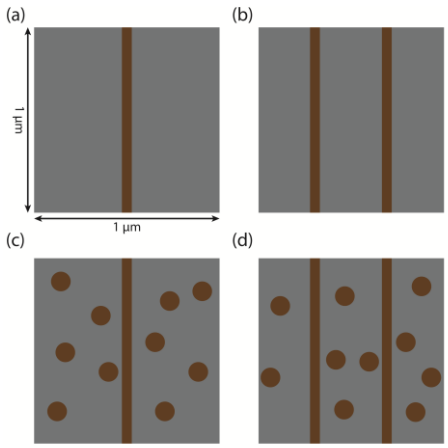

Figure 3.16 Schematic illustrating active site (defect) densities on an area of 1 μm^2 at an HOPG surface (not to scale). Active sites (exaggerated size) are in brown and inactive areas are grey. (a)-(b) strip type only; (c)-(d) strip type plus point defect type. The strip width is either 1 or 5 nm, and the radius of point defects is 5 nm. The strip densities are higher than on typical AM HOPG.

Table 3.2 Predicted minimum heterogeneous rate constant of $Fe(CN)_6^{4-/3-}$ if the redox reaction were confined to defects, with different active site arrangements on an HOPG surface.[a]

Active site arrangement[b]	1 strip		2 strips		1 strip + 0.1 point defects		2 strips + 0.1 point defects		1 strip + 10 point defects		2 strips + 10 point defects	
Strip width (nm)	1	5	1	5	1	5	1	5	1	5	1	5
Active site coverage f_a (%)	0.1	0.5	0.2	1	0.100785	0.500785	0.200785	1.000785	0.1785	0.5785	0.2785	1.0785
Expected minimum ET rate constant at active site, k_s (cm s^{-1})	460	92	230	46	456	92	229	46	258	80	165	43

[a] The area considered is 1 μm^2. [b] The point defect density on HOPG is 0.1 - 10 μm^{-2}.

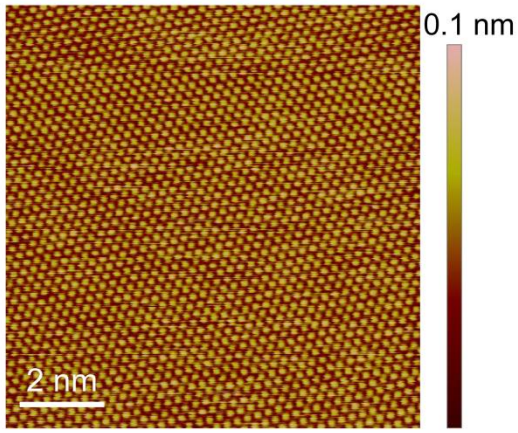

Figure 3.17 Unfiltered STM atomic resolution image (10 × 10 nm^2) of AM grade HOPG.

We take the data for $Fe(CN)_6^{4-/3-}$ on AM HOPG (k_0 > 0.46 cm s^{-1}) herein, as an example, as this has been the most used redox couple to show slow or no ET on the basal plane surface in previous studies.[21,22,24-28,31,88] For the situation where active sites on the surface are closely spaced compared to the diffusion field (concentration boundary) normal to the WE, which is reasonable for the analysis herein, we can write $k_0 = k_s * f_a$,[90,97] where k_s is the

standard ET rate constant at the defect and f_a is the active site fractional surface coverage. The k_s values calculated for different active site arrangements are summarized in Table 3.2. It is found that if activity was confined to defects, the *minimum* k_s values at graphite defects would have to be orders of magnitude higher than k_0 on any metal electrode. Even for the most defective surface, with 2 strips (each 5 nm wide) and 10 point defects in a 1 μm^2 area, k_s is still >2 orders of magnitude higher than measured at Au and Pt electrodes.[69,72,87] Thus, as we have pointed out,[1,14,17,39-44,54] and as is clear from high resolution electrochemical imaging, the scenario of entirely defect-driven activity does not stand up to scrutiny.

There is some prior work on the relative unimportance of the DOS in controlling the ET kinetics of outer-sphere redox processes at electrodes. Thus, it was found that on nine different metal electrodes the k_0 for $Ru(NH_3)_6^{3+/2+}$ (in the range of 0.67–1.29 cm s^{-1}) was not proportional to DOS (that varied by one order of magnitude across the different metals studied).[86,87,98,99] The studies herein extend the DOS of the electrode to lower values (by one-two orders of magnitude compared to the metal electrodes) and yet the reported k_0 values for HOPG are at least as large as those on the metals.[86,87,98,99] We further note that the kinetics for $FcCH_2OH$ and $Ru(NH_3)_6^{3+}$ in aqueous solution on Au and Pt nanoelectrodes was studied using SECM.[100] The k_0 for $FcCH_2OH$ oxidation in aqueous solution on Au (8 ± 1 cm s^{-1}) was very close to that on Pt (6.8 ± 0.7 cm s^{-1}), while the DOS on Pt is ~7.5 times that of Au.[101] Although argued otherwise,[102] this would reasonably indicate that the overall DOS had no direct effect on the ET kinetics and the reaction was adiabatic. For $Ru(NH_3)_6^{3+/2+}$ on Au and Pt, k_0 was considered to be statistically higher on Pt (17.0 ± 0.9 cm s^{-1}) than on Au (13.5 ± 2 cm s^{-1}).[100] However, it should be pointed out that although SECM with nanoelectrodes provides much higher mass transport than other techniques,[98] enabling the measurement of ultra-fast electrode kinetics, such measurements require great care, as nanoelectrodes may be damaged easily by electrostatic discharge and electrochemical etching.[103] This type of damage is not necessarily manifest in the SECM or the steady-state voltammetric response. Thus, without safeguards, and thorough

characterisation of the SECM tip by complementary microscopy techniques like SEM or AFM, there is a danger that erroneous conclusions may be drawn from experimental data obtained with nanoelectrodes.

Although it was suggested that the higher k_0 for $Ru(NH_3)_6^{3+/2+}$ on Pt compared to macroscopic electrodes could be due to diffuse double layer (Frumkin) effects, which may be more pronounced on nanoscale electrodes,[75] it is interesting to note that the highest reported k_0 values for $Ru(NH_3)_6^{3+/2+}$ on distinctly different electrodes are – in fact - rather similar, *e.g.* 10 ± 5 cm s^{-1} on metallic single walled carbon nanotubes,[48] 9 cm s^{-1} on the basal surface of HOPG (free from defects),[8] 9–10 cm s^{-1} on reduced graphene oxide,[75] 13.5 ± 2 cm s^{-1} on Au and 17.0 ± 0.9 cm s^{-1} on Pt.[100] This similarity in values is especially striking in view of the large difference in DOS, electronic structure and the different electrode configurations studied experimentally. Likewise, there is now strong evidence that k_0 for $Fe(CN)_6^{4-/3-}$ is rather similar on very different electrodes, in the range of 0.3–0.5 cm s^{-1} on Pt,[69,86] 0.2–0.4 cm s^{-1} on Au[86,104] and 0.7–1.0 cm s^{-1} on reduced graphene oxide[75] and >0.46 cm s^{-1} on HOPG (data herein).

In summary, our data suggest that the kinetics of the 3 redox couples studied herein are broadly comparable on HOPG and metal electrodes that have a much higher DOS. That the DOS is unimportant in determining the ET kinetics of outer-sphere redox processes is reasonable if there is strong electronic coupling of the redox species to the electrode and the DOS of the electrode material is orders of magnitude higher than that of the redox species.[66,81] For the experimental conditions of this study (which are not uncommon), one can estimate that the DOS of $Ru(NH_3)_6^{3+/2+}$ in the solution is of order of 10^{14} states eV^{-1} cm^{-3}, whereas that of HOPG at the potential of zero charge (close to the potential of the $Ru(NH_3)_6^{3+/2+}$ couple) is of the order of 10^{20} states eV^{-1} cm^{-3}.[3] The DOS of the redox species in solution (D_{Redox}) is the sum of DOS due to O and R molecules and is a function of energy ε as given by[105]

$$D_{Redox}(\varepsilon) = C_O W_O(\varepsilon) + C_R W_R(\varepsilon) \qquad \text{(eq. 3.5)}$$

where C_i is the concentration of species i of the redox couple (O or R), and W_i is the probability density of the electronic states in solution defined by eq. 3.6 for the R and by eq. 3.7 for the O forms:

$$W_R(\varepsilon) = \frac{1}{\sqrt{4\pi\lambda_R kT}} \exp[-(\varepsilon - \varepsilon_R)^2/4\lambda_R kT] \qquad \text{(eq. 3.6)}$$

$$W_O(\varepsilon) = \frac{1}{\sqrt{4\pi\lambda_O kT}} \exp[-(\varepsilon - \varepsilon_O)^2/4\lambda_O kT] \qquad \text{(eq. 3.7)}$$

Here, λ_i is the reorganization energy for R or O, and ε_i is the most probable energy level of the solution states that is related to the standard Fermi level of redox species, ε_F^0, via eq. 3.8 for the R form and eq. 3.9 for the O form:

$$\varepsilon_R = \varepsilon_F^0 - \lambda_R \qquad \text{(eq. 3.8)}$$

$$\varepsilon_O = \varepsilon_F^0 + \lambda_O \qquad \text{(eq. 3.9)}$$

In turn, the standard Fermi level of redox couple is simply an 'energy equivalent' of the standard redox potential, E^0:

$$\varepsilon_F^0 = eE^0 \qquad \text{(eq. 3.10)}$$

The other symbols in eq. 3.7 are the Boltzmann constant, k, and absolute temperature, T.

For $Ru(NH_3)_6^{3+/2+}$, the R and O forms are similar in structural configuration and so we may reasonably write $\lambda_R = \lambda_O = 0.82$ eV.[106] Considering the case of equal concentrations $C_O = C_R \approx 5 \times 10^{-7}$ mol cm^{-3} for the sake of simplicity (and ignoring possible double layer effects on near interface concentrations, which is reasonable for this orders of magnitude calculation), one finds that $D_{Redox} \approx 10^{14}$ states eV^{-1} cm^{-3} in the region around E^0 of $Ru(NH_3)_6^{3+/2+}$ as was given above.

3.4 Conclusions

The ET kinetics of three benchmark redox couples, $IrCl_6^{2-/3-}$, $Ru(NH_3)_6^{3+/2+}$ and $Fe(CN)_6^{4-/3-}$, have been investigated in a droplet cell assembled on freshly cleaved HOPG (within 3 s of cleavage), of different grades, with step edge density spanning up to 2 orders of magnitude. The processes are fast and close to reversible on all surfaces, even at a scan rate of 10 V s^{-1}. We have been able to extract a lower limit for the ET rate constants, taking account of ohmic resistance relevant to the droplet-cell experimental arrangement and identifying means of minimising its influence. This was achieved by modelling the electric field in the droplet cell and optimising experimental conditions as a consequence.

For $IrCl_6^{2-/3-}$ and $Fe(CN)_6^{4-/3-}$, we have shown clearly that k_0 at HOPG, even of the very highest quality (lowest defect density), is at least as high as on Pt (or Au) electrodes. For $Ru(NH_3)_6^{3+/2+}$, our lower limit for k_0 (0.61 cm s^{-1}) is in the ballpark as on a range of macroscopic metal electrodes.[87,98,99] These data indicate that although HOPG has a much lower DOS at the Fermi level than metal (Pt, Au) electrodes, the electronic coupling between HOPG electrodes and these redox couples is sufficiently strong for the electrode kinetics to be at least as fast. Of course, while broadly similar standard rate constants for these redox couples are seen at the wide range of electrode materials discussed, indicating that they can be classified as essentially adiabatic rather than non-adiabatic,[107] it is important to point out that these definitions represent limiting situations and subtle secondary phenomena may also impact, such as double layer effects, and the nature of the metal and electrolyte on the Helmholtz layer (ions and solvent). Thus, while we have found conclusively that the ET kinetics for several outer-sphere processes are at least as fast at HOPG as on metal electrodes, intriguingly, we cannot rule out that in some cases the reactions could actually be faster at HOPG, bearing in mind the secondary factors mentioned, and the different aqueous (and double layer) structures at hydrophobic HOPG compared to metals such as Pt. Along with our other recent work, outlined herein and elsewhere,[1] the studies herein develop the new perspective for the high

activity of the HOPG basal surface for simple outer-sphere and other redox processes. For related sp^2 carbon materials, particularly (monolayer) graphene, where the DOS is much lower (and theoretically zero at the intrinsic Fermi level), an interesting issue to be explored is whether the electronic structure impacts on the ET kinetics for these outer-sphere redox couples. Initial studies suggest that for $Ru(NH_3)_6^{3+/2+}$, the low DOS of graphene does effect the ET kinetics, with k_0 increasing with the number of graphene layers.[108]

3.5 References

(1) Unwin, P. R. *Faraday Discuss.* **2014**, *172*, 521.

(2) McCreery, R. L. *Chem. Rev.* **2008**, *108*, 2646.

(3) Gerischer, H.; McIntyre, R.; Scherson, D.; Storck, W. *J. Phys. Chem.* **1987**, *91*, 1930.

(4) Gerischer, H. *J. Phys. Chem.* **1985**, *89*, 4249.

(5) Gloaguen, F.; Léger, J. M.; Lamy, C.; Marmann, A.; Stimming, U.; Vogel, R. *Electrochim. Acta* **1999**, *44*, 1805.

(6) Zach, M. P.; Ng, K. H.; Penner, R. M. *Science* **2000**, *290*, 2120.

(7) Penner, R. M. *J. Phys. Chem. B* **2002**, *106*, 3339.

(8) Frederix, P. L.; Bosshart, P. D.; Akiyama, T.; Chami, M.; Gullo, M. R.; Blackstock, J. J.; Dooleweerdt, K.; de Rooij, N. F.; Staufer, U.; Engel, A. *Nanotechnology* **2008**, *19*, 384004.

(9) Gorodetsky, A. A.; Barton, J. K. *J. Am. Chem. Soc.* **2007**, *129*, 6074.

(10) Gorodetsky, A. A.; Barton, J. K. *Langmuir* **2006**, *22*, 7917.

(11) Oliveira Brett, A. M.; Chiorcea, A.-M. *Langmuir* **2003**, *19*, 3830.

(12) Rose, F.; Martin, P.; Fujita, H.; Kawakatsu, H. *Nanotechnology* **2006**, *17*, 3325.

(13) Allongue, P.; Delamar, M.; Desbat, B.; Fagebaume, O.; Hitmi, R.; Pinson, J.; Savéant, J.-M. *J. Am. Chem. Soc.* **1997**, *119*, 201.

(14) Kirkman, P. M.; Güell, A. G.; Cuharuc, A. S.; Unwin, P. R. *J. Am. Chem. Soc.* **2014**, *136*, 36.

(15) Tanaka, M.; Sawaguchi, T.; Sato, Y.; Yoshioka, K.; Niwa, O. *Langmuir* **2010**, *27*, 170.

(16) Kibena, E.; Marandi, M.; Sammelselg, V.; Tammeveski, K.; Jensen, B. B. E.; Mortensen, A. B.; Lillethorup, M.; Kongsfelt, M.; Pedersen, S. U.; Daasbjerg, K. *Electroanalysis* **2014**.

(17) Zhang, G.; Kirkman, P. M.; Patel, A. N.; Cuharuc, A. S.; McKelvey, K.; Unwin, P. R. *J. Am. Chem. Soc.* **2014**, *136*, 11444.

(18) Surendranath, Y.; Lutterman, D. A.; Liu, Y.; Nocera, D. G. *J. Am. Chem. Soc.* **2012**, *134*, 6326.

(19) Zhou, Y.; Holme, T.; Berry, J.; Ohno, T. R.; Ginley, D.; O'Hayre, R. *J. Phys. Chem. C* **2009**, *114*, 506.

(20) Kucernak, A. R.; Chowdhury, P. B.; Wilde, C. P.; Kelsall, G. H.; Zhu, Y. Y.; Williams, D. E. *Electrochim. Acta* **2000**, *45*, 4483.

(21) Rice, R. J.; McCreery, R. L. *Anal. Chem.* **1989**, *61*, 1637.

(22) McDermott, M. T.; Kneten, K.; McCreery, R. L. *J. Phys. Chem.* **1992**, *96*, 3124.

(23) Kneten, K. R.; McCreery, R. L. *Anal. Chem.* **1992**, *64*, 2518.

(24) Cline, K. K.; McDermott, M. T.; McCreery, R. L. *J. Phys. Chem.* **1994**, *98*, 5314.

(25) Davies, T. J.; Moore, R. R.; Banks, C. E.; Compton, R. G. *J. Electroanal. Chem.* **2004**, *574*, 123.

(26) Banks, C. E.; Moore, R. R.; Davies, T. J.; Compton, R. G. *Chem. Commun.* **2004**, 1804.

(27) Davies, T. J.; Hyde, M. E.; Compton, R. G. *Angew. Chem. Int. Ed.* **2005**, *44*, 5121.

(28) Banks, C. E.; Davies, T. J.; Wildgoose, G. G.; Compton, R. G. *Chem. Commun.* **2005**, 829.

(29) Ji, X.; Banks, C. E.; Crossley, A.; Compton, R. G. *ChemPhysChem* **2006**, *7*, 1337.

(30) Lee, C.-Y.; Bond, A. M. *Anal. Chem.* **2008**, *81*, 584.

(31) Bowling, R. J.; Packard, R. T.; McCreery, R. L. *J. Am. Chem. Soc.* **1989**, *111*, 1217.

(32) McCreery, R. L.; McDermott, M. T. *Anal. Chem.* **2012**, *84*, 2602.

(33) Lu, M.; Compton, R. G. *Analyst* **2014**, *139*, 4599.

(34) Ji, X.; Banks, C. E.; Xi, W.; Wilkins, S. J.; Compton, R. G. *J. Phys. Chem. B* **2006**, *110*, 22306.

(35) *Understanding Voltammetry*; 2nd ed.; R. G. Compton; Banks, C. E., Eds.; Imperial College Press: London, 2011.

(36) D. A. C. Brownson; Banks, C. E. *The Handbook of Graphene Electrochemistry*; Springer: London, 2014.

(37) Pumera, M. *Chem. Rec.* **2009**, *9*, 211.

(38) Pumera, M. *Chem. Eur. J.* **2009**, *15*, 4970.

(39) Patel, A. N.; McKelvey, K.; Unwin, P. R. *J. Am. Chem. Soc.* **2012**, *134*, 20246.

(40) Patel, A. N.; Collignon, M. G.; O'Connell, M. A.; Hung, W. O.; McKelvey, K.; Macpherson, J. V.; Unwin, P. R. *J. Am. Chem. Soc.* **2012**, *134*, 20117.

(41) Lai, S. C. S.; Patel, A. N.; McKelvey, K.; Unwin, P. R. *Angew. Chem. Int. Ed.* **2012**, *51*, 5405.

(42) Patel, A. N.; Tan, S. Y.; Unwin, P. R. *Chem. Commun.* **2013**, *49*, 8776.

(43) Edwards, M. A.; Bertoncello, P.; Unwin, P. R. *J. Phys. Chem. C* **2009**, *113*, 9218.

(44) Williams, C. G.; Edwards, M. A.; Colley, A. L.; Macpherson, J. V.; Unwin, P. R. *Anal. Chem.* **2009**, *81*, 2486.

(45) Anne, A.; Cambril, E.; Chovin, A.; Demaille, C.; Goyer, C. *ACS Nano* **2009**, *3*, 2927.

(46) Lhenry, S.; Leroux, Y. R.; Hapiot, P. *Anal. Chem.* **2012**, *84*, 7518.

(47) Heller, I.; Kong, J.; Heering, H. A.; Williams, K. A.; Lemay, S. G.; Dekker, C. *Nano Lett.* **2004**, *5*, 137.

(48) Güell, A. G.; Meadows, K. E.; Dudin, P. V.; Ebejer, N.; Macpherson, J. V.; Unwin, P. R. *Nano Lett.* **2014**, *14*, 220.

(49) Byers, J. C.; Güell, A. G.; Unwin, P. R. *J. Am. Chem. Soc.* **2014**, *136*, 11252.

(50) Güell, A. G.; Meadows, K. E.; Dudin, P. V.; Ebejer, N.; Byers, J. C.; Macpherson, J. V.; Unwin, P. R. *Faraday Discuss.* **2014**, *172*, 439.

(51) Corso, B. L.; Perez, I.; Sheps, T.; Sims, P. C.; Gül, O. T.; Collins, P. G. *Nano Lett.* **2014**, *14*, 1329.

(52) Ebejer, N.; Guell, A. G.; Lai, S. C.; McKelvey, K.; Snowden, M. E.; Unwin, P. R. *Annu. Rev. Anal. Chem.* **2013**, *6*, 329.

(53) Macpherson, J. V.; Unwin, P. R. *Anal. Chem.* **2000**, *72*, 276.

(54) Patel, A. N.; Tan, S. Y.; Miller, T. S.; Macpherson, J. V.; Unwin, P. R. *Anal. Chem.* **2013**, *85*, 11755.

(55) Bowler, R.; Davies, T. J.; Hyde, M. E.; Compton, R. G. *Anal. Chem.* **2005**, *77*, 1916.

(56) Bertoncello, P.; Edgeworth, J. P.; Macpherson, J. V.; Unwin, P. R. *J. Am. Chem. Soc.* **2007**, *129*, 10982.

(57) Güell, A. G.; Meadows, K. E.; Unwin, P. R.; Macpherson, J. V. *Phys. Chem. Chem. Phys.* **2010**, *12*, 10108.

(58) Oliveira Brett, A. M.; Chiorcea Paquim, A.-M. *Bioelectrochemistry* **2005**, *66*, 117.

(59) Li, Z.; Wang, Y.; Kozbial, A.; Shenoy, G.; Zhou, F.; McGinley, R.; Ireland, P.; Morganstein, B.; Kunkel, A.; Surwade, S. P.; Li, L.; Liu, H. *Nat. Mater.* **2013**, *12*, 925.

(60) Pharr, C. M.; Griffiths, P. R. *Anal. Chem.* **1997**, *69*, 4673.

(61) Myland, J. C.; Oldham, K. B. *Anal. Chem.* **2000**, *72*, 3972.

(62) Oldham, K. B.; Stevens, N. P. C. *Anal. Chem.* **2000**, *72*, 3981.

(63) *CRC Handbook of Chemistry and Physics*; Lide, D. R., Ed.; CRC Press: USA, 2001.

(64) Simonov, A. N.; Morris, G. P.; Mashkina, E. A.; Bethwaite, B.; Gillow, K.; Baker, R. E.; Gavaghan, D. J.; Bond, A. M. *Anal. Chem.* **2014**, *86*, 8408.

(65) Dickinson, E. J. F.; Limon-Petersen, J. G.; Rees, N. V.; Compton, R. G. *J. Phys. Chem. C* **2009**, *113*, 11157.

(66) A. J. Bard; Faulkner, L. R. *Electrochemical Methods: Fundamentals and Applications*; 2nd ed.; John Wiley& Sons, Inc.: New York, 2001.

(67) Nicholson, R. S. *Anal. Chem.* **1965**, *37*, 1351.

(68) Li, W.; Tan, C.; Lowe, M. A.; Abruña, H. D.; Ralph, D. C. *ACS Nano* **2011**, *5*, 2264.

(69) Macpherson, J. V.; Jones, C. E.; Unwin, P. R. *J. Phys. Chem. B* **1998**, *102*, 9891.

(70) Chen, S.; Kucernak, A. *J. Phys. Chem. B* **2002**, *106*, 9396.

(71) Macpherson, J. V.; Beeston, M. A.; Unwin, P. R. *J. Chem. Soc., Faraday Trans.* **1995**, *91*, 899.

(72) Beriet, C.; Pletcher, D. *J. Electroanal. Chem.* **1994**, *375*, 213.

(73) Beriet, C.; Pletcher, D. *J. Electroanal. Chem.* **1993**, *361*, 93.

(74) Campbell, S. A.; Peter, L. M. *J. Electroanal. Chem.* **1994**, *364*, 257.

(75) Zhang, B.; Fan, L.; Zhong, H.; Liu, Y.; Chen, S. *J. Am. Chem. Soc.* **2013**, *135*, 10073.

(76) Banerjee, S.; Shim, J.; Rivera, J.; Jin, X.; Estrada, D.; Solovyeva, V.; You, X.; Pak, J.; Pop, E.; Aluru, N.; Bashir, R. *ACS Nano* **2012**, *7*, 834.

(77) Kamata, T.; Kato, D.; Hirono, S.; Niwa, O. *Anal. Chem.* **2013**, *85*, 9845.

(78) Kokko, K.; Ojala, E.; Mansikka, K. *Phys. Status. Solidi. B* **1989**, *153*, 235.

(79) *Physical Chemistry, an Advanced Treatise*; Gerischer, H., Ed.; Academic Press: New York, 1970; Vol. IX.

(80) *Advances in Electrochemistry and Electrochemical Engineering*; Levich, V. G., Ed.; Wiley Interscience: New York, 1966; Vol. 4.

(81) Chen, S.; Liu, Y.; Chen, J. *Chem. Soc. Rev.* **2014**, *43*, 5372.

(82) Niimi, Y.; Matsui, T.; Kambara, H.; Tagami, K.; Tsukada, M.; Fukuyama, H. *Phys. Rev. B* **2006**, *73*, 085421.

(83) Kobayashi, Y.; Kusakabe, K.; Fukui, K.-i.; Enoki, T. *Physica E* **2006**, *34*, 678.

(84) Kobayashi, Y.; Fukui, K.-i.; Enoki, T.; Kusakabe, K. *Phys. Rev. B* **2006**, *73*, 125415.

(85) López-Palacios, J.; Heras, A.; Colina, Á.; Ruiz, V. *Electrochim. Acta* **2004**, *49*, 1027.

(86) Iwasita, T.; Schmickler, W.; Herrmann, J.; Vogel, U. *J. Electrochem. Soc.* **1983**, *130*, 2026.

(87) Santos, E.; Iwasita, T.; Vielstich, W. *Electrochim. Acta* **1986**, *31*, 431.

(88) McDermott, M. T.; McCreery, R. L. *Langmuir* **1994**, *10*, 4307.

(89) McCreery, R.; Bergren, A.; Morteza-Najarian, A.; Sayed, S. Y.; Yan, H. *Faraday Discuss.* **2014**, *172*, 9.

(90) Amatore, C.; Savéant, J. M.; Tessier, D. *J. Electroanal. Chem.* **1983**, *147*, 39.

(91) Ruffieux, P.; Melle-Franco, M.; Gröning, O.; Bielmann, M.; Zerbetto, F.; Gröning, P. *Phys. Rev. B* **2005**, *71*, 153403.

(92) Hahn, J. R.; Kang, H. *Phys. Rev. B* **1999**, *60*, 6007.

(93) Chang, H.; Bard, A. J. *J. Am. Chem. Soc.* **1990**, *112*, 4598.

(94) Chang, H.; Bard, A. J. *J. Am. Chem. Soc.* **1991**, *113*, 5588.

(95) Zoval, J. V.; Stiger, R. M.; Biernacki, P. R.; Penner, R. M. *J. Phys. Chem.* **1996**, *100*, 837.

(96) Ma, H.; Lee, L.; Brooksby, P. A.; Brown, S. A.; Fraser, S. J.; Gordon, K. C.; Leroux, Y. R.; Hapiot, P.; Downard, A. J. *J. Phys. Chem. C* **2014**, *118*, 5820.

(97) Wilson, N. R.; Guille, M.; Dumitrescu, I.; Fernandez, V. R.; Rudd, N. C.; Williams, C. G.; Unwin, P. R.; Macpherson, J. V. *Anal. Chem.* **2006**, *78*, 7006.

(98) Iwasita, T.; Schmickler, W.; Schultze, J. W. *Ber. Bunsenges. Phys. Chem.* **1985**, *89*, 138.

(99) Iwasita, T.; Schmickler, W.; Schultze, J. W. *J. Electroanal. Chem.* **1985**, *194*, 355.

(100) Velmurugan, J.; Sun, P.; Mirkin, M. V. *J. Phys. Chem. C* **2009**, *113*, 459.

(101) Gosavi, S.; Marcus, R. A. *J. Phys. Chem. B* **2000**, *104*, 2067.

(102) Batchelor-McAuley, C.; Laborda, E.; Henstridge, M. C.; Nissim, R.; Compton, R. G. *Electrochim. Acta* **2013**, *88*, 895.

(103) Nioradze, N.; Chen, R.; Kim, J.; Shen, M.; Santhosh, P.; Amemiya, S. *Anal. Chem.* **2013**, *85*, 6198.

(104) Peter, L. M.; Dürr, W.; Bindra, P.; Gerischer, H. *J. Electroanal. Chem.* **1976**, *71*, 31.

(105) Sato, N. *Electrochemistry at Metal and Semiconductor Electrodes*; 2nd ed.; Elsevier Science: Amsterdam, 2003.

(106) Smalley, J. F.; Finklea, H. O.; Chidsey, C. E. D.; Linford, M. R.; Creager, S. E.; Ferraris, J. P.; Chalfant, K.; Zawodzinsk, T.; Feldberg, S. W.; Newton, M. D. *J. Am. Chem. Soc.* **2003**, *125*, 2004.

(107) Luque, N. B.; Schmickler, W. *Electrochim. Acta* **2013**, *88*, 892.

(108) Güell, A. G.; Cuharuc, A. S.; Kim, Y. R.; Zhang, G.; Tan, S. Y.; Ebejer, N.; Unwin, P. R. *ACS Nano* **2015**, *9*, 3558.

Chapter 4 Electrochemistry of $Fe^{3+/2+}$ at Highly Oriented Pyrolytic Graphite (HOPG) Electrodes: Kinetics, Identification of Major Electroactive Sites and Time Effects on the Response

In this chapter, the electrochemistry of the $Fe^{3+/2+}$ redox couple, associated with slow ET kinetics has been studied on HOPG samples that differ in step edge density by >2 orders of magnitude. Surface structure (composition) has little effect on the ET kinetics of $Fe^{3+/2+}$, and a k_0 of ~5×10^{-5} cm $s^{-1}$is derived from simulation of the experimental data, which falls in the range reported for metal electrodes. SECCM reactive mapping of HOPG demonstrates the high activity of the basal plane. In line with the results for classical outer-sphere redox species, this study again suggests the DOS is not important in the ET kinetics of $Fe^{3+/2+}$ on HOPG and the basal surface of HOPG has high electroactivity. Moreover, it is found that while time after cleavage of HOPG has an impact on the surface wettability (and possible contamination), this does not have any significant influence on the electrochemistry of $Fe^{3+/2+}$.

4.1 Introduction

Carbon electrodes are studied extensively for both fundamental electrochemistry and myriad practical applications.[1-4] Within the family of carbon materials, HOPG – where sp^2 hybridised carbon atoms in a honeycomb (graphene) arrangement within layers are stacked to make a 3D material – has generated huge research interest. In part, this is because fresh surfaces can be easily prepared, by mechanical or Scotch-tape based exfoliation, to produce well-defined structures, *i.e.* basal plane (terraces) and step edges that are easily characterised by a variety of techniques.[5,6] Further, HOPG is generally regarded as a model to which other sp^2 carbon materials, such as carbon nanotubes[7] and graphene,[8,9] are often compared.

In contrast to early work, which considered the HOPG basal plane to be largely or completely inert, even for outer-sphere redox reactions,[10-14] recent studies have shown that the basal surface of HOPG actually has substantial activity.[2,3,5,15-18] This new finding has come about from a range of measurements[2,3] – macroscopic/microscopic measurements of adsorbed redox species,[17,19] nanoscopic surface electroactivity imaging,[5,20-23] and metal nanoparticle nucleation,[24] and for a wide range of redox reactions, including dopamine oxidation,[16,19] adsorbed anthraquinone reduction,[17] $FcTMA^+$ oxidation,[8,25,26] $Ru(NH_3)_6^{3+}$ reduction,[5,8,18,20,22] $IrCl_6^{2-}$ reduction[18] and $Fe(CN)_6^{4-}$ oxidation.[5,18] In fact, ET kinetics at freshly cleaved HOPG has been shown to be at least as fast as on platinum for $IrCl_6^{2-/3-}$ and $Fe(CN)_6^{4-/3-}$, and the standard heterogeneous ET rate constant (k_0) for $Ru(NH_3)_6^{3+/2+}$ is comparable to that for platinum.[18] Further, the step edge density (which can affect the local density of electronic states[2,3,27,28]) has been found to have little or no impact on the overall ET kinetics of macroscopic HOPG.[15,19] This evidence suggests that these processes are adiabatic.[17,18,29]

In many of the above-mentioned studies, the reactions of the redox species were so fast (close to reversible) as to be effectively limited by diffusion, and so it was only possible to provide lower limits for k_0.[2,3,18] Here, we present a study of the $Fe^{3+/2+}$ redox couple in aqueous solution, which is known to have

much slower ET kinetics (possibly due to the high reorganisation energy in the reaction, as significant changes in bond distances are needed for transferring $Fe(H_2O)_6^{3+}$ to $Fe(H_2O)_6^{2+}$),[30,31] but is still regarded as an outer-sphere process,[29] although one that can be promoted (enhanced) by some adsorbed anions at metals such as platinum.[32,33] Thus, with careful experimental design, this is a very attractive redox system from which to make kinetic comparisons on different electrodes.

In this study, droplet-cell measurements[18,26] were used to acquire macroscopic CVs of $Fe^{3+/2+}$ on two grades (quality) of HOPG that had different step edge coverage (by >2 orders of magnitude). Simulations were performed to interpret the CVs, so as to deduce kinetic values and determine whether step edges had any influence on the kinetics. SECCM,[34,35] was then employed to map the electroactivity of high quality (low step density) HOPG, allowing electroactivity maps to be produced that revealed the activity of different local structures, in particular, of the basal surface, free from step edges.

A consideration in HOPG electrochemistry is electrode history effects,[2,3,5,8,22,25,26] particularly the elapsed time after cleavage during which atmospheric contamination can occur.[2,3,5,36] We have addressed this in some detail in our past work,[2,3,5,8,25,26] and found that it can quickly play a role for some redox reactions (*e.g.* $Fe(CN)_6^{4-/3-}$),[5,20] but the effect on others may be less noticeable. Thus, the possible effect of time after surface cleavage of HOPG, on the electrochemical behaviour of $Fe^{3+/2+}$ has also been briefly explored. The kinetics of the $Fe^{3+/2+}$ couple is sensitive to changes in the surface, when HOPG is left exposed to the air for hours after cleavage and before electrochemical measurements, with the kinetics deteriorating towards values previously reported in the literature for clean HOPG (k_0 ~1.4 × 10^{-5} cm s^{-1}).[11,37] However, over short times, for example on the timescale of electrochemical imaging, such effects are negligible.

4.2 Results and Discussion

4.2.1 $Fe^{3+/2+}$ Voltammetry on HOPG

It is reported that the $Fe^{3+/2+}$ redox reactions can be affected by certain anions in the solution[30,33] and this was taken into consideration for the design of experiments, which were carried out in perchlorate medium, as a consequence. On one hand, ClO_4^- was expected to only weakly adsorb on the HOPG electrodes (if at all) and, on the other hand, most of $Fe^{3+/2+}$ ions would remain free in the aqueous solution,[38] in contrast, for example, to SO_4^{2-}, where various ion pairs with $Fe^{3+/2+}$ are formed.[30]

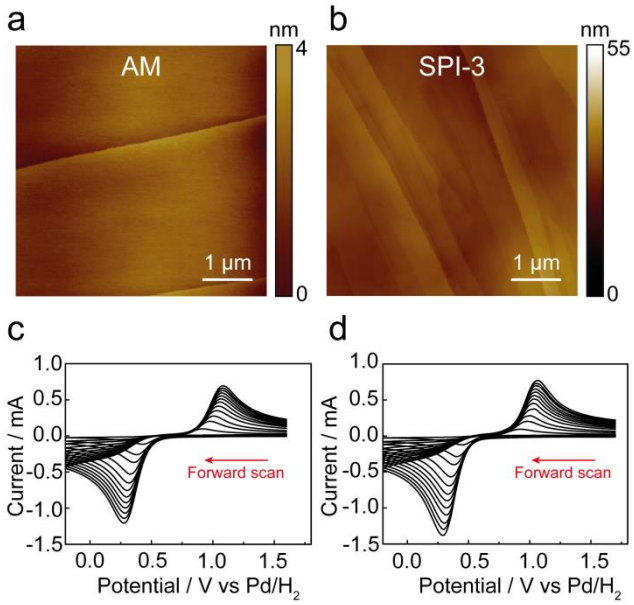

Figure 4.1 5 µm × 5 µm tapping-mode AFM images of (a) AM and (b) SPI-3 grade HOPG. Note the differences in scale. Cyclic voltammograms for the reduction of $Fe(ClO_4)_3$ (5 mM in 0.1 M $HClO_4$ solution) on freshly cleaved (c) AM and (d) SPI-3 HOPG. Scan rates: 0.1 (smallest current), 0.5, 1, 2, 3, 4, 5, 6, 7, 8, 9 and 10 (biggest current) V s^{-1}.

CVs of 5 mM $Fe(ClO_4)_3$ in a supporting electrolyte of 0.1 M $HClO_4$ solution were recorded at a range of scan rates (0.1, 0.5, 1, 2, 3, 4, 5, 6, 7, 8, 9 and 10 V s^{-1}) on freshly cleaved AM and SPI-3 HOPG surfaces. As shown in Figure 4.1, a pair of redox peaks, due to the reduction of Fe^{3+} and subsequent oxidation of Fe^{2+} that is formed, were observed. Although the step edge coverage is very different (by >2 orders of magnitude) between

AM grade and SPI-3 HOPG samples,[5,15] almost identical (irreversible) voltammetry of $Fe^{3+/2+}$ was seen on these two grades of HOPG. Since the electrochemistry of $Fe^{3+/2+}$ is associated with slow ET kinetics, this indicates unequivocally that step edges have no influence on the ET kinetics, and that ET is dominated by the basal surface.

Note that the ΔE_p of the CVs shown in Figure 4.1 increased as a function of scan rate, as shown in Figure 4.2. ΔE_p of 510 ± 19 mV (n=7) and 498 ± 12 mV (n=7) were obtained on AM and SPI-3 HOPG, respectively, at a scan rate of 0.1 V s^{-1}, and increased to 801 ± 21 mV (n=7) and 796 ± 14 mV (n=7) at 10 V s^{-1}. The similarity of CVs (as determined by ΔE_p values) on these two samples indicated that basal plane HOPG is electroactive toward the ET of $Fe^{3+/2+}$ and that step edges contribute little additional activity.[10,11,14]

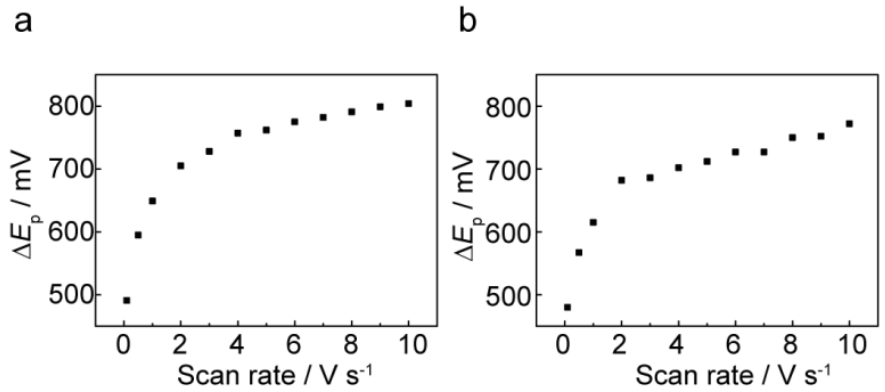

Figure 4.2 Typical example data of peak-to-peak separation plotted against scan rate for the cyclic voltammograms of 5 mM $Fe(ClO_4)_3$ in 0.1 M $HClO_4$ on (a) AM and (b) SPI-3 HOPG (data shown in Figure 4.1).

The large values of ΔE_p obtained on the CVs were predominantly derived from slow ET kinetics of $Fe^{3+/2+}$ rather than the ohmic drop effects, especially at slow scan rates (although this is considered further below, *vide infra*). A 20-fold decrease in Fe^{3+} concentration (to 0.25 mM in 0.1 M $HClO_4$) produced ΔE_p of 514 ± 3.5 mV (at 0.1 V s^{-1}; n=3) to 806 ± 4.7 mV (at 10 V s^{-1}; n=3) on AM grade HOPG (Figure 4.3).

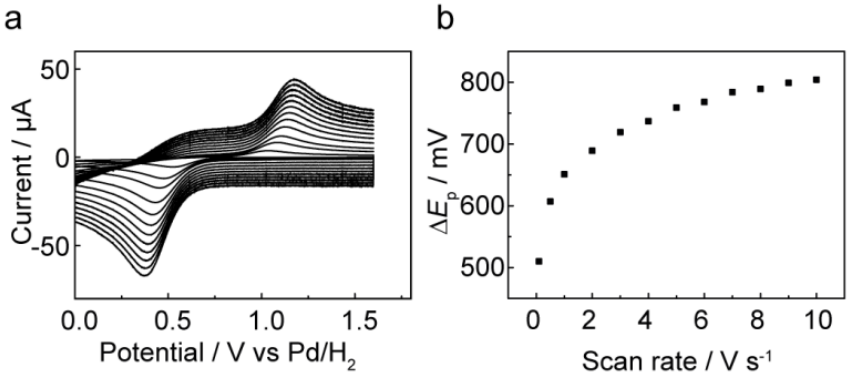

Figure 4.3 (a) CVs for the reduction of $Fe(ClO_4)_3$ (0.25 mM in 0.1 M $HClO_4$ solution) recorded at scan rates of 0.1(smallest current), 0.5, 1, 2, 3, 4, 5, 6, 7, 8, 9 and 10 (biggest current) V s^{-1}. (b) Peak-to-peak separation for the CVs shown in (a) plotted against scan rates.

FEM simulation of the CVs for the reduction of 5 mM Fe^{3+} (in 0.1 M $HClO_4$) were performed at scan rates of 0.1, 0.5, 1, 5, 7 and 10 V s^{-1}, using diffusion coefficients D_O = 4.08×10^{-6} cm^2 s^{-1} for Fe^{3+}, and D_R = 5.51×10^{-6} cm^2 s^{-1} for Fe^{2+} (adopted from the literature[39]). Ohmic drop effects were not significant for the CVs recorded at a scan rate of 0.1 V s^{-1}, but may be a little more important at fast scan rates. Thus, in the model, 0 and 30 ohm (for AM grade), or 28 ohm (for SPI-3 grade) (reasonable for aqueous solutions in the setup used[18]) of uncompensated resistance, R_u, were considered for the CVs simulated at 0.1 V s^{-1} and the remainder of scan rates (0.5, 1, 5, 7 and 10 V s^{-1}), respectively (*vide infra*). As shown in Figure 4.4, the simulated results matched the experimental data reasonably well on AM and SPI-3 HOPG (also see the least squares correlation Φ in Table 4.1), in particular at the slow scan rates (*i.e.* 0.1, 0.5 and 1 V s^{-1}). At fast scan rates (5, 7 and 10 V s^{-1}), the simulation followed the experimental data on AM and SPI-3 HOPG except the post-peak regions where the electrochemical responses were limited by diffusion. Over those areas, the simulated current responses were slightly lower than the experimental CVs, but still in reasonable agreement.

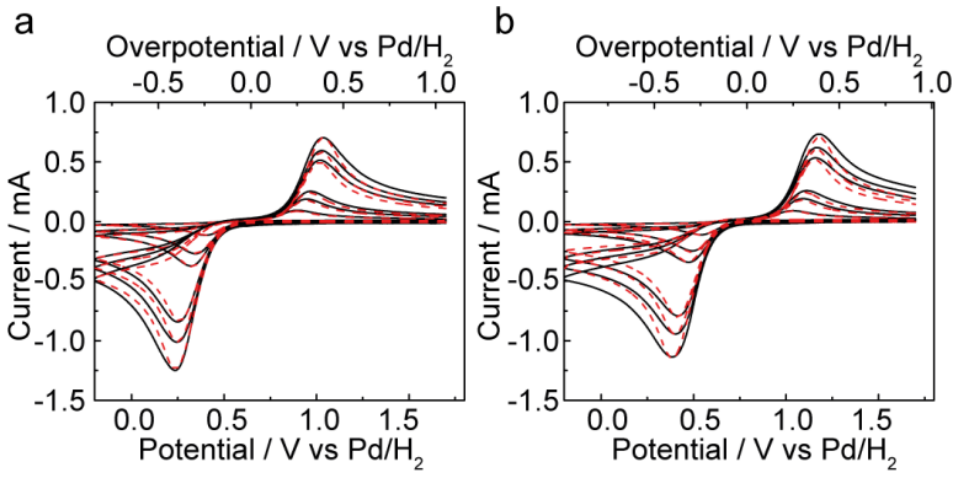

Figure 4.4 Cyclic voltammograms (black) and simulation results (red) for the reduction of $Fe(ClO_4)_3$ (5 mM in 0.1 M $HClO_4$ solution) on freshly cleaved (a) AM and (b) SPI-3 HOPG. Scan rates: 0.1 (smallest current), 0.5, 1, 5, 7 and 10 (biggest current) V s^{-1}.

Table 4.1 Simulation parameters for the $Fe^{3+/2+}$ process on AM and SPI-3 grade HOPG samples shown in Figure 4.4.

v (V s^{-1})	AM				SPI-3			
	Area (cm^2)	k_0 (cm s^{-1})	R_u (ohm)	Φ	Area (cm^2)	k_0 (cm s^{-1})	R_u (ohm)	Φ
0.1	0.18	0.00005	0	99.0	0.178	0.00005	0	99.0
0.5	0.185	0.00005	30	99.4	0.178	0.00005	28	99.0
1	0.185	0.00005	30	99.4	0.178	0.00005	28	98.5
5	0.187	0.00005	30	99.1	0.178	0.00005	28	97.9
7	0.19	0.00005	30	98.9	0.178	0.00005	28	97.6
10	0.195	0.00005	30	98.8	0.180	0.00005	28	97.4

Parameters used for the simulations are summarised in Table 4.1. Note that the kinetic term is consistent across the scan rates, but there is a small variation in the area of droplet, which was allowed to vary by ±10% from the measured value. This is because the electrowetting of HOPG can occur at positive potentials during CV scans in some ClO_4^--containing solutions, due

to intercalation/deintercalation of ClO_4^- ions that introduces ClO_4^- ions from the solution into the top graphene layers of HOPG.[40] In the case studied herein, the redox reactions of $Fe^{3+/2+}$covered a wide potential window (-0.2 to 1.7 V) where slight electrowetting could just begin to occur at the most positive potentials. Note, however, that intercalation does not occur in the potential region where the kinetics is measured and, even at the maximum extent, the amount of intercalation represents <1% or less of the surface[40] and so would have a negligible effect on the ET process measured.

Further CV measurements were carried out using an O-ring to confine the droplet cell, in a solution of 0.25 mM Fe^{3+} in 1M $HClO_4$. These showed slightly larger ΔE_p (Figure 4.5). However, it is important to point out that, the O-ring could impose mechanical strain on the surface of HOPG and introduce defects. In general, the mounting of HOPG in any kind of mechanical cell when studying HOPG should be avoided.[5,41] This again demonstrated the importance of experimental design, to elucidate the ET kinetics on HOPG.

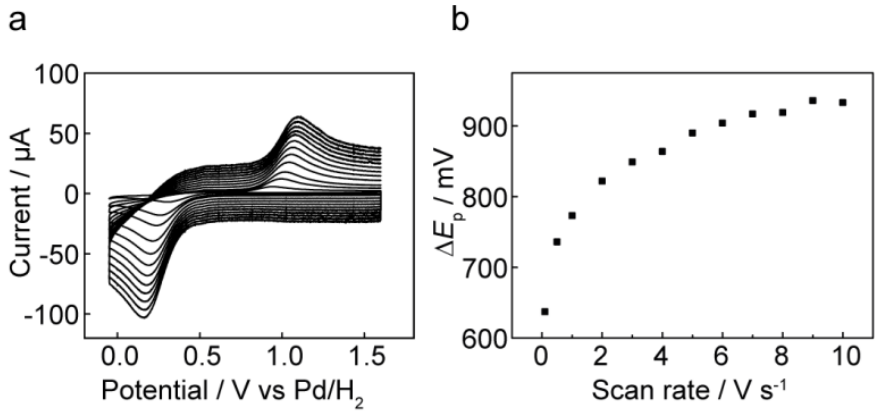

Figure 4.5 (a) CVs for the reduction of $Fe(ClO_4)_3$ (0.25 mM in 1 M $HClO_4$ solution) recorded at scan rates of 0.1(smallest current), 0.5, 1, 2, 3, 4, 5, 6, 7, 8, 9 and 10 (biggest current) V s^{-1}, with an O-ring (radius 3.1 mm) used to confine the working electrode area. (b) Peak-to-peak separation for the CVs shown in (a) plotted against scan rates.

Importantly, there is a good fit in the positions for the redox peaks between simulated and experimental CVs and a kinetic value k_0 of *ca.* (5 ± 1) × 10^{-5} cm s^{-1} was deduced from the simulated curves both for AM and SPI-3 HOPG

(Table 4.1). This value is within the range of those obtained on metal electrodes (*e.g.* Pt and Au), *i.e.* 10^{-5} – 10^{-4} cm s^{-1},[30,33,42] which have much higher DOS at the intrinsic Fermi level (by >2 orders of magnitude on Au than HOPG),[11] and also of the same order of magnitude as the upper range obtained on HOPG in previous studies.[37]

4.2.2 Time Effect on the Electrochemical Responses of $Fe^{3+/2+}$ on HOPG

As mentioned in the Introduction of this chapter, an issue regarding the use of graphite as electrodes can be the contamination on the surfaces by the environment where the substrates are situated.[2,3,5,8,36,43-45] It is reported that wettability of carbon materials (graphene and graphite) can be affected by the accumulation of airborne contaminants (mainly hydrocarbons) deposited on the surface with time, as reflected by an increase in CA of aqueous droplets on those surfaces after being exposed in air (with the biggest CA change seen within 10–15 min).[45] Obviously, the time scale of the effect will depend on the environment (cleanliness) and so we also studied the time effect on the wettability of HOPG by placing a droplet of either 5 mM $Fe(ClO_4)_3$ solution (in 0.1 M $HClO_4$) or pure water on AM HOPG surfaces that were cleaved and exposed in air for different time. As seen from Figure 4.6, the CA of $Fe(ClO_4)_3$ solution on freshly cleaved HOPG surface is smaller than observed previously (and also in this study), with pure water (*vide infra*),[9,40] possibly due to the surface tension changes upon addition of $HClO_4$ solution,[46] which can influence the CA, according to Young's equation.[47] It was found that the CA of a droplet of a $Fe(ClO_4)_3$ solution increased quite significantly after leaving HOPG for periods up to 30 min, from 42° on freshly cleaved surface of HOPG to 66° on the surface aged for 30 min in air. Beyond that, there was little change in the CA of droplets on HOPG surface with time, indicating that a wettability limit, was achieved.

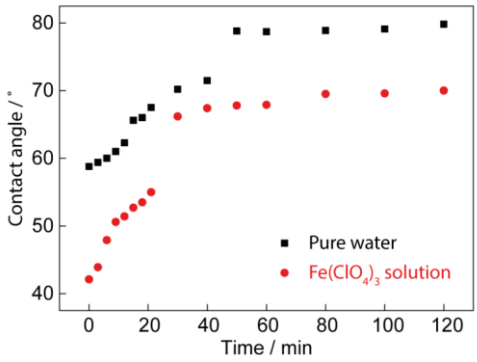

Figure 4.6 Contact angles of a droplet of pure water (black square) and a 5 mM $Fe(ClO_4)_3$ in 0.1 M $HClO_4$ solution (red dot) on AM HOPG plotted against the time after sample cleavage while being exposed in air.

For comparison, CA measurements were also carried out using droplets of pure water. As seen in Figure 4.6, on a freshly cleaved surface of AM HOPG the CA was 59°, and it increased significantly with the time of HOPG surface exposure to air. Compared to the droplet of a $Fe(ClO_4)_3$ solution, a longer time (~50 min) was taken for the CA of pure water droplet to reach a stable (and higher) value (~79°).

Considering the fast time scale for the macroscopic CV measurements, carried out within seconds of the cleavage of the HOPG sample in this study (*vide supra*) and our previous studies,[2,3,5,18,26,40] surface contamination effects on the ET kinetics will evidently be negligible.

It is interesting to investigate the electrochemical responses of $Fe^{3+/2+}$ redox couple on HOPG as a function of exposure time to the atmosphere, during which the surfaces can possibly change. Given that electrochemistry of some other redox couples on graphite electrodes can be potentially affected by time after cleavage of sample.[5,8] Indeed, some redox species, such as $Fe(CN)_6^{4-/3-}$ and $Ru(NH_3)_6^{3+/2+}$, demonstrated deteriorated responses on aged HOPG samples.[5,22] In this study, the effect of elapsed time after HOPG cleavage, but before making the electrochemical cell, was tested for $Fe^{3+/2+}$ on AM and SPI-3 HOPG. After cleavage, the surfaces that were left exposed to air for different times, *i.e.* 0, 10 min, 20 min, 30min, 1 h, 2h, 4h, and 12 h. Over the period of exposure time, two main possible time-dependent factors

(although there may be others) needed to be considered: the accumulation of airborne contaminants on the surface[5,36] and delamination of top graphene layers from HOPG.[8,48]

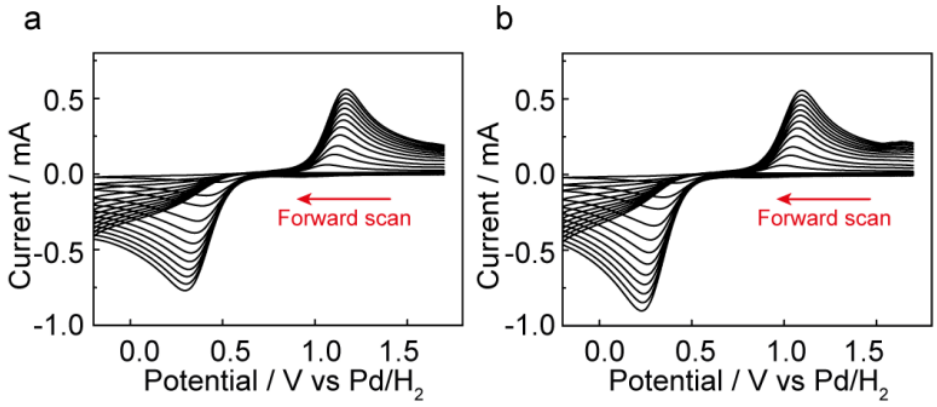

Figure 4.7 Cyclic voltammograms for the reduction of 5 mM $Fe(ClO_4)_3$ (in 0.1 M $HClO_4$ solution) on (a) AM and (b) SPI-3 HOPG that were exposed in air for 12 h after cleavage. Scan rate: 0.1 (smallest current), 0.5, 1, 2, 3, 4, 5, 6, 7, 8, 9 and 10 (biggest current) V s^{-1}.

As shown in Figure 4.7, although the CA of aqueous droplets on HOPG could be significantly affected by surface history (*vide supra*), there was a relatively small difference in the CV responses of $Fe^{3+/2+}$ between freshly cleaved and aged surfaces with the longest exposure time (12 h) in air, for both AM and SPI-3 HOPG samples (*cf.* Figure 4.1).

The ΔE_p values of the CVs for the reduction of Fe^{3+} on fresh and aged AM and SPI-3 HOPG surfaces are plotted against exposure time in Figure 4.8. Given the possible ohmic drop effect at fast scan rates (*vide supra*), only the CVs at the three slowest scan rates (0.1, 0.5 and 1 V s^{-1}) were considered. As seen in Figure 4.8, the ΔE_p increased gradually with the exposure time of the HOPG surface to the atmosphere for all three scan rates, and changed by ~100 mV on HOPG surface that was exposed in air for 12 h after cleavage.

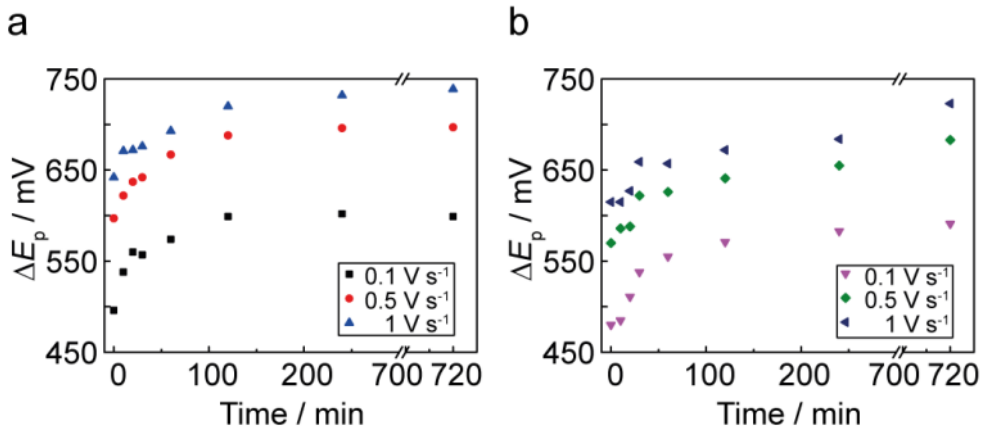

Figure 4.8 Peak-to-peak separation of the cyclic voltammograms for the reduction of 5 mM $Fe(ClO_4)_3$ (in 0.1 M $HClO_4$ solution) plotted against the time after cleavage for (a) AM and (b) SPI-3 HOPG. CV data at 0.1, 0.5 and 1 V s^{-1} were shown.

The k_0 values can be readily estimated from ΔE_p of CVs (shown in Figure 4.8) by using the equation developed by Klingler and Kochi (assume the transfer coefficient = 0.5).[49] As shown in Figure 4.9, k_0 of 4.9 × 10^{-5} cm s^{-1} and 5.8 × 10^{-5} cm s^{-1} were obtained for the CVs recorded at 0.1 V s^{-1} on freshly cleaved AM and SPI-3 grade HOPG, respectively, with 4.1 × 10^{-5} cm s^{-1} and 5.4 × 10^{-5} correspondingly observed at 0.5 V s^{-1}, and 3.8 × 10^{-5} cm s^{-1} and 4.9 × 10^{-5} cm s^{-1} at 1 V s^{-1}. These values are in good accordance with simulation results (*vide supra*), and different scan rates led to similar k_0 values. The slightly higher k_0 values on SPI-3 grade HOPG, as also seen in the CV simulations, correlates with the higher specific surface area for this electrode (higher step edge density), but not higher intrinsic kinetics at the edges. The k_0 values decreased with the elapsed time after cleavage of HOPG and tended to be constant after ~1 h on the two grades of HOPG. With an exposure time of 12 h (the longest time considered in this study), the aged HOPG surfaces displayed kinetic values (from 0.1 V s^{-1}) of k_0 = 1.8 × 10^{-5} cm s^{-1} for AM grade HOPG and k_0 = 2 × 10^{-5} cm s^{-1} for SPI-3 grade. Given the long extent of surface exposure, which would lead to significant changes in the surface, due to possible contamination, delamination, surface oxidation, doping and other processes, the effect on the kinetics is actually relatively small. Interestingly, these k_0 values are similar to those that have been

proposed as characteristic of high quality HOPG,[11,37] and as we have pointed out before,[2,3,5] those measurements[11,37] may be compromised by contamination or other effects, such as delamination of the top surface layers,[5,8] depending on the method of cleavage.

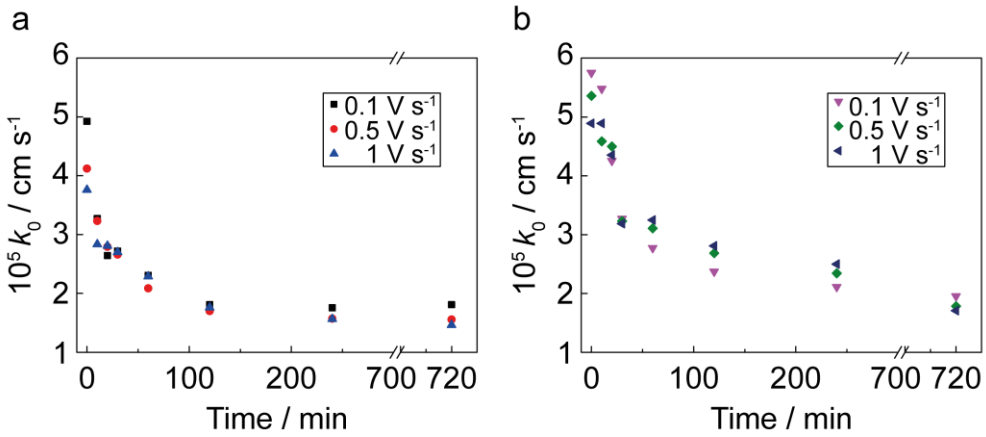

Figure 4.9 Standard heterogeneous rate constant (k_0), obtained from ΔE_p values of CVs shown in Figure 4.8, plotted as a function of the time after exposure to air for (a) AM and (b) SPI-3 HOPG electrodes. Three scan rates (0.1, 0.5 and 1 V s^{-1}) were considered for the CVs obtained with 5 mM $Fe(ClO_4)_3$ in 0.1 M $HClO_4$ solution.

Regarding the possible effects from delamination of the top layers of graphene from graphite that may occur with time,[5,8] the redox potential for $Fe^{3+/2+}$ is far from the intrinsic Fermi level of graphite (and graphene; -0.2 V vs Ag/AgCl),[11] and as a result, the $Fe^{3+/2+}$ redox process may not be as strongly affected by the time-dependent (decoupling) structural changes. As the k_0 values measured herein on freshly cleaved HOPG are similar to metal electrodes, even though the DOS at HOPG is much lower than on metal electrodes,[11] the electrochemistry of the outer-sphere $Fe^{3+/2+}$ shows an adiabatic behaviour.

4.2.3 SECCM Electrochemical Imaging of AM HOPG Surface

As we have shown in many studies,[2,5,7,8,20,34] SECCM is a powerful technique that enables surface electroactivity to be mapped with high temporal and spatial resolution. An advantage of this technique is that measurements can be done shortly after sample preparation (typically within 15 min), minimising

surface history effect. In the case of HOPG, the electroactivity of basal plane alone, or basal plane with intersecting step edges, can be probed separately by a small SECCM pipette, with the working area confined by the meniscus contact.[25] SECCM experiments were carried out on a cleaved AM HOPG surface, using a solution of 0.1 M $HClO_4$ containing 2 mM $Fe(ClO_4)_2$, to investigate the electroactivity of different (localised) surface features. A typical SECCM CV for the one-electron oxidation of Fe^{2+} (at 0.1 V s^{-1}) on the basal plane is shown in Figure 4.10a, where sigmoidal response for nonlinear (spherical segment) diffusion is observed,[50] due to the significantly enhanced mass transport in the tapered pipette, and under a bias applied between the barrels.[51,52] The value of potential difference between the 3/4 and 1/4-wave potentials ($E_{3/4}$-$E_{1/4}$) was ~120 mV, and half-wave potential ($E_{1/2}$) was shifted anodically by 397 mV from the formal potential, indicative of the irreversibility of CVs and slow ET kinetics of $Fe^{3+/2+}$ on HOPG.[50] The standard ET rate constant, k_0, was found to be ~7.4 × 10^{-5} cm s^{-1}, very close to that obtained from simulation of macroscopic CV measurements on the freshly cleaved surface, indicating that the SECCM measurements relate closely to a pristine surface.

SECCM mapping was performed at about 1.2 V (vs Pd/H_2), at the foot of the wave where any differences in ET kinetics across the surface would be revealed most readily. In Figure 4.10b, it should be noted that the first several lines of the image demonstrated slightly higher surface current than the rest of the area probed, which might be due to the electrowetting occurring at positive potentials, as seen for the droplets of perchlorate and sulfate salt solutions on HOPG.[40] This was evidenced by the slightly larger values of the corresponding ion conductance current in this region. After the stabilisation of the meniscus, little variation in surface current was observed across the probed area. Only slightly higher currents were seen at some areas of step edges. Measurements on an aged AM HOPG surface (>2 h in air after cleavage) showed similar behaviour. In part, this could be due to the enhanced meniscus wetting at step edges, as a result of negative charge (functionality) at steps.[53] Slightly higher activity at edges cannot be ruled out completely, but any effect would be very small, based on the macroscopic

measurements reported above. Importantly, SECCM mapping of HOPG surface showed that basal plane HOPG is the predominant site for the ET of $Fe^{3+/2+}$ and is the main feature responsible for the overall behaviour seen in HOPG voltammetry.

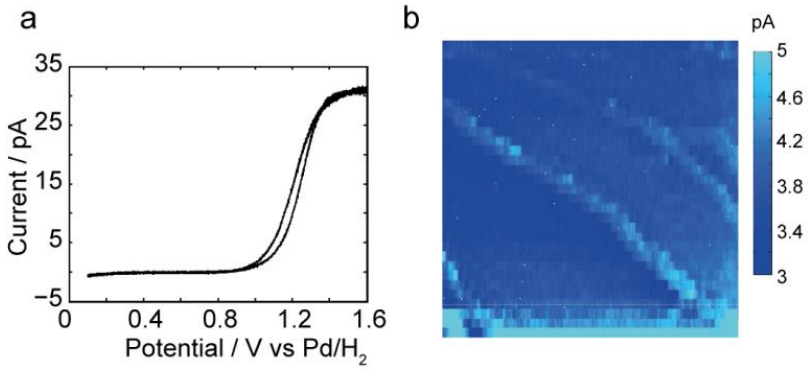

Figure 4.10 (a) A typical CV for the oxidation of 2 mM Fe^{2+} in 0.1 M $HClO_4$, recorded at 0.1 V s^{-1} and (b) SECCM electrochemical activity map of an area of 10 µm × 10 µm on a freshly cleaved AM HOPG surface.

4.3 Conclusions

The electrochemical behaviour of $Fe^{3+/2+}$ redox couple on HOPG has been studied at the macroscale and nanoscale. The standard heterogeneous ET rate constant of $Fe^{3+/2+}$ on HOPG, k_0 ~5 × 10^{-5} cm s^{-1}, deduced from simulations of macroscopic CV results, fell in the range of values obtained for metal electrodes (*e.g.* Pt and Au) and step edge coverage had little effect on the voltammetric responses and ET kinetics. This was further supported by SECCM electroactivity mapping of HOPG surface, where uniform activity of the basal surface of HOPG for the ET of $Fe^{3+/2+}$was revealed (k_0 ~7.4 × 10^{-5} cm s^{-1}). The basal plane is the major electroactive site on cleaved HOPG.

Considering the similar k_0 values obtained for $Fe^{3+/2+}$ on graphite and metal electrodes, and the noticeable difference in DOS between these materials (2.2 × 10^{-3} states $atom^{-1}$ eV^{-1} on HOPG and 0.28 states $atom^{-1}$ eV^{-1} on Au),[11] the DOS does not appear to have much impact on the ET kinetics of $Fe^{3+/2+}$ for the range of DOS values encompassed by HOPG and metals. This is in line with our results for some other outer-sphere redox species on HOPG,[2,3,18] and adds to an expanding body of work that the DOS does not

play a generally important role in outer-sphere redox process, *i.e.* that these processes may be considered to be adiabatic. The $Fe^{3+/2+}$ coupled has been studied less in comparison to other outer-sphere redox probes, such as $Fe(CN)^{4-/3-}$, which is actually more problematic for a number of reasons.[5] We would recommend that it could be considered and used more often for the comparison of different electrode materials. An advantage of $Fe^{3+/2+}$ couple is that the slow kinetics means that quite simple and straightforward electrochemical methods can be used for quantitative studies.

The surface history of HOPG (exposed in air after cleavage) was explored. Exposure to air affects the wettability of HOPG, as evidenced by the increase of the aqueous contact angle on increasingly aged HOPG. There is an associated decrease in the ET kinetics of $Fe^{3+/2+}$, although even on surfaces exposed to air for 12 h, the k_0 values are still of the same order (a factor of 2 or 3 lower) than on freshly cleaved HOPG surface.

4.4 References

(1) Patten, H. V.; Velický, M.; Dryfe, R. A. W. In *Electrochemistry of Carbon Electrodes*; Wiley-VCH Verlag GmbH & Co. KGaA: 2015, p 121.

(2) Unwin, P. R.; Güell, A. G.; Zhang, G. *Acc. Chem. Res.* **2016**, *49*, 2041.

(3) Güell, A. G.; Tan, S.-y.; Unwin, P. R.; Zhang, G. In *Electrochemistry of Carbon Electrodes*; Wiley-VCH Verlag GmbH & Co. KGaA: 2015, p 31.

(4) Macpherson, J. V. *Phys. Chem. Chem. Phys.* **2015**, *17*, 2935.

(5) Patel, A. N.; Collignon, M. G.; O'Connell, M. A.; Hung, W. O.; McKelvey, K.; Macpherson, J. V.; Unwin, P. R. *J. Am. Chem. Soc.* **2012**, *134*, 20117.

(6) Gloaguen, F.; Léger, J. M.; Lamy, C.; Marmann, A.; Stimming, U.; Vogel, R. *Electrochim. Acta* **1999**, *44*, 1805.

(7) Güell, A. G.; Meadows, K. E.; Dudin, P. V.; Ebejer, N.; Macpherson, J. V.; Unwin, P. R. *Nano Lett.* **2014**, *14*, 220.

(8) Güell, A. G.; Cuharuc, A. S.; Kim, Y. R.; Zhang, G.; Tan, S. Y.; Ebejer, N.; Unwin, P. R. *ACS Nano* **2015**, *9*, 3558.

(9) Ashraf, A.; Wu, Y.; Wang, M. C.; Aluru, N. R.; Dastgheib, S. A.; Nam, S. *Langmuir* **2014**, *30*, 12827.

(10) McCreery, R. L.; McDermott, M. T. *Anal. Chem.* **2012**, *84*, 2602.

(11) Cline, K. K.; McDermott, M. T.; McCreery, R. L. *J. Phys. Chem.* **1994**, *98*, 5314.

(12) Rice, R. J.; McCreery, R. L. *Anal. Chem.* **1989**, *61*, 1637.

(13) Davies, T. J.; Hyde, M. E.; Compton, R. G. *Angew. Chem. Int. Ed.* **2005**, *44*, 5121.

(14) Banks, C. E.; Davies, T. J.; Wildgoose, G. G.; Compton, R. G. *Chem. Commun.* **2005**, 829.

(15) Patel, A. N.; Tan, S. Y.; Unwin, P. R. *Chem. Commun.* **2013**, *49*, 8776.

(16) Patel, A. N.; McKelvey, K.; Unwin, P. R. *J. Am. Chem. Soc.* **2012**, *134*, 20246.

(17) Zhang, G.; Kirkman, P. M.; Patel, A. N.; Cuharuc, A. S.; McKelvey, K.; Unwin, P. R. *J. Am. Chem. Soc.* **2014**, *136*, 11444.

(18) Zhang, G.; Cuharuc, A. S.; Güell, A. G.; Unwin, P. R. *Phys. Chem. Chem. Phys.* **2015**, *17*, 11827.

(19) Patel, A. N.; Tan, S. Y.; Miller, T. S.; Macpherson, J. V.; Unwin, P. R. *Anal. Chem.* **2013**, *85*, 11755.

(20) Lai, S. C. S.; Patel, A. N.; McKelvey, K.; Unwin, P. R. *Angew. Chem. Int. Ed.* **2012**, *51*, 5405.

(21) Anne, A.; Cambril, E.; Chovin, A.; Demaille, C.; Goyer, C. *ACS Nano* **2009**, *3*, 2927.

(22) Frederix, P. L.; Bosshart, P. D.; Akiyama, T.; Chami, M.; Gullo, M. R.; Blackstock, J. J.; Dooleweerdt, K.; de Rooij, N. F.; Staufer, U.; Engel, A. *Nanotechnology* **2008**, *19*, 384004.

(23) Wain, A. J.; Pollard, A. J.; Richter, C. *Anal. Chem.* **2014**, *86*, 5143.

(24) Lai, S. C. S.; Lazenby, R. A.; Kirkman, P. M.; Unwin, P. R. *Chem. Sci.* **2015**, *6*, 1126.

(25) Williams, C. G.; Edwards, M. A.; Colley, A. L.; Macpherson, J. V.; Unwin, P. R. *Anal. Chem.* **2009**, *81*, 2486.

(26) Cuharuc, A. S.; Zhang, G.; Unwin, P. R. *Phys. Chem. Chem. Phys.* **2016**, *18*, 4966.

(27) Niimi, Y.; Matsui, T.; Kambara, H.; Tagami, K.; Tsukada, M.; Fukuyama, H. *Phys. Rev. B* **2006**, *73*, 085421.

(28) Kobayashi, Y.; Fukui, K.-i.; Enoki, T.; Kusakabe, K.; Kaburagi, Y. *Phys. Rev. B* **2005**, *71*, 193406.

(29) Schmickler, W.; Santos, E. *Interfacial Electrochemistry*; 2 ed.; Springer-Verlag Berlin Heidelberg, 2010.

(30) Aaronson, B. D. B.; Chen, C.-H.; Li, H.; Koper, M. T. M.; Lai, S. C. S.; Unwin, P. R. *J. Am. Chem. Soc.* **2013**, *135*, 3873.

(31) Yang, H.-H.; McCreery, R. L. *Anal. Chem.* **1999**, *71*, 4081.

(32) Johnson, D. C.; Resnick, E. W. *Anal. Chem.* **1977**, *49*, 1918.

(33) Weber, J.; Samec, Z.; Mareček, V. *J. Electroanal. Chem.* **1978**, *89*, 271.

(34) Ebejer, N.; Guell, A. G.; Lai, S. C.; McKelvey, K.; Snowden, M. E.; Unwin, P. R. *Annu. Rev. Anal. Chem.* **2013**, *6*, 329.

(35) Ebejer, N.; Schnippering, M.; Colburn, A. W.; Edwards, M. A.; Unwin, P. R. *Anal. Chem.* **2010**, *82*, 9141.

(36) Li, Z.; Wang, Y.; Kozbial, A.; Shenoy, G.; Zhou, F.; McGinley, R.; Ireland, P.; Morganstein, B.; Kunkel, A.; Surwade, S. P.; Li, L.; Liu, H. *Nat. Mater.* **2013**, *12*, 925.

(37) McDermott, C. A.; Kneten, K. R.; McCreery, R. L. *J. Electrochem. Soc.* **1993**, *140*, 2593.

(38) Sutton, J. *Nature* **1952**, *169*, 71.

(39) Taylor, R. J.; Humffray, A. A. *J. Electroanal. Chem.* **1973**, *42*, 347.

(40) Zhang, G.; Walker, M.; Unwin, P. R. *Langmuir* **2016**, *32*, 7476.

(41) McDermott, M. T.; Kneten, K.; McCreery, R. L. *J. Phys. Chem.* **1992**, *96*, 3124.

(42) Angell, D. H.; Dickinson, T. *J. Electroanal. Chem.* **1972**, *35*, 55.

(43) Nioradze, N.; Chen, R.; Kurapati, N.; Khvataeva-Domanov, A.; Mabic, S.; Amemiya, S. *Anal. Chem.* **2015**, *87*, 4836.

(44) Li, Z.; Kozbial, A.; Nioradze, N.; Parobek, D.; Shenoy, G. J.; Salim, M.; Amemiya, S.; Li, L.; Liu, H. *ACS Nano* **2016**, *10*, 349.

(45) Kozbial, A.; Li, Z.; Sun, J.; Gong, X.; Zhou, F.; Wang, Y.; Xu, H.; Liu, H.; Li, L. *Carbon* **2014**, *74*, 218.

(46) Weissenborn, P. K.; Pugh, R. J. *J. Colloid Interface Sci.* **1996**, *184*, 550.

(47) Klarman, D.; Andelman, D.; Urbakh, M. *Langmuir* **2011**, *27*, 6031.

(48) Li, G.; Luican, A.; Andrei, E. Y. *Phys. Rev. Lett.* **2009**, *102*, 176804.

(49) Klingler, R. J.; Kochi, J. K. *J. Phys. Chem.* **1981**, *85*, 1731.

(50) A. J. Bard; Faulkner, L. R. *Electrochemical Methods: Fundamentals and Applications*; 2nd ed.; John Wiley& Sons, Inc.: New York, 2001.

(51) Snowden, M. E.; Güell, A. G.; Lai, S. C.; McKelvey, K.; Ebejer, N.; O'Connell, M. A.; Colburn, A. W.; Unwin, P. R. *Anal. Chem.* **2012**, *84*, 2483.

(52) Momotenko, D.; Byers, J. C.; McKelvey, K.; Kang, M.; Unwin, P. R. *ACS Nano* **2015**, *9*, 8942.

(53) Koestner, R.; Roiter, Y.; Kozhinova, I.; Minko, S. *J. Phys. Chem. C* **2011**, *115*, 16019.

Chapter 5 Molecular Functionalisation of Graphite Surfaces: Basal Plane vs Step Edge Electrochemical Activity

In this chapter, the electrochemistry of adsorbed electroactive AQDS has been studied on HOPG, from macroscale to nanoscale. From the macroscopic electrochemistry measurements, identical CVs have been obtained on HOPG surfaces of widely different quality (step edge density), indicating step edge density has no impact on the voltammetric responses. FSCV-SECCM measurements carried out on localised spots of HOPG in contact with meniscus for different times, allowed the adsorption process to be tracked on a very short time scale and complemented by AFM imaging on the same spots. There is no correlation between step edge density and electroactive AQDS surface coverage (orders of magnitude higher). SECCM reactive patterning shows uniform high activity across the basal surface. It is concluded that adsorbed electroactive AQDS cannot be used as a marker of step edges on HOPG and that the basal plane has intrinsically highly electroactivity.

5.1 Introduction

Carbon offers a broad range of electrode materials for electrochemistry and electroanalysis, and is particularly attractive where low background currents, a wide potential window, chemical inertness and biocompatibility are desired.[1-4] GC, boron doped diamond and graphite have long received attention for electroanalytical and electrocatalytic measurements,[5-11] and, more recently, carbon nanotubes and graphene have generated considerable interest.[12-17] However, despite well-defined bulk properties and structure, carbon materials can possess rather complex surface chemistry that may substantially impact the resulting electrochemistry.[6] Indeed, the range of functional groups present at different carbon electrode/electrolyte interfaces is yet to be fully understood[9] and is significantly impacted by electrode preparation.[18] Additionally, a range of surface chemical modifications of carbon materials are readily carried out.[19] Such protocols may provide a means of enhancing electrode performance, for example by improving resistance to fouling, promoting electrocatalysis, suppressing the response of competing interfering species, or creating selectivity towards particular analytes.[20-23]

Surface modifications have also been proposed as a route to measure the quality of carbon electrode surfaces.[24,25] In particular, it has been suggested that the adsorption of redox-active organic molecules, such as quinones, can be used as a measure of the percentage of electrochemically active step edge sites present on graphite.[26,27] Quinones adsorb spontaneously onto a range of surfaces,[28-31] including carbon,[32,33] and readily undergo a $2e^-$ and $2H^+$ reduction in acidic aqueous media.[31,34-36] Studies of basal plane graphite[32,33] are particularly pertinent, in light of the considerable recent revision of, and interest in, the local electrochemical activity of HOPG.[37-41]

Previous studies proposed that the step edge density on basal plane HOPG correlated with various electrochemical measurements in aqueous solution, specifically the double layer capacitance, the electron transfer kinetics for the redox couple ferri/ferrocyanide, and the surface coverage (Γ_{ads}) of adsorbed electroactive AQDS.[26,27,42] These studies found that cleaved HOPG surfaces

with greater step edge coverage tended to display higher Γ_{ads} for AQDS adsorption (at a particular bulk concentration). In turn, surfaces with higher Γ_{ads} also showed a higher standard rate constant, k_0, for ferri/ferrocyanide, and higher double layer capacitance. Hence, these easy to measure parameters became indirect proxies for determining the amount of step edge defects on an HOPG surface. However, the only attempt to correlate step edge density and Γ_{ads} focused on samples with a very narrow range of step densities (from 0.7% to 1.6%) with relatively high uncertainty in the absolute step edge density values.[26] Moreover, the ferri/ferrocyanide couple has since been shown to be problematic on the basal surface of graphite[41] and other surfaces.[43] These various issues, and further points outlined below, raise significant questions as to the validity of AQDS adsorption as a marker of step edge density and, more broadly, the veracity of older models of HOPG electrochemistry.

It is important to point out that the apparent correlation between the measured step edge coverage and AQDS adsorption required 30-times the step edge area than could be accounted for by the steps alone and it was thus proposed that there was a pronounced electronic disturbance at step edges extending 5 nm from step edges (on the top terrace of the step),[26] with no electrochemistry on any other part of the basal surface. This was despite the fact that AFM imaging later indicated extensive multilayer surface coverage (often associated with higher concentrations, due to intermolecular interactions), resulting in a film with a high density of pinholes on the surface.[44] It was thus concluded that AQDS adsorption took place indiscriminately on the basal and step edge sites but *only absorbed material at the step edges was electroactive*. However, recent scanning tunneling microscopy and spectroscopy studies have shown that the DOS is more or less uniform across HOPG, being enhanced only over *ca.* 1 nm of zigzag step edges,[45-47] with little enhancement at armchair step edges, which are the dominant edge sites on graphite.[46,47] In fact, there is negligible effect of step edges on the overall DOS at the HOPG basal surface if terraces with zigzag edges are wider than 10 nm.[45,48] The step spacing is much greater than this for the overwhelming majority of HOPG samples used for

electrochemistry, unless the surface was deliberately damaged by laser ablation.[27] This suggests that the macroscopic electrochemical measurements of basal plane HOPG should be independent of step edge density. This has been found recently for a diversity of electrochemical processes at HOPG surfaces with a wide range of step densities.[40,49,50] Moreover, microscopic and nanoscopic measurements have reported high intrinsic activity of the basal surface,[40,41,49,51-55] in contrast with the earlier literature, which proposed that the basal surface of HOPG was inert or largely inert.[56,57]

In this chapter, detailed investigations of the adsorption and electrochemistry of AQDS on HOPG are reported, with the particular goal of elucidating whether it is an appropriate measure for determining step edge density. More generally, this serves as an important model system to introduce new methodology for localised quantitative measurements of adsorption. To these ends we use macroscopic voltammetry to measure adsorbed electroactive AQDS on freshly cleaved HOPG with high precision. By using four different HOPG grades with step edge densities spanning a range of more than 2 orders of magnitude, and using different cleavage methods, we are able to precisely elucidate the influence of step edge density on fractional coverage of electroactive material, Θ_{ads} (defined as Γ_{ads}/Γ_O^*, where Γ_{ads} is the surface coverage and Γ_O^* is the theoretical maximum coverage). We find no correlation: Θ_{ads} *is independent of the grade of HOPG and cleavage method*. These key results are unequivocally confirmed with innovative fast scan cyclic voltammetry measurements using a new FSCV-SECCM platform in which we are able to track the evolution of adsorbed AQDS as a function of time, in microscopic patches of an HOPG surface and then directly measure the step edge density in the same area. The amount of adsorbed electroactive AQDS is orders of magnitude higher than would be expected if electroactivity was only confined to step edges (even over 5 nm regions of the steps),[26] indicating that most of the electroactivity comes from the graphite basal surface. Moreover, FSCV-SECCM measurements on HOPG of different quality (fractional coverage of steps) show similar responses, indicating that the electron transfer kinetics are in an adiabatic region.[58]

Finally, the high electoactivity of the basal surface is further confirmed through SECCM reactive patterning coupled with AFM imaging,[51] where we find high and uniform electrochemical fluxes across the basal surface of HOPG. Significantly, these studies show that the electrochemistry of adsorbed AQDS cannot be used to measure step edges on graphite surfaces, and add to an increasing recognition of the intrinsic electroactivity of the graphite basal surface.

5.2 Results and Discussion

5.2.1 Impact of HOPG Step Density on Adsorbed Electroactive AQDS

The level of AQDS adsorption from a 10 µM solution (0.1 M $HClO_4$) was first examined at the macroscale employing the O-ring arrangement (see Chapter 2), on all four grades of HOPG: AM, ZYA, SPI-1 and SPI-3, which vary greatly in surface quality, predominantly in terms of their step edge density (*vide infra*). These conditions and concentration of AQDS are analogous to those used previously in the assessment of HOPG quality (step edge density) by adsorption.[25,26] The adsorbed species undergo a two-electron reduction.

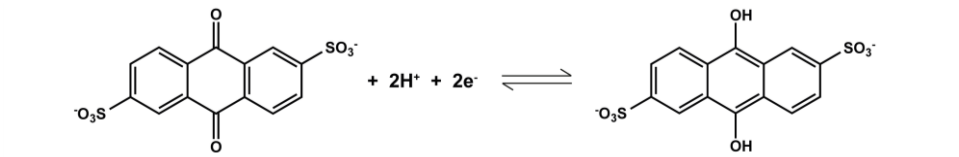

Anthraquinone-2,6-disulfonate (AQDS) Anthrahydroquinone-2,6-disulfonate (AHDS)

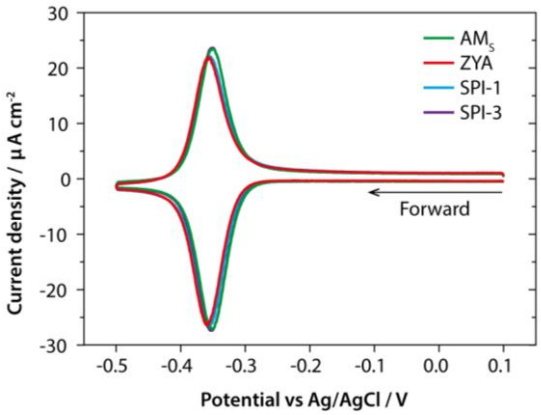

Figure 5.1 CVs (0.1 V s^{-1}) for the reduction of 10 µM AQDS in 0.1 M $HClO_4$ on four grades of freshly cleaved HOPG: AM_S (Scotch tape cleaved), ZYA, SPI-1 and SPI-3.

Figure 5.1 shows representative CVs (0.1 V s^{-1}) for the redox process of adsorbed AQDS on AM_S (green), ZYA (red), SPI-1 (blue) and SPI-3 (purple) grades of HOPG. For each HOPG sample, the CVs are characteristic of an adsorbed species, where the peak separation is nearly zero and the peak width at half-wave height is ~50 mV, close to the theoretical value of 90.6/*n* mV, where *n* is the number of electrons transferred per redox event (*i.e.* *n*=2), for a fast (reversible) process of a surface-bound electroactive species.[59] The adsorbed AQDS surface coverage, Γ_{ads}, was calculated for each sample, as done in previous studies,[25,26,34,44] using the charge associated with the reduction wave, obtained via peak integration. Γ_{ads} values were converted to fractional (or percentage) surface coverage values (Θ_{ads}) using a molecular area of 126 $Å^2$ for AQDS (assuming a flat orientation of the molecule on the surface).[26] Note that, for all HOPG samples, we investigated the timeframe over which the maximum AQDS surface coverage was achieved. CVs recorded within *ca.* 10 s of addition of AQDS solution were the same as those for more extensive periods (of up to 1 hour), from which it was concluded that the limit of AQDS adsorption for this concentration must occur within the 10 s timeframe of the initial CV.

The mean values of Θ_{ads} obtained for each grade of HOPG, along with corresponding standard deviation, are shown in Figure 5.2a. For 7 repeat measurements on the surfaces of each grade of HOPG, freshly prepared, the following Θ_{ads} were obtained: 29.7 ± 1.6% for AM_S; 29.6 ± 2.4% for AM_M; 29.4 ± 1.2% for ZYA grade; 27.5 ± 1.4% for SPI-1 grade; and 28.0 ± 0.6% for SPI-3 grade HOPG. It is clear that all four grades of HOPG show nearly identical Θ_{ads} values, which are in very close agreement with previous studies that employed high quality AM grade HOPG.[26] It is also evident that the fractional surface coverage is not affected by the cleaving method (for AM grade). AFM analysis of the step edge coverage for all four grades of HOPG is presented in Figure 5.2b, highlighting the significant difference in step edge density for the samples. As reported recently,[40,41,49] AM HOPG (with little noticeable difference between Scotch tape and mechanical cleavage) provides the most pristine surface, with the step edge coverage ranging between 0.006–0.48% (mean 0.09%), followed by ZYA (range of

0.03–1%, mean 0.3%) and SPI-1 (range of 0.5–3.4%, mean 1.8%), with SPI-3 showing the highest percentage coverage (range of 10–78%, mean 31%), as summarised in Figure 5.2c. These HOPG samples display increasing step edge density in the order AM, ZYA, SPI-1 and SPI-3, among which the density varies by ~2 orders of magnitude from the highest quality HOPG (AM) to the lowest quality one (SPI-3). Furthermore, AM and ZYA samples predominantly reveal monolayer and bilayer steps, whereas SPI-1 and SPI-3 show a wide range of step heights with a high proportion of multilayer steps.[40] If the adsorption of AQDS, or indeed its electroactive response was to be confined only to the step edges, as proposed,[26,27,44] the resulting surface coverages should show a massive difference among the samples investigated. Instead, the Θ_{ads} values for the different grades of HOPG in Figure 5.2a show negligible variation, strongly indicating the Θ_{ads} for AQDS is independent of step edge density and dominated by the basal surface. Thus, the electrochemistry of adsorbed AQDS at HOPG is analogous to that seen recently for other reactions: it is dominated by the basal surface.[37,40,41,49-55]

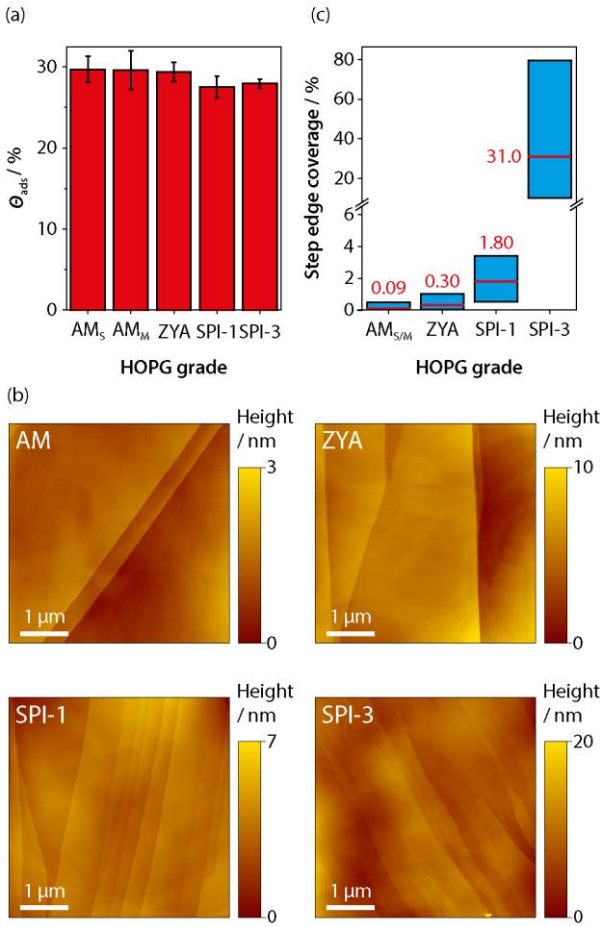

Figure 5.2 (a) The fractional surface coverages (Θ_{ads}) of AQDS (from 10 µM in bulk solution) in 0.1 M $HClO_4$, from voltammetry at 0.1 V s^{-1}, on different grades of freshly cleaved HOPG: AM_S (Scotch tape cleaved); AM_M (mechanically cleaved); ZYA; SPI-1; and SPI-3. Error bars correspond to one standard deviation of 7 measurements on each HOPG grade. (b) AFM images of AM, ZYA, SPI-1 and SPI-3 HOPG samples. (c) Range of step edge coverage on four different grades of basal plane HOPG: AM (AM_S and AM_M); ZYA; SPI-1; SPI-3 (data from Refs. [40] and [49]). The mean value for each data set is marked in red.

5.2.2 Time-resolved Adsorption Measurements: Structure-Activity Analysis

SECCM allows electrochemical measurements to be performed almost immediately after meniscus contact with the surface.[60] Coupled with the analysis of surface-bound redox species via FSCV, this allowed relatively fast adsorption to be followed in real-time. Moreover, by confining the electrochemical cell to the several micron scale, via the meniscus footprint,

further detailed *ex-situ* topographical analysis could be performed on the *entire area of interest* probed in the electrochemical measurement. This approach allowed a *direct and complete assessment* of the impact of surface properties (notably step edge density) on the electrochemical characteristics in the region of interest. A further attribute of the SECCM setup is that multiple experiments can be performed,[61] each on a fresh, pristine area of the substrate. As such, this provides a powerful platform to thoroughly investigate the process of adsorption at surfaces, and is particularly relevant to the present application where the rate of accumulation of redox-active species at the HOPG surface, and its dependence on step edge density, are of paramount importance.

In the FSCV-SECCM configuration, adsorption began immediately upon contact of the confined solution of AQDS, during a pre-determined *hold time* of the meniscus on the HOPG surface. A CV was then performed at 100 V s^{-1}, in which the surface current (i_{act}) was recorded against substrate potential (E_{surf}), to quantify the level of adsorption after the respective *hold time*. Upon completion of the FSCV measurement, the same *hold time* was applied, during which further adsorption occurred, before performing a second FSCV, as illustrated in Figure 5.3a. This process was repeated a total of 10 times, providing information on the evolution of the level of AQDS adsorption with time at a small area of the surface, confined by the tip (~18 μm in diameter, Figure 5.3b). This experiment was performed for a variety of *hold times* (see the experimental section in Chapter 2) with each carried out at a fresh area of HOPG. The use of a high scan rate during FSCV means that the analysis time (18 ms, defined by the potential scan limits and scan rate) was relatively negligible in comparison to the *hold time* during which adsorption occurred (Figure 5.3c), although it is included in the evaluation of the overall adsorption-time curves that are presented below.

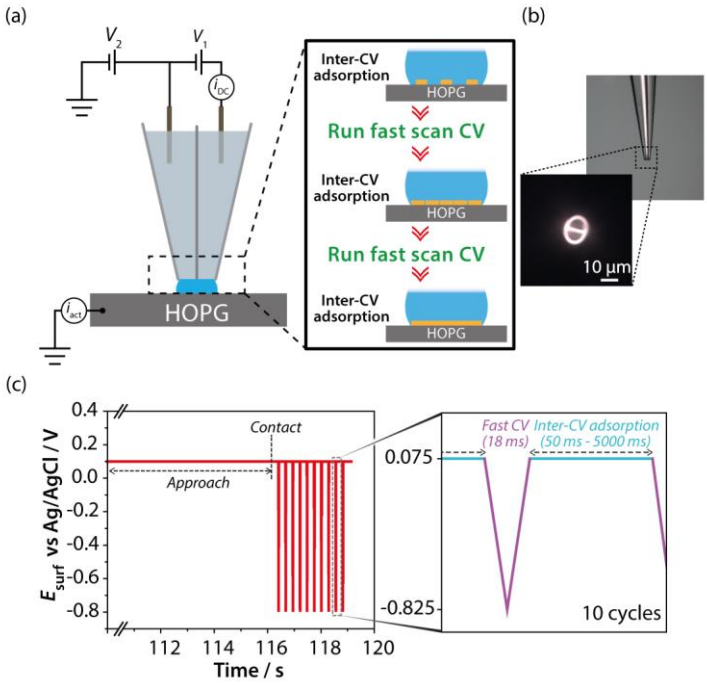

Figure 5.3 (a) Schematic depicting the process for measuring adsorption on HOPG surfaces via FSCV-SECCM (see text for details). (b) An optical microscope image of a typical tip used in this study, with a diameter of ~18 µm. (c) The potential waveform applied to the substrate during pipette approach and upon meniscus contact, with a zoom showing the potential cycle (repeated 10 times) during adsorption and the FSCV analysis.

A typical example of the voltammograms obtained using the FSCV-SECCM configuration is shown in Figure 5.4a, where a total of 10 FSCVs were recorded at 250 ms intervals (*i.e.* a 250 ms *hold time*) at a single position on the surface. It can be seen that the peak current (i_p) values for the oxidation and reduction waves, corresponding to adsorbed AQDS, increase greatly for the first several FSCVs, and then gradually tend to a limiting value with further time. In contrast to the macroscopic measurements (Figure 5.1), the much higher scan rate employed in FSCV-SECCM leads to a large peak-to-peak separation of the potentials of the oxidation and reduction processes, indicating kinetic influence. This does not affect the evaluation of surface coverage from the integration of the charge under these peaks, but opens up interesting possibilities for investigating the impact of step density on kinetics which we explore briefly below.

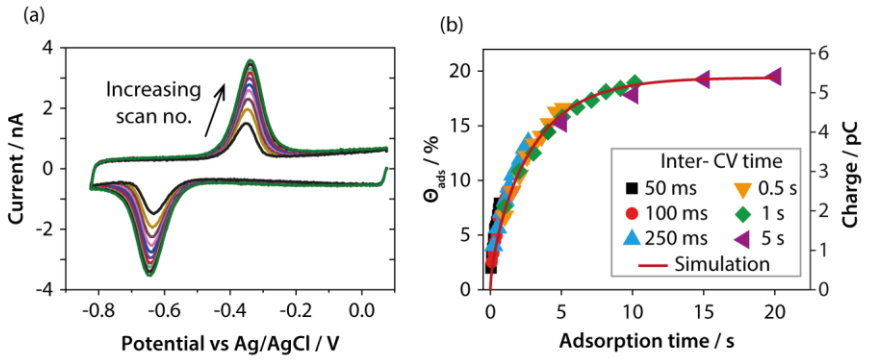

Figure 5.4 (a) FSCVs (10 in total) for the adsorption of 1 µM AQDS in 0.05 M $HClO_4$, recorded at 250 ms intervals with a scan rate of 100 V s^{-1}, at AM grade HOPG. (b) The observed fractional surface coverage of AQDS calculated from the FSCVs (charge) recorded in different parts of an AM HOPG surface at adsorption time intervals of: 50 ms, 100 ms, 250 ms, 0.5 s, 1 s and 5 s, on AM HOPG. Solid line is the simulated behaviour for diffusion-controlled adsorption, with an adsorption constant of 2.4×10^8 cm^3 mol^{-1}.

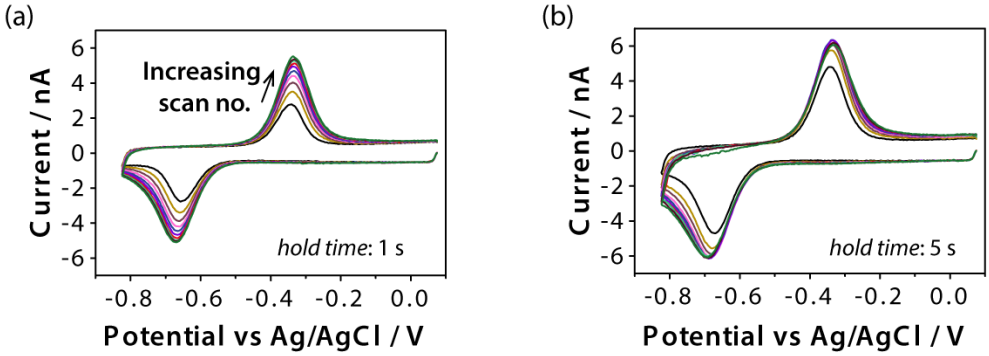

Figure 5.5 FSCVs of 1 µM AQDS (0.05 M $HClO_4$) on two different areas of freshly cleaved AM HOPG, each cycled 10 times at a scan rate of 100 V s^{-1} and recorded at time intervals of: (a) 1 s and (b) 5 s, respectively.

As was done for the macroscale experiments, Θ_{ads} was calculated for each recorded FSCV (FSCVs recorded at 1 s and 5 s time intervals are provided in Figure 5.5). Figure 5.4b shows Θ_{ads} measured from FSCVs in six regions of the surface against the adsorption time. The significant reproducibility across the wide range of investigated *hold times* is evident, with a sharp change in the amount of adsorbed AQDS over the first 6 s, which then slowly

reaches a maximum value at *ca.* 10 s. FEM simulation work was done in order to gain a further understanding of the timescale of the adsorption process. The adsorption process was found to be essentially diffusion-controlled, with an equilibrium adsorption constant of 2.4×10^8 cm^3 mol^{-1}.

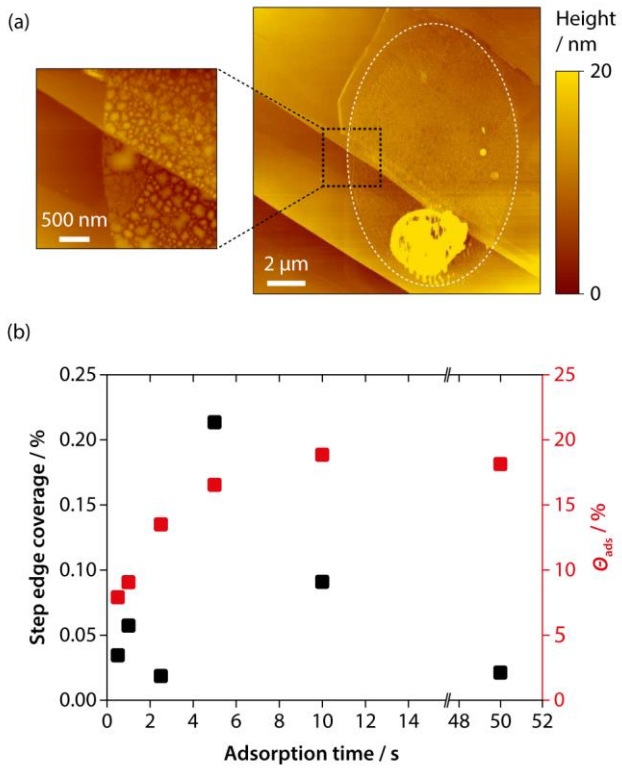

Figure 5.6 (a) Typical AFM image for the analysis of FSCV adsorption spots on the AM grade HOPG surface taken after a total adsorption time *ca.* 10 s, with a 3 × 3 µm higher resolution image of the framed area. The approximate droplet footprint is outlined in white. (b) The percentage of step edges found within 6 adsorption spots where FSCV measurements were made and the observed fractional coverage of electroactive AQDS calculated from the charge at different adsorption times.

Subsequent AFM imaging of the *entire area* covered by each of the FSCV measurements was carried out to allow for a direct comparison between the measured Θ_{ads} and the *actual step edge density*. A typical 15 × 15 µm AFM analysis of an adsorption region after FSCV measurements is shown in Figure 5.6a, where the total adsorption time was *ca.* 10 s (1 s *hold time* × 10 FSCVs) and the Θ_{ads} was measured as ~19%. The AFM image shows adsorption to have occurred over the majority of the working area for which

the step edge coverage was *ca.* 0.091% (expressed as a percentage of the geometric area if the surface was all basal); see also the 3 × 3 μm higher resolution AFM image. Note that the AFM image shows a small spot where a large amount of material is left, which can be attributed to the evaporation of residual solution left behind after retracting the pipette. The important point here is that AFM reveals the precise quantity of step edges compared to basal surface in the area of the experiment.

A comparison of AFM analysis of step edge density and electroactive adsorbed AQDS (expressed as Θ_{ads}) at different *hold times* and hence different total adsorption times, is summarised in Figure 5.6b. Strikingly, this shows that there is no correlation between step edge density and the level of AQDS adsorption, consistent with macroscopic data presented above (Figure 5.2). If step edges were the only sites of electroactivity, then in the case of the adsorption after 50 s, where the step edge density is 0.021%, even taking into account possible electronic disorder and partial charges extending up to 5 nm from a step,[26] this would only give a coverage of 0.066%, which is orders of magnitude below the measured Θ_{ads} (*ca.* 20%). In fact, in all cases in Figure 5.6b, the observed coverage of electroactive AQDS is orders of magnitude higher than would be expected if there was only electrochemistry of adsorbed AQDS at step edges.

For comparison with the AM sample, further measurements of the adsorption of AQDS at an SPI-3 surface were carried out (Figure 5.7). These yielded a fractional coverage of ~19% at adsorption equilibrium, very close to the value obtained on AM grade HOPG, further supporting the data obtained from macroscale studies (*vide supra*). Interestingly, the peak-to-peak separation, ΔE_p, (at 100 V s^{-1}) was 344 ± 1 mV (n=5), closely similar to the value at the AM surface, 341 ± 1 mV (n=5). Since these two substrates differ in step edge density by more than 2 orders of magnitude, and the SPI-3 grade HOPG has step edge coverage in the range 10–78%, mean 31% (Figure 5.2), this indicates clearly that step edges do not influence the reaction kinetics. Furthermore, since the overall DOS on SPI-3 grade HOPG would reasonably be expected to be higher than for AM grade, due to the enhanced DOS at

zigzag edges,[45-47] the similarity of the peak-to-peak separation in the FSCV responses for the two HOPG materials suggests that the electroreduction of adsorbed AQDS at HOPG is likely in the adiabatic regime.[58]

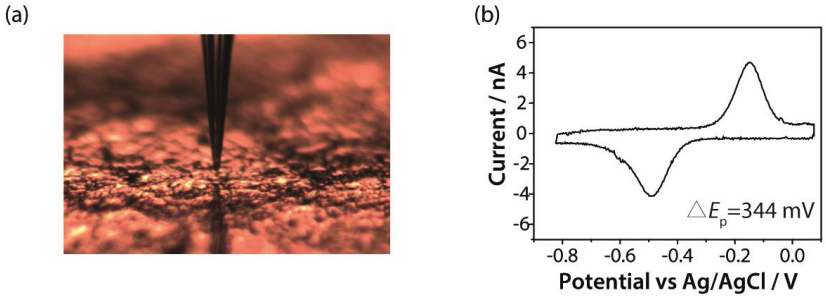

Figure 5.7 (a) Optical image of the surface of freshly cleaved SPI-3 HOPG with an SECCM tip positioned closely above. (b) Typical FSCV of 1 µM AQDS (0.05 M $HClO_4$) on freshly cleaved SPI-3 HOPG, at a scan rate of 100 V s^{-1}, after a long (10 s) *hold time* to achieve equilibrium adsorption, with a tip of ~16 µm in diameter.

5.2.3 SECCM Reactive Patterning

To further examine the sites of AQDS electroactivity on the HOPG surface, SECCM line-patterning[49,51] was carried out to map the electrochemical reaction at high spatial resolution and to use the adsorbed AQDS (and the product of the electrochemical reduction) as a place marker for the location of the electrochemical response. As described in the experimental section in Chapter 2, a much higher concentration of AQDS (100 µM) was used, so that we essentially measured the diffusional flux of reactive AQDS.

Reactive patterning was carried out with an effective surface potential of -0.4 V (-(V_2 + ½V_1)) vs Ag/AgCl, to drive the electrochemical reduction of AQDS, and the line pattern was designed to create a square-spiral line-pattern that could be easily recognised and analysed by a range of complementary techniques. SECCM maps are presented in Figure 5.8 showing: (a) surface activity (current) and (b) DC conductance current (between the SECCM barrels, which informs on the stability of the meniscus during scanning).[62,63] The spiral pattern, which started in the center, is evident. The SECCM surface activity map shows constant and continuous current values (i_{act}),

around -3.25 (± 0.1) pA. Given the size of the meniscus, diameter of 350 nm, which can be estimated from the deposited line width obtained from Figure 5.8f, this corresponds to a flux of *ca.* 10^{-8} mol cm^{-2} s^{-1}, corresponding to a mass transport coefficient of *ca.* 0.1 cm s^{-1}, of the magnitude expected in SECCM for a pure diffusion-limited process.[41,64] A histogram showing the spread of surface activity (Figure 5.8c) for the >40,000 current measurements collected is less than 10%, indicating more or less uniform electroactivity of AQDS throughout the adsorption patterning. Figure 5.8d shows a histogram of i_{DC} values, and the small spread (<3%) highlights the stability of the SECCM meniscus during imaging (also see Figure 5.9). The deposit formed during the patterning can be seen in the electron micrograph in Figure 5.8e, a section of which is shown in the AFM image in Figure 5.8f. It is clear that the electrochemical reactivity data, described above, relates mainly to the basal surface, given the low step density of the AM HOPG surface.[40]

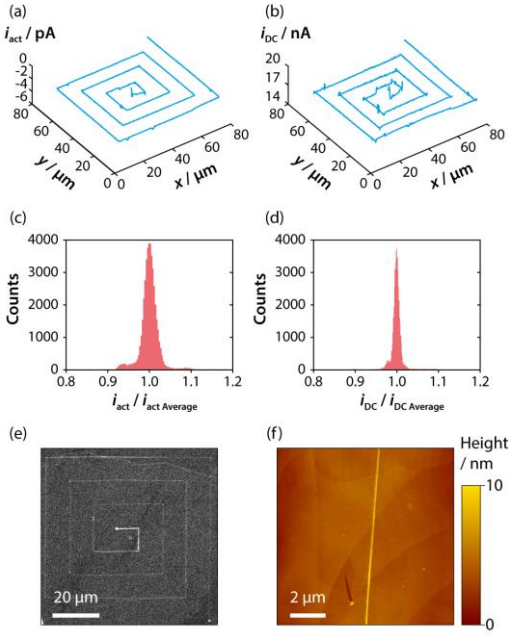

Figure 5.8 SECCM maps of: (a) surface activity (i_{act}) and (b) DC component of conductance current (i_{DC}) for the diffusion-limited reduction of 100 µM AQDS in 0.1 M $HClO_4$ during reactive line-patterning on AM HOPG, at a scan speed of 1 µm s^{-1}. Corresponding histograms of the spread of currents are shown in (c) and (d), respectively. (e) FE-SEM image showing the deposited AQDS line pattern. (f) AFM image of part of the pattern.

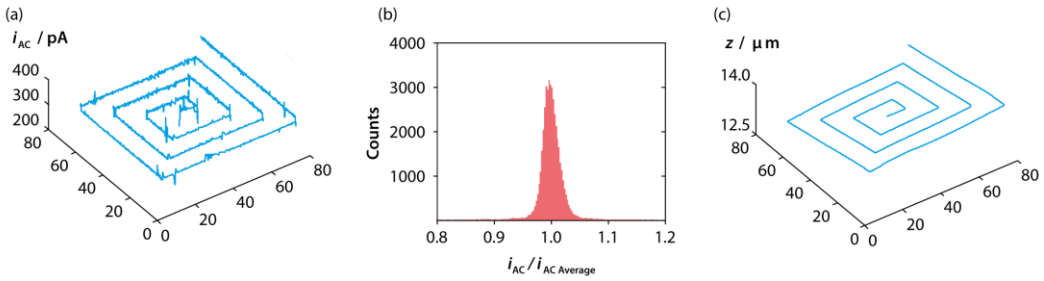

Figure 5.9 Complementary SECCM data to that in Figure 5.8. (a) AC component of conductance current (i_{AC}) used as feedback set point; (b) corresponding histogram showing uniformity of i_{AC}. (c) SECCM surface topography.

Further AFM characterisation is shown in Figure 5.10a, which is a 3.3 × 3.3 µm AFM image of a section of the line-pattern in which the line of adsorbed material travels from a basal terrace over a step edge and onto another basal terrace. The corresponding SECCM maps of: (b) surface activity; (c) DC conductance current and (d) AC feedback current for the same area show that all the currents recorded are stable, and that the electrochemical response is dominated by the basal surface rather than step edges, indicating uniform activity across this area on the spatial resolution of SECCM.

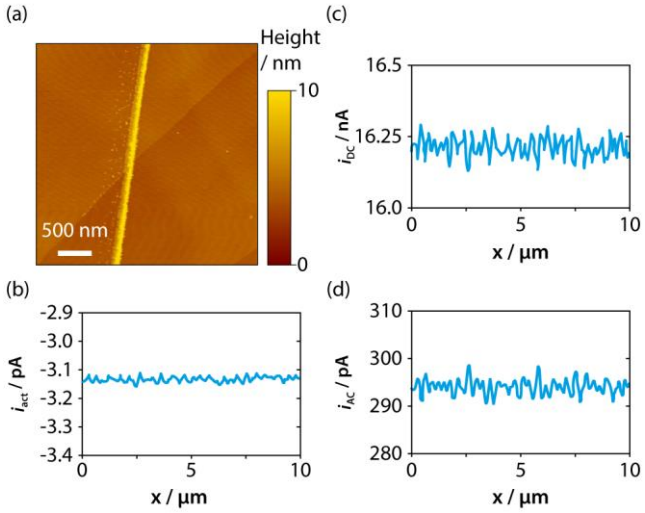

Figure 5.10 (a) AFM image showing a section of the SECCM line pattern, along with the corresponding SECCM profiles *along the same line* for: (b) surface activity (i_{act}); (c) DC component of conductance current (i_{DC}) and (d) AC component of conductance current (i_{AC}), used as a feedback set point.

5.3 Conclusions

A new approach for functionalising and probing the activity of electrode surfaces has been developed, combining the merits of SECCM for high spatial resolution measurements with FSCV to enhance the timescale at which localised surface processes can be probed. These microscale FSCV measurements have allowed the adsorption of AQDS at HOPG to be followed in real time, and for the relative kinetics of electron transfer to be compared on different HOPG grades (differing in step edge density by more than 2 orders of magnitude). The adsorption process has been found to be diffusion-controlled and there is no influence of step edges on the adsorption process or electron transfer kinetics. Importantly, this localised approach allowed direct investigation of surface structure in the region of AQDS adsorption, through AFM imaging of the *entire working area* in which the FSCV measurements were performed. These studies show unambiguously that the rate and amount of AQDS adsorption on HOPG surfaces is independent of the step edge density, and dominated by the basal surface. Moreover, the observed coverage of AQDS is orders of magnitude higher than can be accounted for if only AQDS at steps was electrochemically active, which has been a longstanding and widely held view.[38,44] No evidence was found that could indicate preferential electrochemistry of adsorbed AQDS at or around step sites, even taking into account possible electronic disorder (generously) extending up to 5 nm from the step edges.[26] SECCM reactive line-patterning was employed to further show that AQDS readily undergoes diffusion-controlled reduction at the basal surface of HOPG, highlighting the high activity of the basal surface.

The data presented herein demonstrate indisputably that AQDS adsorption is not an indicator of step edges present on graphitic surfaces and that there is no correlation between electroactive adsorbed AQDS and step edge coverage. This deduction has been made via a variety of techniques on a range of length scales, from macroscale to nanoscale, with high consistency. Macroscale voltammetry, carried out on a range of surfaces varying greatly in step edge density by ~2 orders of magnitude, supports the microscale

measurements by showing the observed AQDS adsorption to be independent of the step edge density.

The electrochemical activity of HOPG has recently undergone considerable revision. Considered (largely) inert for a long period, various nano/microscale[40,41,49,51-55] and macroscopic studies[37,40,49,50] have shown the HOPG basal plane to support reasonably fast electron transfer for a wide range of reactions. The studies in this chapter are not only important in expanding the range of electrochemical systems that are shown to be facile on the basal surface, but also because AQDS adsorption has been proposed[26,27] and widely used[25,38,44] as a means of characterising step edge density, as discussed above. Evidently this older model, and studies which have used it, require major reconsideration.

5.4 References

(1) Ueda, A.; Kato, D.; Kurita, R.; Kamata, T.; Inokuchi, H.; Umemura, S.; Hirono, S.; Niwa, O. *J. Am. Chem. Soc.* **2011**, *133*, 4840.

(2) Güell, A. G.; Meadows, K. E.; Unwin, P. R.; Macpherson, J. V. *Phys. Chem. Chem. Phys.* **2010**, *12*, 10108.

(3) Zhang, L. L.; Zhao, X. S. *Chem. Soc. Rev.* **2009**, *38*, 2520.

(4) Zhou, M.; Zhai, Y.; Dong, S. *Anal. Chem.* **2009**, *81*, 5603.

(5) Pinczewska, A.; Sosna, M.; Bloodworth, S.; Kilburn, J. D.; Bartlett, P. N. *J. Am. Chem. Soc.* **2012**, *134*, 18022.

(6) Wu, Z.; Lv, Y.; Xia, Y.; Webley, P. A.; Zhao, D. *J. Am. Chem. Soc.* **2011**, *134*, 2236.

(7) Singh, Y. S.; Sawarynski, L. E.; Michael, H. M.; Ferrell, R. E.; Murphey-Corb, M. A.; Swain, G. M.; Patel, B. A.; Andrews, A. M. *ACS Chem. Neurosci.* **2010**, *1*, 49.

(8) Patten, H. V.; Lai, S. C. S.; Macpherson, J. V.; Unwin, P. R. *Anal. Chem.* **2012**, *84*, 5427.

(9) McCreery, R. L. *Chem. Rev.* **2008**, *108*, 2646.

(10) Jouikov, V.; Simonet, J. *Langmuir* **2012**, *28*, 931.

(11) Surendranath, Y.; Lutterman, D. A.; Liu, Y.; Nocera, D. G. *J. Am. Chem. Soc.* **2012**, *134*, 6326.

(12) Li, W.; Tan, C.; Lowe, M. A.; Abruña, H. D.; Ralph, D. C. *ACS Nano* **2011**, *5*, 2264.

(13) Güell, A. G.; Ebejer, N.; Snowden, M. E.; Macpherson, J. V.; Unwin, P. R. *J. Am. Chem. Soc.* **2012**, *134*, 7258.

(14) Rodríguez-López, J.; Ritzert, N. L.; Mann, J. A.; Tan, C.; Dichtel, W. R.; Abruña, H. D. *J. Am. Chem. Soc.* **2012**, *134*, 6224.

(15) Yang, W.; Ratinac, K. R.; Ringer, S. P.; Thordarson, P.; Gooding, J. J.; Braet, F. *Angew. Chem. Int. Ed.* **2010**, *49*, 2114.

(16) Lai, S. C. S.; Dudin, P. V.; Macpherson, J. V.; Unwin, P. R. *J. Am. Chem. Soc.* **2011**, *133*, 10744.

(17) Park, J.; Deria, P.; Therien, M. J. *J. Am. Chem. Soc.* **2011**, *133*, 17156.

(18) McCreery, R. L. *Electroanalytical Chemistry*; Dekker: NY, 1991; Vol. 17.

(19) Sundaram, R. S.; Gómez-Navarro, C.; Balasubramanian, K.; Burghard, M.; Kern, K. *Adv. Mater.* **2008**, *20*, 3050.

(20) Hutton, L.; Newton, M. E.; Unwin, P. R.; Macpherson, J. V. *Anal. Chem.* **2009**, *81*, 1023.

(21) Kutner, W.; Wang, J.; L'her, M.; Buck, R. P. *Pure Appl. Chem.* **1998**, *70*, 1301.

(22) Bahr, J. L.; Yang, J.; Kosynkin, D. V.; Bronikowski, M. J.; Smalley, R. E.; Tour, J. M. *J. Am. Chem. Soc.* **2001**, *123*, 6536.

(23) Safavi, A.; Maleki, N.; Moradlou, O.; Tajabadi, F. *Anal. Biochem.* **2006**, *359*, 224.

(24) McCreery, R. L.; Cline, K. K.; McDermott, C. A.; McDermott, M. T. *Colloids Surf. A* **1994**, *93*, 211.

(25) Xu, J.; Chen, Q.; Swain, G. M. *Anal. Chem.* **1998**, *70*, 3146.

(26) McDermott, M. T.; McCreery, R. L. *Langmuir* **1994**, *10*, 4307.

(27) McDermott, M. T.; Kneten, K.; McCreery, R. L. *J. Phys. Chem.* **1992**, *96*, 3124.

(28) Han, S. W.; Joo, S. W.; Ha, T. H.; Kim, Y.; Kim, K. *J. Phys. Chem. B* **2000**, *104*, 11987.

(29) Soriaga, M. P.; Hubbard, A. T. *J. Am. Chem. Soc.* **1982**, *104*, 2735.

(30) He, P.; Crooks, R. M.; Faulkner, L. R. *J. Phys. Chem.* **1990**, *94*, 1135.

(31) Liu, Y.; Freund, M. S. *Langmuir* **2000**, *16*, 283.

(32) Kano, K.; Uno, B. *Anal. Chem.* **1993**, *65*, 1088.

(33) Zhang, J.; Anson, F. C. *J. Electroanal. Chem.* **1992**, *331*, 945.

(34) Forster, R. J. *Langmuir* **1995**, *11*, 2247.

(35) Forster, R. J. *Anal. Chem.* **1996**, *68*, 3143.

(36) Guin, P. S.; Das, S.; Mandal, P. C. *Int. J. Electrochem.* **2011**, *2011*, 1.

(37) Edwards, M. A.; Bertoncello, P.; Unwin, P. R. *J. Phys. Chem. C* **2009**, *113*, 9218.

(38) McCreery, R. L.; McDermott, M. T. *Anal. Chem.* **2012**, *84*, 2602.

(39) Lee, C.-Y.; Guo, S.-X.; Bond, A. M.; Oldham, K. B. *J. Electroanal. Chem.* **2008**, *615*, 1.

(40) Patel, A. N.; Collignon, M. G.; O'Connell, M. A.; Hung, W. O.; McKelvey, K.; Macpherson, J. V.; Unwin, P. R. *J. Am. Chem. Soc.* **2012**, *134*, 20117.

(41) Lai, S. C. S.; Patel, A. N.; McKelvey, K.; Unwin, P. R. *Angew. Chem. Int. Ed.* **2012**, *51*, 5405.

(42) Robinson, R. S.; Sternitzke, K.; Mcdermott, M. T.; Mccreery, R. L. *J. Electrochem. Soc.* **1991**, *138*, 2412.

(43) Pharr, C. M.; Griffiths, P. R. *Anal. Chem.* **1997**, *69*, 4673.

(44) Ta, T. C.; Kanda, V.; McDermott, M. T. *J. Phys. Chem. B* **1999**, *103*, 1295.

(45) Niimi, Y.; Matsui, T.; Kambara, H.; Tagami, K.; Tsukada, M.; Fukuyama, H. *Phys. Rev. B* **2006**, *73*, 085421.

(46) Kobayashi, Y.; Fukui, K.-i.; Enoki, T.; Kusakabe, K. *Phys. Rev. B* **2006**, *73*, 125415.

(47) Kobayashi, Y.; Kusakabe, K.; Fukui, K.-i.; Enoki, T. *Physica E* **2006**, *34*, 678.

(48) Nakada, K.; Fujita, M.; Dresselhaus, G.; Dresselhaus, M. S. *Phys. Rev. B* **1996**, *54*, 17954.

(49) Patel, A. N.; Tan, S. Y.; Unwin, P. R. *Chem. Commun.* **2013**, *49*, 8776.

(50) Patel, A. N.; Tan, S. Y.; Miller, T. S.; Macpherson, J. V.; Unwin, P. R. *Anal. Chem.* **2013**, *85*, 11755.

(51) Patel, A. N.; McKelvey, K.; Unwin, P. R. *J. Am. Chem. Soc.* **2012**, *134*, 20246.

(52) Lhenry, S.; Leroux, Y. R.; Hapiot, P. *Anal. Chem.* **2012**, *84*, 7518.

(53) Williams, C. G.; Edwards, M. A.; Colley, A. L.; Macpherson, J. V.; Unwin, P. R. *Anal. Chem.* **2009**, *81*, 2486.

(54) Anne, A.; Cambril, E.; Chovin, A.; Demaille, C.; Goyer, C. *ACS Nano* **2009**, *3*, 2927.

(55) Frederix, P. L.; Bosshart, P. D.; Akiyama, T.; Chami, M.; Gullo, M. R.; Blackstock, J. J.; Dooleweerdt, K.; de Rooij, N. F.; Staufer, U.; Engel, A. *Nanotechnology* **2008**, *19*, 384004.

(56) Davies, T. J.; Hyde, M. E.; Compton, R. G. *Angew. Chem. Int. Ed.* **2005**, *44*, 5121.

(57) Kneten, K. R.; McCreery, R. L. *Anal. Chem.* **1992**, *64*, 2518.

(58) Chen, S.; Liu, Y.; Chen, J. *Chem. Soc. Rev.* **2014**, *43*, 5372.

(59) A. J. Bard; Faulkner, L. R. *Electrochemical Methods: Fundamentals and Applications*; 2nd ed.; John Wiley& Sons, Inc.: New York, 2001.

(60) Kinnear, S. L.; McKelvey, K.; Snowden, M. E.; Peruffo, M.; Colburn, A. W.; Unwin, P. R. *Langmuir* **2013**, *29*, 15565.

(61) Kirkman, P. M.; Güell, A. G.; Cuharuc, A. S.; Unwin, P. R. *J. Am. Chem. Soc.* **2014**, *136*, 36.

(62) Güell, A. G.; Ebejer, N.; Snowden, M. E.; McKelvey, K.; Macpherson, J. V.; Unwin, P. R. *Proc. Natl. Acad. Sci. U. S. A.* **2012**, *109*, 11487.

(63) Ebejer, N.; Guell, A. G.; Lai, S. C.; McKelvey, K.; Snowden, M. E.; Unwin, P. R. *Annu. Rev. Anal. Chem.* **2013**, *6*, 329.

(64) Snowden, M. E.; Güell, A. G.; Lai, S. C.; McKelvey, K.; Ebejer, N.; O'Connell, M. A.; Colburn, A. W.; Unwin, P. R. *Anal. Chem.* **2012**, *84*, 2483.

Chapter 6 Versatile Polymer-Free Graphene Transfer Method and Applications

This chapter presents a new methodology for CVD graphene transfer. By using an organic-aqueous interface, transfer of graphene on arbitrary substrates is facilitated, generating graphene-coated tools for conductive-AFM and high resolution TEM measurements, while polymeric contamination is avoided. Furthermore, supported and suspended graphene can be readily studied with SECCM using the same sample of graphene TEM grid, opening up new avenues for studying the physical (e.g. wetting) and electrochemical properties of graphene.

6.1 Introduction

Since its discovery in 2004,[1] the outstanding electrical,[2,3] mechanical[4,5] and chemical[6,7] properties of graphene have been revealed, highlighting it as a hugely promising material for the future. The production of pristine graphene flakes was initially achieved through a (Scotch-tape based) mechanical exfoliation[1] method. However, with this time-consuming approach typically yielding micron-sized flakes, it is considered unrealistic for scale up applications, where much larger areas of graphene are needed.[8,9]

Recently, CVD has shown considerable promise for the synthesis of large-scale (with sheets of 30 inches in size reported[10]), high-quality graphene.[11-13] Among the metals used to catalyse the CVD growth of graphene, Cu is the most popular, producing mostly monolayer graphene.[14] However, depending on the application, an effective methodology for the subsequent transfer of such films to substrates of interest is still required.[15] This is far from easy, especially when a large, continuous sheet is desired, or 3D structures are to be covered. Polymer support routes have been extensively employed for such transfer, in which a thin layer of polymer is deposited as a new support (template) on the as-grown (metal-supported) graphene, to allow the removal of the metallic substrate by wet etching or electrochemical delamination, ultimately producing a polymer-supported graphene film.[16,17] PMMA,[18] PDMS[19] and polycarbonate[20] layers (among others) are reported as suitable templates for the transfer of graphene onto a wide variety of planar/flat substrates, with the polymer subsequently removed through dissolution with organic solvents. Despite intensive research into such methods, the resulting graphene surfaces commonly appear littered with stubborn polymer residues,[21,22] which may have a detrimental effect on subsequent applications, including the electronic and electrochemical performance of graphene.[23,24] Consequently, alternative routes of transfer are being sought, with polymer-free methods recently emerging as a fresh and promising way for clean graphene transfer.[25,26]

Herein, we introduce a polymer-free biphasic (liquid/liquid) approach for the transfer of monolayer CVD graphene to a wide range of target substrates. Our approach makes use of an inert non-polar and low viscosity liquid organic layer (hexane) lying on top of an aqueous etchant layer ($(NH_4)_2S_2O_8$), to stabilise and protect the freestanding graphene sheet that is produced during the Cu wet etching and water rinsing processes. Essentially, the hexane layer replaces the deposited polymer layers used in the majority of current graphene transfer methods (*vide supra*), ensuring the freestanding graphene produced after etching of the growth substrate is not torn apart by the surface tension associated with the aqueous etchant solution. Crucially, the lack of heteroatoms and aromatic groups in hexane, as well as its volatility and rapid evaporation, ensures that no residues are left on the graphene surface and that there is no doping after transfer to the desired substrate. Note that, although an organic/water interface was recently used to decorate CVD graphene films with nanoparticles, the process used still relied on polymer coating and removal.[27]

Additionally, we demonstrate the feasibility and versatility of our approach for coating graphene onto coarse surfaces and 3D structures, due to the gentleness of the polymer-free transfer method. Beyond flat substrates (*e.g.* Si/SiO_2), monolayer graphene membranes have been transferred to more topographically challenging substrates, such as AFM tips and TEM grids. The resulting graphene-coated AFM tips and graphene TEM grids open up novel scientific avenues, for example, new capability for conductive AFM mapping and atomic-resolution TEM imaging of nanoparticles. Our method is also very suitable for the production of suspended graphene layers, an important goal in graphene science and technology to understand substrate effects on the resulting graphene properties.[28,29] Indeed, facilitated by this transfer method, we introduce the first studies on the wettability and electrochemistry of suspended graphene sheets.

6.2 Results and Discussion

6.2.1 Polymer-free Transfer of CVD Graphene

The new transfer method is described in Chapter 2. Salient observations from an etching process are presented in Figure 6.1. As shown in Figures 6.1a to 6.1c, there is a gradual etching of the copper foil, eventually leading to a complete and highly transparent graphene film of large area floating at the interface and maintaining its integrity. At this stage, the graphene film was ready to be transferred with a silicon wafer to a new hexane/pure water interface for 5 h, for the removal of any excess etchant salts (Figure 6.1d shows the start of this process), before being scooped out and left to dry.

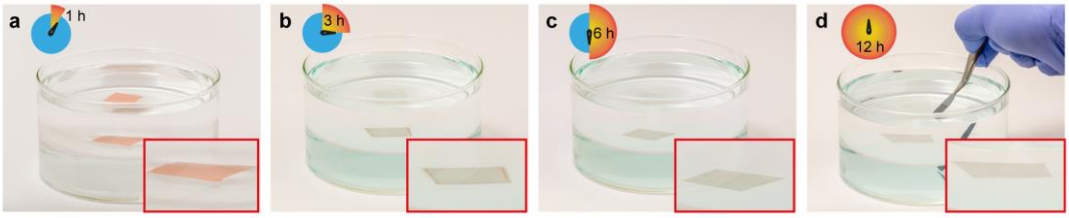

Figure 6.1 (a)-(c) Optical images of an as-grown graphene/copper sample floating at the interface between a hexane layer and a 0.1 M $(NH_4)_2S_2O_8$ aqueous solution during etching. (d) Optical image of the initial moments of the graphene film being scooped out by means of an Si/SiO_2 substrate.

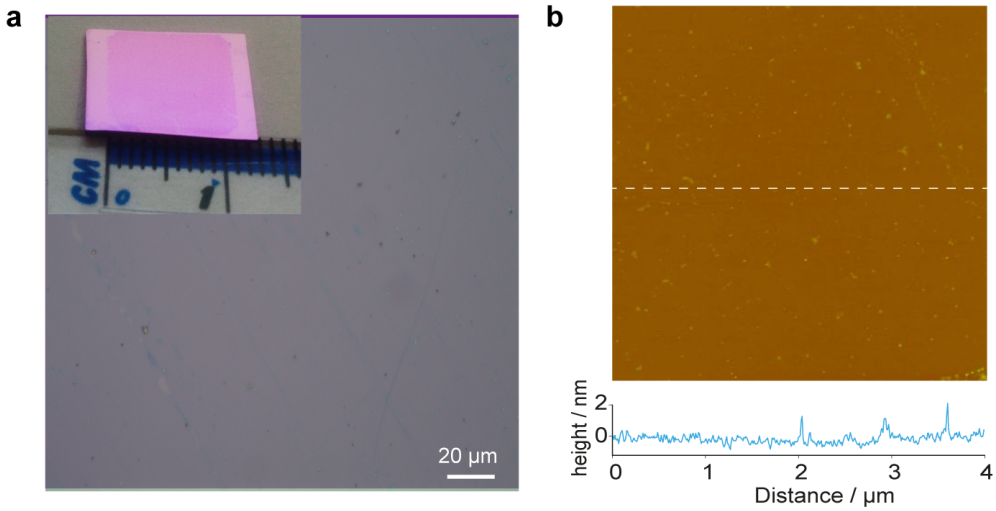

Figure 6.2 (a) Optical microscope and (b) AFM images of transferred graphene on Si/SiO_2 using the polymer-free transfer method.

A clean and complete graphene film was transferred onto Si/SiO_2, as evident by the optical and AFM images obtained after transfer (Figure 6.2). Raman spectroscopy measurements were also carried out to characterise the graphene samples (Figure 6.3). The Raman spectrum of graphene on copper showed a pronounced 2D band at 2664 cm^{-1} and a small G band at 1587 cm^{-1}, with almost no detectable D peak observed. This indicates the CVD growth of relatively high quality monolayer graphene.[19,22,30] When the graphene sheet was fully transferred onto an Si/SiO_2 wafer using our polymer-free transfer method, the intensity ratio of the 2D and G peaks (I_{2D}/I_G) was >2, with an associated FWHM for the 2D band of ~28 cm^{-1}, reaffirming the monolayer nature of the graphene grown. There was a small D band (at 1333 cm^{-1}) in the Raman spectrum of graphene on Si/SiO_2, with a D band intensity (I_D) to G band intensity (I_G) ratio of 0.11, being relatively uniform on the transferred graphene, as shown by the Raman data. This value suggests that relatively low-defect CVD graphene [31] was obtained by our growth and transfer process, of similar structural quality to that from polymer-assisted transfer methods commonly used in the literature and our study (Figure 6.4).[28]

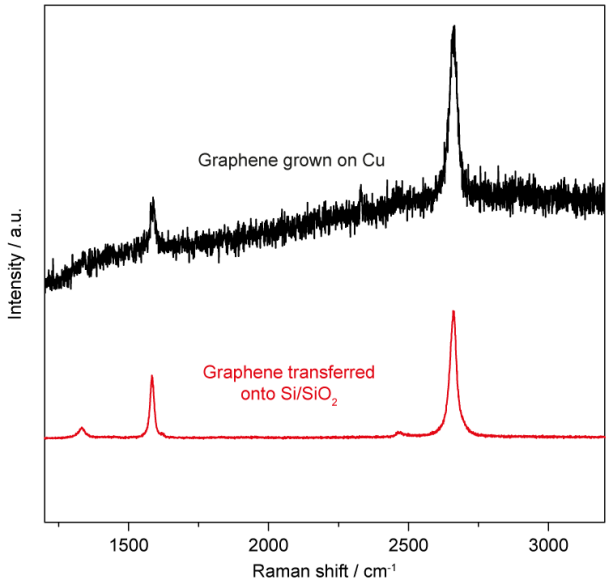

Figure 6.3 (a) Raman spectra of as-grown graphene film on copper, and fully transferred graphene on Si/SiO_2 by the new polymer-free biphasic method. (b) Raman mapping of graphene on Si/SiO_2.

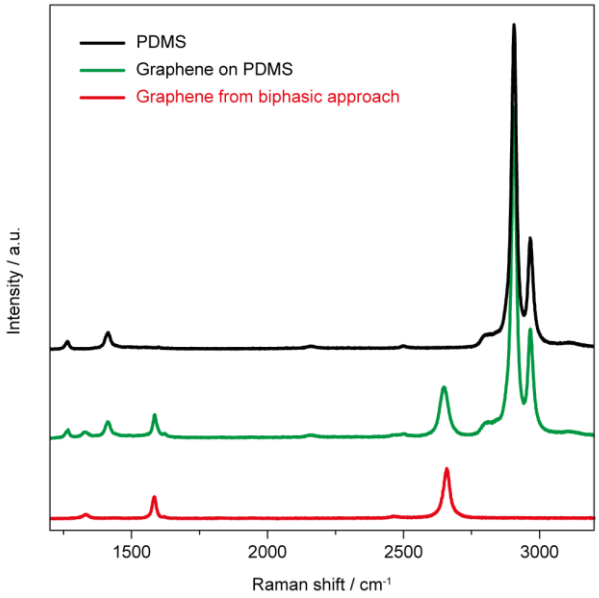

Figure 6.4 Raman spectra of PDMS, graphene on PDMS and graphene transferred onto Si/SiO_2 using the polymer-free biphasic approach.

6.2.2 Fabrication and Utilisation of Conductive Graphene AFM tips

Sheets of graphene find interesting use as an ultrathin template for the characterisation of nanoscale structures trapped on a substrate, including molecules,[32] nanoparticles[33] and biological entities (*e.g.* bacteria[34] or viruses[35]). The polymer-free biphasic method is attractive for the coating of fragile, small and coarse substrates. We exemplified this capability by coating AFM probes with freestanding graphene films.

CVD graphene films were deposited onto AFM probes following the biphasic procedure described in the previous section. After the transfer, the presence of graphene on the AFM probe cantilever was observable under an optical microscope. The tips were further characterised with SEM (Figures 6.5a and 6.5b) and TEM (Figure 6.5c), from which relatively few superficial features can be assigned to folds and wrinkles of the monolayer graphene. The images prove that the layer of graphene conforms very well to the AFM tip geometry, appearing to coat the AFM tip entirely, as well as the back of the cantilever by wrapping around it. Importantly, for AFM probe applications, we were interested in determining that the tip apex was also coated continuously

with graphene, and to rule out the possibility of a perforation of the graphene film by the very sharp end of the tip. TEM imaging (see Figure 6.5c) of graphene-coated AFM tips confirmed the presence of a continuous thin layer at the end of the tip, assigned to the graphene sheet. An attribute of the graphene coating is the thinness of the layer so that there is little change of the tip radius of curvature after coating to produce a conductive tip. This contrasts with metal-coated AFM tips, where several 10s of nm are typically deposited to make a conducting tip,[36,37] with an impact on the spatial resolution of the imaging probe.

We converted as-prepared graphene-coated AFM tips into conductive AFM probes, by evaporating a continuous gold thin film onto the back of the AFM tip chip, wrapped by the graphene layer, to which an electrical contact was made (see the schematics in Figure 6.5d). Simultaneous AFM maps of topography and electrical conductivity of HOPG were recorded. This substrate was chosen for the well-known structure and the electrical heterogeneity of its surface after exfoliation.[38,39] As shown in Figure 6.5e, the surface presents several graphitic planes that show distinct electrical conductivity, in agreement with the behaviour previously reported employing metal-coated AFM probes for its characterisation.[38-41] We found that a single tip could be used for more than 50 hours for conductive AFM measurements without noticeable deterioration in performance (a total of >50 images, each of a 5 μm × 5 μm area). Our transfer method brings to the fore a quick and easy approach for making these tips. Such conducting probes may also serve as a platform for molecular junctions,[42] and other applications, *e.g.* in electrochemistry and electrochemical imaging.

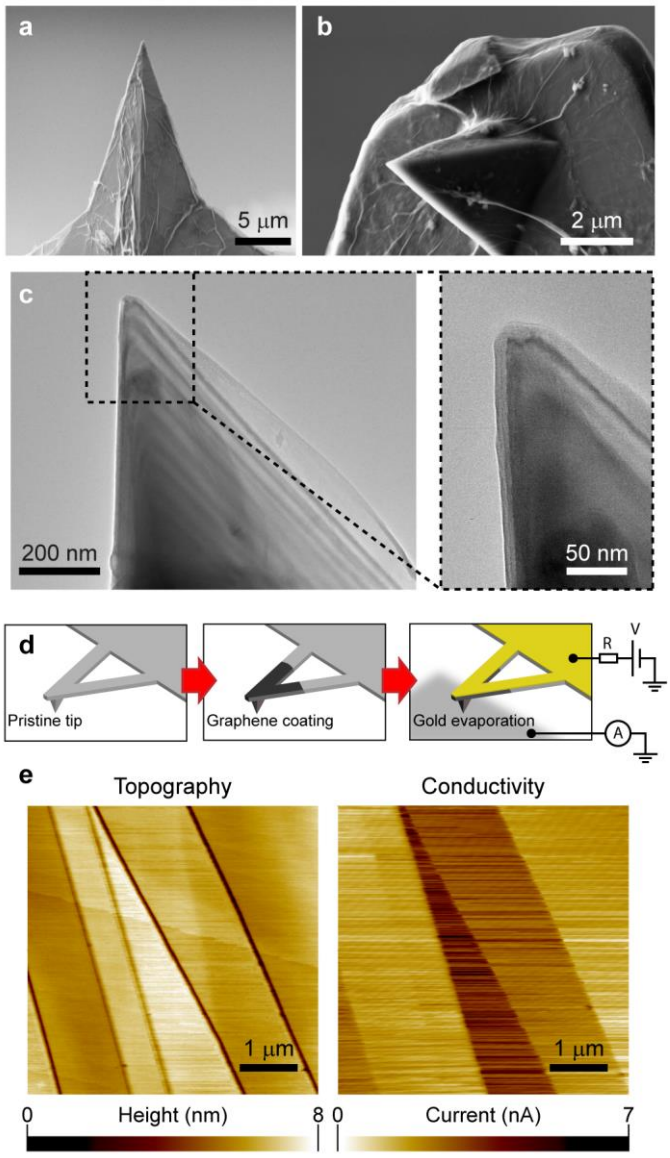

Figure 6.5 (a)-(b) SEM images of two graphene-coated AFM tips. (c) TEM images of the end of a graphene-coated AFM tip. (d) Schematic illustration of the production of a conductive AFM probe by coating graphene on a commercial tip, followed by gold evaporation on the back. (e) Topography and conductivity maps for a 5 μm × 5μm area of high quality HOPG, utilising a graphene-coated conductive AFM tip.

6.2.3 Graphene Coating on TEM Grids

There is currently considerable interest in using graphene films as supports for TEM measurements.[43-45] However, most processes to deposit graphene on holey TEM grids use polymer-assisted routes.[46] One study that was free of polymer, however, involved the etching of an Si/SiO_2 layer, but this is time-consuming and possibly introduces more contaminants to the graphene surface.[47]

In this study, we employed the biphasic graphene transfer method to produce TEM grids with one continuous single layer of CVD graphene as a support. This represents a simple, cheap and quick route to obtain graphene TEM substrates. The original TEM grids were in the form of Cu meshes with holes (11.5 µm × 11.5 µm), so that the transfer of graphene resulted in sections with a suspended graphene membrane (across the holes) and a supported graphene film (on the Cu grid). After the transfer, the coverage was complete for the majority of the grid, and an area of the as-prepared graphene TEM grid was characterised by AFM and SEM (Figure 6.6). In the AFM image of Figure 6.6a, a partially-coated hole in the upper left corner is deliberately displayed to present the contrast between covered-uncovered regions. The whole layer of graphene is therefore well-coated across the grid, with regions of suspended graphene membrane slightly subsiding from the surrounding Cu bars, but remaining continuous, due to its strong mechanical properties (Figure 6.7).

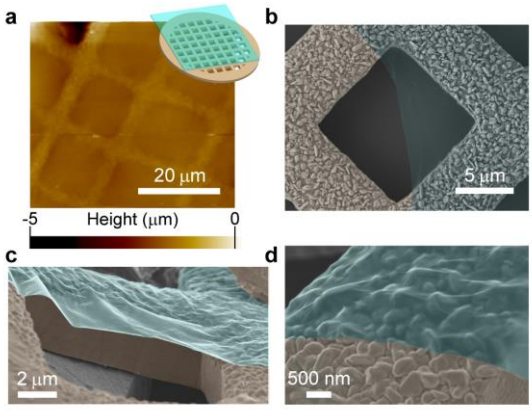

Figure 6.6 (a) 50 μm × 50 μm AFM image of part of the fabricated graphene TEM grid (schematic in the inset), with a partially-coated window observed in the upper left corner. (b) Top and (c)-(d) side views of false-colored SEM images of a graphene partially-coated window of a TEM grid (graphene in blue).

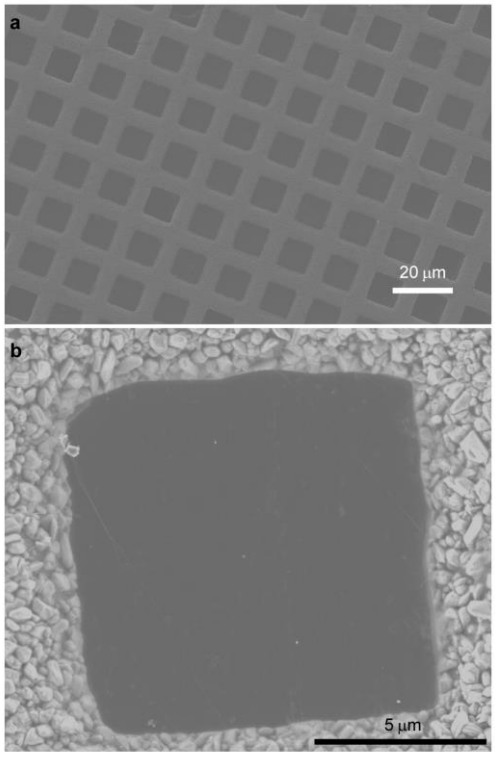

Figure 6.7 SEM image of (a) part of a graphene-coated TEM grid and (b) a graphene fully-covered window on the grid.

SEM images of a partially-covered hole, at the edge of graphene film (Figure 6.6b-d), show that the graphene film provides an excellent conformal coating

over the relatively coarse Cu surface, as was also found for AFM tips. An important factor responsible for the excellent coating is the evaporation of water and hexane trapped between the graphene sheet and the TEM grid after the transfer which can act to pull both materials into intimate contact.[25,47] Compared with transfer methods that are assisted by relatively rigid polymer films, such as PMMA and PDMS, this new method directly utilises a graphene film that is more flexible, while also being free from additional treatments (*e.g.* heating) used to enhance the contact, which are often required for polymer-transferred graphene.[9]

6.2.4 Graphene Membrane as a Support for TEM Characterisation

The two-dimensional ultrathin nature of graphene, and its low atomic number, together with excellent mechanical, thermal and electrical stability, presently make it the ultimate support film for TEM studies.[25,43-46,48,49] Indeed, graphene supports are nearly transparent to electron beams, and enable atomic-resolution imaging of objects, such as biological molecules,[46] gold nanocrystals and its citrate capping agents,[48] or small organic molecules,[49] which would otherwise be very difficult to be observed with TEM using commercial carbon supports.

Herein, we imaged gold nanoparticles (AuNPs) to demonstrate that the suspended graphene membranes obtained with our biphasic method can be used as TEM supports. A drop of solution containing AuNPs was deposited onto the graphene-coated TEM grid, and left in air to dry before TEM imaging was carried out. Figure 6.8a shows several AuNPs loaded on the freestanding graphene membrane. They are of regular shape and similar size (~10 nm diameter), as expected. High-resolution TEM characterisation was also performed, from which the gold atomic structure and ligands (citrate, blurred surroundings) of a single AuNP can be seen (Figure 6.8b).

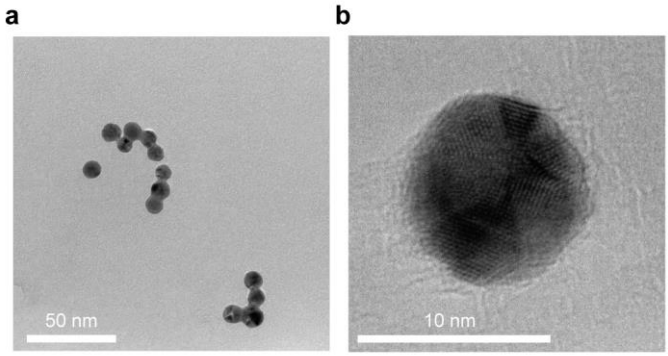

Figure 6.8 (a) Low-magnification TEM image of gold nanoparticles capped by citrate and (b) high-resolution TEM image of a gold nanoparticle, on a suspended graphene membrane over a Cu TEM grid.

6.2.5 Wetting and Electrochemistry of Supported and Suspended Graphene

The graphene TEM substrate opens up further opportunities of investigating electrochemistry at suspended graphene, for the first time, and comparing the response to that of Cu-supported graphene on the same sample. This is possible using SECCM, which essentially brings a small-scale meniscus electrochemical cell and counter/reference electrodes to a surface (working electrode), allowing electrochemical measurements of unusual electrode materials (see Chapter 2).[50-52]

It is well known that the properties of graphene may be strongly influenced by the supporting substrate; hence studies on freestanding graphene are of enormous interest.[53-55] The graphene TEM grid was electrochemically tested with two well-known redox couples; $FcTMA^{+/2+}$ and $Ru(NH_3)_6^{3+/2+}$ using SECCM setup.

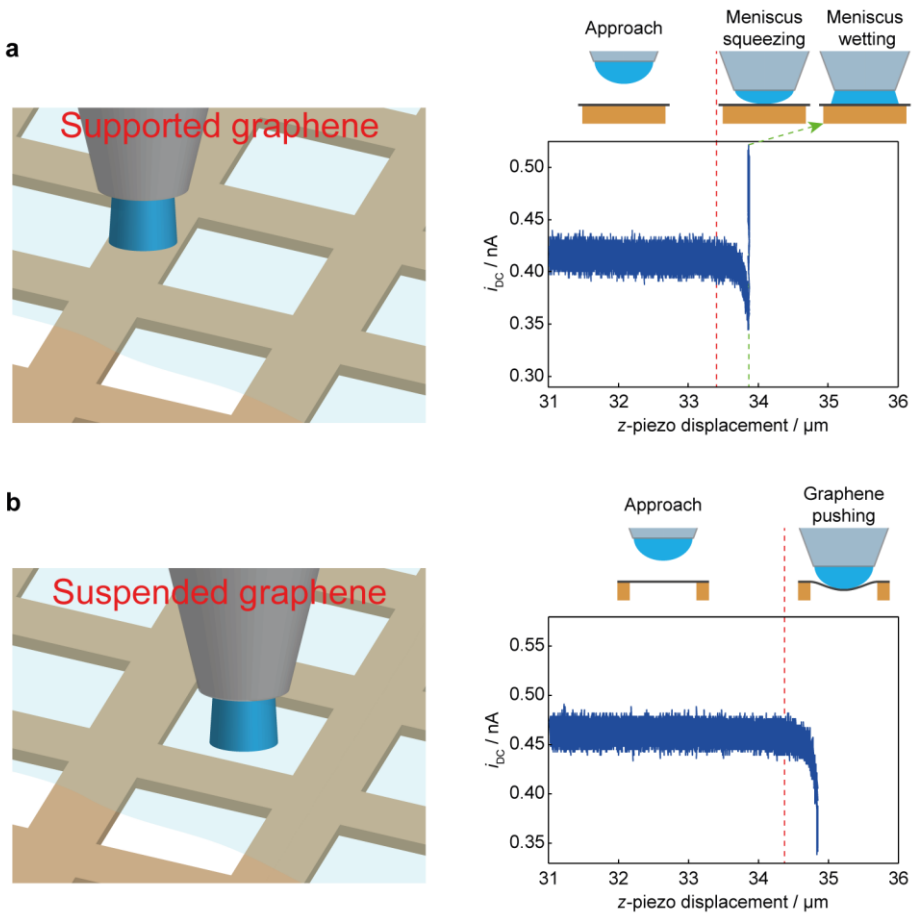

Figure 6.9 Schematic for an SECCM pipette landing on the (a) supported and (b) suspended parts of a graphene membrane over a Cu TEM grid (not to scale), with corresponding typical approach curves demonstrating the change of ion currents (i_{DC}) against *z*-piezo displacement shown. The dashed vertical lines indicate the position where the meniscus first contacted the graphene surface (red) and wetted graphene (green, (a)). These approaches are representative of more than 16 measurements carried out for each of these two scenarios.

In Figure 6.9a and 6.9b, we show representative approaches of i_{DC} vs. *z*-piezo displacement against supported and suspended graphene (representative of >16 experiments in each case). On the supported graphene (Figure 6.9a), after the first contact of the meniscus with the conductive substrate (detected through a current spike in the electrochemical current i_{act}), the meniscus was squeezed against the solid surface, as deduced from the continuous decrease of i_{DC} with the approach.[56] This value dropped by approx. 20 % until a sudden increase in the current was detected

at a piezo displacement of *ca.* 33.9 µm, attributed to the meniscus, under pressure, suddenly wetting the surface. In contrast, when the pipette meniscus came into contact with the suspended graphene sheet (Figure 6.9b), i_{DC} decreased monotonically by up to ~30 %, during squeezing of the meniscus. This provides some qualitative implications about the difference in the wettability of Cu-supported graphene and suspended graphene.

The wettability of graphene is of considerable interest, given the increasing application of graphene-coated materials. Yet, the relatively few studies available are not in agreement, especially on the effect of the substrate.[29,57,58] To the best of our knowledge, the intrinsic wettability of suspended graphene has only been predicted theoretically by molecular dynamics,[59] and has not been measured, due to experimental challenges. Our studies suggest that Cu-supported graphene exhibits stronger wettability compared with a freestanding graphene sheet. This is in line with theoretical studies showing that the contact angle of water on suspended graphene is higher than on Cu-supported graphene.[29,59-61]

To further investigate the wettability of the suspended graphene membrane, approach and retract experiments were carried out in which the meniscus of an SECCM pipette was pushed further against the graphene with the precise control of the *z*-piezo, while i_{DC} against *z*-piezo displacement was recorded, and the reverse (pull-off) of the meniscus was also measured. An example of these approach and retract curves (with ion conductance current i_{DC} normalised to the initial value of the approach i_{Ini}, i_{DC}/i_{Ini}) is presented in Figure 6.10 (which is typical of 3 different experiments). The pipette came into contact with the graphene sheet at position 1 on the approach, and as the pushing continued, a gradual decrease of the ionic current is observed due to meniscus compression (as described for Figure 6.9). The decrease (by ~25 %) stopped at position 2, after which there was a slight increase of the current that we attribute to minor meniscus wetting. This is because the wettability of suspended graphene can be enhanced if strained, due to greater coupling of droplets to the surfaces,[62] and the force on the meniscus between the pipette and graphene may also aid wetting. The pipette was

pushed further until position 3, whereupon the translation of the pipette was reversed. Interestingly, there is clearly an attractive interaction between water molecules and the atomically thin carbon sheet as when the pipette was pulled away from the substrate surface, an increase in i_{DC} is observed (positions 4, 5 and 6), due to the expansion (pulling) of the meniscus formed between SECCM probe and graphene substrate. These observations are consistent with recent theoretical predictions.[58] The meniscus detached at position 7, and the i_{DC} (meniscus confined to the pipette) decreased suddenly to its original value.

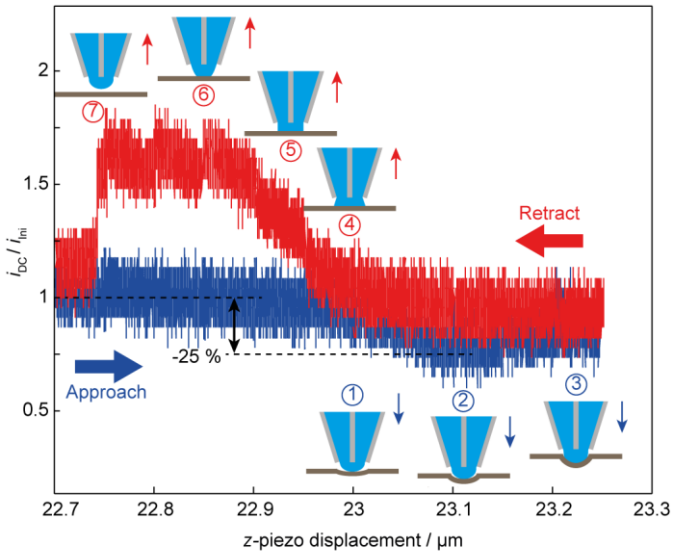

Figure 6.10 Plot of normalised ion conductance current as a function of the *z*-piezo displacement during the approach and retract processes of an SECCM pipette on suspended graphene.

Suspended graphene devices obtained with our biphasic method, in combination with SECCM, were also employed to study electrochemistry at suspended graphene for the first time. Upon meniscus contact with the graphene sheet, the pipette was held and three CVs were recorded at a scan rate of 0.1 V s^{-1} at each landing site for: (i) $FcTMA^{+/2+}$ (oxidation); (ii) $Ru(NH_3)_6^{3+/2+}$ (reduction) in separate experiments (Figure 6.11). The CVs show the sigmoidal response of a microelectrochemical system with non-linear (spherical segment) diffusion,[39,51,63] and are very reproducible. These data are representative of >6 spot measurements for each of the two couples.

For $FcTMA^{+/2+}$, the values of $E_{3/4}$-$E_{1/4}$, which is indicative of the reversibility of the system,[63,64] was similar on Cu-supported graphene (75 ± 2 mV) and suspended graphene (71 ± 2 mV). With respect to $Ru(NH_3)_6^{3+/2+}$, the CVs on Cu-supported graphene film, led to 69 ± 2 mV for $E_{1/4}$-$E_{3/4}$ and an $E_{1/4}$-$E_{3/4}$ value of 72 ± 2 mV was obtained for suspended graphene. All the CVs observed are characteristic of relatively fast (but not reversible) electron transfer kinetics for $FcTMA^{+/2+}$ and $Ru(NH_3)_6^{3+/2+}$ on the CVD graphene prepared herein, and are broadly in agreement with previous studies on Si/SiO_2- and Cu-supported CVD graphene with the same, and similar, redox species.[22,65,66]

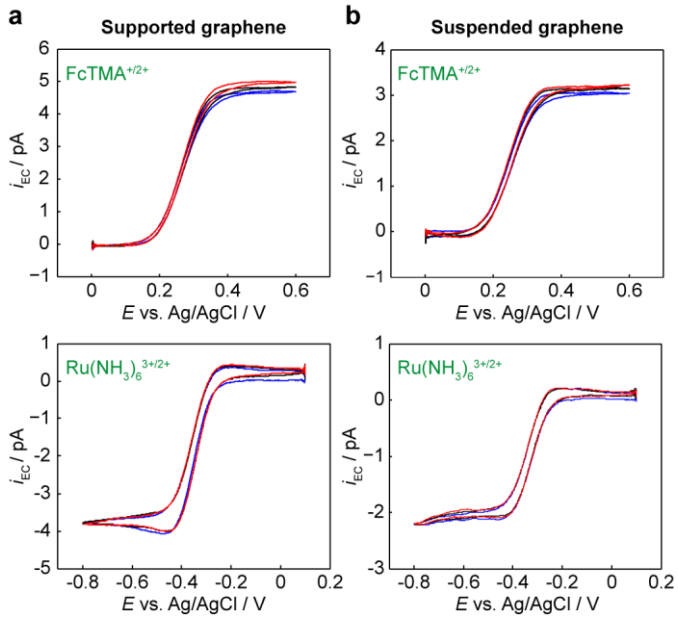

Figure 6.11 Cyclic voltammograms for the oxidation of 1 mM $FcTMA^+$ and the reduction of 1 mM $Ru(NH_3)_6^{3+}$ in 25 mM KCl, recorded at 0.1 V s^{-1} on (a) supported graphene and (b) suspended graphene. Three consecutive cycles are shown for each case: the 1st (blue), 2nd (black) and 3rd (red) scans. The data are representative of measurements in >6 different locations (spots) for each couple.

Cu-supported graphene and suspended graphene on the TEM grid, along with graphene transferred onto Si/SiO_2 (see Figure 6.12), behave in essentially the same way (within experimental error) towards the redox couples studied. There is no detectable substrate effect on the electrochemistry of CVD monolayer graphene, at the spatial resolution of this

study. Note that the limiting currents of $FcTMA^{+/2+}$ and $Ru(NH_3)_6^{3+/2+}$ on suspended graphene, are lower than those of Cu-supported graphene. This is due to the different wettability of the supported and suspended graphene membranes, producing different meniscus contact (working electrode) areas and mass transport rates (*vide supra*, Figure 6.9).

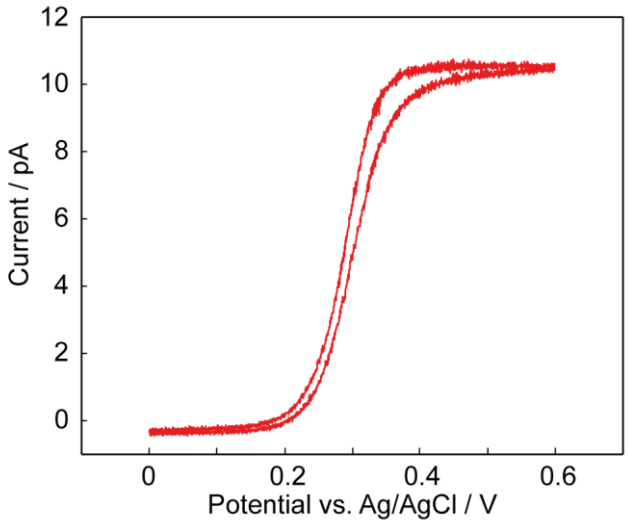

Figure 6.12 An SECCM cyclic voltammogram for the oxidation of 1 mM $FcTMA^+$ in 25 mM KCl on the graphene transferred onto Si/SiO_2, recorded at a scan rate of 0.1 V s^{-1}.

6.3 Conclusions

A new and efficient polymer-free biphasic (liquid/liquid) method for the transfer of monolayer graphene to a variety of substrates has been demonstrated that opens up new applications and avenues for graphene studies. Key advantages of the method are that the graphene films produced are completely free from any polymer contamination and that detrimental treatments, often associated with polymer-supported transfer routes, are minimised.

The new polymer-free transfer process is easy to implement and we have shown the capability of the method for transferring graphene (of centimetre scale) onto arbitrary substrates, including complex 3D objects, such as AFM tips and TEM grids. The transferred graphene has been shown to adapt well

to the substrate surfaces, resulting in high quality conductive graphene-coated AFM tips and graphene TEM grids. Graphene coating of AFM tips is advantageous compared to metal-coated tips in that the spatial resolution is not compromised, due to the thinness of the graphene layer. Note that although graphene transfer was exemplified with single tips, it should be possible to coat batches (wafers) of AFM probes from the transfer of a single graphene sheet, considering that large area graphene films can be produced by CVD growth. The resulting graphene-coated AFM probes would also be amenable to further covalent functionalisation, for example, via the reduction of diazonium molecules, offering a new platform by which to produce probes for molecular recognition applications, as an alternative to the standard thiol modification of gold-coated tips. It is expected that the probes could be further modified into ultramicroelectrodes for use in combined SECM-AFM, among other applications.

Graphene-coated TEM grids have enabled the wettability and electrochemistry of suspended graphene to be explored for the first time, and also provide a powerful platform for high-resolution imaging of nanostructures. The electrochemical activity of suspended graphene (no discernible difference to supported graphene) makes it suitable for use in sensors and other devices. The electrode/TEM grid combination would serve as a powerful platform for the electrodeposition of nanomaterials for subsequent TEM characterisation, and it may also be possible to use the transfer method to fabricate cells for *in-situ* TEM measurements. Further work to explore the graphene coating of soft materials, in particular, could be very worthwhile.

6.4 References

(1) Novoselov, K. S.; Geim, A. K.; Morozov, S. V.; Jiang, D.; Zhang, Y.; Dubonos, S. V.; Grigorieva, I. V.; Firsov, A. A. *Science* **2004**, *306*, 666.

(2) Geim, A. K.; Novoselov, K. S. *Nat. Mater.* **2007**, *6*, 183.

(3) Avouris, P. *Nano Lett.* **2010**, *10*, 4285.

(4) Lee, C.; Wei, X.; Kysar, J. W.; Hone, J. *Science* **2008**, *321*, 385.

(5) Bunch, J. S.; Verbridge, S. S.; Alden, J. S.; van der Zande, A. M.; Parpia, J. M.; Craighead, H. G.; McEuen, P. L. *Nano Lett.* **2008**, *8*, 2458.

(6) Paulus, G. L. C.; Wang, Q. H.; Strano, M. S. *Acc. Chem. Res.* **2013**, *46*, 160.

(7) Elias, D. C.; Nair, R. R.; Mohiuddin, T. M. G.; Morozov, S. V.; Blake, P.; Halsall, M. P.; Ferrari, A. C.; Boukhvalov, D. W.; Katsnelson, M. I.; Geim, A. K.; Novoselov, K. S. *Science* **2009**, *323*, 610.

(8) Van Noorden, R. *Nature* **2012**, *483*, S32.

(9) Suk, J. W.; Kitt, A.; Magnuson, C. W.; Hao, Y.; Ahmed, S.; An, J.; Swan, A. K.; Goldberg, B. B.; Ruoff, R. S. *ACS Nano* **2011**, *5*, 6916.

(10) Bae, S.; Kim, H.; Lee, Y.; Xu, X.; Park, J.-S.; Zheng, Y.; Balakrishnan, J.; Lei, T.; Ri Kim, H.; Song, Y. I.; Kim, Y.-J.; Kim, K. S.; Ozyilmaz, B.; Ahn, J.-H.; Hong, B. H.; Iijima, S. *Nat. Nano.* **2010**, *5*, 574.

(11) Reina, A.; Jia, X.; Ho, J.; Nezich, D.; Son, H.; Bulovic, V.; Dresselhaus, M. S.; Kong, J. *Nano Lett.* **2009**, *9*, 30.

(12) Sutter, P. W.; Flege, J.-I.; Sutter, E. A. *Nat. Mater.* **2008**, *7*, 406.

(13) Li, X.; Cai, W.; An, J.; Kim, S.; Nah, J.; Yang, D.; Piner, R.; Velamakanni, A.; Jung, I.; Tutuc, E.; Banerjee, S. K.; Colombo, L.; Ruoff, R. S. *Science* **2009**, *324*, 1312.

(14) Zhang, Y.; Zhang, L.; Zhou, C. *Acc. Chem. Res.* **2013**, *46*, 2329.

(15) Kang, J.; Shin, D.; Bae, S.; Hong, B. H. *Nanoscale* **2012**, *4*, 5527.

(16) Wang, Y.; Zheng, Y.; Xu, X.; Dubuisson, E.; Bao, Q.; Lu, J.; Loh, K. P. *ACS Nano* **2011**, *5*, 9927.

(17) Cherian, C. T.; Giustiniano, F.; Martin-Fernandez, I.; Andersen, H.; Balakrishnan, J.; Özyilmaz, B. *Small* **2015**, *11*, 189.

(18) Li, X.; Zhu, Y.; Cai, W.; Borysiak, M.; Han, B.; Chen, D.; Piner, R. D.; Colombo, L.; Ruoff, R. S. *Nano Lett.* **2009**, *9*, 4359.

(19) Kim, K. S.; Zhao, Y.; Jang, H.; Lee, S. Y.; Kim, J. M.; Kim, K. S.; Ahn, J.-H.; Kim, P.; Choi, J.-Y.; Hong, B. H. *Nature* **2009**, *457*, 706.

(20) Park, H. J.; Meyer, J.; Roth, S.; Skákalová, V. *Carbon* **2010**, *48*, 1088.

(21) Lin, Y.-C.; Lu, C.-C.; Yeh, C.-H.; Jin, C.; Suenaga, K.; Chiu, P.-W. *Nano Lett.* **2012**, *12*, 414.

(22) Li, W.; Tan, C.; Lowe, M. A.; Abruña, H. D.; Ralph, D. C. *ACS Nano* **2011**, *5*, 2264.

(23) Pirkle, A.; Chan, J.; Venugopal, A.; Hinojos, D.; Magnuson, C. W.; McDonnell, S.; Colombo, L.; Vogel, E. M.; Ruoff, R. S.; Wallace, R. M. *Appl. Phys. Lett.* **2011**, *99*, 122108.

(24) Suk, J. W.; Lee, W. H.; Lee, J.; Chou, H.; Piner, R. D.; Hao, Y.; Akinwande, D.; Ruoff, R. S. *Nano Lett.* **2013**, *13*, 1462.

(25) Regan, W.; Alem, N.; Alemán, B.; Geng, B.; Girit, Ç.; Maserati, L.; Wang, F.; Crommie, M.; Zettl, A. *Appl. Phys. Lett.* **2010**, *96*, 113102.

(26) Lin, W.-H.; Chen, T.-H.; Chang, J.-K.; Taur, J.-I.; Lo, Y.-Y.; Lee, W.-L.; Chang, C.-S.; Su, W.-B.; Wu, C.-I. *ACS Nano* **2014**, *8*, 1784.

(27) Toth, P. S.; Ramasse, Q. M.; Velicky, M.; Dryfe, R. A. W. *Chem. Sci.* **2015**, *6*, 1316.

(28) Wang, Q. H.; Jin, Z.; Kim, K. K.; Hilmer, A. J.; Paulus, G. L. C.; Shih, C.-J.; Ham, M.-H.; Sanchez-Yamagishi, J. D.; Watanabe, K.; Taniguchi, T.; Kong, J.; Jarillo-Herrero, P.; Strano, M. S. *Nat. Chem.* **2012**, *4*, 724.

(29) Rafiee, J.; Mi, X.; Gullapalli, H.; Thomas, A. V.; Yavari, F.; Shi, Y.; Ajayan, P. M.; Koratkar, N. A. *Nat. Mater.* **2012**, *11*, 217.

(30) Gao, L.; Ni, G.-X.; Liu, Y.; Liu, B.; Castro Neto, A. H.; Loh, K. P. *Nature* **2014**, *505*, 190.

(31) Ferrari, A. C.; Basko, D. M. *Nat. Nano.* **2013**, *8*, 235.

(32) Xu, K.; Cao, P.; Heath, J. R. *Science* **2010**, *329*, 1188.

(33) Zong, Z.; Chen, C.-L.; Dokmeci, M. R.; Wan, K.-t. *J. Appl. Phys.* **2010**, *107*, 026104.

(34) Mohanty, N.; Fahrenholtz, M.; Nagaraja, A.; Boyle, D.; Berry, V. *Nano Lett.* **2011**, *11*, 1270.

(35) Khatib, O.; Wood, J. D.; McLeod, A. S.; Goldflam, M. D.; Wagner, M.; Damhorst, G. L.; Koepke, J. C.; Doidge, G. P.; Rangarajan, A.; Bashir, R.; Pop, E.; Lyding, J. W.; Thiemens, M. H.; Keilmann, F.; Basov, D. N. *ACS Nano* **2015**, *9*, 7968.

(36) Wold, D. J.; Frisbie, C. D. *J. Am. Chem. Soc.* **2001**, *123*, 5549.

(37) Xu, D.; Watt, G. D.; Harb, J. N.; Davis, R. C. *Nano Lett.* **2005**, *5*, 571.

(38) Patel, A. N.; Collignon, M. G.; O'Connell, M. A.; Hung, W. O.; McKelvey, K.; Macpherson, J. V.; Unwin, P. R. *J. Am. Chem. Soc.* **2012**, *134*, 20117.

(39) Güell, A. G.; Cuharuc, A. S.; Kim, Y.-R.; Zhang, G.; Tan, S.-y.; Ebejer, N.; Unwin, P. R. *ACS Nano* **2015**, *9*, 3558.

(40) Banerjee, S.; Sardar, M.; Gayathri, N.; Tyagi, A. K.; Raj, B. *Phys. Rev. B* **2005**, *72*, 075418.

(41) Lu, Y.; Muñoz, M.; Steplecaru, C. S.; Hao, C.; Bai, M.; Garcia, N.; Schindler, K.; Esquinazi, P. *Phys. Rev. Lett.* **2006**, *97*, 076805.

(42) Wen, Y.; Chen, J.; Guo, Y.; Wu, B.; Yu, G.; Liu, Y. *Adv. Mater.* **2012**, *24*, 3482.

(43) Wilson, N. R.; Pandey, P. A.; Beanland, R.; Young, R. J.; Kinloch, I. A.; Gong, L.; Liu, Z.; Suenaga, K.; Rourke, J. P.; York, S. J.; Sloan, J. *ACS Nano* **2009**, *3*, 2547.

(44) van de Put, M. W. P.; Patterson, J. P.; Bomans, P. H. H.; Wilson, N. R.; Friedrich, H.; van Benthem, R. A. T. M.; de With, G.; O'Reilly, R. K.; Sommerdijk, N. A. J. M. *Soft Matter* **2015**, *11*, 1265.

(45) Buckhout-White, S.; Robinson, J. T.; Bassim, N. D.; Goldman, E. R.; Medintz, I. L.; Ancona, M. G. *Soft Matter* **2013**, *9*, 1414.

(46) Nair, R. R.; Blake, P.; Blake, J. R.; Zan, R.; Anissimova, S.; Bangert, U.; Golovanov, A. P.; Morozov, S. V.; Geim, A. K.; Novoselov, K. S.; Latychevskaia, T. *Appl. Phys. Lett.* **2010**, *97*, 153102.

(47) Meyer, J. C.; Girit, C. O.; Crommie, M. F.; Zettl, A. *Appl. Phys. Lett.* **2008**, *92*, 123110.

(48) Lee, Z.; Jeon, K.-J.; Dato, A.; Erni, R.; Richardson, T. J.; Frenklach, M.; Radmilovic, V. *Nano Lett.* **2009**, *9*, 3365.

(49) Meyer, J. C.; Girit, C. O.; Crommie, M. F.; Zettl, A. *Nature* **2008**, *454*, 319.

(50) Ebejer, N.; Guell, A. G.; Lai, S. C.; McKelvey, K.; Snowden, M. E.; Unwin, P. R. *Annu. Rev. Anal. Chem.* **2013**, *6*, 329.

(51) Snowden, M. E.; Güell, A. G.; Lai, S. C.; McKelvey, K.; Ebejer, N.; O'Connell, M. A.; Colburn, A. W.; Unwin, P. R. *Anal. Chem.* **2012**, *84*, 2483.

(52) Lai, S. C. S.; Patel, A. N.; McKelvey, K.; Unwin, P. R. *Angew. Chem. Int. Ed.* **2012**, *51*, 5405.

(53) Cai, W.; Moore, A. L.; Zhu, Y.; Li, X.; Chen, S.; Shi, L.; Ruoff, R. S. *Nano Lett.* **2010**, *10*, 1645.

(54) Ni, Z. H.; Yu, T.; Luo, Z. Q.; Wang, Y. Y.; Liu, L.; Wong, C. P.; Miao, J.; Huang, W.; Shen, Z. X. *ACS Nano* **2009**, *3*, 569.

(55) Guimaraes, M. H.; Veligura, A.; Zomer, P. J.; Maassen, T.; Vera-Marun, I. J.; Tombros, N.; van Wees, B. J. *Nano Lett.* **2012**, *12*, 3512.

(56) Chen, C.-H.; Meadows, K. E.; Cuharuc, A.; Lai, S. C. S.; Unwin, P. R. *Phys. Chem. Chem. Phys.* **2014**, *16*, 18545.

(57) Raj, R.; Maroo, S. C.; Wang, E. N. *Nano Lett.* **2013**, *13*, 1509.

(58) Hung, S.-W.; Hsiao, P.-Y.; Chen, C.-P.; Chieng, C.-C. *J. Phys. Chem. C* **2015**, *119*, 8103.

(59) Shih, C.-J.; Wang, Q. H.; Lin, S.; Park, K.-C.; Jin, Z.; Strano, M. S.; Blankschtein, D. *Phys. Rev. Lett.* **2012**, *109*, 176101.

(60) Mugele, F. *Nat. Mater.* **2012**, *11*, 182.

(61) Li, Z.; Wang, Y.; Kozbial, A.; Shenoy, G.; Zhou, F.; McGinley, R.; Ireland, P.; Morganstein, B.; Kunkel, A.; Surwade, S. P.; Li, L.; Liu, H. *Nat. Mater.* **2013**, *12*, 925.

(62) Ma, M.; Tocci, G.; Michaelides, A.; Aeppli, G. *Nat. Mater.* **2016**, *15*, 66.

(63) A. J. Bard; Faulkner, L. R. *Electrochemical Methods: Fundamentals and Applications*; 2nd ed.; John Wiley& Sons, Inc.: New York, 2001.

(64) Güell, A. G.; Ebejer, N.; Snowden, M. E.; Macpherson, J. V.; Unwin, P. R. *J. Am. Chem. Soc.* **2012**, *134*, 7258.

(65) Zhong, J.-H.; Zhang, J.; Jin, X.; Liu, J.-Y.; Li, Q.; Li, M.-H.; Cai, W.; Wu, D.-Y.; Zhan, D.; Ren, B. *J. Am. Chem. Soc.* **2014**, *136*, 16609.

(66) Bosch-Navarro, C.; Laker, Z. P. L.; Rourke, J. P.; Wilson, N. R. *Phys. Chem. Chem. Phys.* **2015**, *17*, 29628.

Chapter 7 Low-Voltage Voltammetric Electrowetting of Graphite Surfaces by Ion Intercalation/De-intercalation

This chapter shows the actuation of aqueous droplets on HOPG surface under much lower voltage range compared with EWOD setup, and proposes a new mechanism for the electrowetting observed. The electrowetting of droplets that contact with HOPG directly is due to the intercalation/deintercalation of anions into graphene layers of HOPG and the extent can be influenced by scan rate, potential polarity, anion type and HOPG quality. This study is important for understanding electrowetting and opening up new routes for the applications.

7.1 Introduction

The wetting of substrates by liquid droplets has long aroused great interest in the scientific community, driven by a number of applications, such as surface coatings,[1] oil/water separation[2] and (nano)pattern fabrication.[3] Electrowetting describes the influence of an electric field on wetting, and has been the subject of many fundamental studies.[4-7] Applications include electronic displays,[8] optical lenses[9] and lab-on-a-chip systems.[10] Electrowetting can be used to electronically control small amounts of liquid, without the mechanical movement of components, which is of paramount importance in microfluidic devices,[4,11] and considerable attention derives from this particular application.

Hitherto, electrowetting has been achieved most readily with an EWOD format.[12,13] In this situation, a liquid droplet is placed on a dielectric-layer coated electrode, with the electrode and droplet essentially acting as the two plates of a capacitor. Through the application of an external potential difference between the substrate electrode and an electrode in the droplet, the electrode/dielectric and droplet/dielectric interfaces can be charged, producing a change of the CA of the droplet.[4,13] An advantage of this configuration is that complications from the electrolysis of the electrolyte are avoided.

EWOD can produce quite large changes in CA, but because of the dielectric film very high voltages (20–300 V) usually have to be applied.[5,12,14,15] The dynamics of electrowetting are rapid in this format, making it difficult to monitor the wetting dynamics.[16] Conductive surfaces, such as steel[17] and graphene/carbon nanotube films,[18] are being thus explored to lower the voltage and increase the timescale of electrowetting. However, the electrowetting is very slow and not readily reversible.[17]

In this work, we demonstrate an entirely new mechanism of electrowetting of a substrate by a droplet, promoted by ion intercalation/de-intercalation into HOPG. The process is promoted by CV conditions over a low potential range (0~+2 V vs Ag/AgCl quasi-reference electrode), and is highly reversible and fairly fast. HOPG is characterised by an easy surface preparation by

mechanical cleavage, and has a well-defined surface structure (*i.e.* extensive basal plane areas and step edges).[19] It is composed of stacked graphene layers, which serve as host sites for ion intercalation, and ion intercalation is considered to be important for the production of graphene flakes via exfoliation.[20] It has been reported that compounds containing ClO_4^-, SO_4^{2-} and NO_3^- ions are graphite intercalators that can expand the spacing between graphitic layers (0.335 nm) at positive potentials, due to their slightly larger ionic size and negative charge. However, there is no intercalation of PO_4^{3-} ions into graphite.[21-23] In the studies herein, we control the potential to avoid exfoliation and explore the factors that promote electrowetting and its associated timescale. Our work provides intriguing insights into the effect of step edge density on electrowetting, with the highest quality HOPG samples that have low step edge density (but monolayer steps) leading to more facile ion intercalation/de-intercalation and thus extensive electrowetting. In contrast, HOPG samples with much higher step edge densities, but with multilayer steps, show much less significant electrowetting. The results we present are thus important not only for characterising this new mechanism of electrowetting, but also for providing significant new information on ion intercalation into carbon electrodes, which has many technical applications (*e.g.* in battery electrodes).[24]

7.2 Results and Discussion

In this study, we applied a set of positive and negative potential windows to the droplet cell (5 µL), by scanning the substrate potential from 0 V (vs Ag/AgCl wire; to which all potentials are referred) up to a defined positive or negative limit. Note that the Ag/AgCl wire has a reasonably stable potential[25] (*ca.* +140 mV vs saturated calomel electrode, as measured in this study). In both directions, the potential limits were gradually expanded to a maximum of ±2 V, enabling the wettability of HOPG to be explored in a variety of potential ranges. Compared to the droplet size, the Ag/AgCl electrode, which was produced on an Ag wire that was polished to generate a sharp end before the deposition of AgCl, had negligible effect on the shape and geometry of the droplet resting on the surface of HOPG. Meanwhile, the

effect of gravity on the droplet can be ignored, as the droplet size (typically 1.4 mm radius) is smaller than the capillary length, expressed as $(\gamma_{LV}/\rho g)^{1/2}$, where γ_{LV} is the liquid-vapour surface tension (typically 72.8 dyn cm^{-1}), with ρ, g respectively representing the density of the aqueous solution (~1 g cm^{-3}) and the gravitational acceleration (9.8 m s^{-2}).[12,26] Therefore, any change in the CA and RCD of the droplets during CV measurements can be ascribed to the applied voltage (*vide infra*).

7.2.1 Voltage Effect on Electrowetting

A CA of ~51° was observed for aqueous (1 mM $NaClO_4$) droplets on freshly cleaved AM HOPG surfaces with no applied electric field. This result is in line with other studies that have shown graphite surfaces to be mildly hydrophilic with a contact angle of about 50°,[27-29] Although higher aqueous contact angle values have been reported in the literature,[30-32] variations are expected depending on the sample quality, measurement environment (including surface contamination which increases the contact angle) and droplet size.[27,28,33] Given the short timescale (<5 s) on which the droplet was deposited after cleavage of surface, the value we report can be taken as the intrinsic CA of 1 mM $NaClO_4$ at AM HOPG, and is in line with theoretical predictions.[28]

When the applied potential was scanned positively, the droplet was found to electrowet the substrate as evidenced by the spreading (advancing) and retraction (receding) of the droplet, as manifest in the changes in CA and RCD (Figure 7.1). In the potential range of 0~+1.2 V (Figure 7.1a), the droplet spread with increasing positive potential, with RCD increasing by *ca.* 11% at +1.13 V, while the CA was reduced from 51° to 38°. Note that similar behaviour was observed with an electrolyte concentration of 0.1 M (Figure 7.2). Interestingly, there is a clear hysteresis of both the CA and RCD between the outgoing and return scans which, in part, is due to the wetting lagging the change of potential at this scan rate. In fact, as a consequence, the maxima of the CA and RCD are seen on the reverse scan. Thus, for electrowetting of AM HOPG by the droplet in Figure 7.1a, a minimum CA of 35° and a maximum RCD of 1.11 are seen at +0.86 V on the reverse scan.

As the potential was returned to zero, the droplet retracted back towards its original shape, increasing the CA to ~50° at 0 V, which was slightly lower than at the beginning of the scan, with a slightly higher RCD (Figure 7.1a).

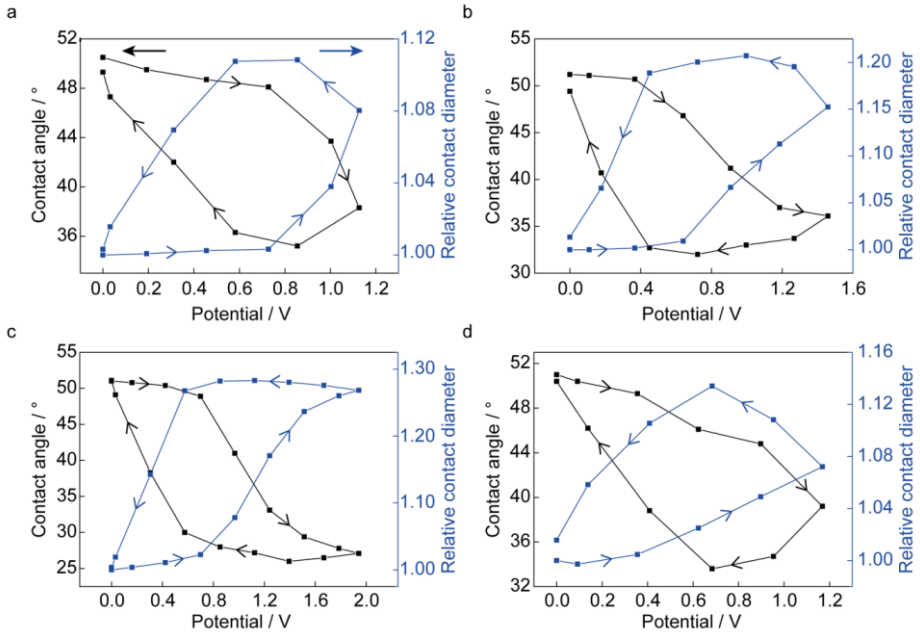

Figure 7.1 Contact angle and relative contact diameter for a droplet of 1 mM $NaClO_4$ solution at the surface of AM HOPG, during cyclic voltammograms recorded in the potential range of (a) 0 to +1.2 V, (b) 0 to +1.5 V, (c) 0 to +2 V and finally (d) 0 to +1.2V after the scan from 0 to +2 V, at a scan rate of 1 V s^{-1} in each case. Note that the differences in the scale of the contact angles and the directions indicated by arrows in each plot.

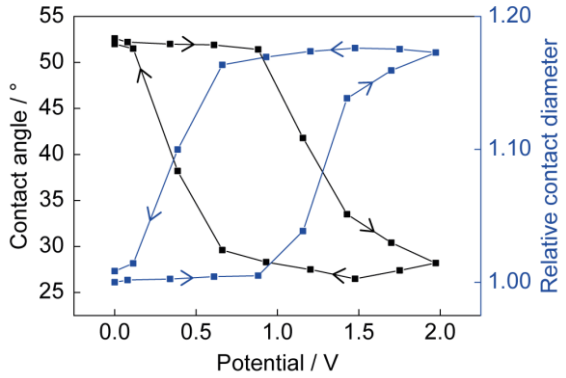

Figure 7.2 Contact angle and relative contact diameter for a droplet of 0.1 M $NaClO_4$ aqueous solution at the surface of AM HOPG, during a cyclic voltammogram recorded in the potential range of 0 V to +2 V, at a scan rate of 1 V s^{-1}.

When the upper potential limit of the CV was increased to +1.5 V on the same sample (Figure 7.1b), there was a decrease of the CA by 15° (from 51° to 36°) and an increase of 15% in RCD. A minimum CA of 32° and a maximum RCD of 1.2 were observed at +0.72 V on the reverse scan. In the case of +2 V being the positive limit (Figure 7.1c), the CA dropped dramatically by 25°, from 51° with no potential applied to 26° at +1.4 V on the reverse scan and meanwhile the RCD was enlarged by 28%. The wettability of AM HOPG after the scan between 0 V and +2 V was revisited by performing a CV in the potential range of 0~+1.2 V. It was found that the electrowetting behaviour of the droplet was enhanced slightly (compare Figure 7.1a to Figure 7.1d), suggesting some change in the surface properties, which we consider further below.

The optical images in Figure 7.3 illustrate the significant droplet electrowetting on AM HOPG during the CV carried out from 0 to +2 V. Good repeatability of this behaviour was observed for at least 20 repetitive cycles (Figure 7.4), although, there is a change of the electrowetting potential region with the number of scans from 1 to 5 (to more cathodic values), with the electrowetting potential window and behaviour remaining fairly consistent thereafter.

Figure 7.3 Snapshot optical images for a droplet of 1 mM $NaClO_4$ solution on AM HOPG during cyclic voltammetry, with the potential swept in the range of 0~+2 V, recorded with the potential increased from (a) 0 V, to (b) +1.4 V and (c) decreased back to 0 V (vs Ag/AgCl), with the corresponding contact angle values indicated. The scan rate was 1 V s^{-1}.

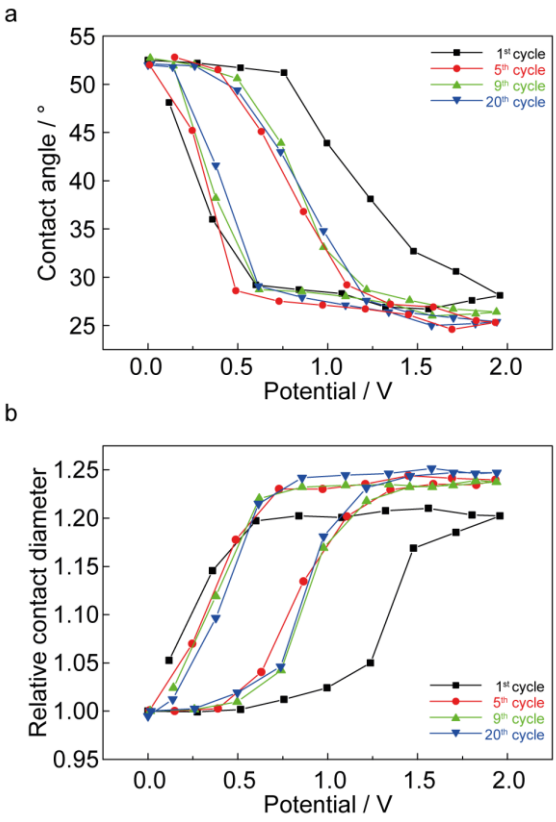

Figure 7.4. (a) Contact angle and (b) relative contact diameter of electrowetting for a droplet of 1 mM $NaClO_4$ solution on AM HOPG, during the 1st, 5th, 9th and 20th cycles of 20 repetitive scans (from 0 to +2 V, 1V s^{-1}).

Our experimental method allowed the electrochemical responses to be recorded simultaneously during voltammetric electrowetting. The data for a 1 mM $NaClO_4$ droplet on AM HOPG are shown in Figures 7.5-7.6. For the anodic scan to a potential limit of +1.2 V, a small oxidation peak at +0.85 V was detected on the outgoing scan, with a hint of reduction at *ca.* +0.2 V on the reverse (Figure 7.5a). When the upper potential limit was increased to +1.4 V for the same HOPG surface, the oxidation feature was again seen, with a clearer reduction peak at +0.3 V (Figure 7.5b). With the positive potential limit increased further to +1.6 V, the anodic peak was seen even more clearly, followed by an anodic process, likely due to the onset of water oxidation. The corresponding reduction peak on the reverse scan became more pronounced and shifted positively to +0.34 V (Figure 7.5c), +0.37 V (Figure 7.5d) and +0.4 V (Figure 7.5e). After the set of voltammetric scans in Figures 7.5a-e, a voltammogram over the potential range of 0~+1.2 V was recorded, and the reduction peak was still noticeable (at +0.31 V vs Ag/AgCl)

on the cyclic voltammogram (Figure 7.5f) and much more prominent than the initial scan over the same range (Figure 7.5a). The development of the reduction peak with the increase in the upper positive potential limit and number of potential scans (also see Figure 7.6) correlates with the enhanced electrowetting behaviour observed for the droplet on AM HOPG (*vide supra*, Figure 7.1).

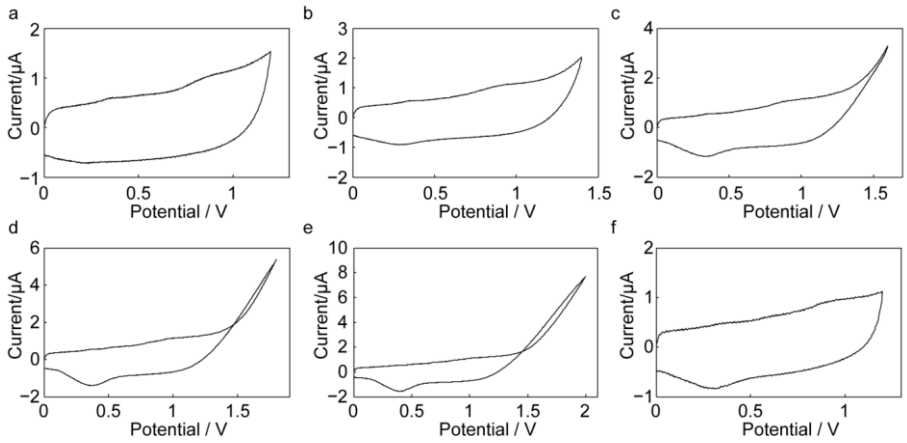

Figure 7.5 Cyclic voltammograms for a droplet of 1 mM $NaClO_4$ on AM HOPG with applied voltage in the range of (a) 0~+1.2 V, (b) 0~+1.4 V, (c) 0~+1.6 V, (d) 0~+1.8 V, (e) 0~+2 V and (f) 0~+1.2 V after the CV swept between 0 and +2 V. Scan rate: 1 V s^{-1}.

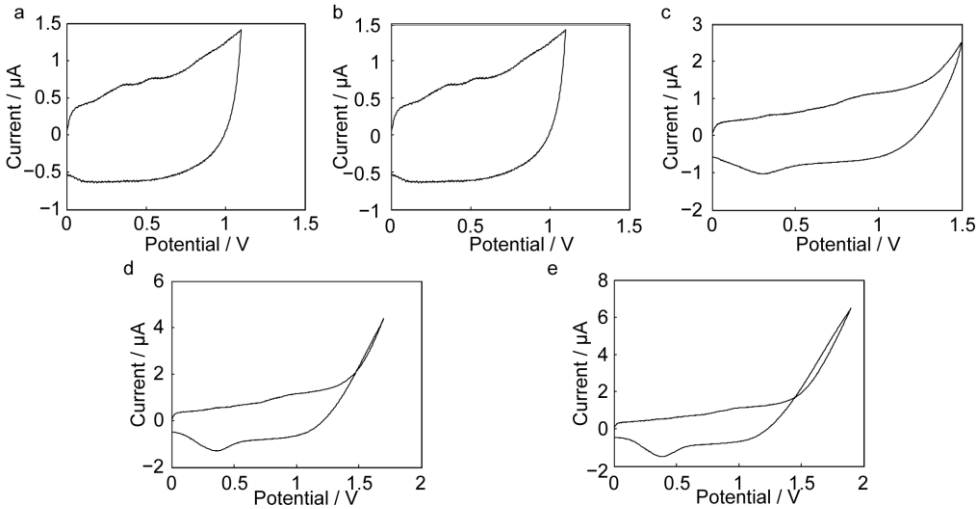

Figure 7.6 Cyclic voltammograms for a droplet of 1 mM $NaClO_4$ solution (on AM grade HOPG) with the voltage swept in the range of (a) 0~+1.1 V, (b) 0~+1.3 V, (c) 0~+1.5 V, (d) 0~+1.7 V and (e) 0~+1.9 V. Scan rate: 1 V s^{-1}.

The oxidation-reduction process observed as the pair of peaks identified could be due to the intercalation/de-intercalation of anions,[34] or related to surface quinone-hydroquinone redox conversion (or other surface oxidation/reduction processes).[35] As we demonstrate below, the former process is most likely and is responsible for the electrowetting seen for the aqueous droplet.

On the forward scan of the CV (oxidation), ClO_4^- ions from the aqueous droplet can be driven into graphite through exposed step edges, overcoming the van de Waals forces between the graphene sheets.[36,37] This intercalation reaction is defined in eq. 7.1, and correlates to the small oxidation peak at ~+0.85 V and beyond:

$$C_x + ClO_4^- \rightleftharpoons C_x^+ ClO_4^- + e^- \qquad \text{(eq. 7.1)}$$

It has also been reported that side reactions, such as carbon oxidation and water splitting, occur at anodic potentials and might be responsible for the anodic currents we see at more positive potentials.[22,34] However, the surface oxidation process is slow and would not be expected to change the surface significantly and promote electrowetting, as we show with further measurements below.[38] Rather extreme conditions of potential, time and electrolyte are needed to produce significant changes to the graphite surface, such as exfoliation,[39,40] and these processes can be ruled out.

On the reverse scan of the CV (reduction), the de-intercalation of ClO_4^- from the graphite leads to the reduction peak observed on the CV (Figure 7.5 and Figure 7.6). As the upper potential limit was increased with further scans, it can be seen that intercalation/de-intercalation becomes more favoured, *i.e.* repetitive cycling leads to a break-in of the surface towards intercalation/de-intercalation. We examined AM HOPG by atomic force microscopy after the application of anodic potentials and found subtle changes in surface morphology around step edges, and also over the basal surface at a density similar to that estimated for point defects (Figure 7.7),[41,42] suggesting these locations (particularly step edges) as possible sites for ion intercalation/de-intercalation.

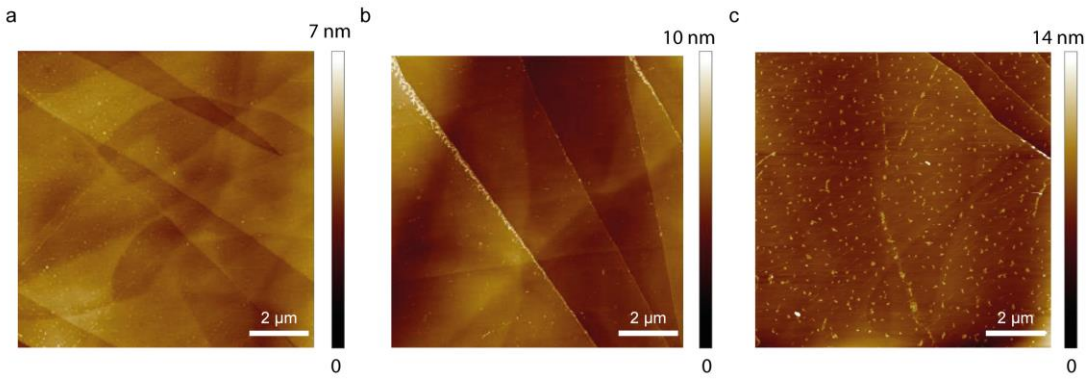

Figure 7.7 10 µm × 10 µm AFM images of AM HOPG after removal of a droplet of 1 mM $NaClO_4$ solution that had resided on the surface (a) for 2 min without any voltage applied, (b) for 2 min with the voltage held at 2 V and (c) with the voltage swept from 0 to 2 V for 30 cycles (1 V s^{-1}).

The reduction peak of the CVs was integrated to produce the charge transferred and the charge density, which is the ratio of charge to the droplet contact area (measured at the de-intercalation potential). The values were plotted against the upper potential limit of CVs, as shown in Figure 7.8. The charge density of the reduction peak increases more or less linearly with the upper limit of CV (and hence time). The surface concentration of ClO_4^- intercalated into AM HOPG can also be obtained, considering the one electron process of intercalation/de-intercalation (see eq. 7.1). The CV with the upper limit of +2 V leads to a surface concentration of 31 pmol cm^{-2}, accounting for 0.5% of the carbon atoms in the top graphene layer. This value is of similar magnitude to the step edge density on AM grade graphite (0.09%),[19] indicating that the extent of the intercalation process causing the electrowetting is rather subtle.

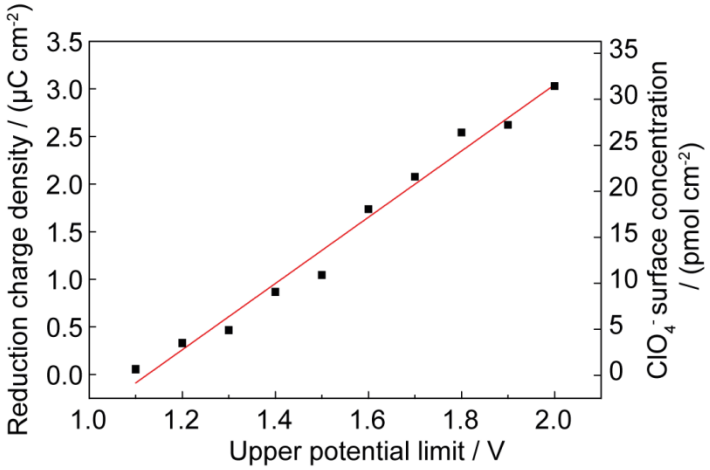

Figure 7.8 Charge density for the reduction peak of the CVs carried out in different potential ranges (at 1 V s^{-1}), and corresponding ClO_4^- surface concentration, plotted as a function of upper potential limit.

XPS measurements were carried out to characterise the compositions of AM HOPG surfaces. In the high-resolution XPS Cl 2p spectrum of the electrochemically-treated AM HOPG sample (Figure 7.9), a pronounced peak at a binding energy of 206.9 eV was observed, corresponding to the Cl $2p_{3/2}$ component arising from the intercalated perchlorate ions.[36] A second bonding environment was also observed, possessing a Cl $2p_{3/2}$ component at a binding energy of 208.3 eV and was attributed to adsorbed ClO_4^-.[43] The associated Cl $2p_{1/2}$ components were found to be at 208.5 eV (intercalated) and 209.9 eV (adsorbed). On the sample without electrochemical treatment, only adsorbed perchlorate ions (207.9 eV and 209.5 eV) were observed, along with a small amount of remnant $NaClO_4$ (209.3 eV and 210.9 eV) from removing the electrolyte droplet (Figure 7.10). The quantity of Cl was found to be significantly higher on the electrochemically-treated HOPG sample, compared with that of the control sample. These data confirm the intercalation of ClO_4^- ions into AM HOPG structure at relatively high anodic potentials, where electrowetting occurs. We believe this is the main effect causing electrowetting, although there may be some contribution from adsorbed ClO_4^-, which may adsorb on HOPG. [36]

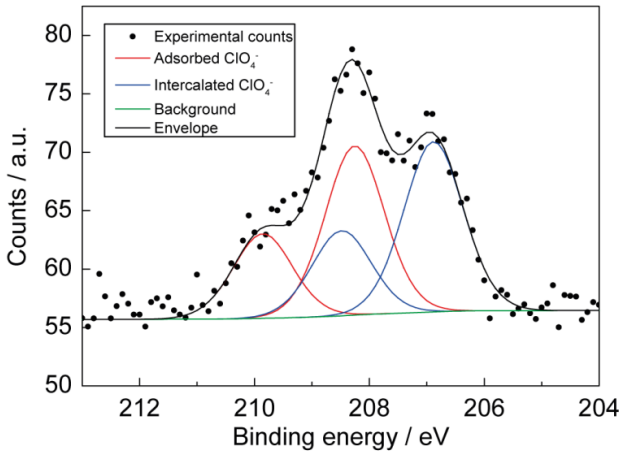

Figure 7.9 XPS spectrum of the Cl 2p region on electrochemically-treated AM HOPG (30 CVs swept from 0 to +2 V at 1 V s^{-1}, with the potential then held at +1.5 V for 30 s), using a droplet of 1 mM $NaClO_4$. The spectrum has been fitted with peaks for different species as indicated in the figure. The sum of fitting curves (black solid line) is consistent with the raw data (black dots).

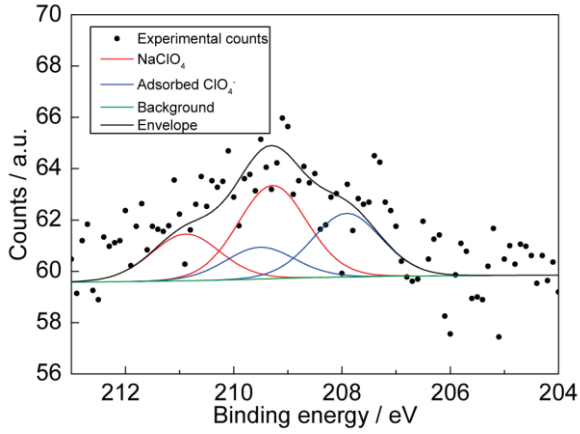

Figure 7.10 XPS spectrum of Cl 2p region on AM HOPG, without electrochemical treatment. The spectrum has been fitted with peaks for different species as indicated in the figure. The sum of fitting curves (black solid line) is consistent with the raw data (black dots).

7.2.2 Scan Rate Effect on Electrowetting

The influence of timescale on the intercalation/de-intercalation of ClO_4^- (1 mM $NaClO_4$) and electrowetting of the droplet was investigated on AM HOPG by comparing scan rates of 0.1, 0.3 and 1 V s^{-1}. Electrowetting behaviour was observed on HOPG at all scan rates employed, but to different extents. As shown in the examples in Figure 7.11a, when a slow scan rate (0.1 V s^{-1}) was employed, the CA for the droplet at a potential of +0.92 V on the forward scan (oxidation) was 34°. A CA of 42° at +0.96 V (on the forward scan) was obtained for the intermediate scan rate (0.3 V s^{-1}). As the scan rate was increased to 1 V s^{-1}, a CA of 44° at +1.09 V (on the forward scan) was obtained. Thus, even though the potential is increasingly higher in this series of images, the scan rate (timescale) has a significant effect. In fact, the corresponding CV responses show that the reduction peak (de-intercalation) shifted negatively, while the oxidation peak (intercalation) shifted positively, and both became less pronounced, with increasing scan rate. The corresponding intercalation charges were 61 nC (0.1 V s^{-1}), 1.8 nC (0.3 V s^{-1}) and 0.5 nC (1 V s^{-1}). At slow scan rates, the intercalation/de-intercalation process clearly occurs more extensively at the HOPG substrate. As a result, a minimum CA of 18° was obtained for the droplet with the CV swept at 0.1 V s^{-1}, compared to that of 20° and 25° for 0.3 and 1 V s^{-1}, respectively (Figure 7.11b). Moreover, the electrowetting process follows the CV response more faithfully at slow scan rate, leading to a smaller hysteresis of CA between the forward and reverse sweeps.

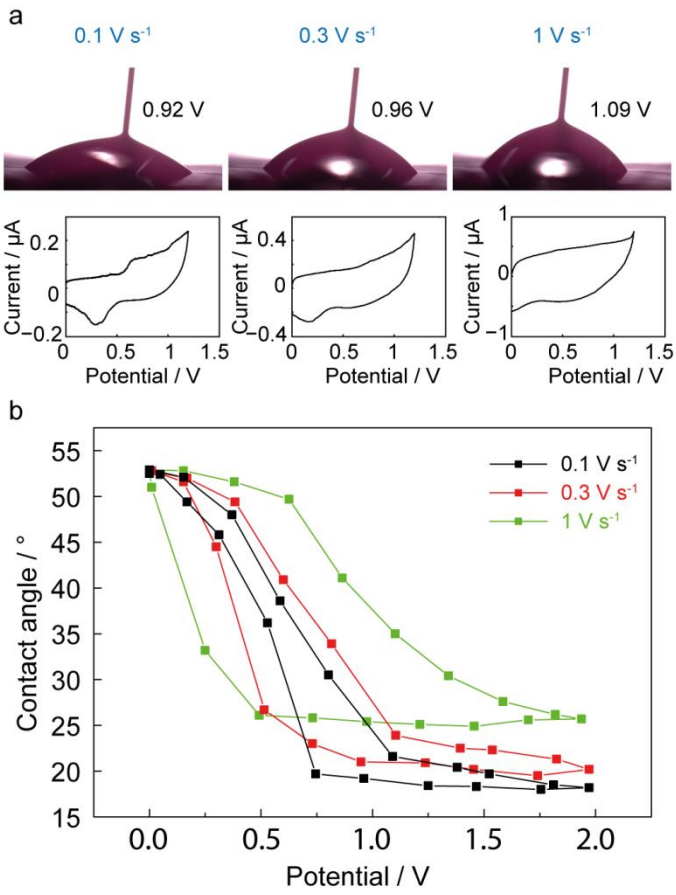

Figure 7.11 (a) Snapshots for droplet electrowetting of 1 mM $NaClO_4$ solution on AM HOPG during the forward scan of a cyclic voltammogram in the potential range of 0~+1.2 V, with scan rates of 0.1, 0.3 and 1 V s^{-1}. The potentials at which the snapshots were taken are indicated and the full cyclic voltammograms are shown below. (b) Contact angle of a 1 mM $NaClO_4$ droplet on AM HOPG plotted against the potential, during CV measurements from 0 to +2 V at scan rates of 0.1, 0.3 and 1 V s^{-1}.

It should be noted that in some cases the droplet could detach from the CE/RE due to the significant electrowetting on AM HOPG at positive potentials. In this situation, the HOPG surface is at the open-circuit potential, yet a low CA and high RCD were found to be maintained. This is excellent evidence that electrochemically-driven intercalation is responsible for the electrowetting. When the cell connection was re-made by moving the CE/RE down into the spread droplet (at 0 V), de-intercalation occurs and the droplet recovered its original morphology (Figure 7.12).

Figure 7.12 Optical images of a droplet (1 mM $NaClO_4$) on AM HOPG during CV performed over the potential range of 0~+2 V, recorded at a potential of (a) 0 V (at the start of CV); (b) +1.68 V (on the forward scan), when the droplet detached from the CE/RE due to significant electrowetting and (c) 0 V (at the end of CV), when the electric circuit was re-connected. Scan rate: 0.3 V s^{-1}. The contact angle is marked in each image.

7.2.3 Potential Polarity Effect on Electrowetting

When CV potential scanning was in the cathodic window with AM HOPG, no obvious changes in CA and RCD of droplet were observed (Figure 7.13), with the same concentration (1 mM) of $NaClO_4$ solution used. The CA only varied by 2^o at most during the CV and the RCD was more or less stable. Thus, electrowetting of the aqueous droplet on HOPG only occurred at positive potentials. This behaviour is in agreement with a study of electrowetting of carbon nanotube membranes,[44] although the effect in that case was attributed to electrochemistry of oxygen-containing surface functional groups. That we only observe electrowetting in the positive potential region, means that the mechanism is different from the EWOD, which is only weakly dependent on the polarity of potential applied, and tends to follow the Young-Lippmann equation.[4,7,12]

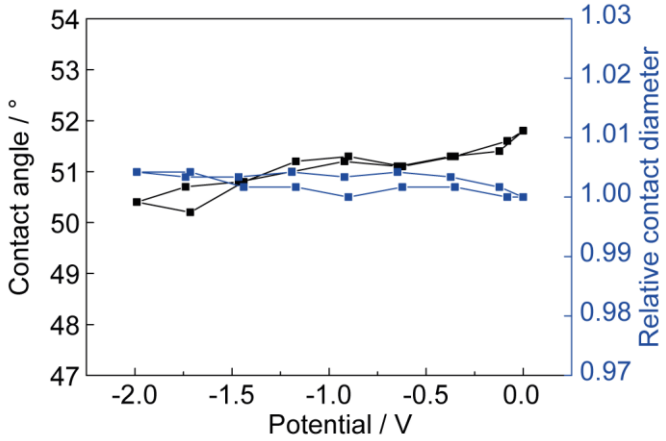

Figure 7.13 Contact angle and relative contact diameter of electrowetting for a droplet of 1 mM $NaClO_4$ solution at the surface of AM HOPG plotted against the potential of a CV carried out in the range of 0~-2 V, with a scan rate of 1 V s^{-1}.

7.2.4 Substrate Effect on Electrowetting

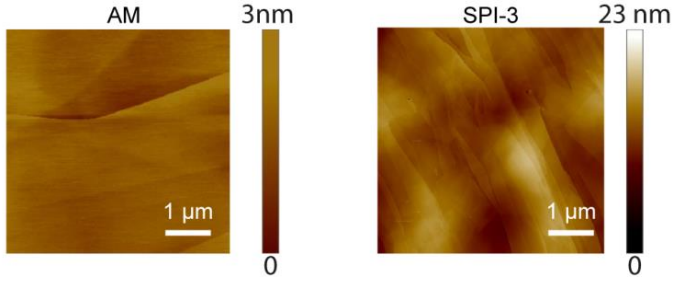

Figure 7.14 5 × 5 µm tapping-mode AFM images of AM and SPI-3 grade HOPG. Note the differences in the height scale.

As the (electro-)wetting of a substrate by a droplet can be affected by the roughness of the substrate,[18,45,46] some droplet-cell experiments (1 mM $NaClO_4$) were also conducted on the surface of SPI-3 grade HOPG, which has more than 2 orders of magnitude more step edges (density) than AM (Figure 7.14), with a predominance of multilayer rather than monolayer step edges.[19,47-49] This leads to higher roughness of SPI-3. According to Wenzel model:[45,46]

$$\cos\theta_r = r_s \cos\theta_0 \qquad \text{(eq. 7.2)}$$

where θ_r and θ_0 are the CA on a rough surface and a flat surface, respectively, and r_s is the surface roughness, defined as the ratio of the actual area of the rough surface to the geometric projected area, one might expect the CA on AM HOPG to be larger than for SPI-3 HOPG at all potentials. However, in contrast to the observations on AM HOPG during CV scanning, only a small amount electrowetting of the droplet was seen on SPI-3 (Figure 7.15). A decrease of 6° in CA was obtained during the scan from 0 to +2 V, while an increase of 4.5% was seen for RCD at a scan rate of 1 V s^{-1}(compare Figure 7.15 with Figure 7.1c). This is a very striking difference in behaviour.

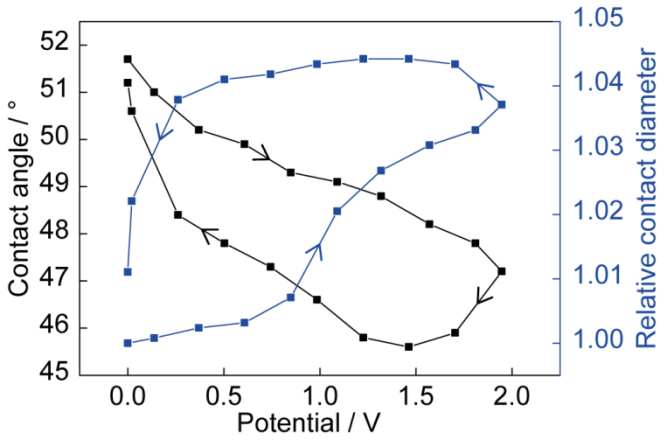

Figure 7.15 Contact angle and relative contact diameter of electrowetting for a droplet of 1 mM $NaClO_4$ solution at the surface of SPI-3 HOPG plotted against the potentials of a CV carried out in the range of 0~2 V, with a scan rate of 1 V s^{-1}.

A total of 20 repetitive CVs between 0 and +2 V (1 V s^{-1}) were carried out on the freshly cleaved surface of each grade of HOPG, to resolve possible electrochemical reactions, with the resulting voltammograms shown in Figure 7.16. On AM HOPG, we observe the development of the cathodic potential peaks that we described earlier, and the anodic oxidation process at the most positive potentials > +1.5 V. In contrast, even over 20 successive scans for SPI-3 HOPG, only the anodic current at > +1.5V was discernible, with little evidence of ion intercalation/de-intercalation. This result, over the potential range shown, is important as it further confirms that the oxidation

process at > +1.5 V are not the dominant factor in droplet electrowetting of AM HOPG.

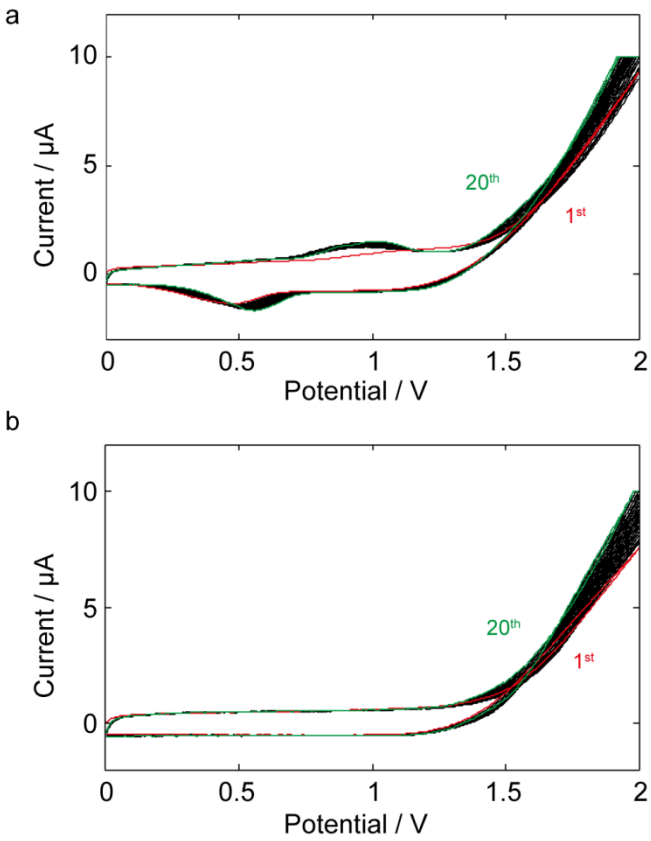

Figure 7.16 Twenty repetitive cyclic voltammograms for a droplet of 1 mM $NaClO_4$ solution on (a) AM grade and (b) SPI-3 grade HOPG, recorded in the potential range of 0~+2 V, at a scan rate of 1 V s^{-1}.

We attribute the difference in the electrochemical responses of these two grades of HOPG to the feasibility (or not) of intercalation/de-intercalation processes. The intercalation of ions requires sufficient energy to overcome the van de Waals forces that hold the graphene layers together in graphite. The energy increases with the number of adjacent graphene layers.[36,37] Since AM HOPG has low step edge coverage of monoatomic steps,[19,48] as illustrated schematically in Figure 7.17a, ClO_4^- ions can be relatively easily inserted into the graphene layers of AM HOPG through the (exposed) step edges during the forward scan of CV (oxidation), which are negatively charged atop a neutral underlying basal surface.[50,51] The intercalation produces enhanced electrowetting of the droplet on graphite through the

introduction of oxygen-containing ions (ClO_4^-). As the scan number is increased, the intercalation/de-intercalation of ClO_4^- becomes easier, causing the reduction peak to shift to positive potentials, for example, as described above. Compared with AM HOPG, SPI-3 HOPG has many more step edges that are predominantly multiple layers.[47,49] This greatly enhances the binding force between the graphene layers, leading to less delamination of step edges with time.[52] Moreover, anion intercalation would be hindered by strong repulsive coulombic forces, due to the large amount of negative charges at the multilayer step edges.[50,51] As a result, considerably more energy is required for the intercalation of ClO_4^- ions into SPI-3 HOPG, making it less vulnerable to the attack of ClO_4^- anions (Figure 7.17b). This mechanism can also be used to explain the asymmetry of the electrowetting droplet observed occasionally in some cases (Figure 7.3), as the step edge density and arrangement on AM HOPG, is non-uniform[19] and determined by the cleavage.

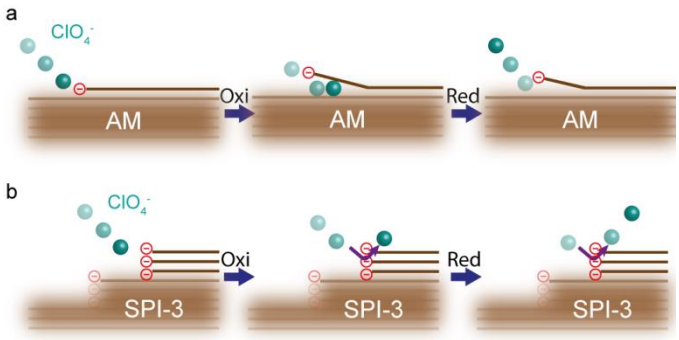

Figure 7.17 Schematic depicting the pathway of ClO_4^- under CV conditions anodically for (a) AM HOPG, leading to the intercalation (oxidation) and de-intercalation (reduction) processes at monolayer step edges and (b) SPI-3 HOPG, where little intercalation/de-intercalation of ClO_4^-occurs at multilayer step edges (not to scale). Note that negative charges at step edges (oxygen-containing moieties) are marked in red.

7.2.5 Anion Effect on Electrowetting

There have been considerable efforts to study anion intercalation into graphite, so as to elucidate the intercalating properties of different types of anions.[21,23] Considering the relationship between intercalation and

electrowetting that we have described, we found that similar effects to those reported above for ClO_4^- were found with SO_4^{2-}, with a typical response of contact angle and relative contact diameter versus potential in 1 mM Na_2SO_4 solution shown in Figure 7.18. The corresponding CV is shown in Figure 7.19. However, two other types of much larger anions, $H_2PO_4^-/HPO_4^{2-}$ (from Na_3PO_4 solution that was adjusted to a pH ~7 with the aid of H_3PO_4 before use, under which conditions the predominant forms of anion in the solution are HPO_4^{2-} and $H_2PO_4^-$ [53]) and fluorescein dianion, with a concentration of 1 mM, were also briefly considered on AM HOPG during CV measurements. Experiments were conducted in the same potential range as for ClO_4^- (*i.e.* 0~+2 V vs Ag/AgCl). We found the droplet containing $H_2PO_4^-/HPO_4^{2-}$ did not electrowet AM HOPG surface, in line with other studies.[21] In the case of fluorescein, the droplet was shown to maintain its shape under the potentials applied and no electrowetting was observed. The corresponding CVs demonstrated no oxidation and reduction peaks for intercalation and de-intercalation of ions (Figure 7.20).

This study further confirms that the intercalation/de-intercalation of specific ions (ClO_4^-), rather than the anodic formation of graphite oxide or, water oxidation is responsible for the electrowetting of graphite that we observe.

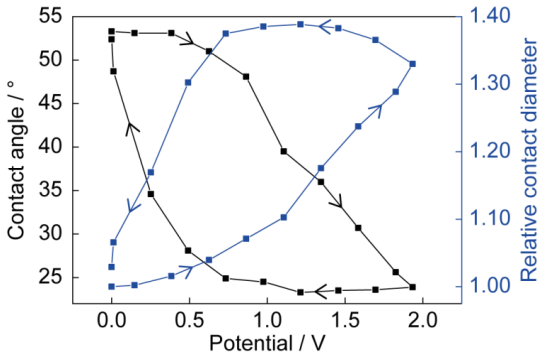

Figure 7.18 Contact angle and relative contact diameter of electrowetting for a droplet of 1 mM Na_2SO_4 solution at the surface of AM HOPG plotted against the potentials of a CV carried out in the range of 0~+2 V, with a scan rate of 1 V s^{-1}.

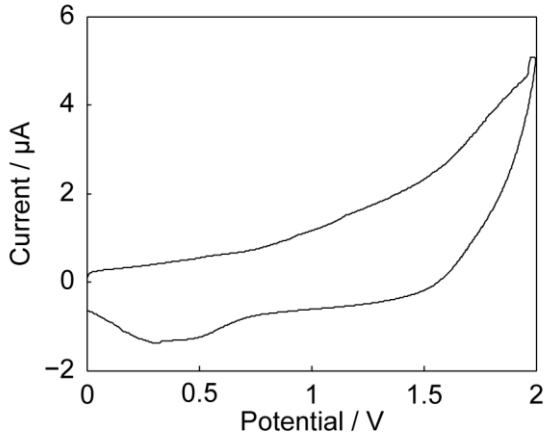

Figure 7.19 Cyclic voltammogram of a droplet of 1 mM Na_2SO_4 solution on AM HOPG, recorded from 0 V to +2 V at a scan rate of 1 V s^{-1}.

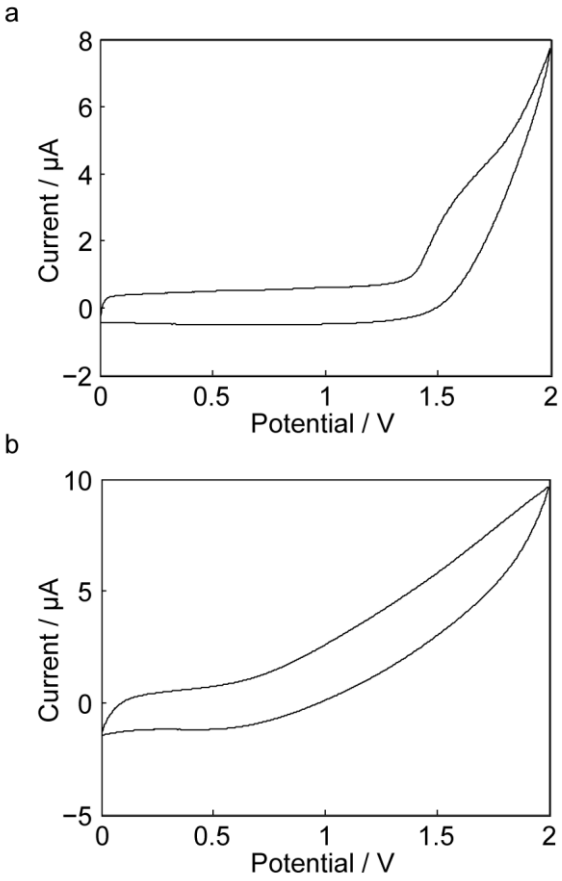

Figure 7.20 Cyclic voltammograms of a droplet of (a) 1 mM Na_3PO_4 solution (pH ~7) and (b) 1 mM sodium fluorescein solution on AM HOPG at a scan rate of 1 V s^{-1}.

7.3 Conclusions

We have demonstrated a new mechanism for electrowetting based on ClO_4^- (and SO_4^{2-}) intercalation/de-intercalation into step edges on the basal surface of HOPG. Intercalation/de-intercalation of ClO_4^- (and SO_4^{2-}) in the top graphene layers of graphite surfaces, induces changes in local surface morphology and charge that alters the wettability of the substrate by the droplet. Electrowetting occurs at moderate positive potentials under CV conditions where ClO_4^- intercalation occurs. The slowest scan rate investigated (0.1 V s^{-1}) leads to more significant intercalation which enhances the electrowetting behaviour. Little electrowetting of $NaClO_4$ aqueous solution was seen on SPI-3 HOPG, as the energy to expand the gaps between graphene layers is greatly enhanced by the strong binding force imposed by the high-density of multilayer step edges.

The work we have presented shows that electrochemistry can be used as a powerful means for tailoring the surface properties of graphite and manipulating the movement of a droplet on it. The possibility of using ion intercalation/de-intercalation to introduce significant, reversible and repeatable electrowetting phenomena on a reasonable timescale opens up new prospects for low voltage electrowetting devices based on layered materials and/or ion intercalation/de-intercalation that do not require an EWOD format.

7.4 References

(1) Frysali, M. A.; Papoutsakis, L.; Kenanakis, G.; Anastasiadis, S. H. *J. Phys. Chem. C* **2015**, *119*, 25401.

(2) Xu, L.; Liu, N.; Cao, Y.; Lu, F.; Chen, Y.; Zhang, X.; Feng, L.; Wei, Y. *ACS Appl. Mater. Interfaces* **2014**, *6*, 13324.

(3) Chowdhury, D.; Maoz, R.; Sagiv, J. *Nano Lett.* **2007**, *7*, 1770.

(4) Paneru, M.; Priest, C.; Sedev, R.; Ralston, J. *J. Am. Chem. Soc.* **2010**, *132*, 8301.

(5) Kornyshev, A. A.; Kucernak, A. R.; Marinescu, M.; Monroe, C. W.; Sleightholme, A. E. S.; Urbakh, M. *J. Phys. Chem. C* **2010**, *114*, 14885.

(6) Taherian, F.; Leroy, F.; van der Vegt, N. F. A. *Langmuir* **2015**, *31*, 4686.

(7) Ricks-Laskoski, H. L.; Snow, A. W. *J. Am. Chem. Soc.* **2006**, *128*, 12402.

(8) Hayes, R. A.; Feenstra, B. J. *Nature* **2003**, *425*, 383.

(9) Kuiper, S.; Hendriks, B. H. W. *Appl. Phys. Lett.* **2004**, *85*, 1128.

(10) Yeo, L.; Friend, J. In *Encyclopedia of Microfluidics and Nanofluidics*; Li, D., Ed.; Springer US: 2014, p 1.

(11) Yeo, L. Y.; Chang, H.-C. *Phys. Rev. E* **2006**, *73*, 011605.

(12) Klarman, D.; Andelman, D.; Urbakh, M. *Langmuir* **2011**, *27*, 6031.

(13) Bhushan, B.; Pan, Y. *Langmuir* **2011**, *27*, 9425.

(14) Restolho, J.; Mata, J. L.; Saramago, B. *J. Phys. Chem. C* **2009**, *113*, 9321.

(15) Annapragada, S. R.; Dash, S.; Garimella, S. V.; Murthy, J. Y. *Langmuir* **2011**, *27*, 8198.

(16) Chen, L.; Li, C.; van der Vegt, N. F. A.; Auernhammer, G. K.; Bonaccurso, E. *Phys. Rev. Lett.* **2013**, *110*, 026103.

(17) Liu, Y.; Liang, Y.-E.; Sheng, Y.-J.; Tsao, H.-K. *Langmuir* **2015**, *31*, 3840.

(18) Pu, J.; Wan, S.; Lu, Z.; Zhang, G.-a.; Wang, L.; Zhang, X.; Xue, Q. *J. Mater. Chem. A* **2013**, *1*, 1254.

(19) Patel, A. N.; Collignon, M. G.; O'Connell, M. A.; Hung, W. O.; McKelvey, K.; Macpherson, J. V.; Unwin, P. R. *J. Am. Chem. Soc.* **2012**, *134*, 20117.

(20) Yoon, G.; Seo, D.-H.; Ku, K.; Kim, J.; Jeon, S.; Kang, K. *Chem. Mater.* **2015**, *27*, 2067.

(21) Hathcock, K. W.; Brumfield, J. C.; Goss, C. A.; Irene, E. A.; Murray, R. W. *Anal. Chem.* **1995**, *67*, 2201.

(22) Alsmeyer, D. C.; McCreery, R. L. *Anal. Chem.* **1992**, *64*, 1528.

(23) Noel, M.; Santhanam, R. *J. Power Sources* **1998**, *72*, 53.

(24) Hui, J.; Burgess, M.; Zhang, J.; Rodriguez-Lopez, J. *ACS Nano* **2016**, *10*, 4248.

(25) Williams, C. G.; Edwards, M. A.; Colley, A. L.; Macpherson, J. V.; Unwin, P. R. *Anal. Chem.* **2009**, *81*, 2486.

(26) McHale, G.; Rowan, S. M.; Newton, M. I.; Banerjee, M. K. *J. Phys. Chem. B* **1998**, *102*, 1964.

(27) Li, Z.; Wang, Y.; Kozbial, A.; Shenoy, G.; Zhou, F.; McGinley, R.; Ireland, P.; Morganstein, B.; Kunkel, A.; Surwade, S. P.; Li, L.; Liu, H. *Nat. Mater.* **2013**, *12*, 925.

(28) Ashraf, A.; Wu, Y.; Wang, M. C.; Aluru, N. R.; Dastgheib, S. A.; Nam, S. *Langmuir* **2014**, *30*, 12827.

(29) Schrader, M. E. *J. Phys. Chem.* **1980**, *84*, 2774.

(30) Hong, S.-J.; Li, Y.-F.; Hsiao, M.-J.; Sheng, Y.-J.; Tsao, H.-K. *Appl. Phys. Lett.* **2012**, *100*, 121601.

(31) Wei, Y.; Jia, C. Q. *Carbon* **2015**, *87*, 10.

(32) Kozbial, A.; Li, Z.; Sun, J.; Gong, X.; Zhou, F.; Wang, Y.; Xu, H.; Liu, H.; Li, L. *Carbon* **2014**, *74*, 218.

(33) Hung, S.-W.; Hsiao, P.-Y.; Chen, C.-P.; Chieng, C.-C. *J. Phys. Chem. C* **2015**, *119*, 8103.

(34) Walker, E. K.; Vanden Bout, D. A.; Stevenson, K. J. *Anal. Chem.* **2012**, *84*, 8190.

(35) Choo, H.-S.; Kinumoto, T.; Nose, M.; Miyazaki, K.; Abe, T.; Ogumi, Z. *J. Power Sources* **2008**, *185*, 740.

(36) Schnyder, B.; Alliata, D.; Kötz, R.; Siegenthaler, H. *Appl. Surf. Sci.* **2001**, *173*, 221.

(37) Alliata, D.; Kötz, R.; Haas, O.; Siegenthaler, H. *Langmuir* **1999**, *15*, 8483.

(38) Goss, C. A.; Brumfield, J. C.; Irene, E. A.; Murray, R. W. *Anal. Chem.* **1993**, *65*, 1378.

(39) Parvez, K.; Wu, Z.-S.; Li, R.; Liu, X.; Graf, R.; Feng, X.; Müllen, K. *J. Am. Chem. Soc.* **2014**, *136*, 6083.

(40) Parvez, K.; Li, R.; Puniredd, S. R.; Hernandez, Y.; Hinkel, F.; Wang, S.; Feng, X.; Müllen, K. *ACS Nano* **2013**, *7*, 3598.

(41) Chang, H.; Bard, A. J. *J. Am. Chem. Soc.* **1991**, *113*, 5588.

(42) Chang, H.; Bard, A. J. *J. Am. Chem. Soc.* **1990**, *112*, 4598.

(43) Moulder, J. F.; Stickle, W. F.; Sobol, P. E.; Bomben, K. D. *Handbook of X-ray Photoelectron Spectroscopy*; Physical Electronics Division, Perkin-Elmer Corporation: Eden Prairie, MN, 1992.

(44) Wang, Z.; Ci, L.; Chen, L.; Nayak, S.; Ajayan, P. M.; Koratkar, N. *Nano Lett.* **2007**, *7*, 697.

(45) Han, Z.; Tay, B.; Tan, C.; Shakerzadeh, M.; Ostrikov, K. *ACS Nano* **2009**, *3*, 3031.

(46) Shirtcliffe, N. J.; McHale, G.; Newton, M. I.; Perry, C. C. *Langmuir* **2005**, *21*, 937.

(47) Patel, A. N.; Tan, S. Y.; Unwin, P. R. *Chem. Commun.* **2013**, *49*, 8776.

(48) Zhang, G.; Kirkman, P. M.; Patel, A. N.; Cuharuc, A. S.; McKelvey, K.; Unwin, P. R. *J. Am. Chem. Soc.* **2014**, *136*, 11444.

(49) Patel, A. N.; Tan, S. Y.; Miller, T. S.; Macpherson, J. V.; Unwin, P. R. *Anal. Chem.* **2013**, *85*, 11755.

(50) Lai, S. C. S.; Patel, A. N.; McKelvey, K.; Unwin, P. R. *Angew. Chem. Int. Ed.* **2012**, *51*, 5405.

(51) Koestner, R.; Roiter, Y.; Kozhinova, I.; Minko, S. *J. Phys. Chem. C* **2011**, *115*, 16019.

(52) Güell, A. G.; Cuharuc, A. S.; Kim, Y. R.; Zhang, G.; Tan, S. Y.; Ebejer, N.; Unwin, P. R. *ACS Nano* **2015**, *9*, 3558.

(53) Weast, R. C. *CRC Handbook of Chemistry and Physics*; 64th ed.; CRC Press: Boca Raton, Florida, 1983.

Chapter 8 Conclusions

In this thesis, the electrochemistry of HOPG has been extensively studied with various experimental frameworks, ranging from macroscale to nanoscale. In the macroscopic measurements using a droplet-cell configuration, the electrochemical responses of redox couples are promptly obtained after cleavage of HOPG surface (minimising possible atmospheric contamination) and thoroughly compared on many different grades of HOPG. By using powerful high resolution approaches, in the form of correlative-electrochemical microscopy, that can target particular local features on the HOPG surface (basal plane or step edges), major new perspectives on electrochemical processes at the nanoscale can be provided, as a result of which, possible structure–activity effects can be elucidated. From the studies presented herein, it is found that basal plane of HOPG is essentially highly active for ET, and is the dominant site in the overall electroactivity of HOPG.

Chapter 3 and Chapter 4 presented a macroscopic study of the electrochemistry of HOPG samples that vary in step edge density by more than 2 orders of magnitude, using redox couples of classical outer-sphere species ($IrCl_6^{2-/3-}$, $Ru(NH_3)_6^{3+/2+}$ and $Fe(CN)_6^{4-/3-}$) and $Fe^{3+/2+}$ (known to show slow ET kinetics). Fast ET kinetics were observed for $IrCl_6^{2-/3-}$, $Ru(NH_3)_6^{3+/2+}$ and $Fe(CN)_6^{4-/3-}$ across all the HOPG grades studied, and it was found that the ET kinetics of $IrCl_6^{2-/3-}$ ($k_0 > 1.9$ cm s^{-1}) and $Fe(CN)_6^{4-/3-}$ ($k_0 > 0.46$ cm s^{-1}) on HOPG was as fast as on Pt electrodes and comparable to Pt electrodes for $Ru(NH_3)_6^{3+/2+}$ ($k_0 > 0.61$ cm s^{-1}) on HOPG. Even for $Fe^{3+/2+}$, there was little impact on ET kinetics from step edges (complemented by SECCM activity mapping data) and the k_0 (~5×10^{-5} cm s^{-1}) was within the range reported on metal electrodes (*e.g.* Pt and Au). Given the significant difference in DOS between graphite and metals, it is concluded that DOS does not play an important role in the ET kinetics of the reactions studied herein, indicative of an adiabatic nature of outer-sphere ET processes.

Chapter 5 provides unequivocal evidence that adsorbed electroactive AQDS is by no means a marker of the active sites of graphite surface. Macroscopic electrochemistry results have shown identical voltammetric responses of adsorbed electroactive AQDS on four grades of HOPG, despite the massive difference in step edge coverage. FSCV-SECCM measurements made on spots with a series of adsorption times allowed adsorption to be tracked on a short time scale, revealing that there was no correlation between AQDS coverage and step edge density (characterised by subsequent AFM imaging). SECCM reactive patterning of HOPG enabled the basal surface or step edges to be targeted individually, and showed uniform high electroactivity across the whole surface probed, in line with the macroscopic and microscopic results.

Chapter 6 demonstrated the development of a polymer-free method for CVD graphene transfer, making use of an etchant-hexane interface. This approach avoids polymeric contamination and the resulting detrimental effects to the graphene properties. Furthermore, it facilitates the fabrication of tools for microscopy studies by transferring graphene onto 3D substrates, such as AFM tips and TEM grids. As a result, graphene-coated AFM tips are suitable for conductive AFM measurements, where topography and electrical properties can be simultaneously and correlatively studied. Graphene TEM grids not only act as good supports for high resolution TEM imaging of nanoparticles, but also provide an integrated platform, allowing for wetting and electrochemistry of supported and suspended graphene to be readily assessed and compared. The results presented in this thesis suggest that supported graphene shows stronger wettability and both forms of graphene exhibit high electroactivity towards the redox species used in this study.

Chapter 7 presented a new mechanism for electrowetting of aqueous droplets on the surface of HOPG. Compared with the widely studied EWOD configuration, the electrowetting of droplets in direct contact with HOPG surface was observed under much lower potential range, with a fast, reversible, and repeatable behaviour for at least 20 consecutive CV scans. The electrowetting was found to be due to the intercalation/ de-intercalation

of some anions (*e.g.* ClO_4^- and SO_4^{2-}) into the graphene layers of graphite with applied anodic potentials, which was reflected by the CV responses and detected by XPS measurements. This phenomenon can be influenced by scan rate, potential polarity, HOPG quality and anion type.

To summarise, a radical new view of the electrochemistry of graphite materials that basal plane is intrinsically high active has been presented, revising the literature model, and with implications for studies of related materials, such as carbon nanotubes and graphene. Moreover, the methodology developed for graphene transfer and the mechanism discovered for the electrowetting on HOPG are crucial to fundamental understanding of the properties and further applications of carbon materials.